

University of Nottingham
UK | CHINA | MALAYSIA

Utilising Micron-Scale 3D Printing to Investigate Particulate Interactions for Respiratory Applications

Georgina Elizabeth Marsh MPharm

Thesis submitted to the University of Nottingham

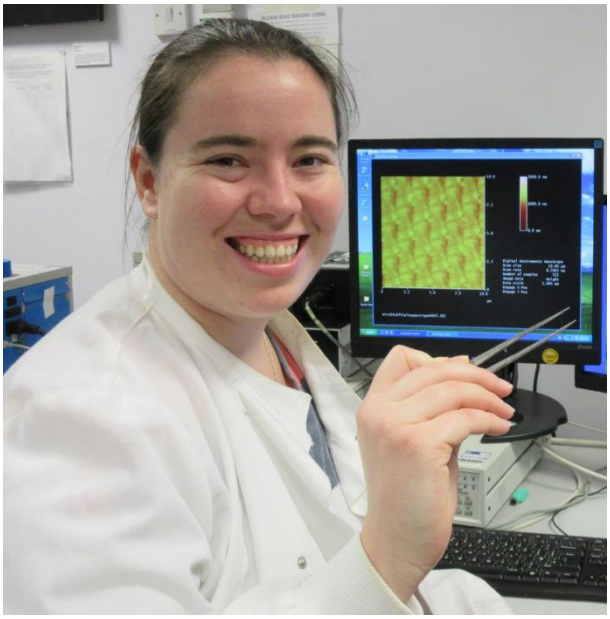
for the degree of Doctor of Philosophy

September 2017

“Man who catch fly with chopstick accomplish anything.”

(or woman who attaches particles to AFM tips)

Mr Miyagi – Karate Kid (1984)



“If you had
One shot
Or one opportunity
To seize everything you ever wanted
In one moment
Would you capture it,
Or just let it slip?”

Eminem – lose yourself

Abstract

In order to achieve drug delivery via the respiratory route, an understanding of particulate interactions is of vital importance. For successful delivery to the distal airways, an aerodynamic diameter of less than 5 µm must be achieved. However, particles of this size presents a difficult formulation challenge, due to the inherent cohesiveness between particles and adhesion to the device, due to the high surface to volume ratio of such small particles, causing the particles to clump together. This tendency will thereby cause a reduction in dispersion, aerosolisation and device efficiency; for this reason dry powder inhalers (DPIs) invariably fail to achieve a fine particle fraction efficiency above 15%.

There are a wide variety of factors which affect particulate interactions including; surface roughness, surface chemistry, particle size or shape and particle mechanical properties. However, these factors are highly interrelated and so previous attempts to investigate their effect on particle adhesion generally have difficulty isolating the impact of each factor. For instance, investigating the effect of morphology on particulate interactions invariably utilise destructive techniques to alter the roughness, which is likely to alter other factors like surface energy and provide limited control for optimisation. With the rise of 3D printing (additive manufacturing) there is now the capability to produce sub- micron morphologies, and so a bottom-up approach to studying the effect of morphology on particulate interactions can be achieved.

The aims of this thesis are therefore twofold. Firstly, to identify, optimise and evaluate a suitable additive manufacturing technique to produce well-defined micron scale morphologies appropriate for furthering the understanding of the importance of morphology on particle adhesion. This is a scale which is at least two orders of magnitude improvement on current state of the art 3D inkjet printers. Secondly, to measure the effect on particle adhesion and deposition to these morphologies, both on an individual particle and on a bulk powder basis, allowing

elucidation and understanding of the effect of surface roughness on particle adhesion, with a specific focus on respiratory drug delivery.

Printing well defined geometries of an appropriate micron scale size range for particle adhesion testing has been achieved, using two photon polymerisation (TPP). TPP is a novel 3D printing technique which as its name suggests involves the curing of usually acrylate containing polymer resins by the absorption of two infra-red photons in the focus of the laser beam. TPP has been shown to produce a sub-diffraction limit lateral resolution of 120 nm. By optimising the printer parameters and experimentation with differing structure fill and input settings the creation of a well- defined curve on a micron scale was achieved. The initial test morphologies comprised of a ridge with a semi-circular top with a diameter of 1 µm, which were shown to be reproducibly printed. These morphologies were then varied in a controllable fashion with varying ridge height and spacing between the ridges. A uniform and consistent surface chemistry was created using a plasma polymerised hexane (ppHex) coating.

In order to evaluate particulate interactions relevant to pulmonary drug delivery both an understanding of the effect of morphology on both individual particle adhesion and bulk powder deposition in a fluid environment is needed. Individual particle-surface adhesion was achieved by testing the TPP structures against three particle types using single particle colloidal probe microscopy (polystyrene beads diameter 10 µm and 5 µm and a lactose particle designed for inhalation formulations). The analysis of this data provides evidence of a clear trend between particle contact area and adhesion recorded both on the ppHex control and the TPP coated morphologies. The TPP morphologies are shown to locally reduce the overall adhesion, in comparison to the flat substrate. The ridge height is also seen to have a significant effect on particle adhesion, with 5 µm < 3 µm < 1 µm for the polystyrene beads, but 3 µm < 5 µm < 1 µm for the Respitose SV003 lactose particle for all ridge spacings. Varying the ridge spacing produced two differing trends in adhesion to the polystyrene beads. If the particle was unable to penetrate the valleys of the roughness, for the 1 µm high ridges, a significant effect on particle adhesion was seen with 3 µm < 1 µm for the polystyrene beads. In contrast, the 3 µm and 5 µm high

ridges showed the opposite trend when the particle is unable to descend between the ridges with 1 µm < 3 µm < 8 µm for the polystyrene beads.

Investigation of the bulk powder deposition of the particles on the TPP structures and any subsequent re-entrainment in a fluid environment was then achieved using a novel methodology developed during the course of this work. This combines the use of a standard next generation impactor, which generally is used to separate out a respiratory formulation based on aerodynamic diameter, with the TPP substrates. This shows that ridge height has a significant effect on particle adhesion with 3 µm < 1 µm < 5 µm. In contrast, the different spacings of the ridges were not shown to produce a significant difference in particle deposition. This is likely due to the conflicting effect of asperity spacing on the processes of particle deposition and re-entrainment.

This thesis therefore highlights the capability of TPP, to produce well-defined micron scale structures with varying morphologies. It then shows that these can be successfully utilised to provide valuable insight into the effect of surface morphology on particle- surface interactions, specifically; adhesion, deposition and re-entrainment.

Acknowledgements

I would like to thank my supervisors Prof. Clive Roberts, Prof. Morgan Alexander, Prof. Ricky Wildman, Dr. Matt Bunker and Dr. Mark Nicholas for their guidance throughout my PhD. However, I would particularly like to thank Clive for putting up with my continual impromptu meetings, his valuable and timely feedback on my thesis chapters and helping to keep me on track. I would like to also acknowledge AstraZeneca and the EPSRC (EP/L01646X) for funding.

I would like to thank Dr. Xinyong Wong for his technical assistance and instruction on the use of the AFM and his unflappable response to equipment failures. Dr Patrik Andersson and Simon Åslund for their help and instruction while I was in AstraZeneca, Sweden. Dr Andrew Hook for his training and guidance on plasma polymerisation. Dr David Scurr and Jatin Mistry for their assistance with Tof-SIMS. Prof. Phil Williams for his time and instruction in both ImageJ analysis and force-curve evaluation and understanding. Finally, my sincere thanks to Christine Grainger-Boultby and Dr Elisabeth Steer and the NMRC for their help with SEM, and the resolution of numerous and always amusingly unexpected machine malfunctions.

The continual support and friendship, in keeping me sane (relatively!), of all my friends is greatly appreciated in keeping me going. Special thanks to everyone in A03, for dragging me out for coffee and helping me to have a laugh even when stressed out with writing, especially; Rebe, Rachael, Sadie, Catherine, Jatin, Emanuele and Gordon! Also, everyone in the CDT, particularly my cohort, including Rosa for being there with me in the end, and Monica for helping me to have fun throughout the

PhD. Also, everyone in the LBSA (now the AMHT) and the TPP group. Finally, the tutors of Cripps Hall, specifically Spandan, Ahmed, Mo, Long, Russell, Say and Alex who have both, buoyed me up and supported me throughout the PhD, with lengthy board game sessions and continual banter.

Finally, I would like to thank my Mum, Dad and my brother Andrew, for always having confidence in my ability to succeed and in always being there for me day or night. Without them I would not have made it to this level, and would not be the person I am today.

Table of Contents

Abstract i

Acknowledgements iv

Table of Contents vi

List of Figures xiv

List of Tables xxiv

List of Abbreviations xxv

List of Symbols xxvii

1 Introduction 1

1.1 Introduction 1

1.2 Particle Adhesion in Industry 1

1.3 PhD Focus 2

1.4 Fundamentals of Particle Interactions 3

1.4.1 Forces Affecting Particle Interactions 3

1.4.2 Material Properties Affecting Particle-Surface Interactions 6

1.4.2.1 Surface Free Energy 6

1.4.2.2 Relative Humidity 7

1.4.2.3 Surface Roughness and Particle Morphology 7

1.4.2.4 Particle Deformation 9

1.5 Adhesion Models 9

1.5.1 The Hertz Model 10

1.5.2 JKR Model 11

1.5.3 DMT Model 12

1.5.4 Maugis-Dugdale Model 14
1.5.5 Rough Particles Adhesion 14
1.6 Methods to measure Particle Adhesion 15
1.6.1 Atomic Force Microscopy 16
1.6.1.1 Types of Imaging Modes 16
1.6.1.2 Force Measurements 19
1.6.1.3 Force Mapping 20
1.6.1.4 Colloidal Probe Microscopy 21
1.7 Pulmonary Drug Delivery 22
1.7.1 Aerosol Generation and Drug Deposition 23
1.7.2 Devices to Deliver Active Pharmaceutical Ingredients to the Lungs 25
1.7.2.1 Pressurised Metered Dose Inhalers (pMDIs) 25
1.7.2.2 Nebulisers 26
1.7.2.3 Dry Powder Inhalers (DPIs) 27
1.8 Surface Modification Methods to Alter Particle Adhesion Properties 28
1.8.1 Formulation Strategies/ Dry Coating 28
1.8.2 Mechanical Modification 29
1.8.3 Silanization 30
1.8.4 Patterned Surfaces 31
1.9 Additive Manufacturing 31
1.9.1 Pharmaceutical Additive Manufacturing 33
1.9.2 Additive Manufacturing in Pulmonary Drug Delivery 34
1.9.3 Two Photon Polymerisation 35
1.10 Thesis Aims 38
1.11 Thesis Objectives 38

1.12 Chapter References 39

2 Material and Methods for Colloidal Probe Production and Characterisation ... 51

2.1 Introduction 51

2.1.1 Scanning Electron Microscopy (SEM) 52

2.2 Chapter Aims 53

2.3 Chapter Objectives 54

2.4 Materials and Methods 54

2.4.1 Scanning Electron Microscopy (SEM) 54

2.4.2 Atomic Force Microscopy (AFM) 55

2.5 Results and Discussion 55

2.5.1 Scanning Electron Microscopy 55

2.5.2 Atomic Force Microscopy (AFM) 57

2.6 Colloidal Probe Production and Characterisation 60

2.6.1 Attachment of Particles to tips 60

2.6.2 Scanning Electron Microscopy of Colloidal Probes 62

2.6.3 AFM Tip Imaging 65

2.7 Chapter References 70

3 Selection and Optimisation of Additive Manufacturing Technique 73

3.1 Introduction 73

3.1.1 Selective Laser Sintering 73

3.1.2 PolyJet Inkjet Printing 74

3.1.3 Nanoscribe Two Photon Polymerisation 78

3.2 Chapter Aims 80

3.3 Chapter Objectives 80

3.4 Materials and Methods 81

3.4.1 Materials 81

3.4.2 Computer Aided Design (CAD) 81

3.4.3 Selective Laser Sintering (SLS) 81

3.4.4 PolyJet Printing 82

3.4.5 Two Photon Polymerisation (TPP) 82

3.4.6 Atomic Force Microscopy (AFM) 83

3.4.7 Scanning Electron Microscopy (SEM) 83

3.4.8 Surface Profilometry 84

3.5 Results and Discussion 85

3.5.1 Characterisation of the Surface Finish of Inhaler Manufacturing Techniques 85

3.5.1.1 SEM Analysis 85

3.5.1.2 Surface Profilometry 87

3.5.2 Optimisation of Two Photon Polymerisation Printing 91

3.5.2.1 Selection of Printing Parameters 91

3.5.2.2 Optimised Ridge Characteristics 102

3.5.2.3 Improving Printing Area 103

3.5.3 Challenges of Two Photon Polymerisation 104

3.6 Chapter Conclusion 105

3.7 Chapter References 107

4 Evaluation of Single Particle Adhesion to Printed Morphologies 112

4.1 Introduction 112

4.1.1 Zeta Profilometry 113

4.1.1.1 Confocal Microscopy 113
4.1.1.2 White Light Interferometry 114
4.1.1.3 Pattern Projection with Focus Detection 115
4.1.1.4 Zeta Optical Profilometry Technology 115
4.1.2 Plasma Polymerisation 116
4.2 Chapter Aims 119
4.3 Chapter Objectives 119
4.4 Materials and Methods 120
4.4.1 Materials 120
4.4.2 Two Photon Polymerisation 120
4.4.3 TPP Morphology Characterisation 120
4.4.3.1 Atomic Force Microscopy 120
4.4.3.2 Zeta Optical Profilometry 121
4.4.4 Plasma Polymerisation 121
4.4.5 Characterisation of the Plasma Polymerisation Coating 122
4.4.5.1 Water Contact Angle Measurements 122
4.4.5.2 Ellipsometry 122
4.4.5.3 Scanning Electron Microscopy 122
4.4.5.4 Time of flight- Secondary Ion Mass Spectrometry 123
4.4.6 Colloidal Probe Microscopy 123
4.4.6.1 Production of Colloidal Probes 123
4.4.6.2 Tip Imaging 124
4.4.6.3 AFM Reverse Tip Imaging 125
4.4.6.4 Zeta Optical Profilometry 126
4.4.6.5 Force-Volume Measurements – Non-printed Substrates 126

4.4.6.6 Force-Volume Measurements – TPP-printed Substrates 126
4.4.6.7 Force-Curve Analysis 127
4.4.6.8 Statistical Analysis 129
4.5 Results and Discussion 130
4.5.1 Production of varying morphologies 130
4.5.1.1 Producing different ridge heights 130
4.5.1.2 Producing different ridge spacings 135
4.5.2 Evaluation of plasma polymerised coating 137
4.5.2.1 Evaluation of ppHex Coating 142
4.5.3 Evaluation of Ridge Coverage 144
4.5.4 Colloidal Probe Microscopy 148
4.5.4.1 Particle Adhesion to Non-printed Hydrophobic Coating 148
4.5.4.2 Effect of Morphology on Particle Adhesion 152
4.6 Chapter Conclusions 174
4.7 Chapter References 176
5 Evaluation of Bulk Powder Deposition to Printed Morphologies 179
5.1 Introduction 179
5.1.1 Bulk Particle Interaction Testing 180
5.1.1.1 The Centrifuge Technique 180
5.1.1.2 Ultrasonic Vibration 181
5.1.1.3 Impact Separation 181
5.1.1.4 Hydrodynamic Technique 181
5.1.1.5 Aerodynamic Techniques 181
5.1.2 Next Generation Impactor 182
5.1.2.1 Aerodynamic Fractionation 184

5.2 Chapter Aims 186

5.3 Chapter Objectives 187

5.4 Materials and Methods 188

5.4.1 Materials 188

5.4.2 Preparation of DPI Formulation 188

5.4.3 Preparation of Substrates for Deposition Experiments 189

5.4.4 Next Generation Impactor (NGI) 189

5.4.4.1 Standard NGI experiment 191

5.4.4.2 Particle Deposition Experiments 192

5.4.5 Ultra Performance Liquid Chromatography 192

5.4.6 Optical Microscopy 192

5.4.7 Image Analysis 193

5.4.8 Statistical Analysis 195

5.5 Results and Discussion 196

5.5.1 Formulation Test and Determination of FPF and MMAD 196

5.5.2 Evaluation of Particle Deposition on Non-Printed Coverslips 197

5.5.3 Evaluation of Initial Two Photon Printed Substrate Run and Methodology Development 199

5.5.4 Evaluation of Effect of Ridge Height on Particle Deposition on Printed Coverslips 203

5.5.5 Evaluation of Effect of Ridge Spacing on Particle Deposition on Printed Coverslips 211

5.6 Chapter Conclusions 216

5.7 Chapter References 217

6 Overall Conclusions and Future Work 221

6.1 General Introduction 221

6.2 Selection and Optimisation of AM Technique 221

6.3 Effect of Morphology on Particle Adhesion 222

6.4 Effect of Morphology on Particle Deposition and Re-entrainment 223

6.5 Future Outlook 223

6.6 Chapter References 225

Appendix A: Nanoscribe Code Used 226

List of Figures

Figure 1.1: Schematic of different interactions depending on surface asperity size. In a) the asperities are small and therefore increase the distance between the particle and the surface, however in b) the asperities are large and therefore the particle becomes entrapped. 8

Figure 1.2: An illustration of different packing of ansiotropically shaped particles, and the different resulting contact areas. 9

Figure 1.3: A representation of the JKR model, which focuses on the attractive forces (red) present within the solid-solid contact zone (purple). The region labelled c is under compressive stress. 12

Figure 1.4: A representation of the DMT model, which focuses on the attractive forces (red) present just outside of the contact zone (purple). The region labelled c is under compressive stress. 12

Figure 1.5: An illustration of the sessile drop water contact angle (Θc) measurement, indicating the three phase interfacial free energies; solid-gas (γ_{SG}), solid-liquid (γ_{SL}) and liquid-gas (γ_{LG}). 16

Figure 1.6: A schematic of the main components of an AFM. The laser is focused on the upper surface of a cantilever which uses a sharp tip to physically touch the surface to be imaged. Any change of topography will cause a deflection in the cantilever which will be detected by the change on the photodiode. Picture adapted from[20]. 17

Figure 1.7: Issue with probe broadening caused by the interaction of the side of the tip with the topography being imaged. 19

Figure 1.8: A schematic of the key phases in a force-distance curve. On approach the cantilever is in resting position, which as it approaches the surface, may jump to contact due to attractive forces. The tip will then continue down until the maximum load is reached, at which point the tip will begin to withdraw. The cantilever may then undergo a negative deflection as the probe sticks to the surface, until there is sufficient tip-sample separation to overcome this adhesion and the cantilever returns to resting position. Picture adapted from[38,39]. 20

Figure 1.9: An array of force curves are collected over the area to be imaged, allowing the generation of a map of probe-surface interactions. 21
Figure 1.10: Representation of the structure of the human lung. Picture adapted from[52–54]. 24
Figure 1.11: A visual representation of the three main mechanism of particle deposition in the lungs. Picture adapted from Fröhlich and Salar-Behzadi 2014[57]. 25
Figure 1.12: Formulation Strategies – An illustration of the use of fines (green) to reduce adhesion between API (blue) and carrier particles (peach) in A) a binary formulation and B) a ternary formulation for dry powder inhalers. 29
Figure 1.13: An overview of the additive manufacturing processes. SLS = selective laser sintering, EBM = electron beam melting, 3DP = 3D printing, TPP = two photon polymerisation, FDM = fused deposition modelling. Adapted from Wong et al. 2012[12] 32
Figure 1.14: Radical Polymerisation Reaction; resulting in the generation of free radicals (R) from the excited photoinitiator (I). Thereby producing radical monomers (M) and eventual formation of polymers (Mn). 35
Figure 1.15: Photon Absorption. One-photon absorption (1PA) of a UV photon excites a photon from the grounded to the excited state. On the right, two photon absorption (TPA), involving two near IR photons exciting an electron via an intermediate state. 36
Figure 1.16: An illustration of temporal and spatial compression to produce sufficient photon density at the focal spot, achieved using a pulsed laser and an objective with a high numerical aperture. On the right a cross section of two photon absorption profile. Picture adapted from Spangenberg et al. 2013[18] and Hiroaki et al. 2010[114] 37
Figure 2.1: Schematic of the components of an SEM[4] 52
Figure 2.2: SEM images of the three particle types to be used in colloidal probe microscopy. A) Polystyrene 10 µm beads, B) Polystyrene 5 µm beads and C) Respitose SV003 particles. 57
Figure 2.3: An example of AFM topography images and their respective 3D processed image to evaluate surface roughness of a 1 µm x 1 µm scan size of A) a

polystyrene 10 µm bead, B) a polystyrene 5 µm bead and C) a Respitose SV003 particle and D) 5 µm x 5 µm scan size of a Respitose SV003 particle. 59

Figure 2.4: Schematic showing the attachment of particles on AFM tips. A) The tip is lowered into contact with glue (shown in green) and is then withdrawn. B) The tip is then moved and lowered onto an isolated particle (shown in blue) leading to particle attachment. 62

Figure 2.5: An example of an SEM image collected of a colloidal probe, post attachment of a 10 µm polystyrene bead, demonstrating significant charging using the previous settings. 63

Figure 2.6: An SEM image of an example of each of the particles used in the colloidal probe microscopy mounted on an AFM tip. A) Polystrene 10 µm bead, B) Polystyrene 5 µm bead and C) Respitose SV003 particle. 64

Figure 2.7: An SEM Image of the array of spikes seen on the TGT-01 tip characterisation grating[19]. 65

Figure 2.8: An example of the AFM topography image generated when performing tip imaging. A) An array of the surface of a polystyrene 5 µm bead. B) An AFM image focused on one of the particle surface repeat images. 66

Figure 2.9: An example of a Respitose particle and the gradual change in surface morphology seen throughout the colloidal probe experiments. A) The particle before use, with fines clearly seen on the surface, B) The particle after the first use, a smoothing effect has occurred, but certain asperities have become exposed as identified by the red arrows and C) The particle after multiple uses, separate asperities recede flattening into one larger asperity. 69

Figure 3.1: An overview of the Selective Laser Sintering Process[11]. 74

Figure 3.2: The PolyJet Process, the photopolymer is jetted along the X-axis using multiple nozzles, which are subsequently cured using UV bulbs integrated in the jetting head in a layer- by- layer process. Picture adapted from PolyJet: 3D Printing[26] 77

Figure 3.3: Cross-section schematic of the setup in the Nanoscribe Photonic Professional. The objective is submerged in dropcast immersion oil on the lower side of the substrate, allowing the laser beam to be focused into the resist on the upper substrate surface. 79

Figure 3.4: The Nanoscribe Photonic Professional GT system and inset the components of the stage. Picture adapted from Nanoscribe Theoretical Training Presentation 2014[27]. 79

Figure 3.5: SEM Images of the surface topology of the mouthpiece of the handihaler manufactured by A) Commercial injection moulding, B) Selective Laser Sintering and C) Inkjet Printing.....86

Figure 3.6: An example of the calculation of surface roughness using Ra (the arithmetic mean). Firstly, the deviation from the centre is highlighted, and then the "troughs" of the roughness are inverted and an average is taken which is the calculated Ra (red line). Picture adapted from[28] 88

Figure 3.7: Talysurf Profilometry 2D Images (left) and their respective 3D representation (right) of the mouthpiece of the handihaler manufactured by A) Commercial injection moulding, B) Selective Laser Sintering and C) Inkjet Printing. 89

Figure 3.8: Issues with Printing Reproducibility; A) the red circle highlights a section of the ridge seemingly damaged and in B) the blue arrows highlight changes in ridge dimensions. 93

Figure 3.9: A CAD design of the initial test structure; a semi-circular 50 µm long ridge. 95

Figure 3.10: The process of importing a 3D structure into the Describe software. First, the object is imported in STL format from a CAD software, and then the object is sliced into layers, providing the Nanoscribe with the trajectories needed to print the object in an additive process. Finally, the hatching parameters are set to dictate the surface resolution and structure integrity. 96

Figure 3.11: The resultant surface profiles extracted from AFM images collected of the ridges printed with differing hatching parameters, see Table 3.2 for complete parameters. A) Printed in solid hatching mode with 20 contours at 0.1 µm spacing. B) 1st iteration of the hatching parameters, produced in shell and scaffold mode with C) and D) v2 and v3 respectively. 101

Figure 3.12: A 3D representation of an AFM image of a single TPP ridge, showing a height of 0.9 µm and a width of 1.9 µm. 102

Figure 3.13: A top view of a single TPP ridge collected in SEM, showing a width of 1.32 µm. 103

Figure 4.1: Schematic of the principles of confocal microscopy. A beam of light is focused on the surface using an aperture through an initial pinhole, on reflection from the surface this is then passed through a second confocal pinhole, so only light reflected from the focal plane under investigation reaches the detector. As the scan height is adjusted varying levels of the surface will come into focus and will be imaged. These focal images can then be stitched together to form a topographical image. Picture from[4] 114

Figure 4.2: A schematic of the principles of Interferometry. A coherent beam of light is split between a sample surface and a reference surface, the reflected light is then recombined, and the interference pattern is evaluated, if the two beams are in phase the intensities will be combined and a bright spot will be seen, if however there is a difference in the distance the two beams have travelled the beams will be out of phase and destructive interference will be seen. Picture adapted from[6,7] 115

Figure 4.3: An overview of the Zeta 20 Optical Profilometer, the sample is evaluated as a series of focal plane slices. At each focal plane, the ZDots interferometric pattern is projected on the surface and areas in focus can be determined based on evaluation of the distortion of the pattern. Picture from[8].....116

Figure 4.4: Schematic of the multitude of propagation and recombination mechanisms in plasma polymerisation. This shows the upper cycle formed from monoradicals and the lower cycle from diradicals. Picture adapted from[9,12].118

Figure 4.5: Initial SEM images of the particles used for colloidal probe microscopy. A) Polystyrene 10 µm beads, B) Polystyrene 5 µm beads and C) Respitose SV003 particles. 125

Figure 4.6: An example of a truncated force-curve recorded between a polystyrene 10 µm bead and the TPP morphologies. 128

Figure 4.7: A series of TPP 1 um high ridges shown by A) Zeta Profilometry with multiple cross-sections over the 50 µm long ridge displayed and then by AFM as a B) 2D image and C) in the 3D representation. 132

Figure 4.8: A series of TPP 3 um high ridges shown by A) Zeta Profilometry with multiple cross-sections over the 50 µm long ridge displayed and then by AFM as a B) 2D image and C) in the 3D representation. 133
Figure 4.9: A series of TPP 5 um high ridges shown by A) Zeta Profilometry with multiple cross-sections over the 50 µm long ridge displayed and then by AFM as a B) 2D image and C) in the 3D representation. 134
Figure 4.10: A 2D representation of a series of TPP ridges, captured using the Zeta Profilometer (above) and the distances recorded between the markers (below). 136
Figure 4.11: Chemical structure of hexane. 137
Figure 4.12: Chemical Structure of Acrylic Acid. 138
Figure 4.13: A comparison of WCA measurements of plasma polymerised coated surfaces. On the left a ppHex coated glass coverslip, with a WCA of 96^{o} and on the right a ppAAc coated coverslip with a WCA of 64^{o}. 138
Figure 4.14: Tof-SIMS Spectra displaying positive ions up to m/z 150 for A) an uncoated glass coverslip, B) ppHex coated glass coverslip and C) a ppAAc coated glass coverslip. 140
Figure 4.15: An overview of the substrate: A) Uncoated, B) Coated with ppHex and C) Coated with ppAAc, showing the surface coverage of three characteristic ions demonstrating a successful surface coverage with the two plasma polymerisation chemistries. 141
Figure 4.16: Representative AFM topographical image of a ppHex coating on a glass coverslip. 142
Figure 4.17: A profile of the ppHex plasma coat and then an area that had been scratched away by AFM, to evaluate the thickness of the ppHex coating. 143
Figure 4.18: The change of WCA (mean ± S.D.) with time post-coating with ppHex. 144
Figure 4.19: Cartoon representation of the TPP ridges printed on a glass coverslip for Tof-SIMS analysis. 145
Figure 4.20: Chemical Structure of 2-(hydroxymethyl)-2- [[(1-oxoallyl)oxy]methyl] -1,3-propanediyl diacrylate (IP-L). 146

Figure 4.21: Tof-SIMS Spectra displaying negative ions up to m/z 150 for A) uncoated glass coverslip post-TPP processing, B) uncoated TPP ridges and C) ppHex coated ridge and glass coverslip. 147

Figure 4.22: An overview of the substrate with a series of TPP ridges in the centre: A) Uncoated and B) Coated with ppHex showing the surface coverage of three characteristic ions demonstrating a successful surface coverage with the plasma polymerisation hexane.....148

Figure 4.23: An example of the adhesion between a polystyrene 10 µm bead and a non-printed ppHex coated substrate showing the force-volume A) height and B) adhesion map.....150

Figure 4.24: A comparison of histograms of particle adhesion to the non-printed ppHex substrate for A) a polystyrene 10 um bead, B) a polystyrene 5 µm bead and C) a Respitose SV003 particle.....151

Figure 4.25: Histograms displaying the force of adhesion calculated from the force-curves collected with all particles of each type. Each curve is normalised to total count, to account for differing scan number. Adhesion to 1 µm (blue), 3 µm (orange) and 5 µm (purple) ridge heights for A) polystyrene 10 µm beads, B) polystyrene 5 µm beads and C) Respitose SV003 particles is displayed. 153

Figure 4.26: Force-Volume Maps collected with CPM of a series of 1 µm high ridges, showing the topography and respective adhesion collected over the scan area with A) a polystyrene 10 µm bead, B) a polystyrene 5 µm bead and C) a Respitose SV003 particle. 155

Figure 4.27: Force-Volume Maps collected with CPM of a series of 3 µm high ridges, showing the topography and respective adhesion collected over the scan area with A) a polystyrene 10 µm bead, B) a polystyrene 5 µm bead and C) a Respitose SV003 particle. 157

Figure 4.28: Force-Volume Maps collected with CPM of a series of 5 µm high ridges, showing the topography and respective adhesion collected over the scan area with A) a polystyrene 10 µm bead and B) a Respitose SV003 particle. 158

Figure 4.29: An overview of the mean force of adhesion, with the interquartile range for each combination of ridge height and spacing against A) polystyrene 10 µm beads, B) polystyrene 5 µm beads, C) Respitose SV003 particles. 160

Figure 4.30: Schematic demonstrating how Pythagoras's theorem can be utilised to evaluate the spacing (2b) needed for a spherical particle with radius (c) to fit between the ridges for a specific ridge height. The dimensions of the particle at the ridge height can be calculated from the particle radius minus the ridge height (a). The central point of the particle is represented by the black dot. 162

Figure 4.31: A schematic representation of a 5 µm polystyrene bead interaction with 1 µm (left) and 5 µm (right) high ridges, with 1 µm spacing. This drawing is to scale and the contact area between the particle and the ridges is shown in red. 164

Figure 4.32: An overview of the mean force of adhesion, with the interquartile range to evaluate the effect of changing ridge height for 1 µm and 3 µm ridge spacing against A) polystyrene 10 µm beads, B) polystyrene 5 µm beads, C) Respitose SV003 particles. 165

Figure 4.33: An overview of the mean force of adhesion, with the interquartile range to evaluate the effect of changing ridge spacing for 1 µm and 5 µm ridge height against A) polystyrene 10 µm beads, B) polystyrene 5 µm beads, C) Respitose SV003 particles. 167

Figure 4.34: An example of the average profiles of the height (black) and adhesion (blue) of a polystyrene 10 µm bead scan for A) 1 µm high ridges and B) 5 µm high ridges. 168

Figure 4.35: An example of the average profiles of the height (black) and adhesion (blue) of a polystyrene 5 µm bead scan for 1 µm high ridges. 170

Figure 4.36: A cartoon representation of a 5 µm polystyrene bead interaction with A) 1 µm high ridges and B) 5 µm high ridges, with 1 µm (left) and 3 µm (right) spacing. This drawing is to scale and the contact area between the particle and the ridges is shown in red. 171

Figure 4.37: An example of the average profiles of the height (black) and adhesion (blue) of a Respitose SV003 particle scan for A) 1 µm high ridges and B) 5 µm high ridges. 173

Figure 5.1: Photographs of a Next Generation Impactor closed (top) and in the open position (bottom) to reveal the inner collection pans. Images adapted from[12]. 183

Figure 5.2: A schematic of an NGI stage with the key parameters for aerodynamic diameter assessment labelled. Adapted from Marple et al[13]. 184
Figure 5.3: An overview of the substrate design with the nine different morphologies being trialled. On the bottom row, all three patterns are 1 µm high, with 8 µm, 3 µm and 1 µm spacing respectively. The second row all the designs have a ridge height of 3 µm and on the top row all the ridges have a height of 5 µm. 189
Figure 5.4: The Next Generation Impactor setup used for these experiments, with key components labelled.....190
Figure 5.5: Photographs of "Screenhaler" from above (left) and from the outlet (right) used for fine particle assessment which is basically a cylindrical channel. The outlet is connected to the NGI via the USP throat. The diameter is 7.0 mm and the length is 45 mm. 191
Figure 5.6: An example of the processing of images using the ImageJ software to highlight the particle clusters. A) The printed area to be investigated is determined including any particles associated with the ridges. B) The image is now a binary black and white image after thresholding to just highlight the particle clusters. C) The particle analysis function of the software is used to identify the clusters and calculate the cluster area. This is then repeated with the image of the same area focused on the substrate and the particles are amalgamated into one result. 194
Figure 5.7: Fine particle assessment of BDP in the formulation, showing particle deposition in micrograms ± S.D. at various stages of the NGI. 196
Figure 5.8: Optical microscopy images of the particle deposition on the non-printed substrate A) in the non-nozzle area and B) in the area directly under the nozzle. 198
Figure 5.9: An example of the particle deposition in the initial experiments damage to the TPP ridges in A) the pre-separator which may have been caused by the large carrier particle seen and B) in CP2. 200
Figure 5.10: A photograph of the substrate affixed on the NGI collection surface, showing the particle deposition pattern (in white) in relation to the position of the TPP morphologies (black dot). 202

Figure 5.11: A comparison of the particle deposition on the area of printed substrate normalised to their control area evaluating ridges of differing height using. A) An example of the normalised data set, scaled so the control is 0, and bar charts of the mean ± SEM (with control shown in red) of B) the particle area coverage and C) individual manual particle count following aerosolisation at 77 L/min in the NGI. 205

Figure 5.12: Histograms showing the distribution of the particle cluster sizes of the control versus ridge area for A) 1 µm high ridges, B) 3 µm high ridges and C) 5 µm high ridges following aerosolisation at 77 L/min in the NGI. 207

Figure 5.13: An example of the type of particle clusters seen on A) 1 µm high ridges showing multiple independent particles and B) 3 µm high ridges showing more particle clusters. 208

Figure 5.14: A cartoon representation of the TPP ridge morphologies and to scale the small individual particle fines. Showing that for 1 µm high ridges only one particle can deposit adhered to the side of the ridge without protruding above the structure, however in contrast the lower image shows the 3 µm high ridges and an agglomerate of particles all enclosed and so sheltered from the air flow by the ridges.....210

Figure 5.15: A comparison of the particle deposition on the area of printed substrate normalised to their control area evaluating ridges of differing spacing using. A) An example of the normalised data set, scaled so the control is 0, and bar charts of the mean ± SEM (with control shown in red) of B) the particle area coverage and C) individual manual particle count following aerosolisation at 77 L/min in the NGI. 213

Figure 5.16: Histograms showing the distribution of the particle cluster sizes of the control versus ridge area for A) 1 µm spaced ridges, B) 3 µm spaced ridges and C) 8 µm spaced ridges following aerosolisation at 77 L/min in the NGI.....215

List of Tables

Table 2.1: A summary of the surface roughness calculated as RMS over three 1 µm x 1 µm areas for three different particles of each particle type. 58

Table 2.2: An overview of the starting Contact Areas of the Particles to be used as Colloidal Probes at an indentation depth of 0.5 nm.....68

Table 2.3: An example of the change of asperity contact area of a Respitose SV003 particle after use as a colloidal probe for force measurements.....68

Table 3.1: Surface roughness, documented as Ra, of the handihaler mouthpiece using the three different manufacturing techniques.....87

Table 3.2: Selected hatching setting parameters in the surface resolution optimisation of Nanoscribe printed structures. 98

Table 5.1: The cut off particle sizes for each of the stage of the NGI at varying flow rates. Adapted from Marple et al[13].....186

Table 5.2: A summary of the fine particle fraction (FPF), defined as the percentage of particles less than 5 µm of the delivered dose, the mass median aerodynamic diameter (MMAD) and the geometric standard deviation (GSD) of the formulation. 197

Table 5.3: An overview of the particle coverage on the non-printed substrate in the area directly under the nozzle versus the non-nozzle area.....198

List of Abbreviations

1PA	**-**	**One Photon Absorption**
3DP	**-**	**Three Dimensional Printed**
AFM	**-**	**Atomic force microscopy**
AM	**-**	**Additive Manufacturing**
API	**-**	**Active Pharmaceutical Ingredient**
BDP	**-**	**Beclomethasone Dipropionate**
CAD	**-**	**Computer Aided Design**
CFD	**-**	**Computational Fluid Dynamics**
CIJ	**-**	**Continuous inkjet**
CPM	**-**	**Colloidal Probe Microscopy**
COPD	**-**	**Chronic Obstructive Pulmonary Disease**
DMT	**-**	**Derjaguin-Muller-Toporov**
DOD	**-**	**Drop-on-demand**
DPIs	**-**	**Dry powder inhalers**
EBM	**-**	**Electron Beam Melting**
FDM	**-**	**Fused Deposition Modelling**
FPF	**-**	**Fine Particle Fraction**
GWL	**-**	**General Writing Language**
JKR	**-**	**Johnson-Kendall-Roberts**
IR	**-**	**Infrared**
MMAD	**-**	**Mass Median Aerodynamic Diameter**
NA	**-**	**Numerical aperture**
NGI	**-**	**Next Generation Impactor**
QnM	**-**	**Quantitative nanomechanical measurements**
ppAAc	**-**	**Plasma Polymerised Acrylic Acid**
ppHex	**-**	**Plasma Polymerised Hexane**
pMDIs	**-**	**Pressurised Metered Dose Inhalers**
PGMEA	**-**	**Propylene Glycol Monomethyl Ether Acetate**
RH	**-**	**Relative Humidity**

RMS	**-**	**Root mean square**
SEM	**-**	**Scanning electron microscopy**
SLM	**-**	**Selective Laser Melting**
SLS	**-**	**Selective Laser Sintering**
STL	**-**	**Standard Tessellated Language**
TFA	**-**	**Triflouroacetic Acid**
TPA	**-**	**Two Photon Absorption**
TPP	**-**	**Two Photon Polymerisation**
ToF-SIMS	**-**	**Time-of-flight Secondary Ion Mass Spectrometry**
UV	**-**	**Ultraviolet**
WCA	**-**	**Water Contact Angle**

List of Symbols

α	-	Characteristic length of ink droplet
α_0	-	Resultant contact area between two elastic spherical objects
$A, A_{11}, A_{12}, A_{22}$	-	Hamaker constants
C_{ae}	-	Cunningham slip factor
d	-	Separation between two charged particles
d	-	Cantilever deflection
d_{50}	-	Particle cut-off
d_{ae}	-	Particle aerodynamic diameter
D	-	Diameter of spheres
Dc	-	Diameter of nozzle cluster
E	-	Young's modulus
E^*	-	Reduced Young's modulus
ε	-	Permittivity
$h\varpi$	-	Lifshitz van der Waals constant
F	-	Van der Waals forces
F_{ADH}	-	Force of adhesion
F_{el}	-	Electrostatic forces
F_{on}	-	Applied force
I	-	Polymerisation initiator
k	-	Spring constant of the cantilever
M	-	Polymerisation monomer
Mn	-	Polymer
n	-	Number of nozzles in an NGI stage
n	-	Refractive index
η	-	Dynamic viscosity of ink
Oh	-	Ohnesorge number
ρ	-	Air/ ink density
ρ_{ae}	-	Particle density

q	-	**Charge present on charged particles**
Q	-	**Flow rate**
r	-	**Distance between two spheres**
r	-	**Centre of rotations**
R	-	**Polymerisation free radical**
R	-	**Radius of the sphere/ probe**
R	-	**Contact radius**
Re	-	**Reynold's number**
rms	-	**Root mean square roughness**
rms_1	-	**Longer peak to peak distance root mean square of roughness**
rms_2	-	**Smaller peak to peak distance root mean square of roughness**
S	-	**Distance between nozzle and impaction plate**
St	-	**Stoke's number**
μ	-	**Air viscosity**
υ	-	**Poisson's ratio**
V_0	-	**Average velocity of air through the nozzles**
ω	-	**Angular rotation**
W	-	**Nozzle diameter**
W_{ADH}	-	**Work of adhesion**
We	-	**Weber number**
Xc	-	**Cross-flow parameter**
γ	-	**Ink surface tension**
γ_{SG}	-	**Interfacial free-energy at liquid-gas interface**
γ_{SG}	-	**Interfacial free-energy at solid-gas interface**
γ_{SL}	-	**Interfacial free-energy at solid-liquid interface**
Z_0	-	**Interatomic equilibrium separation**
λ	-	**Elasticity parameter**
Θc	-	**Static contact angle**

1 Introduction

1.1 Introduction

Powders are ubiquitous in many industries and an improved understanding of particle-surface interactions that occur is vital for optimising numerous processes. In the pharmaceutical industry powders play an important role for accurate dosage filling, and formulation performance. This importance is especially evident in dry powder inhalers (DPIs), due to the particles' need to possess an aerodynamic diameter of less than 5 μm for therapeutic effect. However, particles of this size possess an inherent cohesiveness, resulting in poor device efficiency. With the rise of 3D printing there are increasing opportunities to investigate the effect of bespoke sub- micron morphologies on particle adhesion.

The focus of this chapter is therefore to provide an overview and highlight relevant background to this project available in the literature. This includes the fundamentals and modelling of particle adhesion, along with the variety of methods available to quantify this, with specific focus on atomic force microscopy. Secondly, an evaluation of the problem with particle adhesion currently experienced in pulmonary drug delivery and strategies to mitigate these effects. Finally, an introduction into the wide-ranging field of 3D printing is provided and its current use in the pharmaceutical industry.

1.2 Particle Adhesion in Industry

An understanding of powders and the interaction between individual particles is key to improving numerous processes in a range of industries. Solid particles are produced synthetically and also occur naturally as dust, pollen and organic matter[1]. A range of sizes are encompassed in the definition of particles, from nanoparticle (<1 μm) applications to large particles (>mm) present in mining applications. In the semiconductor industry for example, natural particles adhere to integrated circuits

resulting in a substantial decrease in the manufacturing yield achieved[1]. In the petroleum industry the issue lies with the cracking catalyst particles needed to produce gasoline[2]. Within this process the rate of diffusion of the reactant and product molecules within the catalyst particle can drastically affect the catalyst efficiency; therefore an increased understanding on how to reduce particulate adhesion would be beneficial. Particle characteristics, such as particle size and particulate interactions and their variance due to storage, mixing and distribution are vitally important in both the particle fluidisation and diffusion modulus[3].

Particle adhesion can also be particularly problematic in the pharmaceutical industry as most pharmaceutical formulations are solid for at least a portion of their production cycle, powders are hence ubiquitous throughout the pharmaceutical industry[4]. The active pharmaceutical ingredient (API) is typically milled to control particle size and size distribution, mixed with excipients and then possibly compacted into tablets[5], dispersed into a suspension or delivered as a powder for sachets or in dry powder inhalers (DPIs). Therefore, every step involved in powder processing will be influenced by the extent of the presence of interparticulate interactions, and can physically or chemically alter the particles affecting downstream behaviour[6].

1.3 PhD Focus

As particle adhesion is considered a critical problem in numerous industries, an increase in fundamental understanding of the causes of particle adhesion are needed. In order to investigate the effect of surface morphology, on particle adhesion in isolation from other factors, well-defined and controllable morphologies on the micron scale are needed. This will therefore allow a bottom up approach to improving fundamental understanding on the effect of surface morphology on particle adhesion. Although, multiple methods exist for the fabrication of morphologies, additive manufacturing (AM) was decided upon as a novel approach for the work in this thesis. AM allows not only for scalability and bespoke production but also has the capability for close to nanoscale resolution, which is needed to produce differing morphologies on the micron scale. However, currently

development is needed to combine both the resolution and surface finish needed for an investigation into morphology on an appropriate scale.

To develop these technologies and assess their suitability, this thesis concentrates on an initial control pattern of micron-scale semi-circular ridges. These allow an investigation of differing height and spacing of surface roughness. Semi-circular ridges were chosen to assess the ability to print well defined curves and to allow evaluation of surface finish. These patterns will then be tested against a range of particles and their relative adhesion assessed, both on an individual basis and in a bulk particle system. As this PhD is based on the area of Pharmacy, an initial focus has been chosen on the application of the particle adhesion understanding in the field of pulmonary drug delivery. Therefore, particles selected for these adhesion investigations have been selected with this field in mind. However, the fundamental insight and techniques developed is applicable to other fields of study.

1.4 Fundamentals of Particle Interactions

1.4.1 Forces Affecting Particle Interactions

Interparticulate forces can be divided into cohesive, between particles of the same material, or adhesive, between two different materials. A particle's surface free energy exists, because a solid possesses internal chemical bonds which are energetically favourable[7], therefore on the surface the lack of bonds available to form, provides a higher energy state, it is therefore favourable for the surface molecules to form intermolecular bonds. Group I "long range" attractive interactions, include van der Waals forces and electrostatic forces which are crucial in helping produce interparticulate adhesive forces[1].

Van der Waals derive from polarizations or electron density changes of the component atoms and molecules[1] and can be subdivided into London, Keesom and Debye interactions[8]. London forces, often cause dispersive forces ensuing from the momentary positioning of electrons, resulting in the production of a dipole, this then polarizes a nearby neutral atom producing an attraction between them. This

interaction far exceeds the Keesom interactions generated from the force between two permanent dipoles and Debye interactions between one permanent and one induced dipole[9]. These forces become especially apparent with particles less than 20µm in diameter and separated by 0.2 – 1nm[10]. In order to calculate these interactions the Hamaker and the Lifshitz approaches can be utilised[1]. Hamaker assumed an additive component of these forces between pairs of atoms and molecules, whereas Lifshitz accounted for bulk properties[11]. According to Hamaker, using the Hamaker constant, *A*, van der Waals forces (*F*) between two spheres of the same material with diameters d_1 and d_2, r distance apart can be defined as:

$$F = \frac{A}{12r^2}\left(\frac{d_1 d_2}{d_1 + d_2}\right) \quad (1.1)$$

The Lifshitz-van der Waals theory yields the same equation, but containing the Lifshitz-van der Waals constant, $h\varpi$ which is related to the Hamaker constant by:

$$A = \frac{3}{4\pi} h\varpi \quad (1.2)$$

For particles of different materials, an approximation of the Hamaker/Lifshitz van der Waals constant A_{12} can be calculated based on means of the individual coefficients A_{11} and A_{22}:

$$A_{12} = \sqrt{A_{11}A_{22}} \quad (1.3)$$

For different materials, van der Waal forces can therefore either be attractive or repulsive, depending on the medium[11].

The other Group I interparticulate force important in adhesion is electrostatic force. In the simplest form, this is the attraction or repulsion of two charged particles. According to Coulomb's law, the force between two charged particles is proportional

to the product of their charges (q_1q_2) and is inversely proportional to the square of the distance, d, of separation[11]:

$$F_{el} = \frac{q_1 q_2}{4\pi\varepsilon d^2} \quad (1.4)$$

where $\mathcal{E}$ is the permittivity. However, electrostatic forces can also be generated from the induced charge when a neutral particle contacts a charged particle, resulting in the transfer of electrons, or a differential in work when two uncharged particles collide. Finally, a process resulting from friction between particles, "triboelectric charging" can occur producing electrical charges[10].

In dry conditions, these two forces constitute the majority of the adhesive forces between particles, with van der Waals, usually the dominant force for small particles[10]. However, when asperities are present on the surface of the particle the resulting decrease in contact can allow the electrostatic forces from differential work to become the primary force[1]. When sufficiently soft though, the asperities can begin to deform under the particle adhesion contact, thereby increasing contact and once again restoring van der Waals as the predominant interaction. The majority of predictions are only valid for a dry powder, as the addition of any moisture can generate capillary forces, which can equal or surpass van der Waals forces.

Capillary forces can form due to the condensation of water vapour on particles as a result of the particle's free surface energy. As the water condensed on the particles increases a liquid bridge can form between the particles[9]. This liquid bridge can greatly increase the attractive forces between the particles, or indeed between a surface and the particles. The presence of liquid can affect the interparticulate forces in a variety of ways, firstly interparticulate forces will increase due to capillary forces, the surface energy of the particle will be affected, and finally the presence of water can diminish the effects of electrostatic force[10] by alteration of the surface conductivity[11].

Other forces can also be of importance in interparticulate interactions depending on the storage conditions, for instance sintering is a group II interaction along with capillary forces[1], this involves the fusion of particles below the melting point of the material, but occurs with increased likelihood during extended storage especially with an increased temperature[10]. With higher temperatures group III forces like chemical bonds and hydrogen bonds between particles may become significantly active and are highly dependent on the particle or surface materials[1].

1.4.2 Material Properties Affecting Particle-Surface Interactions

The adhesion between a particle and a surface is a highly complex and multi-factorial interaction. As shown above the contact area plays a key role in the adhesion between two bodies, therefore any changes in surface roughness, morphology or orientation can affect the adhesion. Material properties also play a key role, as materials that deform easily, will allow a greater contact between a particle and a surface and so will also increase the adhesion. Likewise, the surface chemistry, will define the reactivity of the surface and so the extent of surface free energy which increases the adhesiveness of two bodies. Finally, environmental factors like humidity can influence the interaction as they introduce capillary forces which can have a significant impact on adhesion.

1.4.2.1 Surface Free Energy

A major factor in the interaction between a particle and a surface is the surface free energy. Surface energy, occurs as the molecules at the surface of a material have fewer neighbouring molecules and so are freer than the molecules in the interior[11]. Unlike liquids the surface energy of a solid particle can vary over the surface as molecules are less able to move around to re-distribute the energy and form a lower energy state[11]. Surface tension in liquids or surface free energy in materials are defined as the amount of work required to increase the surface area of a substance by $1m^2$ [9]. The processing that powders undergo play an important role in the

resultant surface energy[12]. This surface energy, however will increase the cohesiveness and adhesiveness of a particle or surface as they will try to bind to energetically favourable surfaces[9]. The higher the surface energy, generally the higher adhesive characteristics[12], and once adhered the stronger the bond formed.

1.4.2.2 Relative Humidity

Relative humidity (RH) is an important factor in the adhesion between a particle and a surface, as it can result in liquid bridges forming, due to moisture condensation in the gap between the two surfaces[13]. This liquid bridge forms a concave meniscus between the particle and the surface, creating a pressure which acts to pull together the two objects[14]. This Laplace pressure is, however, highly dependent on contacting asperities and surface energy of the interacting bodies. If the surface is rough, an increased amount of condensed moisture is needed to fill the asperities. Surface energy, is important as moisture can easily condense on hydrophilic surfaces in the cracks and pores, resulting in a sharper increase in adhesion with increasing RH.

Therefore, the resulting adhesion measured over changes in RH can be drastically different. This can range from an initial increase in RH cause an increase in adhesion forces, until a peak in adhesion is reached, as the RH reaches around 50%, and then a decrease [15]. Or a continual rise in adhesion, until the adhesion becomes independent of the RH[13].

1.4.2.3 Surface Roughness and Particle Morphology

Powders often have particles of varying shape and roughness present, often making calculation of interparticulate and particle-surface adhesion difficult, as the theoretical equations are often based on spheres with smooth surfaces[11]. Particle size is an important factor controlling the interparticulate interactions in powders. As the size of a particle increases, there is a proportional increase in attraction due to an increase in contact area and hence van der Waal attractions[11]. The behaviour of

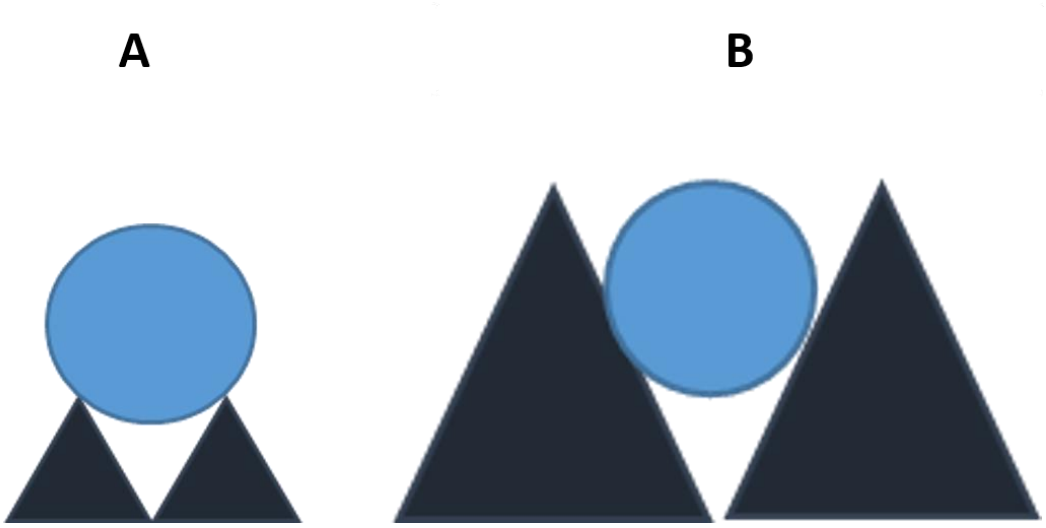


Figure 1.1: Schematic of different interactions depending on surface asperity size. In a) the asperities are small and therefore increase the distance between the particle and the surface, however in b) the asperities are large and therefore the particle becomes entrapped.

small particles (<10 µm), is dominated by van der Waals forces and they have a high surface to volume ratio resulting in inherent adhesive and cohesiveness[16].

However, as van der Waals forces are only really significant when particles are between 0.2 – 1 nm separation [17], any surface asperity capable of increasing the effective separation will therefore decrease the adhesion between the two interacting bodies[11]. However, this surface roughness must be relatively small in comparison to the probing particle, otherwise the particle may become entrapped in the roughness, increasing the effective contact area and hence adhesion. Large scale roughness on both objects, may also result in mechanical interlocking where the particle will become entangled with the surface which also significantly increase adhesion[18]. In pharmaceutical processing, this is a key issue as most pharmaceutical particles have extremely rough surfaces, with varying asperities and therefore contact areas available.

The influence of particle shape is therefore also important as this will also affect the distance between particles, as non-spherical particles may experience a wide range of adhesional forces depending on their orientation[11], between the particles themselves there can be a highly variable cohesion due to differences in contacting surface area (Figure 1.2). However, when this is applied to particle surface interactions, if a needle shaped particle is attached point down, this will result in a

very low contact area and hence low adhesion. Conversely, if attached on its side, there will be a significantly greater contact area available and hence adhesion measured.

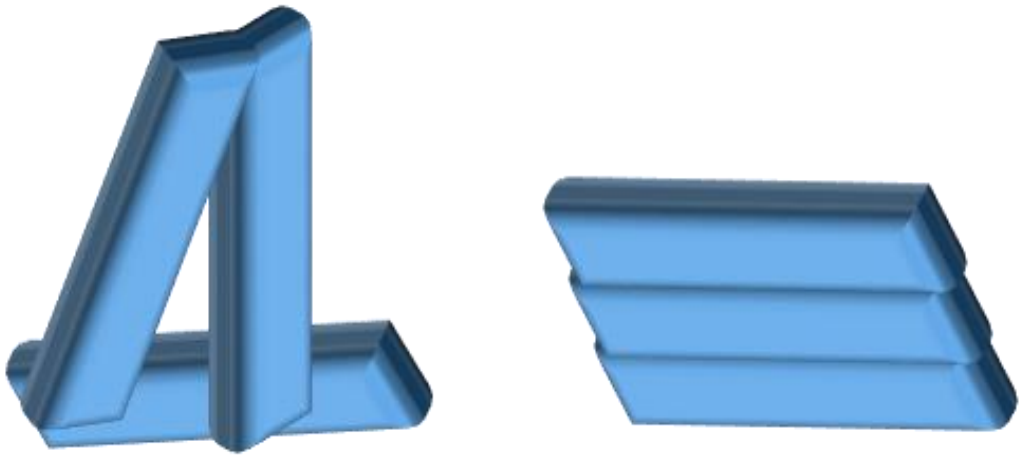


Figure 1.2: An illustration of different packing of ansiotropically shaped particles, and the different resulting contact areas.

1.4.2.4 Particle Deformation

The Young's modulus (E), defines how easily a solid surface deforms. The ability of a material to change its conformation, when a load is applied dictates the resulting contact area when two bodies interact and hence the resultant adhesion. This is interwoven with the effect of surface roughness, as relatively sharp asperities with a small contact area may easily deform upon contact, thereby creating a far larger contact area and hence adhesion[19]. A high E value signifies a hard surface, unlikely to deform, whereas a low E value represents a material that is more likely to deform.

1.5 Adhesion Models

There are a range of models available for providing insight into the interactions between particles, these range from extremely simplistic models like the Hertz model

which does not account for adhesive forces, to extremely complex and convoluted contact mechanics simulations that incorporates a wide range of factors[13]. However, the vast majority of studies investigating the adhesion of particles use one of four main models, it is these that will be the focus of this section[20].

1.5.1 The Hertz Model

The Hertz model is one of the earliest models available to describe the interaction of a particle with another particle. This model describes the contact of two homogeneously smooth, elastic spherical objects and the resultant contact area (α_0) formed based on the deformation of the two bodies:

$$a_0^3 = \frac{3F_{on}R}{4E^*} \quad (1.5)$$

where F_{on} is the applied force, R is the radius of the sphere and E^* is the reduced Young's modulus as described in the following equation:

$$\frac{1}{E^*} = \frac{1-{v_1}^2}{E_1} + \frac{1-{v_2}^2}{E_2} \quad (1.6)$$

where E_1 and E_2 are the Young's modulus of the two spherical bodies and v_1 and v_2 are their Poisson's ratios.

However, while the Hertz model is still in use, the model is based on some significant assumptions. Firstly, no attractive forces are accounted for in the model[21] and therefore zero applied force, gives zero contact radius[20]. Secondly, there is an assumption that both spheres deform with a linear elastic response[13]. Finally, there is the assumption that the contact radius is small compared to the particle radius and that the load applied is in a normal direction[22]. Two models were therefore developed to attempt to mitigate some of these issues, but predominantly account

for the attractive forces between two bodies. The Johnson-Kendall-Roberts (JKR) and Derjaguin-Muller-Toporov (DMT) models focus on the interaction between a sphere and a flat surface.

1.5.2 JKR Model

The JKR model focuses on the attractive forces present within the solid-solid contact zone (Figure 1.3), these forces cause a deformation between the two contacting surface forming a “neck” region. The JKR model is best suited for soft materials, with a strong adhesion and large radius of curvature and therefore, describes an interaction where the two bodies will abruptly separate once the pull-off force is reached:

$$F_{ADH} = 3/2\pi R W_{ADH} \quad (1.7)$$

where F_{ADH} is the force of adhesion, R is the contact radius and W_{ADH} is the work of adhesion. Unlike in the Hertz model, an applied load of zero will still produce a contact region which is logical given the attractive forces that would be pulling the sphere and surface together. Therefore, true separation does not occur, until the contact radius is 0.63 times the value at zero applied force.

1.5.3 DMT Model

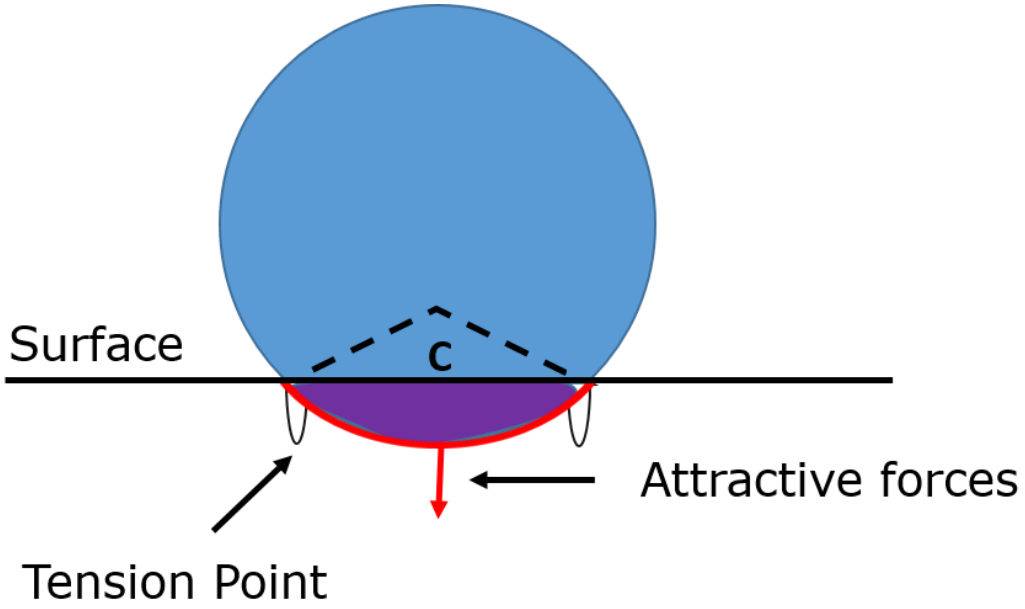


Figure 1.3: A representation of the JKR model, which focuses on the attractive forces (red) present within the solid-solid contact zone (purple). The region labelled c is under compressive stress.

The DMT model provides a simple model for a sphere interacting with a flat surface, for interactions at the opposite end of the spectrum to the JKR model. The DMT model focuses on the attractive forces in a ring on the outside of the contact region. This means that it is appropriate for long-range intersurface forces, as seen with stiff materials, weak adhesion and small contact radiuses.

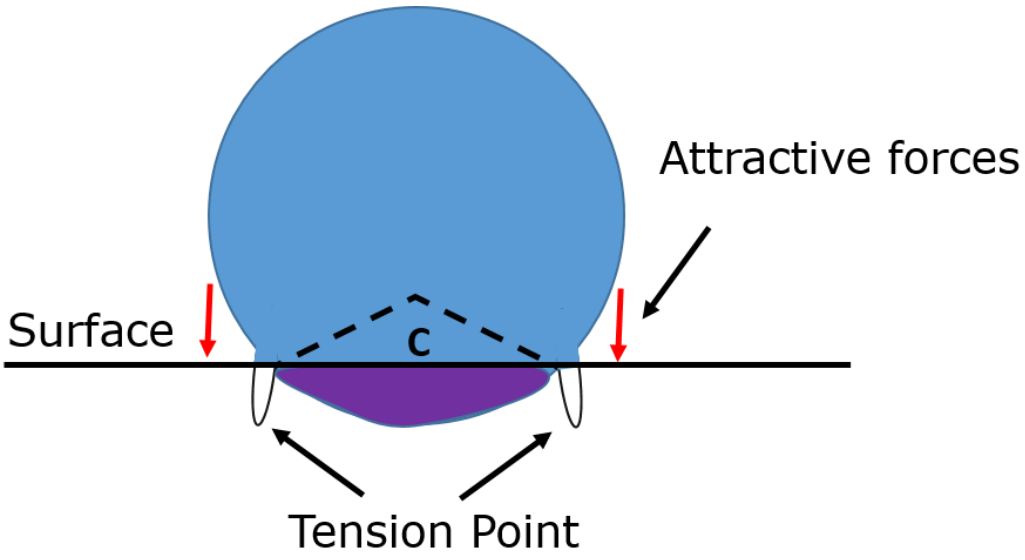


Figure 1.4: A representation of the DMT model, which focuses on the attractive forces (red) present just outside of the contact zone (purple). The region labelled c is under compressive stress.

Unlike, the JKR model however, no neck is formed and therefore during removal, the contact region reduces to zero, resulting in a smaller non-zero contact radius than the JKR model. The pull off forces required to separate the two bodies can be calculated using the following equation:

$$F_{ADH} = 2\pi R W_{ADH} \quad (1.8)$$

As previously mentioned, the JKR and DMT models provide insight into different types of interactions[19]. Neither model, accounts for adhesive forces both inside and outside the two interacting bodies. Therefore, in order to determine which model is appropriate for two interacting bodies the Tabor equation was developed[23]. The Tabor constant evaluated the relative heights of the neck formed when a particle comes into contact with a surface and the equilibrium separation of atoms of the bodies. If these two heights are comparable attractive forces outside of the contact region cannot be ignored and therefore the DMT model should be used. However, this was later developed to the elasticity parameter (λ) by Maguis *et al.* to acknowledge that these two models did not encompass the whole spectrum of interactions as previously suggested, but instead were opposite end of the spectrum.

$$\lambda = \frac{2.06}{Z_0}\left(\frac{R{W_{ADH}}^2}{\pi {E^*}^2}\right)^{1/3} \quad (1.9)$$

Where R is the probe radius, E^* is the reduced elastic modulus and Z_0 is the interatomic equilibrium separation (usually considered 0.16 nm[20]). When λ is greater than 5 the JKR model, whereas the DMT model is appropriate when λ is smaller than 0.1[24]. This has led to the development of the Maugis-Dugdale model to represent interactions between these two extremes.

1.5.4 Maugis-Dugdale Model

This model accounts for both long and short range attractive forces, by implementing a constant attractive force out to a designated distance. However, unlike the JKR and DMT models this does not produce a singular equation and therefore two of three possible parametric equations must be solved iteratively[20]. An in depth discussion of this model is beyond the scope of this thesis.

1.5.5 Rough Particles Adhesion

All of the highlighted models are dependent on smooth surfaces. As discussed earlier intermediate roughness can result in a decrease in contact area and so adhesion. This is further complicated by the possibility of wear and deformation of particle asperities. Rabinovich *et al.* have attempted to account for non-spherical particle asperities on the nanoscale utilising the RMS roughness and peak to peak distance of asperities[25].

$$F_{ADH} = \frac{A_{1,2}R}{6{z_0}^2}\left[\frac{1}{1+\frac{R}{1.48rms}} + \frac{1}{\left(1+\frac{1.48rms}{z_0}\right)^2}\right] \quad (1.10)$$

where *A* is the Hamaker constant, *R* is the probe radius, *rms* is the root mean square of roughness on the surface, based on two scales of roughness:

$$rms = \sqrt{{rms_1}^2{rms_2}^2} \quad (1.11)$$

where rms_1 represents longer peak to peak distances and rms_2 is associated with smaller peak to peak distances. However, this model only accounts for the roughness

of the surface and not the particle and so often overestimates the adhesion between two interacting bodies[26]. This model also fails to account for changes in asperities and struggles if the roughness increases above the nanoscale[24].

1.6 Methods to measure Particle Adhesion

Factors affecting particle cohesion and adhesion are therefore highly complex and often interrelated, and a need to measure the surface energy and adhesion of a particle is essential, especially for smaller particles which are inherently adhesive[11]. There are a range of methods that have been used to quantify these properties. One of these allows for the theoretical calculation of the adhesion properties of a surface by measuring the water contact angle (WCA) of a bulk material by placing a droplet on a powder compact[12]. The finite shape produced by the droplet on the surface is captured (Figure 1.5). The static contact angle (Θc) measured at the three phase interface is the angle between the tangential line of the sessile drop and the solid surface[27]. If the adhesive forces, exerted by the surface is higher than the cohesion between liquid molecules, favourable interactions form between the material and water, spreading of the droplet will occur and a low contact angle will be seen (<90°). If however, the cohesive strength of the droplet is greater than the surface energy of the surface the drop will bead and a high contact angle will be formed (>90°)[28]. However WCA, for practical reasons is often performed on compressed or smoothened surfaces and so provides little practical information about the interaction between a pharmaceutical particle and a surface.

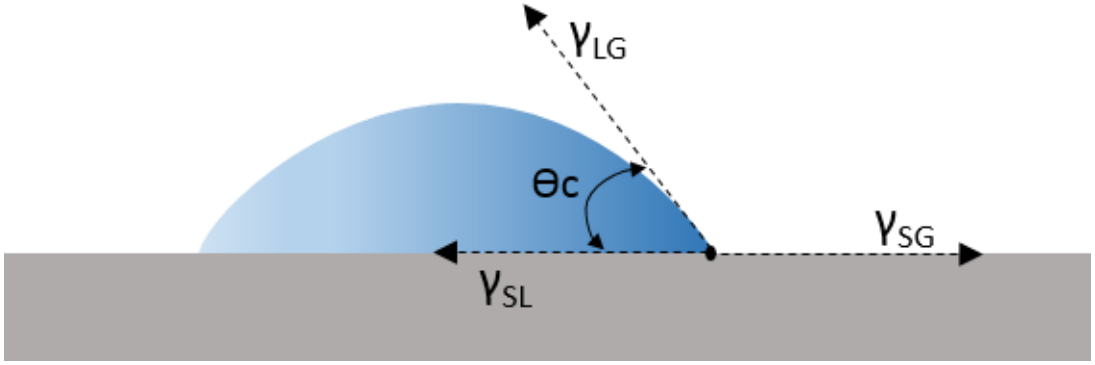


Figure 1.5: An illustration of the sessile drop water contact angle (Θc) measurement, indicating the three phase interfacial free energies; solid-gas (γ_{SG}), solid-liquid (γ_{SL}) and liquid-gas (γ_{LG}).

Further bulk powder adhesion measurement approaches will be discussed in greater detail in Chapter 5, however although these techniques can provide useful information about the interplay of particles and the adhesion to a surface these convolve several components of adhesion and therefore, isolating out the effect of these components can be extremely difficult[29]. In order to more fully understand the effects of a range of factors on the interaction of a particle with a surface colloidal probe microscopy is considered the gold standard[19].

1.6.1 Atomic Force Microscopy

1.6.1.1 Types of Imaging Modes

Atomic Force Microscopy (AFM), first described by Binnig *et al.*[30], is an imaging and analytical tool capable of subnanometre spatial resolution on a wide range of materials[20,31]. AFM is used in a wide range of fields from material sciences, physics, and in more recent years biomedical and pharmaceutical sciences[32]. AFM is a technique involving the use of a very sharp tip which is rastered over a surface and forms an image of surface topography by physically measuring the surface height at an array of pixels across the scan area. In Figure 1.6 the main components of an AFM are shown schematically. A sharp micron-sized tip is mounted on a flexible cantilever, which bends or deflects if force is exerted, indicating an interaction with the surface

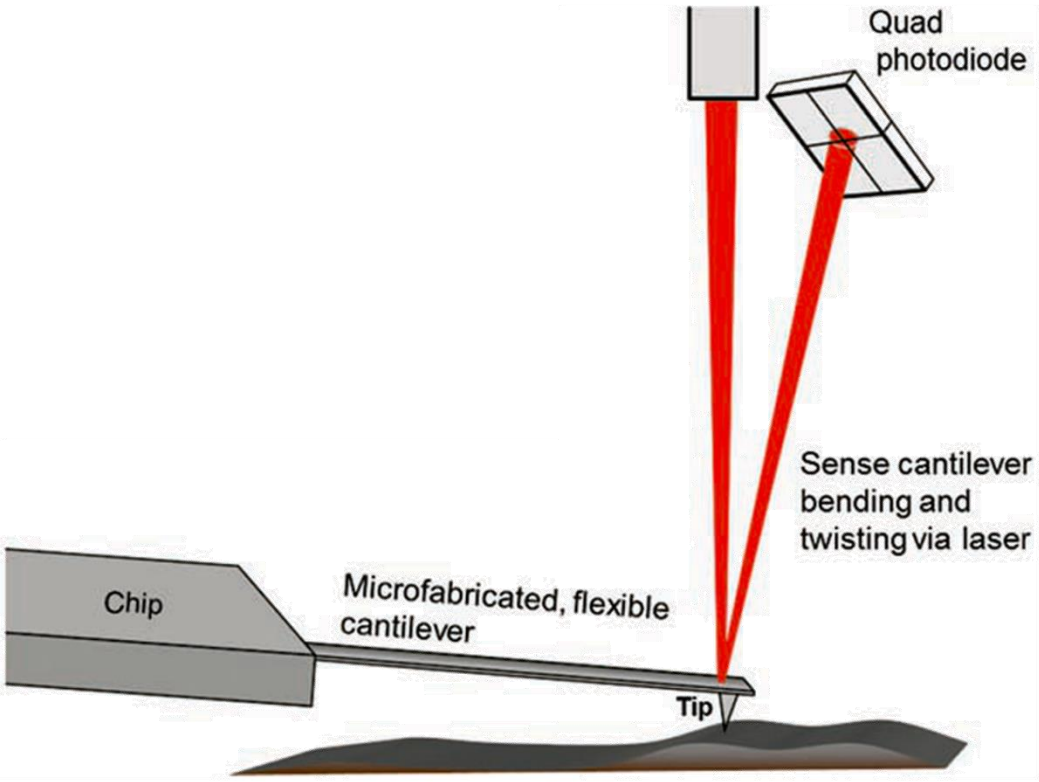


Figure 1.6: A schematic of the main components of an AFM. The laser is focused on the upper surface of a cantilever which uses a sharp tip to physically touch the surface to be imaged. Any change of topography will cause a deflection in the cantilever which will be detected by the change on the photodiode. Picture adapted from[20].

being analysed[33]. By aligning a laser to reflect off of the upper surface of the cantilever (often coated with a thin layer of gold to improve reflectivity[34]) this deflection can be quantified, by evaluating the movement of the reflected laser on a position sensitive photodiode.

There are two main types of imaging mode; contact and non-contact. Contact mode, as its name suggests, keeps the tip in continuous contact with the surface as it scans the sample surface. For relatively smooth samples constant height mode can be used, this involves measuring the deflection up and down of the cantilever as it moves over the surface, to record surface height[20]. However, as the surface roughness increases excessive cantilever bending can cause both tip and sample damage as the force being used to image the sample will vary dramatically. Likewise, if the surface descends away from the tip, the cantilever will be unable to follow and the tip will disengage from the surface and the image will be lost. This led to the more commonly

employed type of contact imaging called constant force mode. This involves an AFM using a piezoscanner, separate from the one for X-Y movement, to move the whole cantilever up and down. By actively monitoring the feedback the amount of force applied to the surface can be kept consistent. For instance, if the surface starts to rise the feedback loop will detect an increase in the force being applied and the tip will raise away from the surface correcting to the desired set force[32]. However, both types of contact mode fundamentally involve dragging a tip across a surface[35].For relatively soft materials, like certain polymers and biological materials, this can result in damage to the surface. This damage can be reduced by using intermittent or non-contact modes. The most common of which is called tapping mode. In order to achieve minimal contact with the surface the cantilever is oscillated at or close to its resonance frequency, allowing for multiple approaches towards the surface per pixel[20]. As the tip approaches the surface adhesion or repulsion forces between the tip and sample will begin to dampen the oscillation of the tip. To keep contact to a minimum, the Z scanner now receives feedback and moves the cantilever to ensure consistency in the amplitude (or frequency) of the tip oscillation. This allows the generation of a topographical image of the surface, nevertheless as the tip is not in constant contact with the surface during large part of its oscillation cycle there is a slight loss in spatial resolution compared to contact mode. However, by evaluating the surface effects on the oscillation of the tip, additional information can be extracted about the mechanical and adhesion properties of the surface[35].

The overall resolution of the topographical imaging, however is still limited by the radius of curvature of the tip, as the resulting image is a convolution of the surface topography and the tip profile. For high aspect ratio features, considerable “probe broadening” will occur, where the features appear stretched (Figure 1.7)[36]. As the probe travels over the feature, the side of the probe may make contact with the feature and the resultant sides actually reflect the slope of the probe, however the height shown will be correct[20]. This is particularly problematic when surface features and those on the probe are on the same scale.

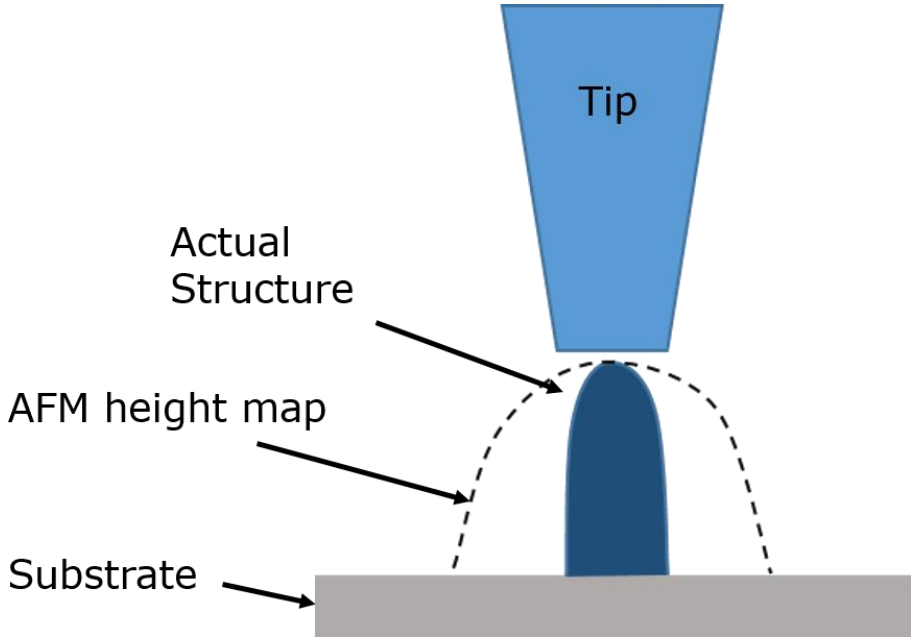


Figure 1.7: Issue with probe broadening caused by the interaction of the side of the tip with the topography being imaged.

1.6.1.2 Force Measurements

A key feature of AFM lies in its ability to measure surface and interfacial forces. Force-distance curves, or force curves for short, involve the lowering of the AFM tip towards the surface, contacting the surface and then withdrawal from the surface[32]. The deflections of the cantilever versus the distance moved as the tip and the sample are brought together can then be plotted (Figure 1.8). As the probe begins its descent, the cantilever is in the rest position (Figure 1.8 A), as it approaches the surface it may be deflected by attractive forces like van der Waals or electrostatic forces eventually causing a "jump to contact" as the spring constant of the lever is exceeded[33] (Figure 1.8 B). The cantilever will then continue its approach until the pre-set maximum load is reached, at which point the direction of motion will reverse and it will begin to withdraw (Figure 1.8 C). In this retract phase, the cantilever and sample will begin to separate. A hysteresis is often seen at this point on the force-curve which represents the adhesion between the tip and the sample (Figure 1.8 D). Therefore, the cantilever will experience a negative deflection, which will continue until sufficient separation is reached and the probe is pulled away from the sample[20]. By measuring this

negative deflection (*d*), as the cantilever behaves as a spring, Hooke's Law (equation 1.12) can be used to calculate the force of adhesion (F_{ADH}) between the probe and the sample.

$$F_{ADH} = -kd \qquad (1.12)$$

In this case, k is the spring constant of the cantilever, which in this thesis is calculated using the thermal tune method[37].

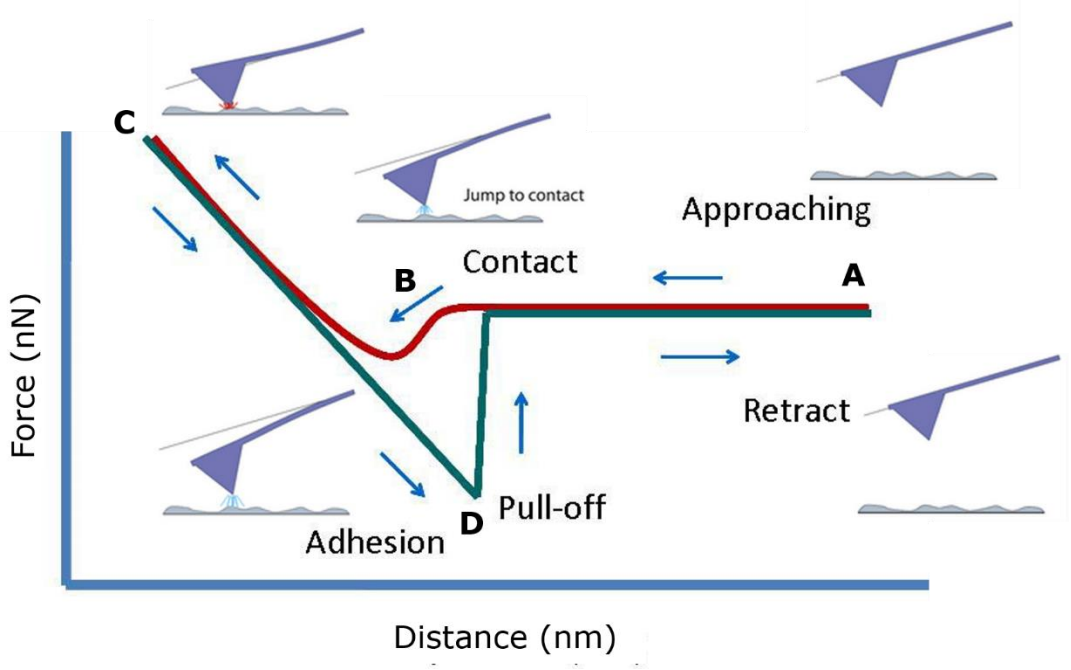


Figure 1.8: A schematic of the key phases in a force-distance curve. On approach the cantilever is in resting position, which as it approaches the surface, may jump to contact due to attractive forces. The tip will then continue down until the maximum load is reached, at which point the tip will begin to withdraw. The cantilever may then undergo a negative deflection as the probe sticks to the surface, until there is sufficient tip-sample separation to overcome this adhesion and the cantilever returns to resting position. Picture adapted from[38,39].

1.6.1.3 Force Mapping

The measurement of force curves at single points, provides information about the substrate at that point. It is relatively straightforward to carry this measurement out in the X-Y plane at adjacent pixel to form a map, for substrates with varying morphologies or chemistries (Figure 1.9) [33].

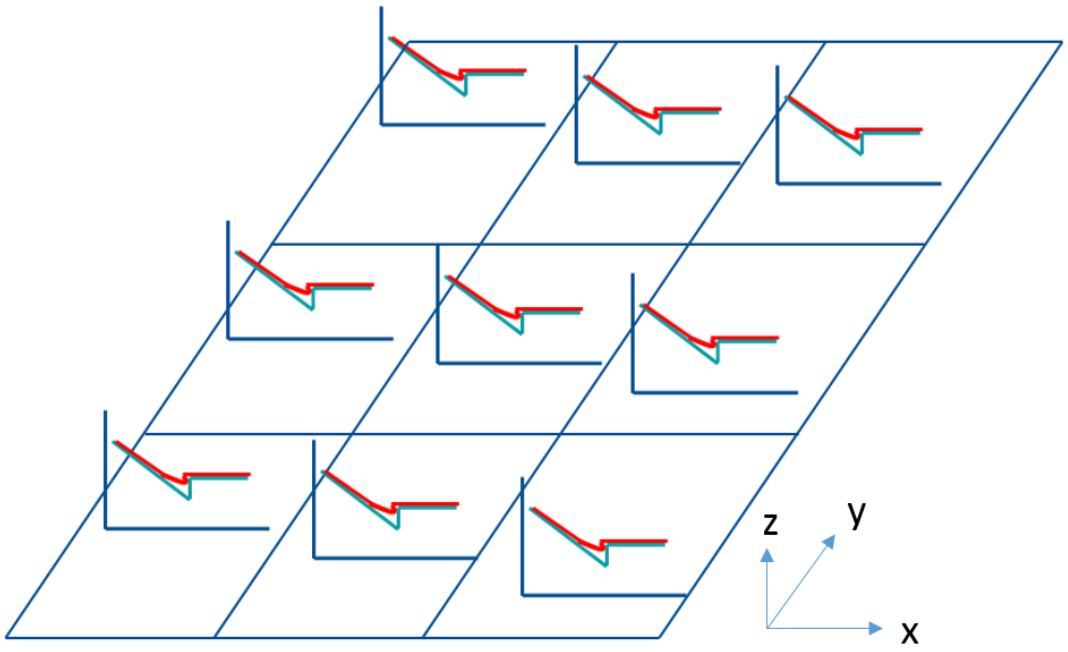


Figure 1.9: An array of force curves are collected over the area to be imaged, allowing the generation of a map of probe-surface interactions.

1.6.1.4 Colloidal Probe Microscopy

Although, the adhesion measurements performed using an AFM tip are useful, they provide limited information about the interactions between a pharmaceutical particle and a surface. A modification to the cantilever, termed colloidal probe microscopy (CPM), overcomes this limitation by attaching particles or micron sized spheres usually with a minimal amount of glue to the end of an AFM tip[40]. There are two main ways of producing a colloidal probe by micromanipulators, by placing a tiny amount of glue on the end of a cantilever and the manoeuvring the colloidal probe onto this spot, using fine wires[34]. The other method involves using the cantilever itself and lowering it first onto the glue and then onto the particle to be attached[31]. However, both of these methods are time consuming and labour intensive, so the number of particles used in CPM is generally limited [40].

Initially, CPM used model spheres like silica beads as outlined by Ducker *et al.*[41,42], allowing for a well- defined contact geometry. This then progressed to the attached of "real" pharmaceutical particles, like lactose carrier particles by Ibrahim *et al*[43].

However, the use of these types of particles presents a problem with comparability of results, as even when the same type of particle is used, changes in surface roughness, mounting angle and size can result in highly variable adhesion data[44]. One way of mitigating this variation is by using the same particle to image multiple surfaces, thereby allowing a direct comparison and ranking of adhesion[40]. However, during use the repeated contact of the tip with the surface can induce morphological changes in the particle and so alter the contact area and adhesion[21]. Therefore, a normalisation for contact area is needed which will allow comparison between particles, and indeed the same particle at different stages of measurement. One approach to measure this is by tip self-imaging using the AFM, before and after every measurement[45].

It is worth noting that both environmental and experimental conditions, play a significant role in particle adhesion measurements[14]. Therefore, it is essential that humidity must be controlled during measurements and that factors involved in the collection of force-curves like maximum load, approach and retract speed and contact time are kept consistent[34,40,46].

Adhesive forces measured by colloidal probe microscopy, is therefore dependent on the size and shape of the probe, the surface morphology and roughness of both the probe and the substrate, the depth of interaction and hence the actual contact area of interaction. All of these factors inter-relate and therefore isolating out the effect of one of these factors is extremely difficult[19]. Therefore, a methodology that enables the generation of a homogenous and well defined surface is sorely needed.

1.7 Pulmonary Drug Delivery

Drug delivery to the lung has been a delivery route of long standing and sustained interest in the pharmaceutical industry. Pulmonary drug delivery provides the most direct and efficacious treatment for respiratory conditions like asthma, chronic obstructive pulmonary disease (COPD) and cystic fibrosis. Also, the large alveoli surface area (80-100m^2) [10], extensive blood perfusion[47], first-pass-effect avoidance[48]

and delivery convenience, presents a viable alternative for systemic delivery. Inhalation has been utilised for the delivery of many drugs related to respiratory disease and also therapeutics such as insulin, human growth hormones, and oxytocin[48]. Particles are generally considered to be deposited in the airways by three physical processes; inertial impaction, sedimentation and diffusion[49]. For successful delivery to the desired sections of the lung, a device must possess both a high emitted dose and a high fine particle fraction, i.e. a significant proportion of particles with an aerodynamic diameter of less than 5 µm[11]. A larger particle size would impact in the trachea on inhalation (via inertial impaction) and therefore not penetrate the airways sufficiently, while particles less than 1 µm are believed to be exhaled before deposition[47]. However, particles of such a small size are known to aggregate, due to their high surface area to volume ratio, making such formulations problematic to develop and an understanding of particle-particle interactions critical[50].

1.7.1 Aerosol Generation and Drug Deposition

The effectiveness of a device for pulmonary drug delivery is critically influenced by the anatomy of the respiratory system. The lungs are a series of progressively branched and narrowing airways (Figure 1.10), which can broadly be divided into two main sections[51]. From the oropharynx down to the terminal bronchioles (generation 16) is considered the conducting zone which accommodates the bulk intake of air during inspiration. The second section is termed the respiratory zone starting at the respiratory bronchioles (generation 17) and continues until the alveolar sacs (generation 23). The respiratory region possesses a far greater surface area and is responsible for the gas-exchange.

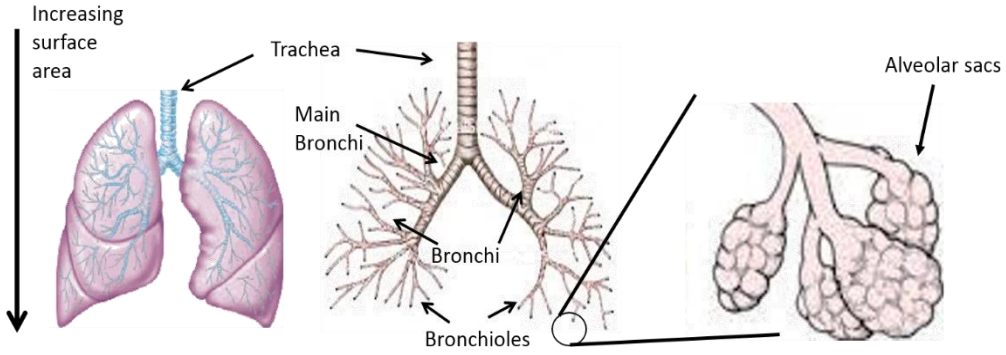


Figure 1.10: Representation of the structure of the human lung. Picture adapted from[52–54].

Once the drug is aerosolised the deposition location is dependent on the aerodynamic particle size, airway geometry and velocity of the inspiration[55]. As stated there are three main mechanisms of particle deposition in the respiratory system[49]; firstly inertial impaction, this mainly influences particles with an aerodynamic diameter greater than 5 µm[11,55]. In the first ten generations (e.g. bifurcation levels) of the lung, larger particles tend to be unable to navigate the bifurcations, and are therefore carried by their inertia into the wall of the airway. These particles will then be swallowed (following transport up the airways through the so-called mucocilliary escalator) and so will have negligible therapeutic effect[55,56]. The next mechanism of particle deposition is sedimentation, this is due to the effect of gravitational forces acting on the particle causing them to settle[11,51]. Sedimentation is a time dependent process and is therefore more likely to occur in low air velocities in the deeper lung where the airway diameter is small and so is most commonly seen in the smaller airways and alveolar[11]. As the probability of a particle settling by sedimentation increases with the square of the particle diameter[55] this normally affects particle of 1-8 µm[18]. Finally, particles less than 1 µm require a far longer settling time and therefore are often exhaled from the lungs. However, in the alveolar region where airflow is minimal[51], Brownian diffusion from the bombardment of gas molecules on the particle[18] causing an irregular motion can cause particle deposition.

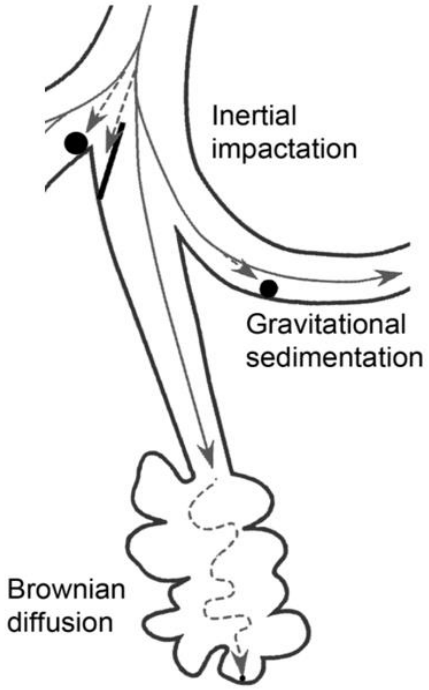


Figure 1.11: A visual representation of the three main mechanism of particle deposition in the lungs. Picture adapted from Fröhlich and Salar-Behzadi 2014[57].

1.7.2 Devices to Deliver Active Pharmaceutical Ingredients to the Lungs

Currently there are three main types of devices on the market; dry powder inhalers (DPIs), pressurised metered dose inhalers (pMDIs) and nebulisers[11]. Device choice is an important factor in the successful delivery of the therapeutic agent to the targeted area of the lungs[48].

1.7.2.1 Pressurised Metered Dose Inhalers (pMDIs)

Pressurised Metered Dose Inhalers (pMDIs) are currently the most commonly used device on the market to deliver APIs to the respiratory tract, as they are relatively cheap and easy to manufacture and are portable, so convenient for the patient[58]. They comprise a propellant and a solution or suspension of the therapeutic agent, with the metering valve dispensing a set volume of the formulation during actuation[47]. Upon actuation, the metered dose is released from the holding chamber

as a jet of droplets containing the volatile propellant and the drug[56]. As this jet travels during the inspiration, the now de-pressurised propellant evaporates, with the drug remaining as respirable particles or droplets[59]. This platform allows consistent dosing irrespective of the patient's inspiration, however, patients must synchronise their breathing with the actuation of the dose or the dose will impact on the back of the patient's throat[60]. This co-ordination issue is a common problem among patients, which, along with concerns regarding the environmental impact of the propellants[51] used, often leads to a desire to utilise other devices.

1.7.2.2 Nebulisers

Nebulisers atomise an aqueous solution of the drug by means of energy application, forming droplets that are inspired via a facemask[10,47]. Currently, nebulisers are used primarily in the niche area of the critically ill, geriatrics and paediatrics, due to the generally bulky, complicated nature of the devices[10]. However, they almost completely eliminate the need for the patient to co-ordinate their breathing which is highly advantageous.

They are broadly divided into three different types; jet, ultrasonic and mesh nebulisers. Jet nebulisers generate a respirable aerosol using a compressed air supply which also serves to generate a pressure differential. Thereby drawing the formulation from the liquid reservoir to the orifice via the Bernoulli principle[49,61]. They can be further sub-divided based on whether the output is produced only on or enhanced on inhalation, or entirely independent of inhalation with a constant output. The ultrasonic nebuliser vibrates a piezoelectric crystal at a high frequency (1-3 MHz) in the liquid reservoir generating a standing wave which results in the formation of respirable droplets[48,61]. Finally, the mesh nebuliser is the newest class, which work on the same principle as the ultrasonic nebuliser, but forces the liquid through a perforated plate or mesh[48].

1.7.2.3 Dry Powder Inhalers (DPIs)

As their name suggests, dry powder inhalers (DPIs) work by dispersing a dry powder to form particles of the API in the respirable range. This is often preferable to nebulisers and pMDIs as the formulation will possess improved physico-chemical stability as a solid, which is of increasing importance with the advent of biologic and protein APIs[62]. They can also achieve a higher delivered dose compared to pMDIs. DPIs can be broadly divided into two types of device; single dose or multi-dose devices[18]. For single dose DPIs, like the Handihaler™, an individual dose, often encompassed in a capsule, must be loaded before each actuation. Multi-dose DPIs by contrast either have a reservoir of the formulation, which is metered into individual doses by the inhaler, or work by piercing individual blisters in a pre-loaded strip[18]. An example of these are the Turbuhaler™ and Diskhaler™ respectively. Multi-dose DPIs are often preferred especially for medication that may need to be taken quickly, for instance in the course of an asthma attack[11]. Finally, DPIs can also be classified as active or passive, with most commercial DPIs falling into the latter category. A passive DPI's sole source of energy to successfully disperse the formulation, originates from the patient's inspiration. However, due to the inconsistency of a patient's flow rate, more DPIs are being designed to aid in the dispersion, using an active component like a vibrating mesh or spring mechanism[10,63].

As mentioned previously for an API to exert its therapeutic action, it must possess an aerodynamic diameter between one and five microns. In order to achieve this a bulk powder must undergo two main steps; fluidisation, where the bulk powder is resuspended in the airflow, and deagglomeration, which involves the separation of the particle aggregates into their primary particles[10,64]. However, particles of this size, due to their high surface area to mass ratios, are inherently cohesive and adhesive. The powder formulation therefore often forms aggregates that do not disperse on inhalation, or adheres strongly to the device walls, resulting in many DPIs possessing efficiencies less than 20%[18].

1.8 Surface Modification Methods to Alter Particle Adhesion Properties

As particle adhesion is of critical importance in numerous industries, including pharmaceutical processing, there have been various methods used to modify the surfaces of particles or substrates, either by changing the surface chemistry or morphology. These changes have then been evaluated for their resultant effect on particle-surface adhesion and the resultant performance of dry powder inhalers.

1.8.1 Formulation Strategies/ Dry Coating

As small particles in particular are inherently adhesive and cohesive, accurate dosing and aerosolisation of DPI powders is often problematic[10]. There have been a range of formulation strategies employed to attempt to mitigate these issues. The first of which is to formulate the API with a secondary particle called a carrier particle. By adding coarse carrier particles (50 – 100 µm), usually lactose[11], the dose to be delivered can be increased and flowability improved, resulting in better accuracy of dispensing due to the increased volume. The coarse particles also act as an additional source of agitation and promote fluidisation of the drug particles during inhalation[65].

However, the presence of amorphous regions on the surface of lactose creates 'active' surface sites with a metastable thermodynamic state with high free energy for drug particle adhesion[66] on the coarse particles (Figure 1.12 A). Also, surface asperities can result in the entrapment of the smaller drug particles and a reduction in delivery efficiency[10,11]. In order to overcome this issue, ternary formulations have been developed which also include fines, these are particles usually in the nanoscale range, often of the same material as the carrier particles. Removal of fines have been shown to more than halve the fine particle fraction in mixtures of salbutamol sulphate with lactose as a carrier. These fines help improve the fluidisation of the drug particles in two ways, firstly they will bind preferentially to the active binding sites on the carrier particles (Figure 1.12 B), this helps to reduce the adhesion between the API and the carrier, they also increase the separation between particles, reducing the van der Waals attractions and so improving fluidisation[67].

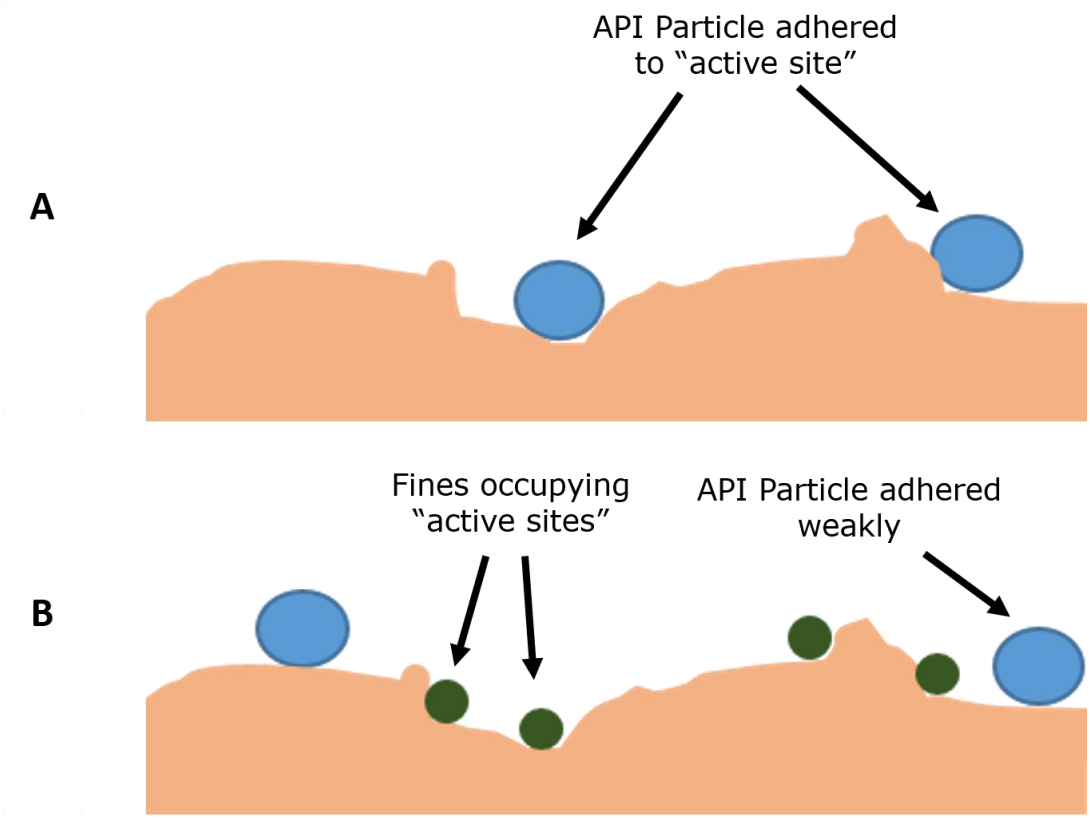


Figure 1.12: Formulation Strategies – An illustration of the use of fines (green) to reduce adhesion between API (blue) and carrier particles (peach) in A) a binary formulation and B) a ternary formulation for dry powder inhalers.

This strategy has also been employed in general to reduce adhesion and cohesion of powders with "dry coating," or simply put, the surface coverage of one particle with nanoscale particles, to help improve flowability of cohesive powders[68] and reduce particle adhesion[69,70]. In order to improve this reduction of adhesion, this dry coating has also been extended to the use of "force-control agents" like leucine[70] and magnesium stearate[51,71], which are thought to reduce surface passivation of high surface free energy sites[51].

1.8.2 Mechanical Modification

As stated earlier surface roughness plays a key role in the adhesion and cohesion of particles, however the true extent of this role is not yet fully elucidated[72]. Therefore, there have been a range of techniques employed to attempt to modify the surface roughness of particles in order to evaluate the resultant effect on particle adhesion.

These include particle smoothing; using a small amount of solvent and a series of wetting and drying steps[73,74], coating the particles with an aqueous solution, to smooth the particle and produce a homogenous surface chemistry[70] or modification of the crystallisation process to produce varying surface roughnesses[75,76].

There have also been attempts to do the opposite to create a rough surface either by milling the particle themselves[77] or a model sphere like a glass bead followed by a coat of some sort[78–80].

However, all of these techniques either also change the surface energetics of the particle in question, or provide limited control in the surface topography generated and therefore allow limited scope for an investigation into how surface morphologies can effect particle adhesion.

1.8.3 Silanization

Silanization is often used to control and modify both particle surfaces[8,69,81] and the surface of the substrate[13] in colloidal probe measurements. Silanes are organic silicon chemicals, which can be hydrolysed to react with a surface[13]. These can alter the surface energy, making it either hydrophobic or hydrophilic depending on the silane chosen[82]. Silanization with methyltrichlorosilane has been shown to effectively reduce particle adhesion of aluminium powders by Jallo *et al.*[69]. It has also been used to attempt to decouple the effect of surface chemistry on particle adhesion by Heng *et al*[83]. The particles can then be modified, for instance by milling or selection of differing crystal habit, and then silanized to produce a consistent surface chemistry and hence isolate the effect of surface energy from the resultant adhesion measurements[81,83,84]. However, despite this being a good method to modify the surface energy of a surface, this has been shown to in fact backfill nano-roughness[85] a key factor in the particle-substrate adhesion.

1.8.4 Patterned Surfaces

There have been limited examples of this currently, however, a range of micro and nano-textured surfaces have been produced by Bhushan *et al*[86] using soft lithography, spin coating and moulds for an investigation in the effects of surface roughness on particle adhesion in the field of micro-electronics. However, these processes required multiple steps and still provided limited morphological control.

Therefore, the scope of this thesis is to identify, evaluate and develop the capability of additive manufacturing, to produce the desired controllable morphological changes on an appropriate micron scale for the purposes of investigating the effect of surface roughness on particle adhesion.

1.9 Additive Manufacturing

In commonly employed, so-called subtractive manufacturing, a material is removed from a block of the original raw material, for instance by cutting or drilling to form the desired object[87]. In recent years a new technique, additive manufacturing (AM), has been established, which involves the layer by layer addition of material to form a desired object[88]. An initial CAD (computer aided design) file containing the 3D model data is transferred into an STL (standard tessellated language) file and finally printed into the finished product[89]. The ability to produce products utilising AM can reduce processing time, human input reliance and provides the opportunity to explore a range of designs that is restricted in normal subtractive manufacturing[87].

The main AM processes currently in use can broadly be divided into two main categories (Figure 1.13); powder based and liquid based. The powder based category can further be subdivided into melting processes like; selective laser sintering (SLS)[90] or electron beam melting (EBM) or binding processes like 3DP (3D Printing)[91], which utilises a binder to fuse particles together[87]. In liquid processes, the liquid is either deposited in fine beads into the shape desired; fused deposition modelling (FDM), jetted and subsequently cured; inkjet[92] or solidified by polymerisation sterolithography[93].

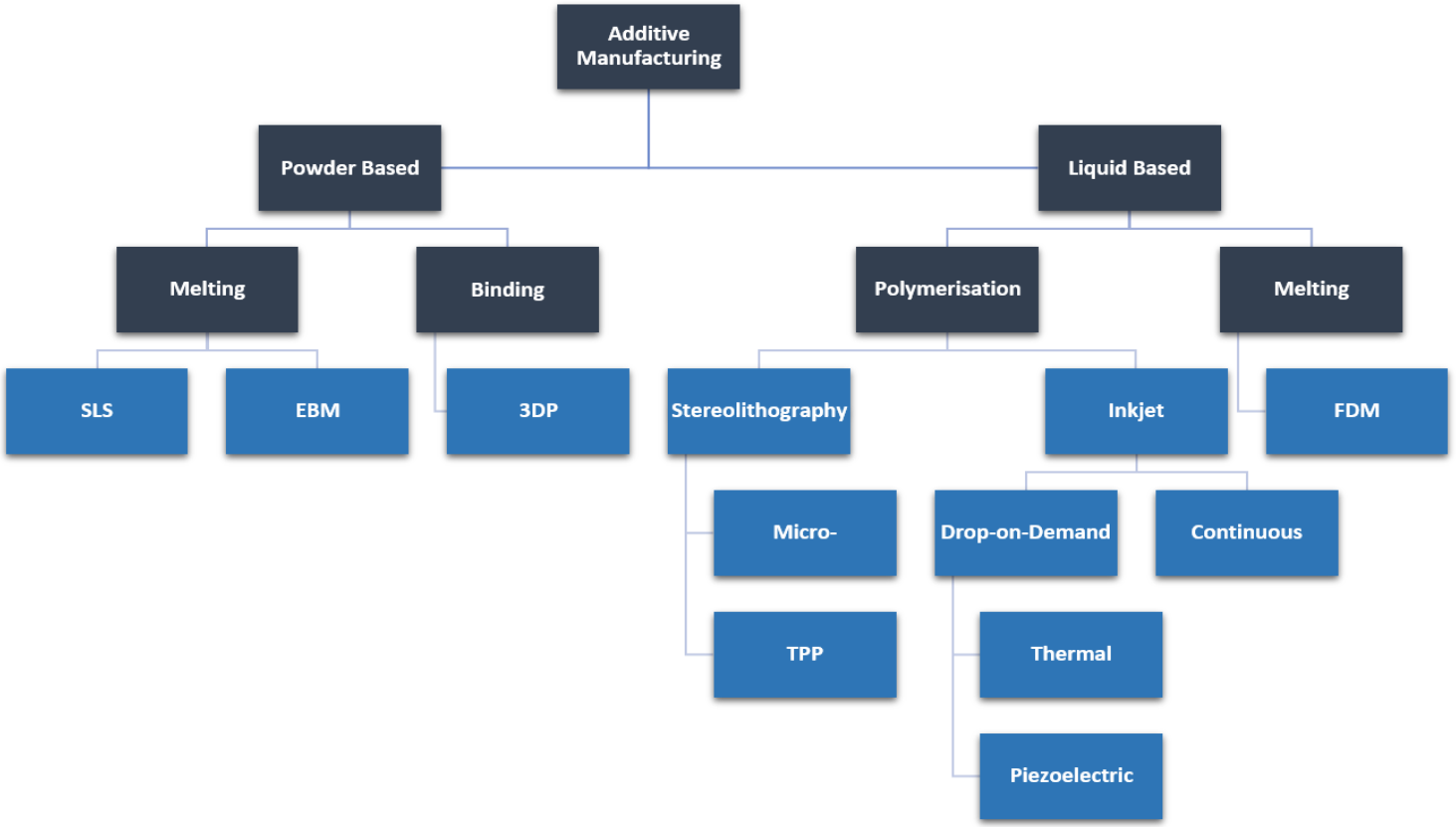


Figure 1.13: An overview of the additive manufacturing processes. SLS = selective laser sintering, EBM = electron beam melting, 3DP = 3D printing, TPP = two photon polymerisation, FDM = fused deposition modelling. Adapted from Wong et al. 2012[12]

1.9.1 Pharmaceutical Additive Manufacturing

AM is already becoming an established research avenue in the pharmaceutical industry[94]. Current conventional manufacturing processes, often require multiple steps and are conducted at a central manufacturing plant. However, the use of AM technologies will allow highly accurate dosing[88], that can be easily adjusted based on the patient's requirements[95], and has been shown to be quick and relatively low cost[5]. The main motivations for the use of AM in pharmaceuticals are; increased product complexity, personalisation and on-demand manufacturing[96].

First increased complexity provides the potential to explore products that would be otherwise unachievable by traditional manufacturing methods, for instance bespoke geometries, high accuracy or high porosity formulations. This is best demonstrated by the recent FDA approval of a 3DP powder-layered tablet SPRITAM® in 2015[97], an oral solid dosage formulation containing levetiracetam. This tablet was printed with higher porosity levels than achievable standard tablet compression, thereby allowing faster dissolution. AM also allows an investigation and production of various dosage form geometries with varying release profiles[98,99]. The high accuracy of the deposition of APIs has also been explored in the manufacture of microneedles with inkjet printing being used to produce metal microneedles coated with different drug/ polymer combinations[100]. Finally, the high resolution of two photon polymerisation has been utilised in the investigation of the importance of pore positioning on hollow microneedles[101].

The potential of the ability to personalise formulations has also been shown to highly beneficial in the printing of medicines with multiple active pharmaceutical ingredients[5]. Finally, the ability to produce dosage forms on-demand, may allow prescriptions to be manufactured to order in pharmacies, allowing expanded capabilities for the provision of medicines in surgical or emergency situations[96].

1.9.2 Additive Manufacturing in Pulmonary Drug Delivery

The use of AM in the field of pulmonary drug delivery is currently very limited. There have been some attempts to use AM to prototype different device designs, in order to evaluate their effect on the formulation efficiency. Behara *et al*, utilised stereolithography to evaluate the effect of the orientation of the capsule chamber in comparison to the main flow passage[102] and capsule chamber air inlets positioning and quantity[103]. A FDM printer has also been used to produce a modified induction port for a cascade impactor based on CT scans of the human trachea[104]. However, in 2017 AM, specifically PolyJet inkjet printing has been used to produce a recently approved "smart" inhaler in Israel for the inhalation of medical marijuana. This inhaler allows controllable metered doses and provides inhalation data via the internet for medical practitioners or researchers to evaluate[105], overcoming some of the regulatory issues of medical marijuana.

However, currently the use of AM in pulmonary drug delivery has focused on the design and production of whole inhaler parts. However, in order to effectively investigate the effect of morphologies on the surface of inhalers, a method that provided enhanced resolution and control for the production of well-defined micron scale morphologies was needed.

Two photon polymerisation (TPP) was selected as an appropriate additive manufacturing technique to proceed with for the fabrication of the micron scale 3D structures in this thesis. This was decided upon as it provides both the capabilities to manufacture features in the desired size range, but also provides scope for complex 3D designs not available with other nano-fabrication techniques. As techniques like e-beam or X-ray lithography, may be capable of producing down to 10 nm resolution, however they lack the ability to print the 3D complexity that may be desired[106,107]. With the advent of two photon polymerisation, resolution of 120 nm has been achieved, combined with an ability to print 3D shapes, without the need for supports or masks[91,93,108]. TPP was therefore used for the micron scale morphologies used in this thesis.

1.9.3 Two Photon Polymerisation

In recent years, there has been a drive to produce items with AM at ever decreasing size and improved resolution. In the electronic industry especially, there is a desire to produce microelectronics with increased processing and memory availability. Photolithography has been of great importance in producing ever-smaller transistors[106] desired in accordance with the trend predicted by "Moore's Law".

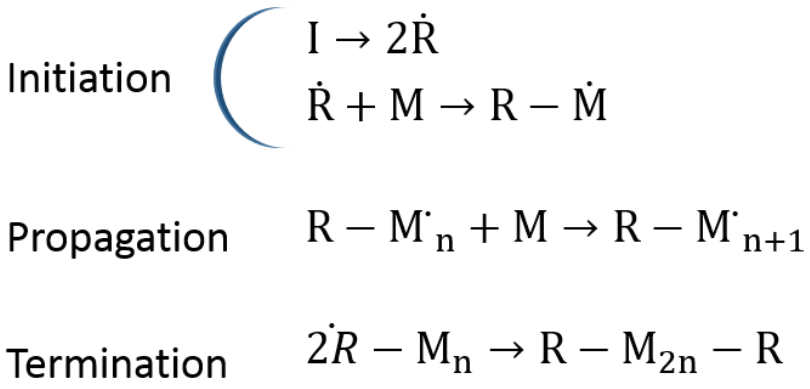


Figure 1.14: Radical Polymerisation Reaction; resulting in the generation of free radicals (R) from the excited photoinitiator (I). Thereby producing radical monomers (M) and eventual formation of polymers (Mn).

Photolithography involves the use of a resin which contains a monomer, often an acrylate derivative, and a photoinitiator. The photopolymerisation reaction that occurs (Figure 1.14), involves radical polymerisation, where an excited initiator (I) becomes a free radical (R). The radicals produced will then radicalise the monomers (M) and oligomers by cutting the double bonds of the carbons in the acrylyl groups. This process will then cascade until the process is terminated by the combination of two radicals forming polymers (M_n)[109,110] and the resin will solidify.

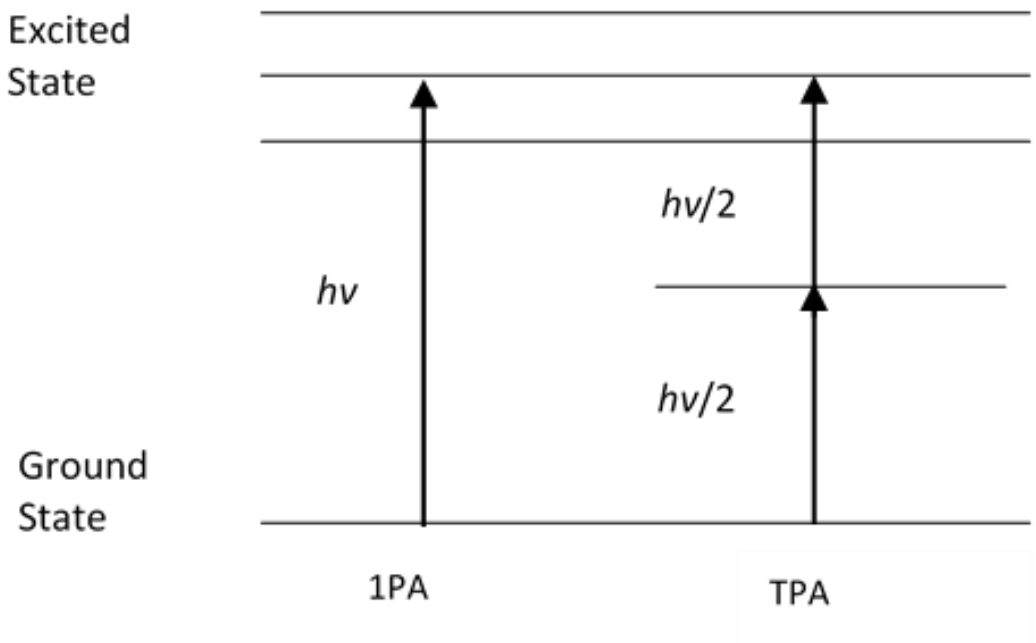


Figure 1.15: Photon Absorption. One-photon absorption (1PA) of a UV photon excites a photon from the grounded to the excited state. On the right, two photon absorption (TPA), involving two near IR photons exciting an electron via an intermediate state.

However, in conventional lithography, there is a poor spatial resolution, with off-target polymerisation resulting in millimetre resolution[109] and a requirement of 3D structures built with layer-by-layer polymerisation[111], restricting the 3D structures that can be formed[109]. Two photon polymerisation (TPP), by contrast, employs two photon absorption (TPA), which is a non-linear optical process and therefore polymerises a small focal volume within the focal plane[112].

On absorption of a photon, electrons present in an atom can be excited into a higher energy state, which on relaxation releases a photon. This phenomenon is utilised in numerous applications, for instance in fluorescent lights and televisions generating light. However, in 1931, Marie Goeppert-Mayer[106] hypothesised the ability for more than one photon to be absorbed, producing the same excited state (Figure 1.15). TPA involves the simultaneous absorption of two photons of half the energy, via a virtual intermediate state[110]. For TPA to occur successfully there is an extremely narrow window (~ 10^{-15}s) for the second photon to be absorbed[106], for this reason the use of TPA needs an extremely high density of photons. The advent of the laser, specifically a Ti: Sapphire femto-pulsed laser[106,112] combined with a high numerical aperture

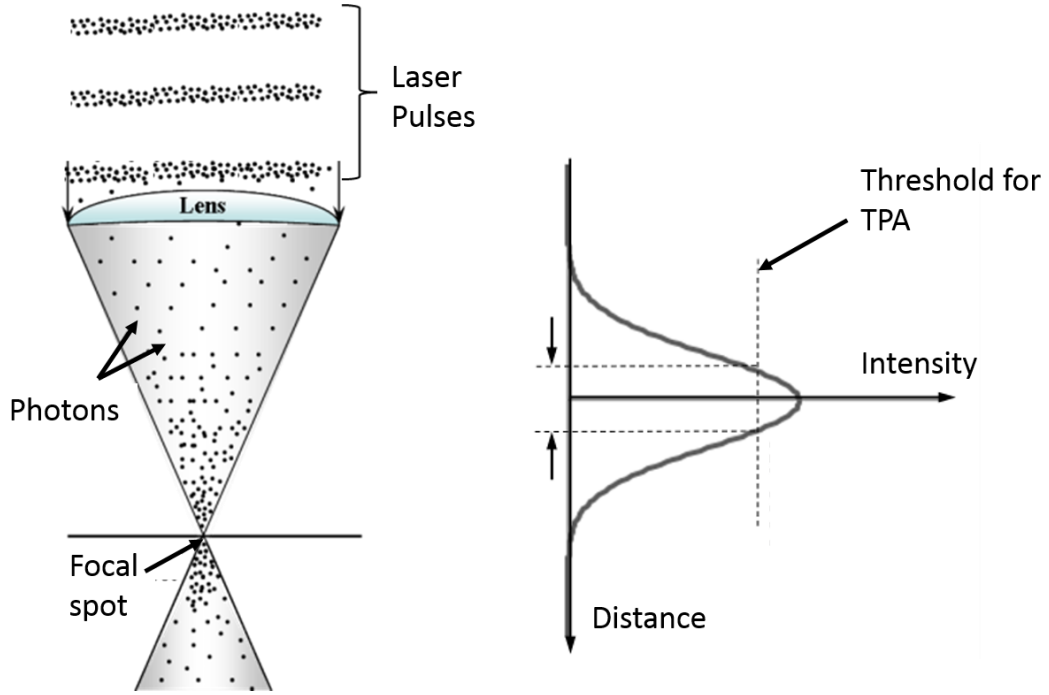


Figure 1.16: An illustration of temporal and spatial compression to produce sufficient photon density at the focal spot, achieved using a pulsed laser and an objective with a high numerical aperture. On the right a cross section of two photon absorption profile. Picture adapted from Spangenberg et al. 2013[18] and Hiroaki et al. 2010[114].

objective has provided this photon density (Figure 1.16) and allowed an increase of the use of this process for applications such as fluorescence imaging[112]. This need for a high density of photons, is also the reason for the improved resolution of TPP over conventional sterolithography, as the rate of polymerisation is proportional to the density of photons squared, resulting in sufficient photons only at the focal point[108] (Figure 1.16). TPP has been shown to produce a sub-diffraction limit lateral resolution of 120 nm[113]. The other advantage of this localisation using TPA, is that the polymer resin is transparent to the near- IR light, so structures polymerised at different depths do not cause much laser beam attenuation, so structures do not need to be built in layers[109], allowing true 3D structure capability.

1.10 Thesis Aims

The aims of this thesis are two-fold, to identify, optimise and evaluate a suitable additive manufacturing technique to produce well-defined micron scale morphologies appropriate for furthering the understanding of the importance of morphology on particle adhesion. Secondly, to measure the effect on particle adhesion and deposition to these morphologies, both on an individual and on a bulk powder basis, allowing elucidation and understanding of the effect of surface roughness on particle adhesion.

1.11 Thesis Objectives

In order to achieve these aims there are a series of objectives which will be covered during the course of this thesis:

- Assess a range of AM techniques to evaluate their capability to produce morphologies on the appropriate scale and their resultant surface finish.
- The development of Two Photon Polymerisation (TPP), once selected as the AM technique used for the duration of this thesis, both in terms of resolution, surface finish and reproducibility working on the decided control pattern.
- Utilisation of the printing capability, to produce a series of well- defined control patterns, with varying morphologies.
- Produce a consistent surface chemistry on the well-defined morphologies.
- Produce a series of colloidal probes appropriate to respiratory drug delivery, and utilise these to assess particle adhesion on an individual particle basis using atomic force microscopy force-distance curves.
- Develop a bulk powder system capable of evaluating particle adhesion in an environment appropriate for respiratory drug delivery.
- Test the control patterns in a bulk powder system and evaluate the findings in light of the individual particle adhesion understanding.

1.12 Chapter References

1. Bowling, R. A. An Analysis of Particle Adhesion on Semiconductor Surfaces. *J. Electrochem. Soc.* **132,** 2208 (1985).

2. Holdich, R. G. *Fundamentals of Particle Technology*. (Midland Information Technology and Publishing, 2002).

3. Johnson, M. F. L., Kreger, W. E. & Erickson, H. Gas Oil Cracking by Silica-Alumina Bead Catalysts. *Ind. Eng. Chem.* **49,** 283–287 (1957).

4. Aulton, M. . *Aulton's Pharmaceutics: The design and manufacture of medicines*. (Churchill Livingstone, 2007).

5. Khaled, S. A., Burley, J. C., Alexander, M. R. & Roberts, C. J. Desktop 3D printing of controlled release pharmaceutical bilayer tablets. *Int. J. Pharm.* **461,** 105–111 (2014).

6. Feeley, J. C., York, P., Sumby, B. S. & Dicks, H. Processing effects on the surface properties of α -lactose monohydrate assessed by inverse gas chromatography (IGC). *J. Mater. Sci.* **37,** 217–222 (2002).

7. Solution, T. S. The Total Sorption Solution The Surface Energy Solution About the Technique. *Surf. Meas. Syst.* at <http://www.thesorptionsolution.com/files/P-SEA-001 v1.0 22NOV2010 SEA 6pg brochure EMAIL INDIVIDUAL PAGES.pdf>

8. Gamble, J. F. *et al.* Surface energy analysis as a tool to probe the surface energy characteristics of micronized materials--a comparison with inverse gas chromatography. *Int. J. Pharm.* **422,** 238–44 (2012).

9. Podczeck, F. (The S. of P. U. of L. *Particle-particle Adhesion in Pharmaceutical Powder Handling*. (Imperial College Press, 1998).

10. Daniher, D. I. & Zhu, J. Dry powder platform for pulmonary drug delivery. *Particuology* **6,** 225–238 (2008).

11. Zeng, X. M., Martin, G. P. & Marriott, C. *Particulate Interactions in Dry Powder Formulations for Inhalation*. (Taylor & Francis, 2001).

12. Buckton, G., Choularton, A., Beezer, A. E. & Chatham, S. M. The effect of the comminution technique on the surface energy of a powder. *Int. J. Pharm.* **47,** 121–128 (1988).

13. Mittal, K. L. & Jaiswal, R. *Particle adhesion and removal*. *Part. Adhes. Remov.* (2015). doi:10.1002/9781118831571

14. Hooton, J. C. *et al.* An Atomic Force Microscopy Study of the Effect of Nanoscale Contact Geometry and Surface Chemistry on the Adhesion of Pharmaceutical Particles. *Pharm. Res.* **21,** 953–961 (2004).

15. Xiao, X. & Qian, L. Investigation of Humidity-Dependent Capillary Force. *Langmuir* **16,** 8153–8158 (2000).

16. Yang, J., Sliva, A., Banerjee, A., Dave, R. N. & Pfeffer, R. Dry particle coating for improving the flowability of cohesive powders. *Powder Technol.* **158,** 21–33 (2005).

17. Visser, J. Van der Waals and other cohesive forces affecting powder fluidization. *Powder Technol.* **58,** 1–10 (1989).

18. Colombo, P., Traini, D. & Buttini, F. *Inhalation Drug Delivery*. (John Wiley & Sons, 2013).

19. Weiss, C., McLoughlin, P. & Cathcart, H. Characterisation of dry powder inhaler formulations using atomic force microscopy. *Int. J. Pharm.* **494,** 393–407 (2015).

20. Haugstad, G. *Atomic Force Microscopy: Understanding basic modes and advanced applications*. (John Wiley & Sons, Inc., 2012). doi:10.1002/9781118360668

21. Butt, H.-J., Cappella, B. & Kappl, M. Force measurements with the atomic force

microscope: Technique, interpretation and applications. *Surf. Sci. Rep.* **59,** 1–152 (2005).

22. James, J. The Interaction of Drug Particles with Materials Employed in Inhaled Delivery Devices. (2009).

23. Tabor, D. Surface forces and surface interactions. *J. Colloid Interface Sci.* **58,** 2–13 (1977).

24. Leite, F. L., Bueno, C. C., Da Róz, A. L., Ziemath, E. C. & Oliveira, O. N. Theoretical Models for Surface Forces and Adhesion and Their Measurement Using Atomic Force Microscopy. *Int. J. Mol. Sci.* **13,** 12773–12856 (2012).

25. Rabinovich, Y. I., Adler, J. J., Ata, A., Singh, R. K. & Moudgil, B. M. Adhesion between Nanoscale Rough Surfaces. *J. Colloid Interface Sci.* **232,** 17–24 (2000).

26. Laitinen, O., Bauer, K., Niinimäki, J. & Peuker, U. A. Validity of the Rumpf and the Rabinovich adhesion force models for alumina substrates with nanoscale roughness. *Powder Technol.* **246,** 545–552 (2013).

27. Hewitt, G. F., Delhaye, J. M. & Z., Z. *Multiphase Science and Technology (Volume 1)*. (Hemisphere Publishing Corporation, 1982).

28. Wang, G., Guo, Z. & Liu, W. Interfacial effects of superhydrophobic plant surfaces: A Review. *J. Bionic Eng.* **11,** 325–345 (2014).

29. Piggott, M. J. Characterising the force balance between active pharmaceutical ingredients for inhalation and its impact on deposition. (2013).

30. Binnig, G. & Quate, C. F. Atomic Force Microscope. *Phys. Rev. Lett.* **56,** 930–933 (1986).

31. Eve, J. K., Patel, N., Luk, S. Y., Ebbens, S. J. & Roberts, C. J. A study of single drug particle adhesion interactions using atomic force microscopy. *Int. J. Pharm.* **238,** 17–27 (2002).

32. Eaton, P. & West, P. *Atomic Force Microscopy*. *Oxford Univ. Press* (2010).

doi:10.1093/acprof:oso/9780199570454.001.0001

33. Allen, S., Davies, M. C., Roberts, C. J., Tendler, S. J. B. & Williams, P. M. Atomic force microscopy in analytical biotechnology. *Trends Biotechnol.* **15,** 101–105 (1997).

34. Kappl, M. & Butt, H.-J. The Colloidal Probe Technique and its Application to Adhesion Force Measurements. *Part. Part. Syst. Charact.* **19,** 129–143 (2002).

35. Davies, R. Powder Technology: Fundamentals of Particles, Powder Beds, and Particle Generation. *Measurement* 13–32 (2007).

36. Morris, V. J., Kirby, A. R. & Gunning, A. P. *Atomic Force Microscopy for Biologists*. *At. Force Microsc. Biol.* **81,** (Imperial College Press, 2009).

37. Hutter, J. L. & Bechhoefer, J. Calibration of atomic-force microscope tips. *Rev. Sci. Instrum.* **64,** 1868–1873 (1993).

38. Ederth, T. Research: Surface Force Measurements. *Linköping Univ.* at <https://www.ifm.liu.se/applphys/molphys/research/surface_force/force-curve_big.jpg>

39. Instruments, J. Tutorials: Force Spectroscopy. at <http://www.jpk.com/introduction-to-force-spectroscopy.437.en.html>

40. Roberts, C. J. What can we learn from atomic force microscopy adhesion measurements with single drug particles? *Eur. J. Pharm. Sci.* **24,** 153–157 (2005).

41. Ducker, W. a., Senden, T. J. & Pashley, R. M. Direct measurement of colloidal forces using an atomic force microscope. *Nature* **353,** 239–241 (1991).

42. Ducker, W. A., Senden, T. J. & Pashley, R. M. Measurement of Forces in Liquids Using a Force Microscope. *Langmuir* **8,** 1831–1836 (1992).

43. Willing, G. A., Ibrahim, T. H., Etzler, F. M. & Neuman, R. D. New Approach to the Study of Particle–Surface Adhesion Using Atomic Force Microscopy. *J.*

Colloid Interface Sci. **226,** 185–188 (2000).

44. Tsukada, M. *et al.* Adhesion force measurement of a DPI size pharmaceutical particle by colloid probe atomic force microscopy. *Powder Technol.* **141,** 262–269 (2004).

45. Hooton, J. C. *et al.* Characterization of particle-interactions by atomic force microscopy: effect of contact area. *Pharm Res* **20,** 508–514 (2003).

46. Biggs, S. & Spinks, G. Atomic force microscopy investigation of the adhesion between a single polymer sphere and a flat surface. *J. Adhes. Sci. Technol.* **12,** 461–478 (1998).

47. Jones, D. *Pharmaceutics - Dosage Form and Design*. (Pharmaceutical Press, 2008).

48. Patil, J. S. & Sarasija, S. Pulmonary drug delivery strategies: A concise, systematic review. *Lung India* **29,** 44–9 (2012).

49. Groneberg, D. a, Witt, C., Wagner, U., Chung, K. F. & Fischer, a. Fundamentals of pulmonary drug delivery. *Respir. Med.* **97,** 382–7 (2003).

50. Karner, S. & Anne Urbanetz, N. The impact of electrostatic charge in pharmaceutical powders with specific focus on inhalation-powders. *J. Aerosol Sci.* **42,** 428–445 (2011).

51. Peng, T. *et al.* In fl uence of physical properties of carrier on the performance of dry powder inhalers. **6,** 308–318 (2016).

52. Elaine, M. & Katja, H. *Human anatomy & physiology*. (Pearson Education Limited, 2007). at <http://lib.myilibrary.com/ProductDetail.aspx?id=803991>

53. Culley, J. Trachea and Bronchioles Anatomy Digital Color Image – Medical Stock Images Company. at <https://www.medicalstockimages.net/products/trachea-and-bronchioles-anatomy>

54. Dorland, W. A. N. (William A. N. *Dorland's illustrated medical dictionary.* (Saunders, 2000). at <https://www.ncbi.nlm.nih.gov/nlmcatalog/100956114>

55. Demoly, P., Hagedoorn, P., De Boer, A. H. & Frijlink, H. W. The clinical relevance of dry powder inhaler performance for drug delivery. *Respir. Med.* **108,** 1195–1203 (2014).

56. Sung, J. C., Pulliam, B. L. & Edwards, D. a. Nanoparticles for drug delivery to the lungs. *Trends Biotechnol.* **25,** 563–70 (2007).

57. Fröhlich, E. & Salar-Behzadi, S. Toxicological Assessment of Inhaled Nanoparticles: Role of in Vivo, ex Vivo, in Vitro, and in Silico Studies. *Int. J. Mol. Sci.* **15,** 4795–4822 (2014).

58. Aggarwal, B. & Gogtay, J. Use of pressurized metered dose inhalers in patients with chronic obstructive pulmonary disease: review of evidence. *Expert Rev. Respir. Med.* **8,** 349–356 (2014).

59. Ariyananda, P. L., Agnew, J. E. & Clarke, S. W. Aerosol delivery systems for bronchial asthma. *Postgrad. Med. J.* **72,** 151–156 (1996).

60. Barnes, P. J. & Page, C. P. *Pharmacology and Therapeutics of Asthma and COPD*. **237,** (Springer International Publishing, 2017).

61. Labiris, N. R. & Dolovich, M. B. Pulmonary drug delivery. Part II: The role of inhalant delivery devices and drug formulations in therapeutic effectiveness of aerosolized medications. *Br. J. Clin. Pharmacol.* **56,** 600–612 (2003).

62. Yang, M. Y., Chan, J. G. Y. & Chan, H. K. Pulmonary drug delivery by powder aerosols. *J. Control. Release* **193,** 228–240 (2014).

63. Saleem, I. Y., Diez, F., Jones, B. E., Kayali, N. & Polo, L. Investigation on the aerosol performance of dry powder inhalation hypromellose capsules with different lubricant levels. *Int. J. Pharm.* **492,** 258–263 (2015).

64. Finlay, W. H. *The Mechanics of Inhaled Pharmaceutical Aerosols*. *Mech.*

Inhaled Pharm. Aerosols (2001). doi:10.1016/B978-012256971-5/50009-2

65. Alavi, S. & Caussat, B. Experimental study on fluidization of micronic powders. *Powder Technol.* **157,** 114–120 (2005).

66. Kinnunen, H. M. Active site, agglomerates or increased cohesion? Investigations into the mechanism of how lactose fines improve dry powder inhaler performance. (2012).

67. Zeng, X. M., Martin, G. P., Tee, S. & Marriott, C. The role of fine particle lactose on the dispersion and deaggregation of salbutamol sulphate in an air stream in vitro. *Int. J. Pharm.* **176,** 99–110 (1998).

68. Zhu, X. *et al.* Validation of surface coating with nanoparticles to improve the flowability of fine cohesive powders. *Particuology* **30,** 53–61 (2017).

69. Jallo, L. J., Chen, Y., Bowen, J., Etzler, F. & Dave, R. Prediction of inter-particle adhesion force from surface energy and surface roughness. *J. Adhes. Sci. Technol.* **25,** 367–384 (2011).

70. Islam, N., Tuli, R. A., George, G. A. & Dargaville, T. R. Colloidal drug probe: Method development and validation for adhesion force measurement using Atomic Force Microscopy. *Adv. Powder Technol.* **25,** 1240–1248 (2014).

71. Tuli, R. A., Dargaville, T. R., George, G. A. & Islam, N. Polycaprolactone Microspheres as Carriers for Dry Powder Inhalers: Effect of Surface Coating on Aerosolization of Salbutamol Sulfate. *J. Pharm. Sci.* **101,** 733–745 (2012).

72. Zhou, Q. T. & Morton, D. A. V. Drug-lactose binding aspects in adhesive mixtures: controlling performance in dry powder inhaler formulations by altering lactose carrier surfaces. *Adv. Drug Deliv. Rev.* **64,** 275–84 (2012).

73. Ferrari, F. *et al.* The surface roughness of lactose particles can be modulated by wet-smoothing using a high-shear mixer. *AAPS PharmSciTech* **5,** 69–74 (2004).

74. Young, P. M. *et al.* Characterization of a surface modified dry powder inhalation carrier prepared by 'particle smoothing'. *J. Pharm. Pharmacol.* **54,** 1339–1344 (2002).

75. Larhrib, H., Zeng, X. M., Martin, G. P., Marriott, C. & Pritchard, J. The use of different grades of lactose as a carrier for aerosolised salbutamol sulphate. *Int. J. Pharm.* **191,** 1–14 (1999).

76. Zeng, X. M., Martin, G. P., Marriott, C. & Pritchard, J. The influence of carrier morphology on drug delivery by dry powder inhalers. *Int. J. Pharm.* **200,** 93–106 (2000).

77. Wang, Z. *et al.* Measuring the sticking of mefenamic acid powders on stainless steel surface. *Int. J. Pharm.* **496,** 407–413 (2015).

78. Zellnitz, S., Schroettner, H. & Urbanetz, N. A. Influence of surface characteristics of modified glass beads as model carriers in dry powder inhalers (DPIs) on the aerosolization performance. *Drug Dev. Ind. Pharm.* **41,** 1710–1717 (2015).

79. Zellnitz, S., Redlinger-Pohn, J. D., Kappl, M., Schroettner, H. & Urbanetz, N. A. Preparation and characterization of physically modified glass beads used as model carriers in dry powder inhalers. *Int. J. Pharm.* **447,** 132–138 (2013).

80. Renner, N., Steckel, H., Urbanetz, N. & Scherließ, R. Nano- and Microstructured model carrier surfaces to alter dry powder inhaler performance. *Int. J. Pharm.* **518,** 20–28 (2017).

81. Shah, U. V. *et al.* Decoupling the contribution of dispersive and acid-base components of surface energy on the cohesion of pharmaceutical powders. *Int. J. Pharm.* **475,** 592–596 (2014).

82. Mader-Arndt, K. *et al.* Single particle contact versus particle packing behavior: model based analysis of chemically modified glass particles. *Granul. Matter* **16,** 359–375 (2014).

83. Shah, U. V *et al.* Effect of crystal habits on the surface energy and cohesion of crystalline powders. *Int. J. Pharm.* **472,** 140–147 (2014).

84. Shah, U. V *et al.* Decoupling the Contribution of Surface Energy and Surface Area on the Cohesion of Pharmaceutical Powders. *Pharm. Res.* **32,** 248–259 (2015).

85. Ting, L. H., Feghhi, S., Han, S. J., Rodriguez, M. L. & Sniadecki, N. J. Effect of Silanization Film Thickness in Soft Lithography of Nanoscale Features. *J. Nanotechnol. Eng. Med.* **2,** 41005–41006 (2011).

86. Bhushan, B. & Jung, Y. C. Wetting, adhesion and friction of superhydrophobic and hydrophilic leaves and fabricated micro/nanopatterned surfaces. *J. Phys. Condens. Matter* **20,** 225010 (2008).

87. Wong, K. V. & Hernandez, A. A Review of Additive Manufacturing. *ISRN Mech. Eng.* **2012,** (2012).

88. Gaisford, S. Printing medicines. *Eur. Ind. Pharm.* 7–8 (2013).

89. Gibson, I., Rosen, D. W. & Stucker, B. *Additive Manufacturing Technologies*. *Springer* (2010). doi:10.1007/978-1-4419-1120-9

90. Kruth, J.-P., Mercelis, P., Vaerenbergh, J. Van, Froyen, L. & Rombouts, M. Binding mechanisms in selective laser sintering and selective laser melting. *Rapid Prototyp. J.* **11,** 26–36 (2005).

91. Shirazi, S. F. S. *et al.* A review on powder-based additive manufacturing for tissue engineering: selective laser sintering and inkjet 3D printing. *Sci. Technol. Adv. Mater.* **16,** 33502 (2015).

92. Scoutaris, N., Ross, S. & Douroumis, D. Current Trends on Medical and Pharmaceutical Applications of Inkjet Printing Technology. *Pharm. Res.* **33,** 1799–1816 (2016).

93. Wendel, B. *et al.* Additive processing of polymers. *Macromol. Mater. Eng.* **293,**

799–809 (2008).

94. Wang, L.-N. Printing medicines: a new era of dispensing and drug formulation? | News | Pharmaceutical Journal. *Pharm. J.* 25 (2013). at <http://www.pharmaceutical-journal.com/news-and-analysis/news/printing-medicines-a-new-era-of-dispensing-and-drug-formulation/11122986.article>

95. Scoutaris, N., Alexander, M. R., Gellert, P. R. & Roberts, C. J. Inkjet printing as a novel medicine formulation technique. *J. Control. Release* **156,** 179–85 (2011).

96. Norman, J., Madurawe, R. D., Moore, C. M. V., Khan, M. A. & Khairuzzaman, A. A new chapter in pharmaceutical manufacturing: 3D-printed drug products. *Adv. Drug Deliv. Rev.* **108,** 39–50 (2017).

97. Highlights of Prescribing Information— Spritam. *United States Food Drug Adm.* (2015). at <https://www.accessdata.fda.gov/drugsatfda_docs/label/2015/207958s000lbl.pdf>

98. Kyobula, M. *et al.* 3D inkjet printing of tablets exploiting bespoke complex geometries for controlled and tuneable drug release. *J. Control. Release* **261,** 207–215 (2017).

99. Goyanes, A., Robles Martinez, P., Buanz, A., Basit, A. W. & Gaisford, S. Effect of geometry on drug release from 3D printed tablets. *Int. J. Pharm.* **494,** 657–663 (2015).

100. Uddin, M. J. *et al.* Inkjet printing of transdermal microneedles for the delivery of anticancer agents. *Int. J. Pharm.* **494,** 593–602 (2015).

101. Ovsianikov, A. *et al.* Two Photon Polymerization of Polymer–Ceramic Hybrid Materials for Transdermal Drug Delivery. *Int. J. Appl. Ceram. Technol* **4,** 22–29 (2007).

102. Behara, S. R. B., Longest, P. W., Farkas, D. R. & Hindle, M. Development and

comparison of new high-efficiency dry powder inhalers for carrier-free formulations. *J. Pharm. Sci.* **103,** 465–477 (2014).

103. Behara, S. R. B., Farkas, D. R., Hindle, M. & Longest, P. W. Development of a high efficiency dry powder inhaler: Effects of capsule chamber design and inhaler surface modifications. *Pharm. Res.* **31,** 360–372 (2014).

104. Berkenfeld, K., Bernauer, M., McConville, J. T. & Lamprecht, A. Investigating cascade impactor performance using a modified 3D printed induction port. *Int. J. Pharm.* **535,** 402–409 (2018).

105. Peels, J. A Kosher High with a 3D Printed Medical Marijuana Inhaler | 3DPrint.com | The Voice of 3D Printing / Additive Manufacturing. *3D Print.com* (2017). at <https://3dprint.com/191217/3d-printed-marijuana-inhaler/>

106. Spangenberg, A. *et al. Updates in Advanced Lithography*. (InTech, 2013). doi:10.5772/3348

107. Sun, H.-B. *et al.* Real three-dimensional microstructures fabricated by photopolymerization of resins through two-photon absorption. *Opt. Lett.* **25,** 1110 (2000).

108. Maruo, S. & Fourkas, J. T. Recent progress in multiphoton microfabrication. *Laser Photonics Rev.* **2,** 100–111 (2008).

109. Maruo, S., Nakamura, O. & Kawata, S. Three-dimensional microfabrication with two-photon-absorbed photopolymerization. *Opt. Lett.* **22,** 132–134 (1997).

110. Wang, I., Bouriau, M., Baldeck, P. L., Martineau, C. & Andraud, C. Three-dimensional microfabrication by two-photon-initiated polymerization with a low-cost microlaser. *Opt. Lett.* **27,** 1348–1350 (2002).

111. Maruo, S., Kawata, S. & Microfabrication, T. Two-photon-absorbed near-infrared photopolymerization for three-dimensional microfabrication. *J. Microelectromechanical Syst.* **7,** 411–415 (1998).

112. Denk, W., Strickler, J. H. & Webb, W. W. Two-photon laser scanning fluorescence microscopy. *Science* **248,** 73–76 (1990).

113. Kawata, S., Sun, H. B., Tanaka, T. & Takada, K. Finer features for functional microdevices. *Nature* **412,** 697–698 (2001).

114. Nishiyama, H. & Hirat, Y. in *Lithography* (InTech, 2010). doi:10.5772/8170

2 Material and Methods for Colloidal Probe Production and Characterisation

2.1 Introduction

As discussed in Chapter 1, in order to directly study and quantify adhesion between a particle and a surface, AFM force-curves can be collected and analysed with colloidal probes. To evaluate the effect of well-defined two photon polymerised three dimensional printed (3DP) morphologies on particle adhesion, a series of colloidal probes were prepared. To gain fundamental insight into the factors affecting particle-substrate adhesion, a model spherical particle was selected. A sphere was chosen as this is a "typical" particle shape used for particle- surface interactions as seen in the adhesion models in Chapter 1. The first particle chosen to be used as a colloidal probe consisted of a 10 µm polystyrene bead. As discussed in Chapter 1, an understanding of particle-surface interactions is particularly important in pharmaceutical applications, other probes were therefore selected that are relevant to respiratory drug delivery formulations. In DPIs, these involve an active pharmaceutical ingredient (API), between one and five microns, and a larger lactose carrier particle, in possession of a lower surface to volume ratio, and therefore designed to disperse the API and prevent agglomeration. Therefore, a polystyrene 5 µm bead was selected to represent the API, and also allow a direct evaluation of the effect of particle size on particle-surface interactions in comparison with the polystyrene 10 µm bead. A Respitose SV003 particle was chosen as it is commonly used in respiratory formulations and possesses a well-defined narrow particle size distribution. For the interactions of these particles with differing morphologies to be evaluated, the particles must first be characterised and their subsequent attachment to AFM cantilevers and asperities available for contact assessed. This chapter will focus on these characterisations and evaluations.

2.1.1 Scanning Electron Microscopy (SEM)

Scanning Electron Microscopy (SEM) is a high resolution surface imaging technique capable of imaging to around 1 nm[1]. It creates an image by detecting signals emitted from the surface which is raster scanned with a fine beam of electrons, conducted under vacuum, to prevent gas scattering of the electron beam[2]. Figure 2.1 shows the main components of an SEM, firstly electrons are emitted at the top of the column, either; thermionically, using a heated filament tip in an electron gun, or using a field emission source[2]. The electrons are then accelerated down, usually by 20kV and passed through condenser and objective lenses, a set of scan coils and an aperture to produce a focused beam of electrons which hits the surface of the sample. Electrons emitted by the specimen are detected, amplified and the signal results in a scan being generated on a computer monitor[2,3].

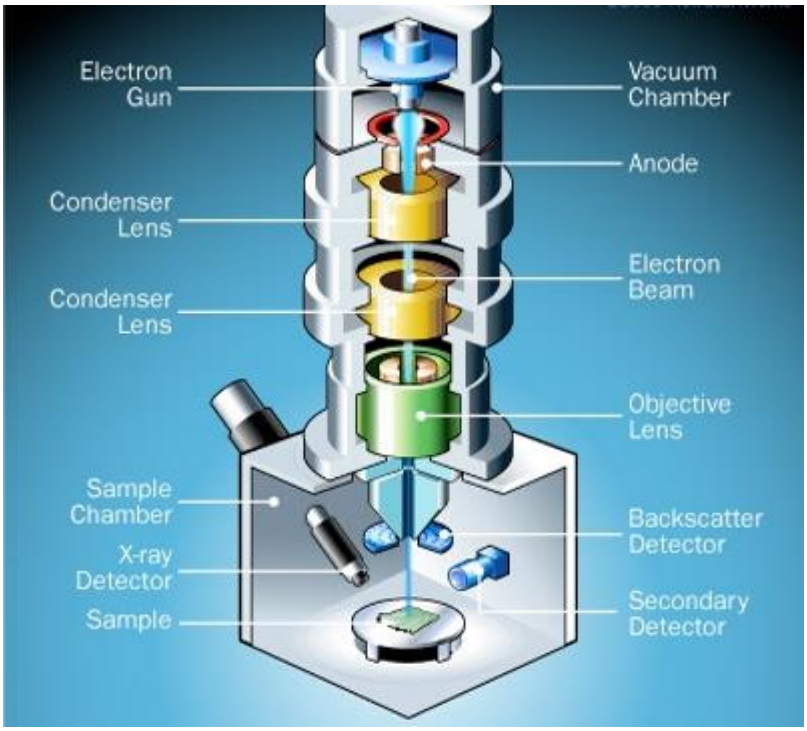


Figure 2.1: Schematic of the components of an SEM[4].

On impacting the surface, the electrons will produce secondary signals, for instance; secondary electron ions, backscatted electrons and characteristic X-rays[5]. Secondary electrons originate from within a few nm from the surface[1]. The varying topography of the surface produces differing signal strengths allowing the contrast needed for

an image providing surface structure, and topographic information[4]. In contrast backscattered electrons are elastically scattered electrons emitted from much deeper within the sample (a few μm below the surface), with a higher energy[6]. They therefore provide compositional information, but give lower resolution images. Finally, X-rays provide elemental information about the sample.

The resolution of the SEM is determined by a multitude of factors. Firstly, the size of the spot size of the incident beam, as this decreases spatial resolution increases, but at the cost of beam current, which determines the signal strength[7]. Resolution also depends on accelerating voltage. This is because higher energy electrons are less affected by passing through the lenses. Finally, reducing the working distance, also improves resolution, however, this is also on balance as too close and the lenses will be unable to focus on the surface[7].

One of the main issues with SEM imaging is surface charging, which occurs with non-conductive specimens, as the electrons from the incident beam are unable to dissipate[2]. This is generally overcome by coating the surface with a thin layer of a conductive material, like gold or metal[8]. However, this is a destructive process, and any sample being imaged, like AFM tips could then not be used. With certain SEMs this can be mitigated to a certain extent by using “low vacuum” mode, which operates as its name suggests with a lower vacuum and a small presence of air vapour in the chamber. The molecules in the air become positively charged and neutralize the negatively charged regions on the surface.[8] However, this mode is inherently associated with a worse resolution, and therefore settings must be carefully controlled to optimize the collected images[2].

2.2 Chapter Aims

The aim of this chapter is to evaluate the particle types to be utilised for colloidal probe microscopy and subsequently optimise the characterisation of the attached

particle. This will allow the verification of the suitability of each probe for assessing the effect of surface morphology on particle adhesion.

2.3 Chapter Objectives

- To evaluate the characteristics of the particle types to be used for the production of colloidal probes.
- To evaluate and if necessary optimise the characterisation of particles post-attachment to AFM cantilevers.

2.4 Materials and Methods

Polystyrene beads for attachment to colloidal probes were obtained from Sigma-Aldrich. All atomic force microscopy (AFM) probes were purchased from Bruker (Cambridge, UK). Respitose SV003 particles were supplied by AstraZeneca, having been purchased from DFE Pharma, Goch, Germany.

2.4.1 Scanning Electron Microscopy (SEM)

Scanning Electron Microscopy (SEM) images were captured using a JSM-6490 LV (JEOL) of the particles to be used in the colloidal probe microscopy (CPM). The samples were loaded unto aluminium stubs with carbon tabs pre-fixed. In order to prevent charge build up, samples were then coated with a thin layer of gold using an SCD 030 (Balzers Union) sputter coater for 2 minutes at 30 mA. Images were then collected using the secondary electron imaging setting, in high vacuum.

SEM Images were also collected in low vacuum mode of the particles once attached to the colloidal probes, see Section 2.6.2 for more details.

2.4.2 Atomic Force Microscopy (AFM)

Atomic Force Microscopy (AFM) images of the particles pre-attachment were all captured in tapping mode on a Fast Scan Bio Icon (Bruker, Coventry, UK) with RTESPA-300 cantilevers (Bruker), using a scan rate of 1.0 Hz. Images were collected over a spatial area of 1 µm x 1 µm, Respitose SV003 was also scanned over a 5 µm x 5 µm area as the particles were larger. All images were processed using Gwyddion software (version 2.44) (Czech Metrology Institute, Brno), and were levelled using a mean plane subtraction. Three of each of the particle types were imaged, with three separate locations chosen for surface roughness measurements. The smaller scan sizes were evaluated for surface roughness using the root mean square (RMS) of the average height deviations of the surface.

The tips post attachment were reverse imaged using a tip characterisation grating (TGT01, NT-MDT, Moscow), resulting in an AFM artefact, resulting in an inversion of the imaging process, generating a topography map as an array of images of the particle surface. A second image is then collected focusing on just one of the repeat images, to allow a higher resolution image which can be used for contact area analysis. An in-house excel macro was then used to undertake a bearing analysis resulting in a histogram of height data. A plot of contact area against depth can then be produced. Due to the rigidity of the samples to be analysed, a nominal depth of 0.5 nm was used to calculate the contact area of the probes, for subsequent adhesion normalisation.

2.5 Results and Discussion

2.5.1 Scanning Electron Microscopy

In order to evaluate the initial characteristics of the particles to be used in the CPM, SEM images were captured of the three different types of particles as seen in Figure 2.2. The SEM images collected show that the polystyrene 5 µm and polystyrene 10 µm beads possess a uniform size (Figure 2.2 A and B respectively) and at this scale a smooth surface. However, in contrast the Respitose SV003 particles (Figure 2.2 C) are

a range of sizes, although the majority are in the tens of microns size range. They also possess a far rougher surface with multiple surface asperities clearly seen.

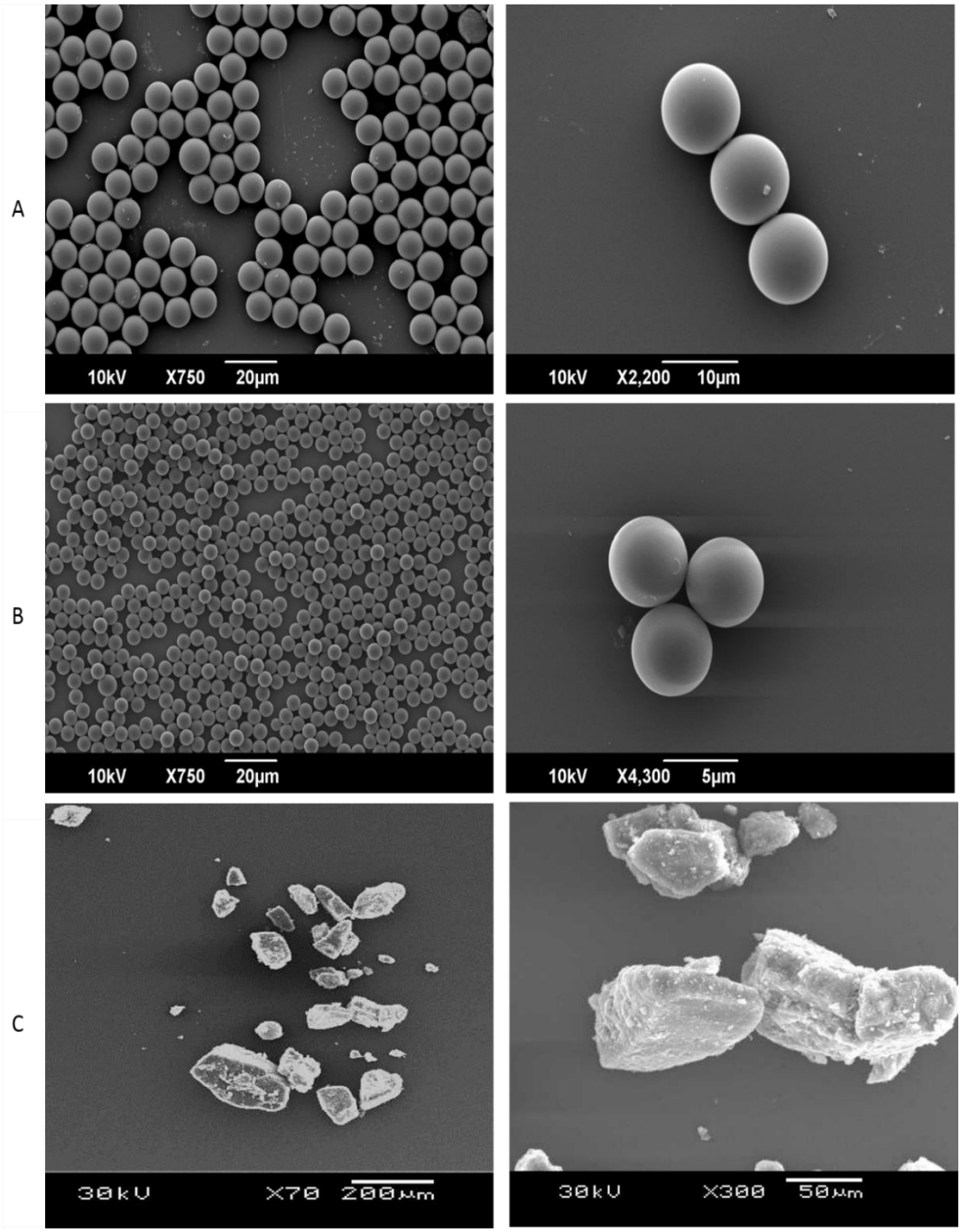


Figure 2.2: SEM images of the three particle types to be used in colloidal probe microscopy. A) Polystyrene 10 µm beads, B) Polystyrene 5 µm beads and C) Respitose SV003 particles.

2.5.2 Atomic Force Microscopy (AFM)

An example of an AFM topographical image of the polystyrene 10 µm and 5 µm beads, as well as the Respitose SV003, are shown in Figure 2.3. Images were collected

over a spatial area of 1 µm x 1 µm, Respitose SV003 was also scanned over a 5 µm x 5 µm area as the particles were larger. Three of each of the particle types were imaged, with three separate locations chosen for surface roughness measurements. The smaller scan sizes were evaluated for surface roughness using the root mean square (RMS) of the average height deviations of the surface (Table 2.1).

Table 2.1: A summary of the surface roughness calculated as RMS over three 1 µm x 1 µm areas for three different particles of each particle type.

	RMS (nm) N=3			
	Particle 1	**Particle 2**	**Particle 3**	**Overall**
Polystyrene 10 µm bead	78 ± 4.9	133 ± 7.0	144 ± 6.0	118 ± 31.1
Polystyrene 5 µm bead	73 ± 2.6	68 ± 4.4	185 ± 4.0	109 ± 57.3
Respitose SV003 particle	390 ± 43.6	370 ± 60	730 ± 264.6	497 ± 222.7

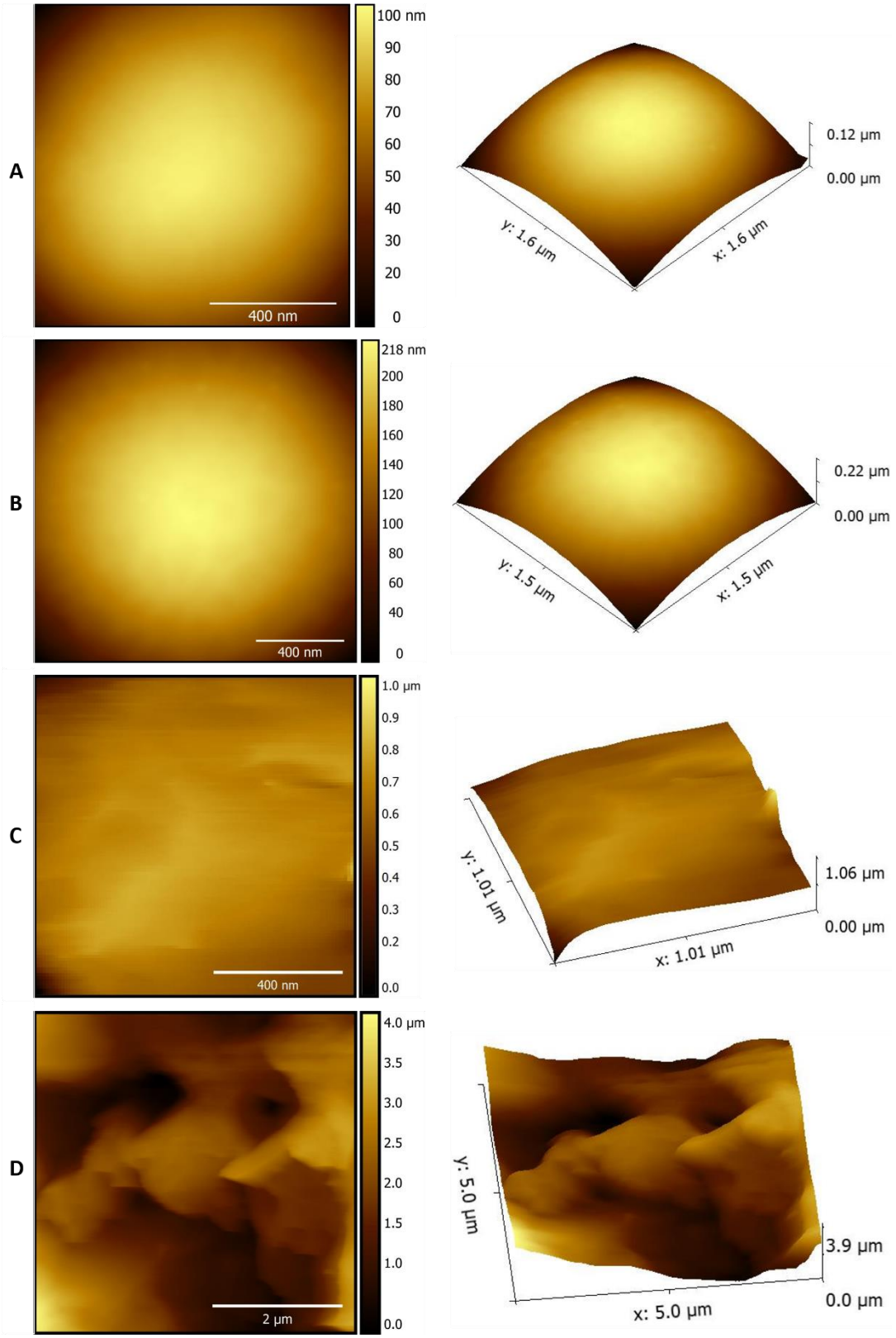


Figure 2.3: An example of AFM topography images and their respective 3D processed image to evaluate surface roughness of a 1 µm x 1 µm scan size of A) a polystyrene 10 µm bead, B) a polystyrene 5 µm bead and C) a Respitose SV003 particle and D) 5 µm x 5 µm scan size of a Respitose SV003 particle.

From Figure 2.3, it can be seen that the polystyrene 10 µm and 5 µm beads have a very smooth surface. However, the Respitose SV003 possesses a rougher surface and multiple asperities, which can be seen in the 5 µm scan size image (Figure 2.3 C). An evaluation of the RMS roughness over a 1 µm scan size (Table 2.1) confirms that the two polystyrene beads have very similar surface roughness which is to be expected. However, at this scale of observation Respitose only shows a five times greater roughness than the polystyrene beads as only the microscale roughness is being accounted for due to the small scan size. This is in contrast to the clear differences in macroscale roughness as seen in Figure 2.2 C and in the 5 µm scan size in Figure 2.3 C compared with the 1 µm scan size. The RMS values, also show a far higher standard deviation which is to be expected due to the extreme variation in surface morphology seen in the SEM images. A thorough evaluation of the Respitose SV003 particles using both techniques, before and after using them to collect force-curves, is advisable as there may be multiple asperities in contact with the surface at any one time.

2.6 Colloidal Probe Production and Characterisation

2.6.1 Attachment of Particles to tips

In order to evaluate a range of particles; Respitose SV003, polystyrene 10 µm and polystyrene 5 µm beads were chosen. However, on standard AFM cantilevers, the tip protrudes around 11 µm from the surface of the cantilever. Therefore, after attachment of either of the polystyrene beads, this tip would still be the main probe. Therefore, tipless cantilevers were selected. MLCT-O10 cantilever F (Bruker), v-shaped silicon nitride cantilevers were chosen, as they are suitable for contact mode and possess a relatively low spring constant (k~0.4 N/m), which provides a greater sensitivity to particle-surface interactions. It was decided that in line with previous work a V-shaped cantilever would also allow better particle attachment[2].

As discussed in Chapter 1, in order to calculate the force of adhesion from a force-distance curve, an accurate spring constant for the cantilever must be known. As manufacturers of AFM tips use wide tolerances for spring constants[9], the spring constant of each cantilever must be calculated prior to use for adhesion

measurements. There are several different methods available for the calculation of spring constant, however Sader's method and the thermal tune method are two of the most popular as they are non-destructive. Sader's method[10] utilises the dimensions of the cantilever, combined with the frequency spectrum of the cantilever[11], this method is most suitable for rectangular cantilevers[12]. The other commonly used dynamic method for calculating the spring constant is the thermal tune method[13], which models the cantilever as a simple harmonic oscillator, using the work conducted by Hutter *et al.*[14] relating to a cantilever's fundamental oscillation, and how this is affected by Brownian motion due to thermal energy. This method is suitable for V-shaped cantilevers and so was used for the cantilevers in these experiments. The thermal tune method[14] was calculated using the Nanoscope (Bruker) AFM software, by first recording a force-curve with the tip on a pre-cleaned silicon surface. The deflection sensitivity was then calibrated and the tip is withdrawn and raised away from the substrate. In the software a range of 5-2000 kHz and a deflection sensitivity correction of 1.144 was used in line with manufacturer's advice[12]. A power spectrum density plot is then generated and the fundamental resonance peak of the lever is selected. Finally, after fitting a curve to the peak, the spring constant is calculated.

Particles were attached using a MMAFM-2 Multimode AFM system (Bruker). Epoxy resin was dotted onto a pre-cleaned silicon wafer and spread into thin lines using a sacrificial probe. This tip was then replaced with the silicon nitride v-shaped tipless cantilever (MLCT-O10 F) to be functionalised, which was lowered until in visual contact with the glue, and then withdrawn (Figure 2.4 A). This cantilever was then moved to an area with the particles to be attached dispersed, and aligned with an isolated particle. The cantilever was then lowered manually onto the particle chosen for attachment (Figure 2.4B). Once the particle had been added the tip was retracted and allowed to air dry for 24 hours before characterisation and use.

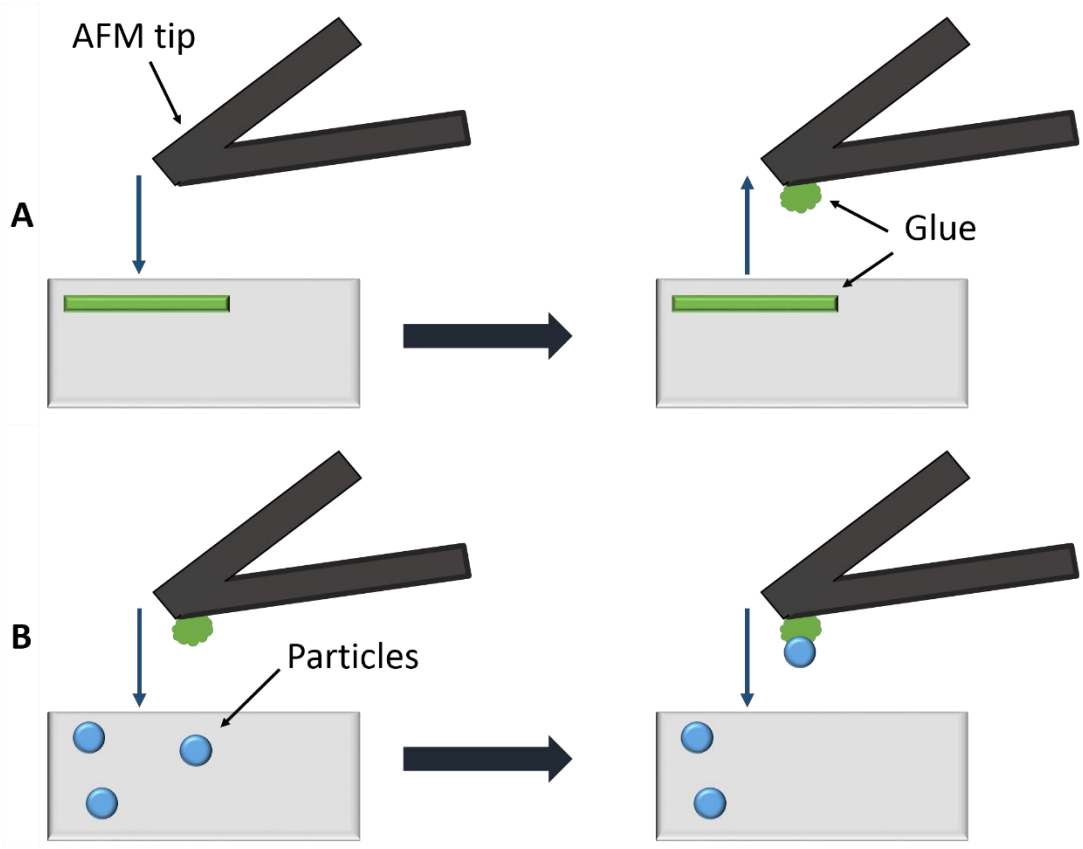


Figure 2.4: Schematic showing the attachment of particles on AFM tips. A) The tip is lowered into contact with glue (shown in green) and is then withdrawn. B) The tip is then moved and lowered onto an isolated particle (shown in blue) leading to particle attachment.

2.6.2 Scanning Electron Microscopy of Colloidal Probes

After 24 hours, SEM images of the attached particles were collected for verification of probe attachment. As discussed in Section 2.1.1, in order to prevent significant charging, objects to be imaged are usually either conductive or are gold coated[15]. However, as gold coating is a destructive process, which would mean the particle could therefore not then be used as a colloidal probe, the tips had to be imaged without a coating. In order to reduce this coating previous attempts at resolving the produced colloidal probe use low vacuum mode in order to reduce charging via charge compensation[16]. An initial attempt to collect SEM images of the attached particles was conducted, by placing the colloidal probe onto a small section of silica gel, as previously used by Piggott *et al*[2]. However, significant charging was still seen and clear determination of the suitability of the particle surface for adhesion

measurements was difficult to achieve with the spherical probes as seen in Figure 2.5.

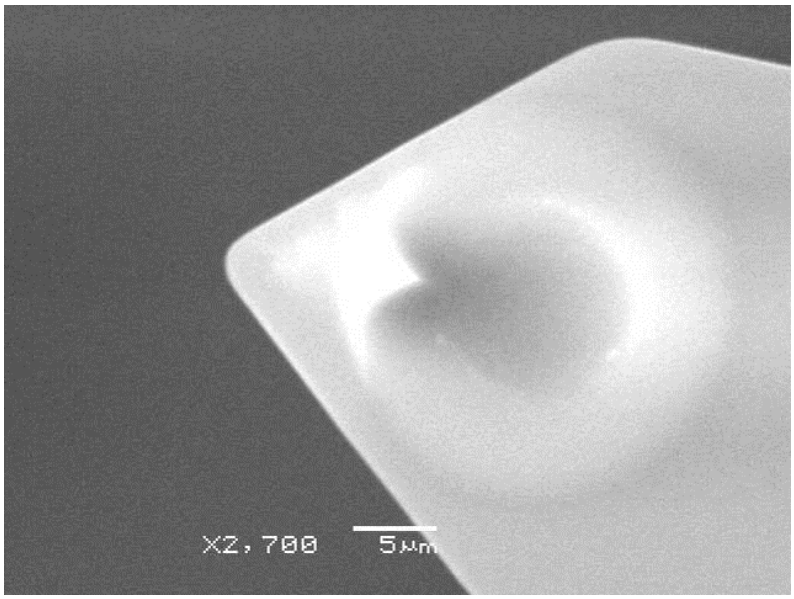


Figure 2.5: An example of an SEM image collected of a colloidal probe, post attachment of a 10 µm polystyrene bead, demonstrating significant charging using the previous settings.

Therefore conditions were optimised by gold coating the AFM tip mount, and adjusting the spot size and scan height resulting in better resolution images (Figure 2.6). A square of silica gel was mounted on an SEM stub using a carbon disc. This was then coated with gold, using an SCD 030 (Balzers Union) sputter coater for 2 minutes at 30 mA, post coating an AFM tip, with particle attached, was placed on the silica gel for SEM imaging. The final imaging conditions used were; low vacuum mode at 50 Pa, using 20kV and a spot size of 50 nm. For the polystyrene 5 µm beads, it was difficult to get a clear high quality SEM image to definitively ensure that no glue was present on the surface, these tips were therefore also inspected using the Zeta optical profiler (Zeta Instruments).

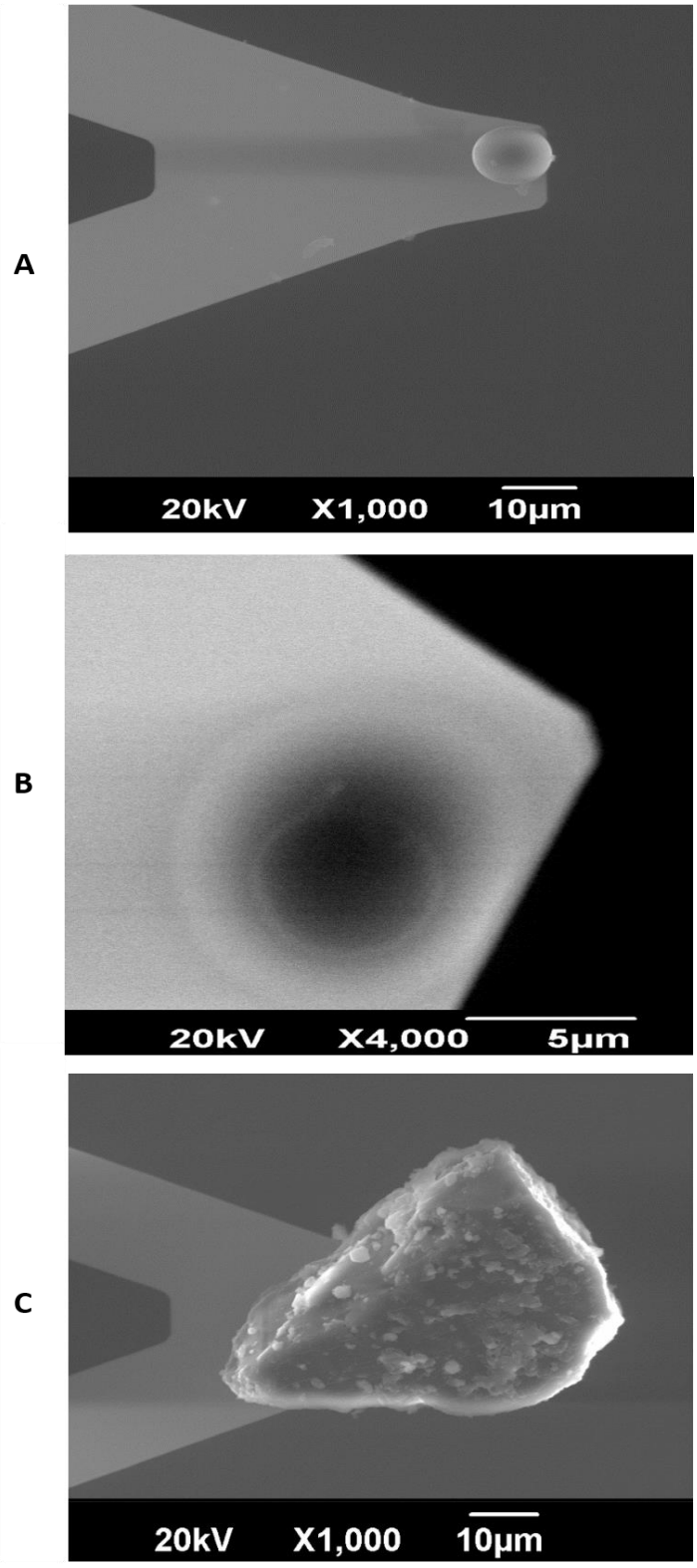


Figure 2.6: An SEM image of an example of each of the particles used in the colloidal probe microscopy mounted on an AFM tip. A) Polystrene 10 µm bead, B) Polystyrene 5 µm bead and C) Respitose SV003 particle.

2.6.3 AFM Tip Imaging

Before, particle adhesion measurements were performed, the contact area of the colloidal probe was evaluated. The imaging was done as outlined by Hooton *et al.*[17], who first used this technique for a pharmaceutical particulate system. In order to achieve this the probes were imaged using a tip characterisation grating (TGT01, NT-MDT, Moscow) which consists of a matrix of inverted sharp spikes (Figure 2.7). As the spikes are sharper than the particle being imaged, an AFM artefact occurs resulting in an inversion of the imaging process[18]. Therefore, the sample acts as the AFM probe, and the topography map generated is an array of images of the particle surface (Figure 2.8 A). A second image is then collected focusing on just one of the repeat images, to allow a higher resolution image which can be used for contact area analysis (Figure 2.8 B).

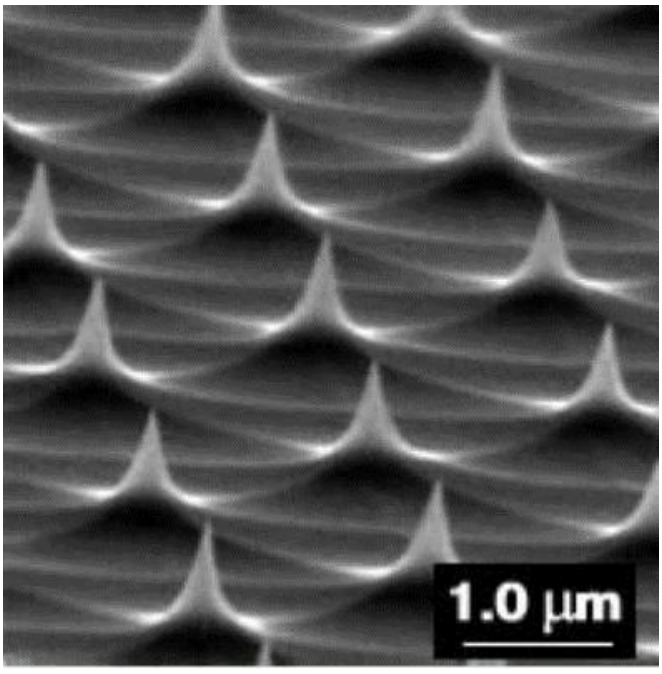


Figure 2.7: An SEM Image of the array of spikes seen on the TGT-01 tip characterisation grating[19].

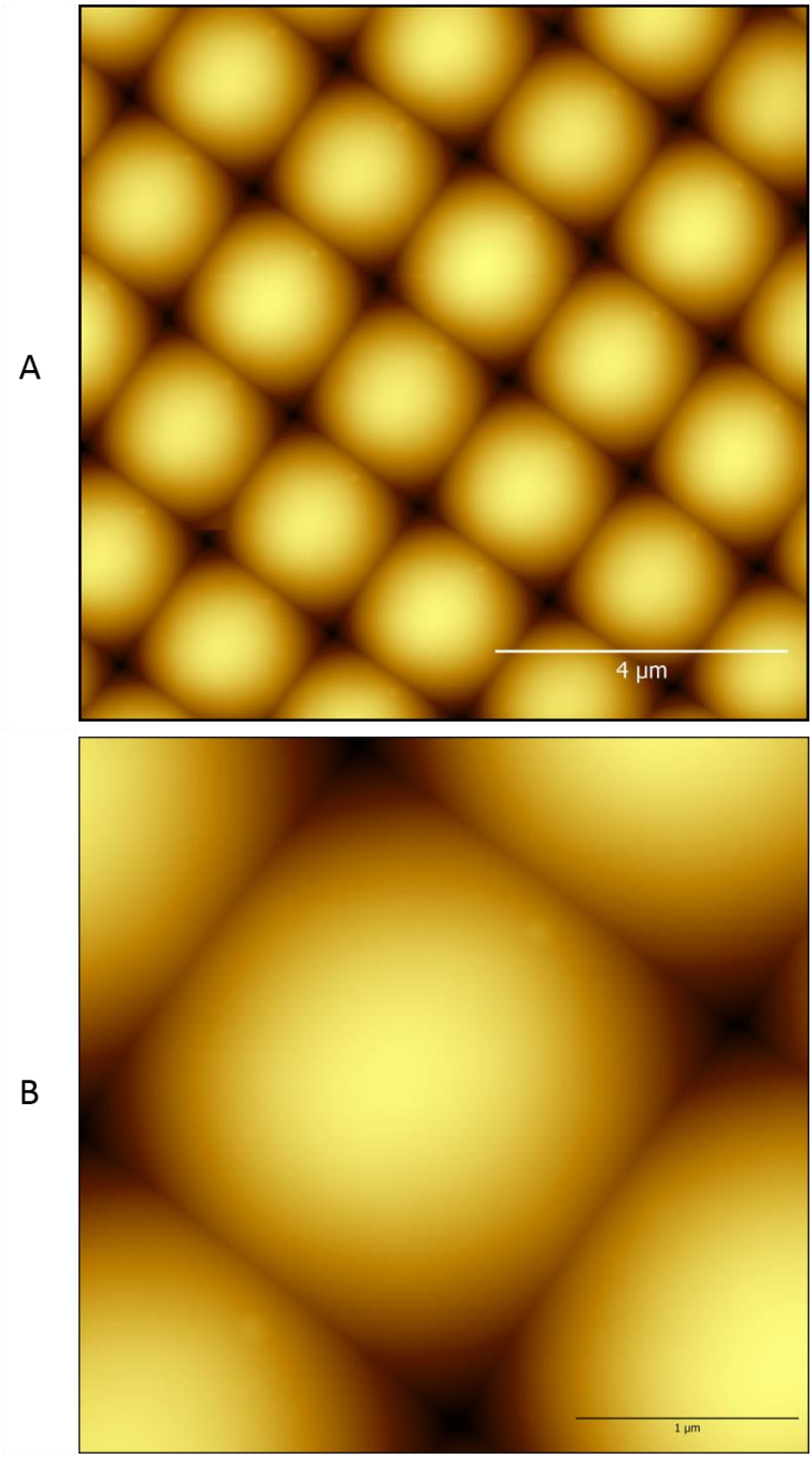


Figure 2.8: An example of the AFM topography image generated when performing tip imaging. A) An array of the surface of a polystyrene 5 µm bead. B) An AFM image focused on one of the particle surface repeat images.

As discussed in Chapter 1, one of the main factors affecting the adhesion between a particle and a surface is the effective contact area. Therefore, in order to compare the adhesion between different particle types and a surface prior to morphological modification a measurement of the particle area which will be in contact with the surface is necessary. Table 2.2 shows the starting contact area of the particles used in the colloidal probe microscopy. As expected the polystyrene 5 µm beads generally have a smaller contact area than then 10 µm beads. The Respitose SV003 possess far smaller contact areas than the beads, which initially seems counter-intuitive as the particles are so much larger. However, on consideration of the surface morphology as seen by the SEM and AFM, it is apparent that this contact area would be surface asperities as opposed to the main body of the particle. As many of these asperities are fairly sharp the apparent contact area would be less than that of a sphere. However, in previous studies it has been shown that the morphology of particles can change during use in colloidal probe microscopy[20,21]. Therefore each of the colloidal probes were imaged before and after use to assess if there was any major changes in morphology as this would in turn affect the particle contact area and hence particle adhesion, as even small particle surface changes have been shown to significantly affect particle-surface interactions[22]. For the polystyrene beads, no change in morphology was seen during the colloidal probe work. However, it can be seen in Figure 2.9 that the Respitose particle undergoes various changes during the CPM measurements, involving a gradual deformation and wear on the particles used in the experiment. With an initial smoothing of any fines adhered to the particles used in the experiment, this is to be expected in line with previous studies[23], since lactose is a softer material than the polystyrene beads. Firstly, between Figure 2.9A and B it can be seen that a smoothing effect has occurred, as many of external fines have been removed, this is likely to have occurred as the force of impact with the surface was sufficient to dislodge these particles. It can also be seen that small scale roughness has been flattened out, however this has exposed certain asperities that were previously unseen, as outlined by the red arrows in Figure 2.9B. Reductions of these asperities are then seen which is to be expected as these regions will experience the highest contact pressure and hence wear (Figure 2.9C). Table 2.3 shows the difference these morphological changes have on the contact area of the

asperity. The particle surface morphology of each colloidal probe was assessed before and after every use. However, the adhesion recorded to the surfaces with modified morphologies will not be adjusted based on particle contact area as a model would be needed to ascertain precisely which parts of the asperities were contacting with the surface for each contact which is beyond the scope of this project.

Table 2.2: An overview of the starting Contact Areas of the Particles to be used as Colloidal Probes at an indentation depth of 0.5 nm.

	Contact Area at 0.5 nm (nm^2)		
	Particle 1	**Particle 2**	**Particle 3**
Polystyrene 10 µm bead	6400	7540	9280
Polystyrene 5 µm bead	3160	7920	4950
Respitose SV003 particle	730	450	2250

Table 2.3: An example of the change of asperity contact area of a Respitose SV003 particle after use as a colloidal probe for force measurements.

	Contact Area at 0.5 nm (nm^2)		
	Pre-use	**Post 1st use**	**Post 2nd use**
Respitose SV003 particle	730	440	760

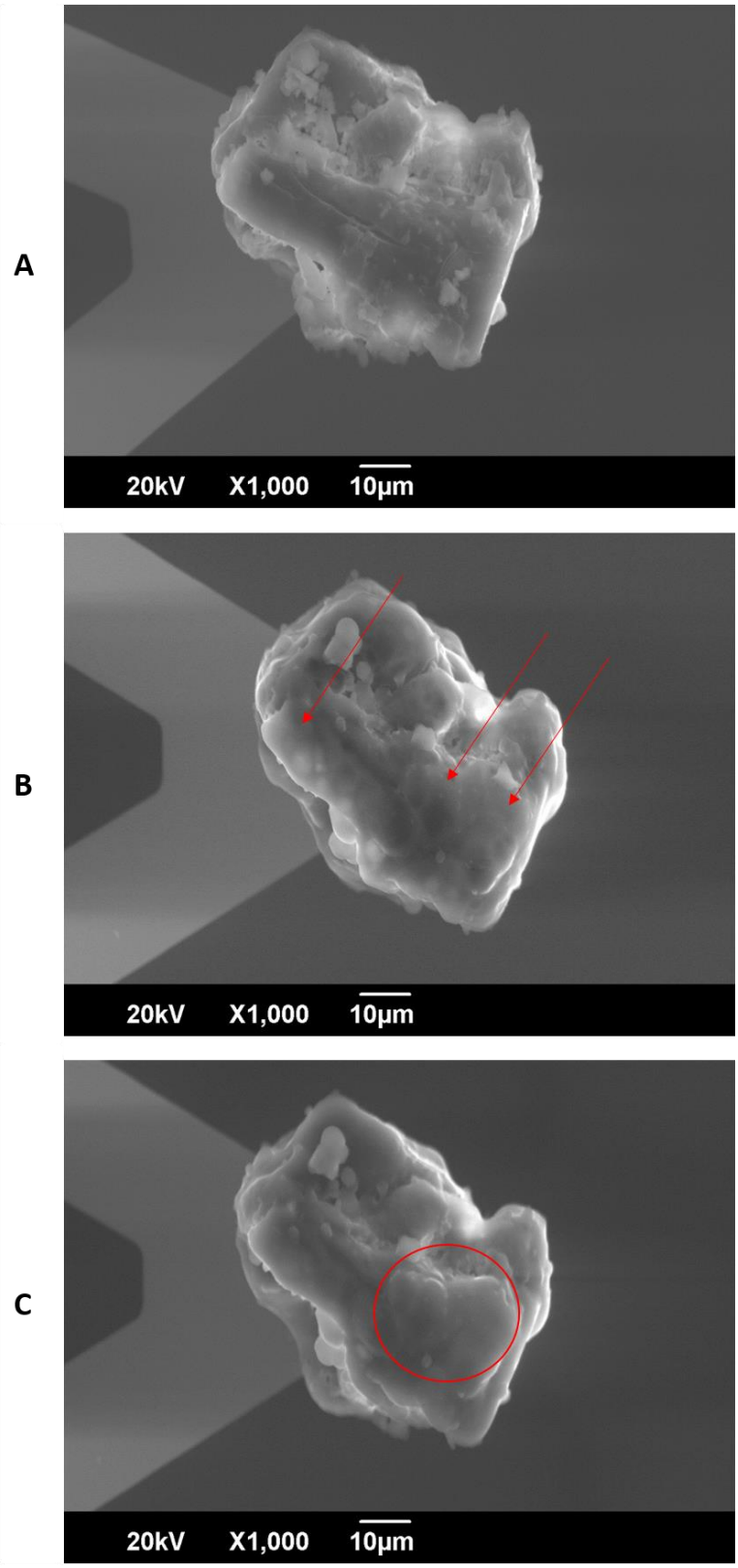


Figure 2.9: An example of a Respitose particle and the gradual change in surface morphology seen throughout the colloidal probe experiments. A) The particle before use, with fines clearly seen on the surface, B) The particle after the first use, a smoothing effect has occurred, but certain asperities have become exposed as identified by the red arrows and C) The particle after multiple uses, separate asperities recede flattening into one larger asperity.

2.7 Chapter References

1. Butt, H.-J. H. *et al. Physics and Chemistry of Interfaces*. *Phys. Chem. Interfaces* (Wiley-VCH, 2006). at <http://www.inquimae.fcen.uba.ar/materias/fqs/libros/PhysChemInt.pdf%5Cnhttp://dx.doi.org/10.1002/3527602313.ch12%5Cnhttp://www.mlajournals.org/doi/abs/10.1632/074069503X85526%5Cnhttp://dx.doi.org/10.1002/3527602313.app1%5Cnhttp://doi.wiley.com/10.1002/352>

2. Piggott, M. J. Characterising the force balance between active pharmaceutical ingredients for inhalation and its impact on deposition. (2013).

3. Instruments, N. How an SEM works. at <https://www.nanoscience.com/technology/sem-technology/how-sem-works/>

4. Atteberry, J. How Scanning Electron Microscopes Work. *How St. Work.* at <https://science.howstuffworks.com/scanning-electron-microscope2.htm>

5. Instruments, N. Sample-Electron Interaction. at <https://www.nanoscience.com/technology/sem-technology/sample-electron-interaction/>

6. Labs, S. V. High Resolution Imaging with SEM. at <http://iitkgp.vlab.co.in/?sub=40&brch=263&sim=1582&cnt=3311>

7. Peter J. Goodhew, F. J. Humphreys, R. B. *Electron microscopy and analysis*. *Electron Microsc. Anal.* (Crc Press, 2001).

8. Sammons, R. & Marquis, P. Application of the low vacuum scanning electron microscope to the study of biomaterials and mammalian cells. *Biomaterials* **18,** 81–86 (1997).

9. Langlois, E. D., Shaw, G. A., Kramar, J. A., Pratt, J. R. & Hurley, D. C. Spring constant calibration of atomic force microscopy cantilevers with a piezosensor transfer standard. *Rev. Sci. Instrum.* **78,** 93705 (2007).

10. Sader, J. E., Chon, J. W. M. & Mulvaney, P. Calibration of rectangular atomic force microscope cantilevers. *Rev. Sci. Instrum.* **70,** 3967–3969 (1999).

11. Haugstad, G. *Atomic Force Microscopy: Understanding basic modes and advanced applications*. (John Wiley & Sons, Inc., 2012). doi:10.1002/9781118360668

12. Ohler, B. *Practical Advice on the Determination of Cantilever Spring Constants*. at <http://nanoscaleworld.bruker-axs.com/nanoscaleworld/media/p/143.aspx>

13. Gibson, C. T., Johnson, D. J., Anderson, C., Abell, C. & Rayment, T. Method to determine the spring constant of atomic force microscope cantilevers. *Rev. Sci. Instrum.* **75,** 565–567 (2004).

14. Hutter, J. L. & Bechhoefer, J. Calibration of atomic-force microscope tips. *Rev. Sci. Instrum.* **64,** 1868–1873 (1993).

15. Sim, K. S., Tan, Y. Y., Lai, M. A., Tso, C. P. & Lim, W. K. Reducing scanning electron microscope charging by using exponential contrast stretching technique on post-processing images. *J. Microsc.* **238,** 44–56 (2010).

16. Butt, H.-J., Cappella, B. & Kappl, M. Force measurements with the atomic force microscope: Technique, interpretation and applications. *Surf. Sci. Rep.* **59,** 1–152 (2005).

17. Hooton, J. C. *et al.* Characterization of particle-interactions by atomic force microscopy: effect of contact area. *Pharm Res* **20,** 508–514 (2003).

18. Drelich, J. (Jaroslaw) & Mittal, K. L. *Atomic force microscopy in adhesion studies*. (CRC Press, 2005).

19. Neto, C. & Craig, V. S. J. Colloid Probe Characterization: Radius and Roughness Determination. *Langmuir* **17,** 2097–2099 (2001).

20. James, J. The Interaction of Drug Particles with Materials Employed in Inhaled

Delivery Devices. (2009).

21. Bunker, M. J. The Nanoscale Characterisation of Particle Interactions and Tribology. (2006).

22. Kaialy, W. On the effects of blending, physicochemical properties, and their interactions on the performance of carrier-based dry powders for inhalation — A review. *Adv. Colloid Interface Sci.* **235,** 70–89 (2016).

23. Felicetti, M. A., Salazar-Banda, G. R., Coury, J. R. & Aguiar, M. L. Influence of Particle Size, Applied Compression, and Substratum Material on Particle−Surface Adhesion Force Using the Centrifuge Technique. *Ind. Eng. Chem. Res.* **48,** 877–887 (2009).

3 Selection and Optimisation of Additive Manufacturing Technique

3.1 Introduction

As discussed in the introduction, previous attempts have been made to isolate the effects of surface morphology on particle adhesion, however many of these techniques provided limited control over the type of surface morphologies produced or even the extent of surface coverage[1,2].

The focus of this chapter is therefore identifying a technique that provides the ability to fabricate well-defined micron scale morphologies in a controllable, flexible and scalable fashion. This will therefore allow a bottom up approach to improving fundamental understanding on the effect of surface morphology on particle adhesion. As previous additive manufacturing in the field of pulmonary drug delivery has focused on prototyping whole inhaler parts[3,4], to begin with this work will be conducted by printing a replica of a handihaler, and then evaluating the scope to modify the surface within this technique.

3.1.1 Selective Laser Sintering

Selective Laser Sintering (SLS) involves the layer by layer production of a 3D object by fusing or sintering loose powders of around 10-150 µm[5] in size together in the required shape (Figure 3.1). Fresh powder is rolled onto the build tray[6] and pre-heated using auxiliary heaters. The particles are then raised in temperature to the glassy transition state using a CO_2 or Nd:YAG laser,[7] directed using galvo mirrors or an X-Y stage[8] to fuse the powders in the shape required. After the powders have been fused for each layer, a piston moves down a layer and another layer of loose powder is swept across, and a new layer is fused building up the desired 3D shape[9]. SLS can produce parts from a range of materials, like; ceramics, metals and polymers. SLS can

therefore be further sub-divided based on the binding mechanism, as polymers like nylon involve solid state sintering, whereas materials like ceramics often require an additive to be added to melt first[7]. Finally, metals, often involve selective laser melting (SLM), which is another subdivision requiring full melting[7]. The main disadvantage of SLS is the restriction of resolution based on the particle size used[10].

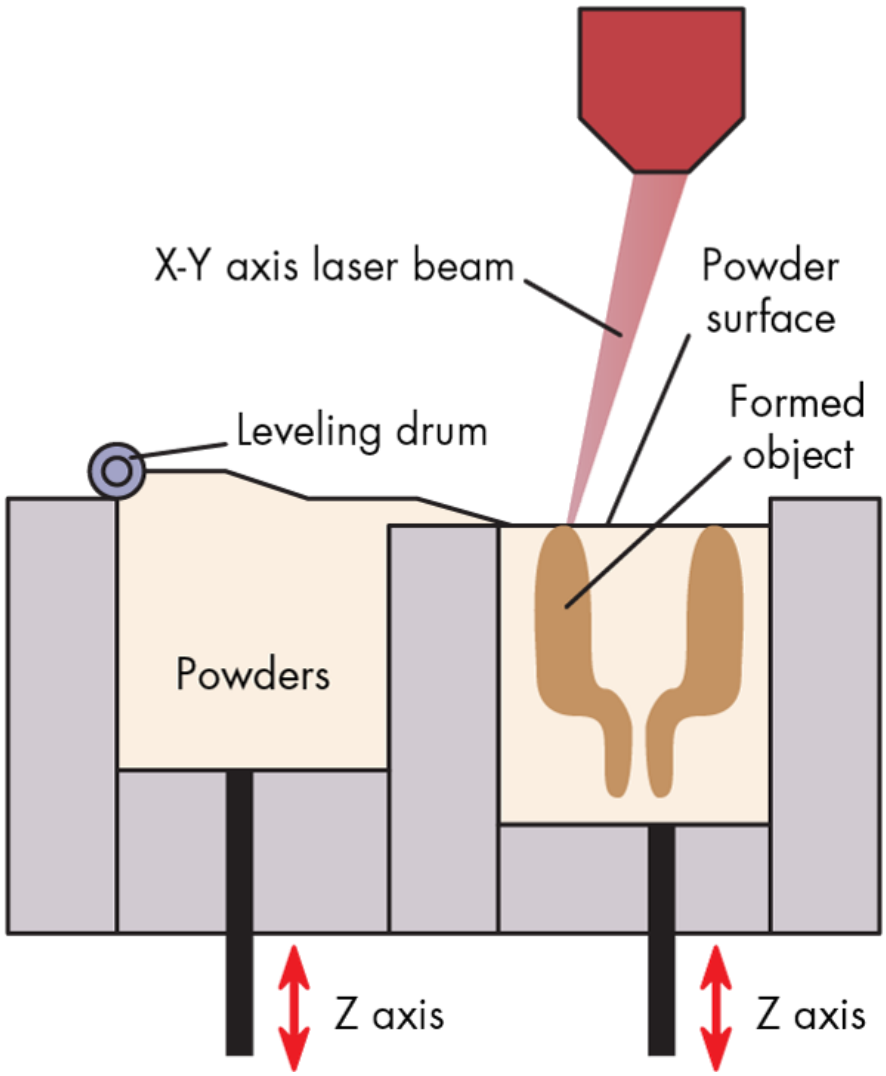


Figure 3.1: An overview of the Selective Laser Sintering Process[11].

3.1.2 PolyJet Inkjet Printing

Inkjet printing is an extension of normal commercial ink-jet printing, and involves the deposition of droplets of ink from a print head[12] in each layer[10]. The inks used

comprise a solute which has been dissolved or suspended in a solvent[13]. Depending on the material used, the drops may be allowed to evaporate, dry thermally, or be photopolymerised using ultraviolet light (UV) forming a solid layer to be printed on[12,14]. One of the critical factors of successful inkjet printing is the suitability of the material. Printable inks are restricted by their physical properties namely viscosity, surface tension and density which determine the successful ejection of the droplet from the nozzle and formation of a stable spheroidal droplet[15]. There have been numerous studies investigating the relationship of these factors. The suitability of materials for printing is then a combination of these factors and can be combined in terms of their Z number[16]. The Z number is the inverse of the Ohnesorge number (Oh) which is defined as the square root of the Weber number(We) divided by the Reynold's number (Re), where ρ, η and γ are the density, dynamic viscosity and surface tension of the ink respectively and v is the velocity and a the characteristic length of the droplet.

$$Re = \frac{v\rho a}{\eta} \quad (3.1)$$

$$We = \frac{v^2\rho a}{\gamma} \quad (3.2)$$

$$Oh = \frac{\sqrt{We}}{Re} \quad (3.3)$$

Computationally, Reis and Derby[17], determined that to be printable, a material should fall within the range $1 < Z < 10$, however there is some disagreement of the exact range as experimental observations reported by Jang and Moon[18] suggested $4 \leq Z \leq 14$. At lower Z values, materials are limited by the dissipation of pulse energy due to excessive ink viscosity, resulting in the droplet not ejecting from the nozzle or the generation of long droplet filaments, that lengthen the time to spheroidal droplet generation[15,18]. Higher Z values than this range, often form a spray with satellite

droplets instead of single well-defined droplets[18]. In practice, this means that material viscosity should be generally less than 20mPa·s, with a surface tension between 28 mN/m and 350 mN/m, for successful inkjet printing[16].

Inkjet printers are generally divided into two modes of operation, depending on their print head; continuous inkjet (CIJ) or drop-on-demand (DOD) inkjet printing[19]. CIJ produces a jet of material ejected through a nozzle under pressure, droplets are then formed due to the Rayleigh instability often combined with periodic pressure fluctuations[15,16]. This continuous stream of droplets are produced with a slight charge imparted from the nozzle, allowing the deflection of the droplet stream using charged deflector plates[15]. As the name suggests the production of droplets are continuous, and therefore the droplets impact onto the substrate in the desired shape, or if not needed for that section of the print they are deflected into a gutter for recycling[15]. Drop-on-demand (DOD) inkjet printing, by contrast, produces droplets as required when the nozzle is positioned above the correct substrate location for the printing process[15].

In DOD inkjet printing, a pressure pulse is generated in the ink reservoir forcing a droplet out of the nozzle. There are two types of DOD printer based on how the pressure wave is created. Firstly, thermal DOD inkjet printers, which contain a heating element in the reservoir allowing rapid heating of the adjacent ink when a current is applied to the element. As the ink exceeds its boiling point, this causes the creation of a bubble which expands the volume of the ink and results in the ejection of a droplet[20]. After the current through the element is removed, the bubble rapidly collapses drawing fresh ink into the reservoir[15]. Piezoelectric DOD inkjet printers are the second type of DOD inkjet printer and instead generate a pressure pulse by applying a voltage signal that produces a deformation of the piezoelectric material, physically altering the ink reservoir dimensions, forcing the ejection of a droplet[21].

DOD inkjet printers are more widely used, as CIJ produces droplets that are around 100 µm whereas DOD inkjet printers generate drops with a diameter of 20-50 µm providing a higher deposition accuracy[15,16]. In addition, for material and life sciences applications the material collected in the gutter in CIJ cannot be reused due to the

contamination risk, resulting in a higher degree of waste[15]. As thermal inkjet printing requires the production a vapour bubble, this generally limits the choice of inks to aqueous based solvents[16] which restricts the selections of polymers and active pharmaceutical ingredients which can be used[22]. Therefore, the vast majority of inkjet printers used for published work utilise a piezoelectric DOD inkjet head[15].

PolyJet is a process used in Stratasys inkjet printers to manufacture 3D objects[23]. The PolyJet uses a piezoelectric DOD inkjet head, which is capable of depositing multiple UV curable materials, as well as the support material using different nozzles[24]. The print head moves along the X axis jetting the photopolymer onto a build tray in the desired design, as seen in Figure 3.2, followed by a second pass along the same axis to allow for the curing of the material using the UV bulbs, integrated in the print head[25]. The printer will then move along the Y axis to align for the next X axis printing path. Once a pass is completed, a small roller then flattens these drops to provide a consistent foundation for the next layer[24]. Once, a layer is complete the build tray will then lower by 16 µm allowing the next layer to be produced, and the object is printed in this layer- by- layer process[23]. As parts produced using this technique tend to be weaker than other AM techniques, the object needs to be surrounded and supported with a gel-type polymer which is removed with a water jet in post-processing[10].

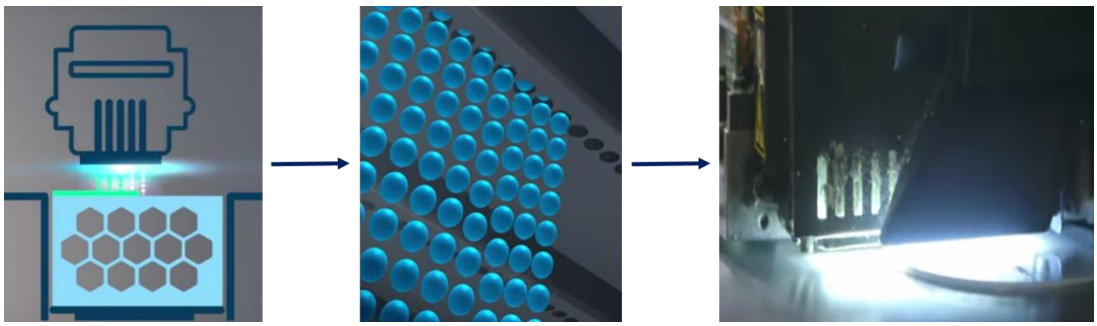


Figure 3.2: The PolyJet Process, the photopolymer is jetted along the X-axis using multiple nozzles, which are subsequently cured using UV bulbs integrated in the jetting head in a layer- by- layer process. Picture adapted from PolyJet: 3D Printing[26]

3.1.3 Nanoscribe Two Photon Polymerisation

The micron scale morphologies used in this thesis were produced using a Nanoscribe Photonic Professional GT, a commercial two photon polymerisation printer. The Nanoscribe system utilises a near infrared 100 fs pulsed fibre laser at a wavelength of 780 nm to polymerise a defined voxel of the resist. The resist to be printed in, is dropcast on the substrate, in this case a glass coverslip, which is mounted in one of the provided sample holders (Figure 3.3). Immersion oil is then applied on the lower surface of the substrate for the submersion of the 63x 1.4 NA objective lens. Once the sample holder is mounted, the substrate can be moved, using either the stage or the piezo for fine positioning, as seen in Figure 3.4.

The focusing of the beam, combined with the use of a pulsed laser, allows for the spatial and temporal compression needed to overcome the threshold for two photon absorption as discussed in Section 1.9.3 and hence polymerisation occurs in an extremely localised area. This allows for the production of well-defined micron scale morphologies of arbitrarily complex design as seen in Figure 3.3.

The Nanoscribe system produces the desired 3D structure by following a series of pre-programmed trajectories and printing parameters. These are inputted into the NanoWrite software in a GWL (General Writing Language) file format. This is a script language providing the laser the co-ordinates of the writing path as well as the laser power needed for each particular section. These GWLs can be generated from standard tessellated language (STL) files produced in any CAD software, using the DeScribe software.

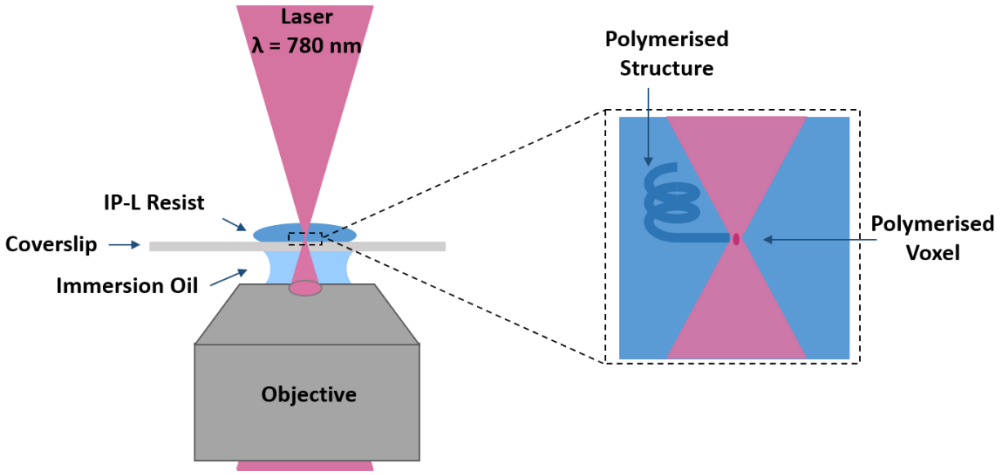


Figure 3.3: Cross-section schematic of the setup in the Nanoscribe Photonic Professional. The objective is submerged in dropcast immersion oil on the lower side of the substrate, allowing the laser beam to be focused into the resist on the upper substrate surface.

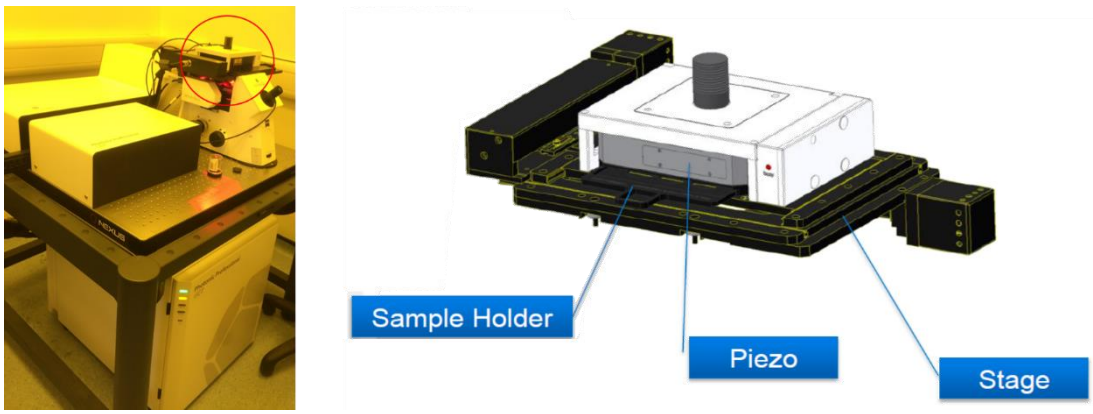


Figure 3.4: The Nanoscribe Photonic Professional GT system and inset the components of the stage. Picture adapted from Nanoscribe Theoretical Training Presentation 2014[27].

3.2 Chapter Aims

The aim of this chapter is to identify a suitable additive manufacturing technique to produce morphologies appropriate for furthering the understanding of the importance of morphology on powder interaction in DPIs. Once this technique has been selected a subsequent evaluation and optimisation of the fabrication capabilities of the printer is required to produce the desired surface resolution.

3.3 Chapter Objectives

- Characterise the surface finish produced using different additive manufacturing techniques using the 'handihaler' device as a test object.
- Optimise the printing parameters of the Nanoscribe Photonic Professional GT to produce an improved surface finish.
- Produce well-defined micron scale morphologies, using a semi-circular ridge structure as an initial test structure.

3.4 Materials and Methods

3.4.1 Materials

A commercially manufactured handihaler was donated by Boehringer Ingelheim (Inhelheim, Germany). For the production of selective laser sintered surfaces Polyamide 12 powder (PA2200) was obtained from EOS GmbH (Krailling, Germany). Objet VeroClear (FullCure 720) resin was purchased from Objet and used as received. All solvents were obtained from Sigma-Aldrich unless otherwise stated.

All printing reagents were used as purchased from Nanoscribe GmBH (Eggenstein-Leopoldshafen, Germany), unless otherwise stated. Two photon polymerisation was conducted using IP-L 780 as a photoresist, which consists of >95% 2-(Hydroxymethyl)-2-2[[(1-oxoallyl)oxy]methyl]-1,3-propanediyl diacrylate and 5% of the photoinitiator 7-(Diethylamino)-3-(2-thienylcarbonyl)-2H-1-benzo 2-one.

3.4.2 Computer Aided Design (CAD)

The handihaler CAD design was produced by Mr Joseph White using AutoCAD. Structures to be printed on the Nanoscribe Photonic Professional GT were designed in PTC Creo Parametric 3.0 and converted into a GWL format using Describe (Nanoscribe).

3.4.3 Selective Laser Sintering (SLS)

Parts were manufactured by selective laser sintering (SLS) using an EOS Formiga P100, with the assistance of Mr Joseph White. The PA 12 powder was pre-heated in the chamber to 173^{o}C and the part was sintered using a laser power of 21W, with a 2500 mm/s scan speed and a scan spacing of 0.25 mm.

3.4.4 PolyJet Printing

The handihaler mouthpiece was printed by Mr Joseph White, using an Objet Connex 500 PolyJet printer using VeroClear. Several mouthpieces were assembled in the build tray and printer settings are automatically inputted once the material is selected.

3.4.5 Two Photon Polymerisation (TPP)

All two photon polymerisation work shown was conducted on the Nanoscribe Photonic Professional GT (Nanoscribe) equipped with an inverted Carl Zeiss Axio Observer microscope (Zeiss) using a 63x immersion objective, numerical aperture = 1.4. The structures were fabricated in a commercially available acrylate based resin (IP-L 780, Nanoscribe) using, 22 mm x 22mm glass coverslips, with a thickness of 0.17 mm, as substrates. The cover slips were cleaned according to manufacturer's instructions with acetone, isopropanol and distilled water and then dried using compressed air. After the substrate was fixed to the holder using four strips of 3M™ Scotch™ 851 sticky tape (Nanoscribe), two drops of immersol 518F immersion oil (Nanoscribe) were dropcast on the underside. The substrate holder was then inverted and a drop of the UV-curable photoresist, IP-L 780 was then spread around the substrate by tilting the substrate holder. The sample holder was then loaded into the stage and a piezo stage device calibration was performed, which calibrates the piezo to the current mass load and improves writing accuracy. The structure was then fabricated, see Section 3.5.2.1 for more details. The unexposed region of the resist was then dissolved using two, thirty minute submerges of the glass coverslip in propylene glycol monomethyl ether acetate (PGMEA ≥ 99.5%) followed by a two minute isopropanol (≥ 99.9%) wash before drying with compressed air.

Single ridges were polymerised on the glass surface using the Piezo printing mode, the laser intensity was optimised using a laser intensity screen and final settings with a laser power of 30 mW and power scaling of 0.85 were chosen. Finally, for optimal surface feature resolution perfect shape quality, a path

optimisation feature was used. In order to import the STL file into the software, a slicing thickness setting of adaptive was used, with a minimum slicing distance of 0.1 µm and maximum of 0.3 µm. Shell and scaffold settings were optimised, as discussed in Section 3.5.2.1.3, the final shell chosen consisted of a hatching distance of 0.1 µm with 10 contours. The scaffold settings chosen were wall spacing of 1 µm and floor spacing of 0.5 µm with a base slice count of 1.

3.4.6 Atomic Force Microscopy (AFM)

Atomic force microscopy (AFM), both in tapping and quantitative nanomechanical measurements (QNM) mode was used to characterise the TPP geometries produced. A FastScan Bio Icon AFM (Bruker, Coventry, UK) was used with RTESPA-300 tips (Bruker, Coventry, UK), at a scan rate of 0.977 Hz.

All images were processed using Gwyddion software (version 2.44) (Czech Metrology Institute, Brno), and were levelled using a mean plane subtraction. Extracted profiles of three separate TPP ridges were then evaluated for surface roughness using the arithmetic mean (Ra) and the root mean square (RMS) of the average height deviations of the surface.

3.4.7 Scanning Electron Microscopy (SEM)

The surface finish of the mouthpiece of the inhalers manufactured utilising differing methods (Handihaler, SLS and PolyJet) was imaged using Scanning Electron Microscopy (SEM) on a JSM-6060 LV (JEOL). The samples were cut from bulk and loaded unto aluminium stubs with carbon tabs pre-fixed. These stubs were sputter coated (Balzers Benchtop Sputter Coater SCD 030) with gold in an argon atmosphere at 30 mA for 5 minutes. Images were then collected in high vacuum mode in the secondary electron imaging setting.

3.4.8 Surface Profilometry

A Talysurf CLI 1000 (Taylor/Hobson Precision, UK) contact autofocus profilometer was used for topographical evaluation of the surface finish of the handihaler mouthpieces' manufactured by injection moulding, SLS and PolyJet over an area of 5mm x 5mm. A diamond tipped inductive stylus was used to scan the surface of the sample. The work piece was moved at a transverse speed of 500 µm/s. Surface roughness was quantified using the arithmetic mean (Ra) of the average height deviations measured from extracted profiles using the instrument software (TalyMap Universal 3.2.0), with microroughness filtering with a ratio of 2.5 µm.

3.5 Results and Discussion

3.5.1 Characterisation of the Surface Finish of Inhaler Manufacturing Techniques

Previously in pulmonary drug delivery additive manufacturing has focused on prototyping whole inhaler parts[3,4]. Therefore, an initial investigation was conducted to attempt to print a handihaler and evaluate the surface finish of inhalers produced by varying manufacturing techniques. A technique was needed that produced a similar surface finish to an injection moulded inhaler, but with the capability to produce well defined and controllable micron scale morphologies. This would then allow the production of an entire inhaler with an optimal pattern printed on the internal surface, which would provide a viable manufacturing option for inhalers of this type in the future. A handihaler mouthpiece was therefore chosen to be the test fabrication model for the characterisation of surface finish.

3.5.1.1 SEM Analysis

SEM images of the surface topology of the inhalers prepared using different manufacturing methods (injection moulded, SLS and inkjet) are shown in Figure 3.5. The commercially available injection moulded handihaler (Figure 3.5A) shows an extremely smooth surface with only slight scratches and the occasional micron sized feature, probably introduced by the manufacture or post-processing of the inhaler. In contrast, however the SLS inhaler surface (Figure 3.5B) shows at 50 x magnification clear parallel line structures, representing the layer-by-layer manufacture of the inhaler. Within each layer, the individual particles within the printed material are still clearly distinct, and are around 60 µm in diameter, creating an extremely rough and non-homogenous surface. Finally, SEM images of the Polyjet printed inhaler mouthpiece (Figure 3.5C) show well- defined ridges, characteristic of the Objet printing surface finishing process. The 120 x magnification image shows multiple features in the tens of microns size range as well as several micron sized holes.

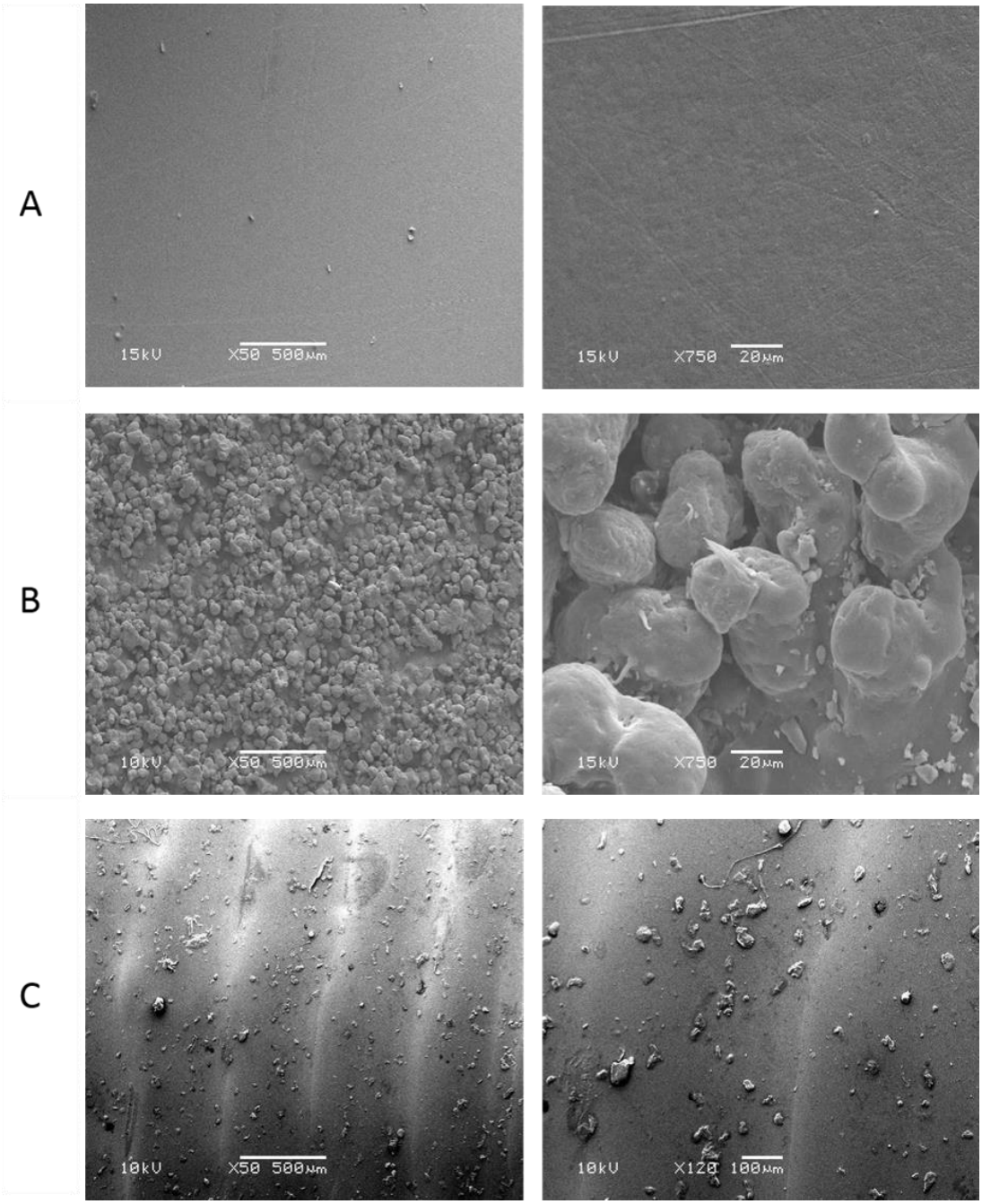


Figure 3.5: SEM Images of the surface topology of the mouthpiece of the handihaler manufactured by A) Commercial injection moulding, B) Selective Laser Sintering and C) Inkjet Printing.

3.5.1.2 Surface Profilometry

The mouthpiece of the handihalers manufactured using different methods was also imaged using surface profilometry over a 5 mm x 5 mm area as seen in Figure 3.7 and their respective surface roughness (Ra) was calculated as seen in Table 3.1. In agreement with the visual observations as seen in SEM, the injection-moulded mouthpiece had the smoothest surface with an Ra of 0.038 µm in contrast with the SLS printed mouthpiece with an Ra of 0.72 µm, with the individual particles creating a roughness clearly seen in the 3D image in Figure 3.7B. Finally, with a Ra of 0.055 µm the inkjet printed mouthpiece has a similar surface roughness to the injection moulded mouthpiece, with the exception of the clear ridges seen in the 3D image (Figure 3.7C).

Table 3.1: Surface roughness, documented as Ra, of the handihaler mouthpiece using the three different manufacturing techniques

Manufacturing Technique	Ra (µm) **± S.D.**
Injection Moulded	0.038 ± 0.0084
Selective Laser Sintered	0.72 ± 0.016
Inkjet Printed	0.055 ± 0.00014

Initially it seems counterintuitive that the injection moulded mouthpiece has such a similar Ra to the inkjet printed mouthpiece, as the 3D talysurf images show a series of ridges on the inkjet version. When the meaning of Ra and the line profile used to produce this calculation are considered, however it becomes understandable. The Ra, calculates an average of the deviation from the average, with no accounting for direction of variation (Figure 3.6). Therefore, as the inkjet printed mouthpiece roughness has a relatively reproducible waviness (Figure 3.7 C), when the “troughs” are inverted to be in line with the “peaks,” the average will be calculated as half of the height of the peaks. Therefore, the variation will be effectively halved.

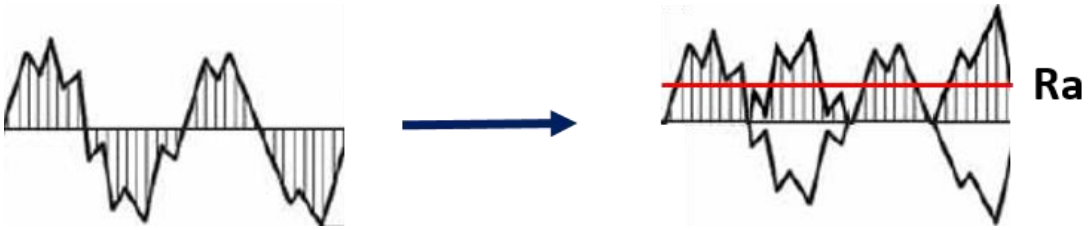


Figure 3.6: An example of the calculation of surface roughness using Ra (the arithmetic mean). Firstly, the deviation from the centre is highlighted, and then the "troughs" of the roughness are inverted and an average is taken which is the calculated Ra (red line). Picture adapted from[28]

This is then compared with the injection moulded inhaler, which although possesses a smooth surface finish, possesses a larger curvature within the scan area (see Figure 3.7 A), which results in two broad “peaks” and two broad “troughs”, which when processed in the same fashion, produces a similar “average” deviation.

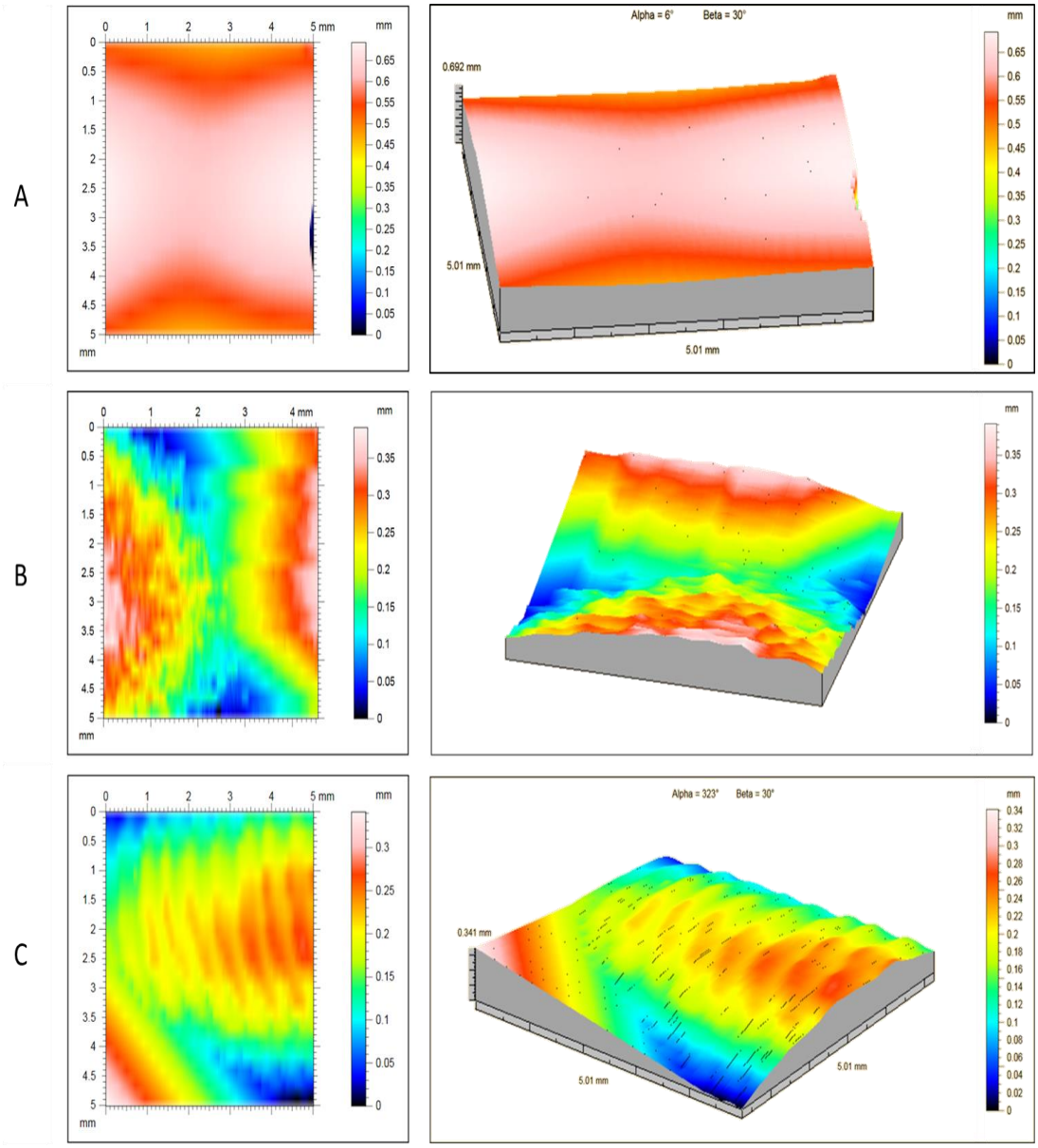


Figure 3.7: Talysurf Profilometry 2D Images (left) and their respective 3D representation (right) of the mouthpiece of the handihaler manufactured by A) Commercial injection moulding, B) Selective Laser Sintering and C) Inkjet Printing.

The surface finish produced with the different manufacturing techniques, clearly demonstrated that these AM techniques would be ill suited to the task of the production of controllable micron scale morphologies, as both were dominated by the fabrication process utilised in the technique. The SLS inhaler surface, clearly shows the individual particles comprising the initial powder which are subsequently fused into the desired structure. In order to obtain micron scale features a sub-micron particle size would be required, however due to agglomeration and oxidation issues, the minimum particle size is usually 20 µm[6]. Which makes the lowest minimum feature size to be on the scale of hundreds of microns, as it would require multiple of these particles, and complex geometries on this scale would be impossible. Likewise, the PolyJet process builds up the object by lowering the build tray, to produce the next layer, restricting the resolution to 16 µm with better surface resolution only achieved by coating the surface in support material[24]. It was therefore decided that in order to pursue an extensive evaluation of the effect of micron scale morphology on particle adhesion, an additive manufacturing technique was required with improved resolution. A reproducible design as seen on the surface of the PolyJet printed handihaler was desirable, however a smaller scale was needed for applicability to the field of particle adhesion in pulmonary drug delivery. Also, this pattern was fabricated as a by-product of the printing process and therefore provides insufficient scope for the operator to modify this pattern. In order to print on a nano-scale there are a variety of lithographic techniques available. However, whilst techniques like e-beam or X-ray lithography, may be capable of producing down to 10 nm resolution, they lack the ability to print the 3D complexity that may be desired[29,30]. With the advent of two photon polymerisation, resolution of 120 nm has been achieved, combined with an ability to print 3D shapes, without the need for supports or masks[7,9,31]. Therefore, an investigation into the production optimisation of well-defined micron scale morphologies was instigated utilising two photon polymerisation.

3.5.2 Optimisation of Two Photon Polymerisation Printing

As the Nanoscribe was a newly acquired piece of equipment in the University and there has been limited publications investigating surface finish of two photon polymerised structures especially in the sub- micron range, an initial investigation was required to ascertain the abilities of the equipment and the optimal parameters needed for printing with the desired surface resolution.

3.5.2.1 Selection of Printing Parameters

3.5.2.1.1 Printing Mode

The first step of defining the settings used on the Nanoscribe is to decide on the printing mode to utilise. There are three possible options, which together outline the positioning process and the laser beam focusing system. The first of these is piezo scan mode, in this mode, the laser beam is fixed and the substrate is moved with fine control using the piezo stage over the beam[32]. This means the polymerised area will consistently be in line with the centre of the objective, resulting in increased printing accuracy of several nanometers[33]. Galvo scan mode, utilises two galvo mirrors to deflect the laser beam in order to polymerise areas in the X-Y direction and the use of the piezo stage or stage for z movement[27]. As the laser is being deflected this requires significantly less settling time and mechanical movement and is therefore capable of greater speeds and consequently printing large areas, however has an accuracy of around 100 nm[32,33]. Finally, the third mode is the stage scan mode, which moves the whole stage to produce X-Y movement, however this is an extremely coarse positioning method and is therefore generally only used for large distance movements, for instance between prints[32]. As this project is specifically interested in pursuing high-resolution morphologies on a micron scale, piezo scan mode using continuous printing was selected, as this provides a higher degree of accuracy and greater resolution than the other two modes.

There are however, several parameters within piezo scan mode that can be modified, including; scan speed, laser intensity and interface identification, all of

which have a significant impact on the resulting quality of the final structures. As high quality surface resolution of the design was critical in this project, the PerfectShape algorithm was employed. This algorithm automatically adjusts the substrate velocity depending on the complexity and trajectory of the shape to be printed, instead of having a fixed scan speed for the entire structure. PerfectShape Quality was selected which is the slowest mode, but provides the highest quality structures[32].

3.5.2.1.2 Printing Reproducibility

In order to evaluate the capabilities of the equipment, a semi-circular 1 µm diameter 50 µm length ridge was chosen as a test structure as this would allow the evaluation of the ability of the Nanoscribe to produce smooth curves on the micron scale.

However, on reviewing the initial print there were several issues with the printing reproducibility. Firstly, there was an inconsistency with the resultant ridge dimensions and secondly printing defects were seen with ridges failing to print or certain sections appearing damaged or unfinished (Figure 3.8). On evaluation of the possible causes, there were several considered; firstly insufficient laser intensity could have resulted in incomplete polymerisation as seen by Kurselis et al.[34]. Secondly, the substrate may have been at a slight angle, resulting in areas of printing not fully attaching to the substrate. Finally, the post-development process itself could be responsible, despite following the manufacturer's guidelines.

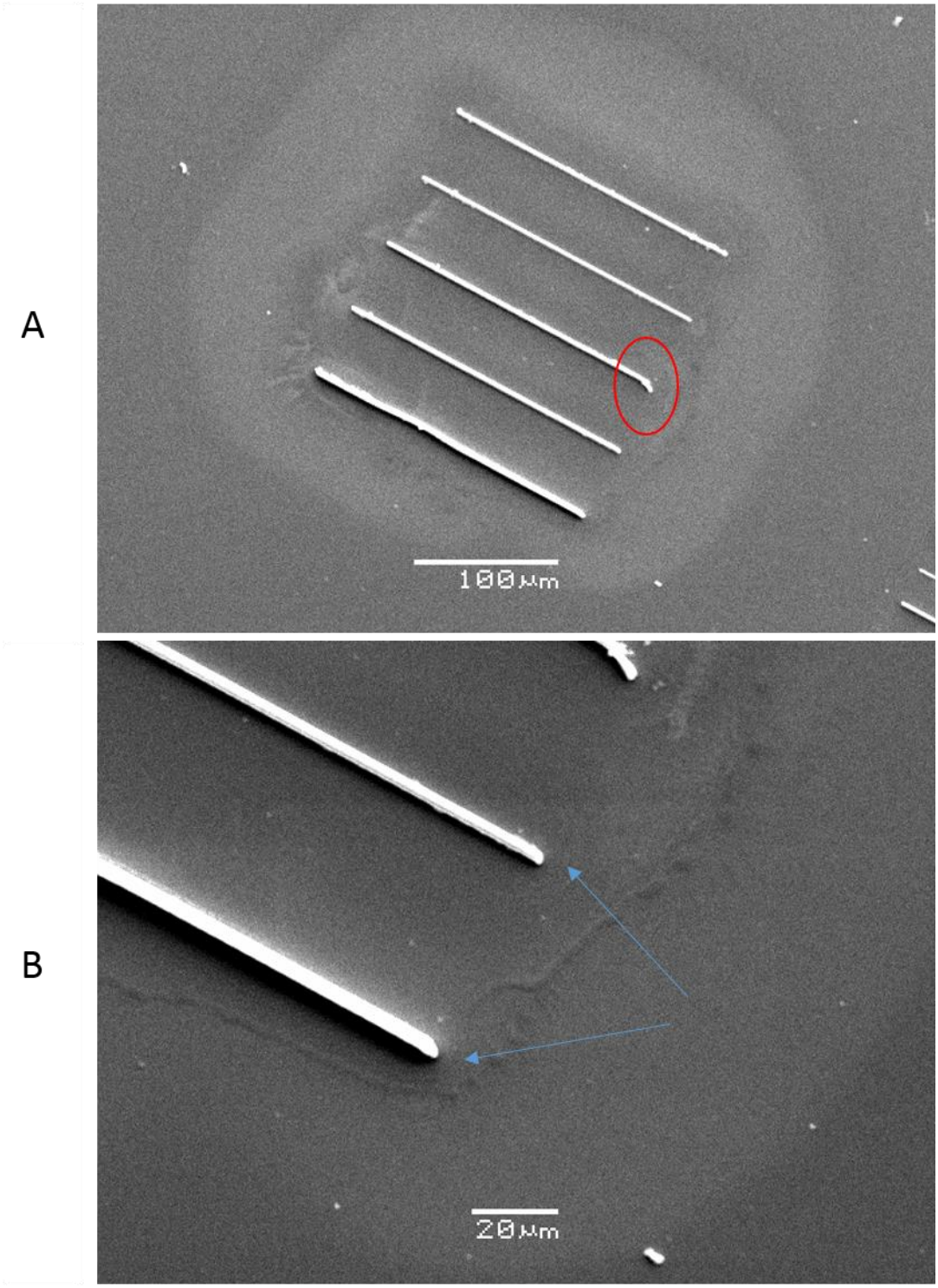


Figure 3.8: Issues with Printing Reproducibility; A) the red circle highlights a section of the ridge seemingly damaged and in B) the blue arrows highlight changes in ridge dimensions.

Initially, the laser intensity settings were investigated, during the print this is calibrated by the multiplication of two commands; the power scaling (0-1) and the laser power (0-100). A power screen was therefore undertaken involving gradually adjusting the power scaling setting from 0.5 to 1 in 0.05 increments, while keeping the laser power fixed. However, the resin began to bubble and burnt sections were seen, on all the structures with higher power scaling settings, indicating that the laser intensity was not the issue, as an increase in laser intensity had exceeded the explosion threshold.

The next most plausible cause of the issue was substrate adhesion problems caused by the lowest voxels not contacting the substrate sufficiently, an issue evaluated by different researchers[35,36]. In order for the structure to be firmly in contact with the substrate, the "truncation effect" must be utilised[37,38], this involves submerging the focal voxel into the substrate resulting in the production of a partial polymerised voxel. If insufficiently submerged the voxel and hence structure will only be lightly in contact with the substrate, therefore the subsequent post-processing steps may be sufficient to wash the structure away[38].

An understanding is therefore needed of the Nanoscribe system's automatic identification of the interface. This works by projecting an image of a grid through the substrate and into the resist, the change in refractive index between these two mediums results in the reflection of part of the image back through the objective. This is then projected on a tilted camera sensor chip. By adjusting the z height of the objective, the grid pattern will be moved until it lights up an area of pixels which have been defined in the software as the interface z-position[32]. However, when multiple structures are fabricated an alteration in the z position, equivalent to the interface, can occur due to substrate tilt or substrate roughness, resulting in polymerised voxels being submerged to a greater or lesser extent. This will therefore cause some structures to appear thinner, as the broader structure base was not polymerised above the substrate in the resin, or some structures to either not form or be washed away during the post-processing. To overcome this issue, Nanoscribe advises instructing the software to find the interface at a lower level, for instance 0.5 µm below the surface, ensuring the truncation of the voxels and sufficient contact with

the structure. As the initial design was only 0.5 µm, a second design was constructed which encompassed an extra 0.5 µm section beneath the semi-circle which would be the main area submerged during fabrication. A 50 µm length ridge with a semi-circle of diameter 1 µm on a 1 x 0.5 µm rectangle was therefore chosen as a test structure (Figure 3.9)

In order to negate the effect of substrate tilt throughout the printable region, code was introduced which instructed the Nanoscribe system to find the interface at a range of points across the printable area and use this to evaluate the angle of the substrate, applying a tilt correction in Piezo Scan Mode (see code 1 in Appendix A). In addition, before every ridge was printed, an extra command of *FindInterface* was introduced which should also reduce printing defects caused by substrate roughness. This successfully resolved the issue and objects printed became more reproducible.

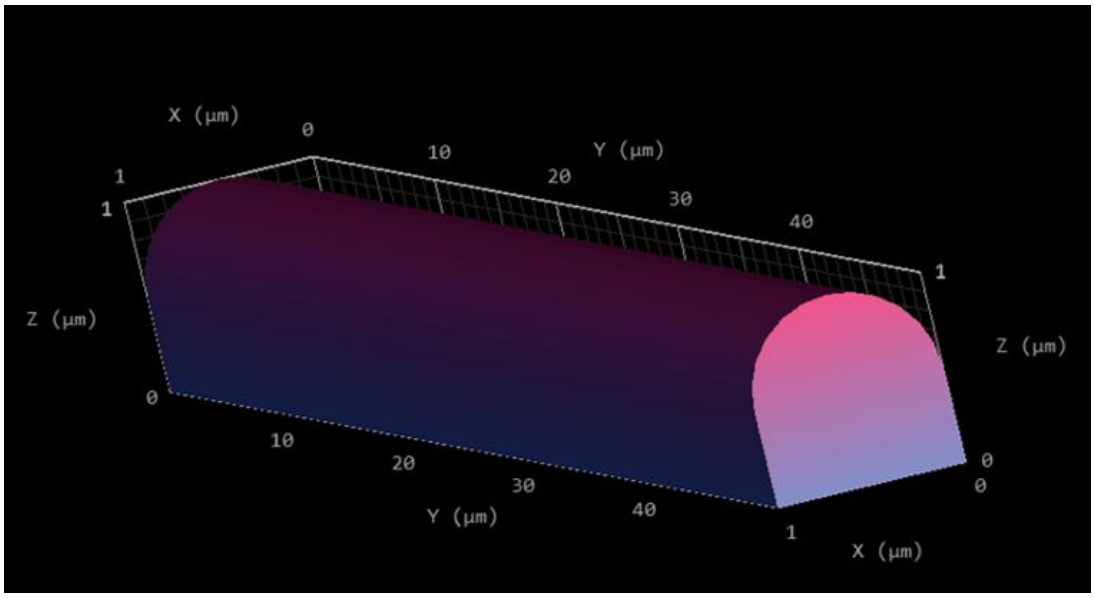


Figure 3.9: A CAD design of the initial test structure; a semi-circular 50 µm long ridge.

3.5.2.1.3 STL Conversion Settings

As mentioned in Section 3.1.3, the Nanoscribe system is accompanied by an STL conversion software named DeScribe. The first step of importing the structure to be

printed, is selecting the slicing parameters (Figure 3.10). In order to produce a smooth curve, a small slicing distance is needed, however using the smallest slicing distance of 10 nm, caused an issue with reproducibility with certain ridges not fabricating successfully. Following advice from Nanoscribe, a larger slicing distance was chosen, 100 nm slicing distance was tried as this had previously been used in other publications requiring fine control[39,40]. The resultant ridges were reproducible and possessed a good surface resolution. To improve writing speed, adaptive slicing was chosen, as this increases slicing distance as the printed curvatures decreases (i.e. where highest resolution is not required). For optimal curvature of the ridges, a slope evaluation setting of max was used.

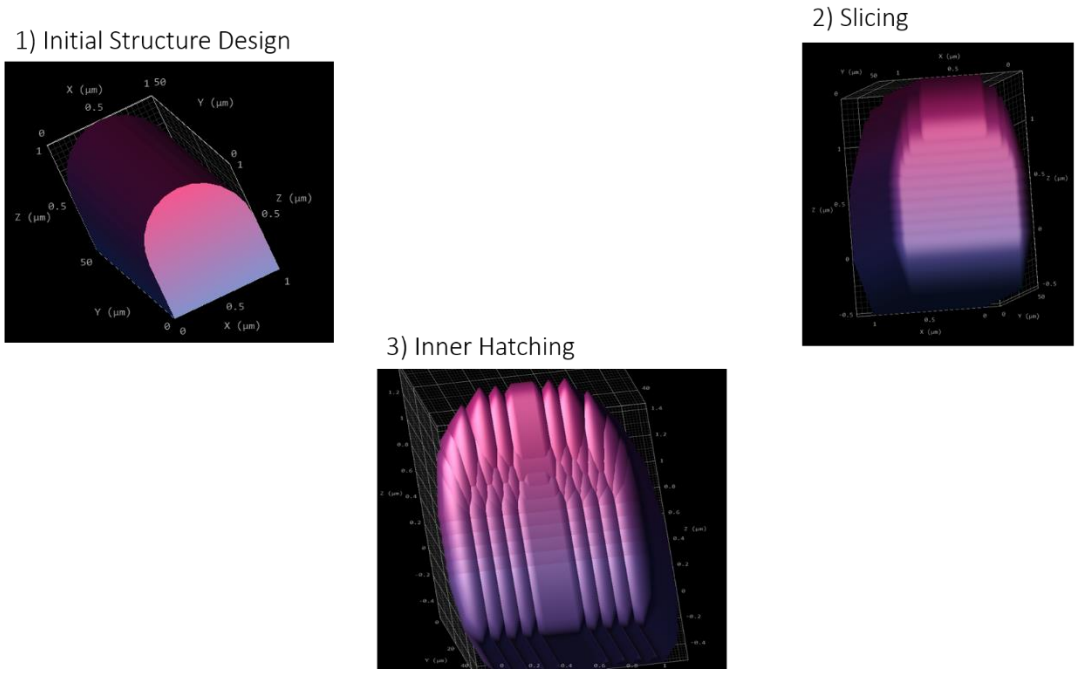


Figure 3.10: The process of importing a 3D structure into the Describe software. First, the object is imported in STL format from a CAD software, and then the object is sliced into layers, providing the Nanoscribe with the trajectories needed to print the object in an additive process. Finally, the hatching parameters are set to dictate the surface resolution and structure integrity.

The next set of parameters to decide upon are the hatching settings. Unfortunately, during the course of this work the version of DeScribe was updated to 2.4, so the parameters that define the shape and so surface resolution of the structure changed. In order for the subsequent alteration of morphologies to be printed, all structures

had to be fabricated based on GWLs from the latest version of DeScribe. This optimisation, therefore occurred in the final stages of this study, resulting in certain time limitations. In the latest version of the DeScribe software, the hatching settings of the structure can either be fabricated in; "solid" mode, involving consistent hatching throughout the structure or "shell and scaffold" mode, which as the name suggests, defines the outline of the structure fabricated with the shell settings, and the scaffold defines the interior. As the real advantage of using "shell and scaffold" mode is to allow big structures to be fabricated in a time efficient manner, by allowing less writing in the centre of the structure, the solid setting was initially investigated. The main input required for this mode was selection of the shell hatching spacing, which is the pitch from contour to contour. Previous studies have assessed the effect of this spacing on surface roughness, although mainly focusing on flat surfaces[41]. Takada *et al*.[41] found that surface resolution improves with decreasing hatching distance until a critical pitch is reached, below which there is a negligible increase in surface roughness. They attribute this effect to the degree of polymerised voxel overlap in the structure, with the optimal overlap considered as 20% of the voxel size[38,41]. The voxel size is however, dependent on a multitude of factors including; laser power, scan speed, numerical aperture (NA) of the objective, the wavelength of the laser, as well as other resist specific factors. Due to the decision to utilise the perfect shape algorithm, however the voxels used to produce the final structure in the prints will vary throughout the shape, so there is no single optimal voxel size[33,36,42]. Decisions on voxel overlap were therefore instead based on theoretical voxel dimensions, attainable with the NA and refractive index (*n*) of the medium. Webb et al[43] provided the following equations for this calculation for a *NA* > 0.7:

$$r_{xy} = \frac{0.325\lambda}{\sqrt{2}\,NA^{0.91}} \qquad r_z = \frac{0.532\lambda}{\sqrt{2}}\left[\frac{1}{n-\sqrt{n^2-NA^2}}\right] \qquad (3.4)$$

where λ is the wavelength of the laser.

For the parameters used with the fabrication in the Nanoscribe; with λ = 780 nm, NA = 1.4 and n = 1.48, the estimated voxel dimensions are a lateral diameter of ~ 263 nm and an axial diameter of ~ 596 nm. This however, has been shown to underestimate the axial dimension[44], with actual voxels generally possessing an aspect ratio of between 3 and 6 with more of an ellipsoidal shape[39]. This would indicate that for a flat surface a hatching pitch distance of around 130 nm should be sufficient. However, the selected well-defined structures are only a micron in diameter and as the top surface in not flat, but curved, a more conservative hatching distance of 100 nm, the minimum setting available was selected as this produced the best surface finish when tested by Power et al[39], who were operating with similar theoretical voxel dimensions.

With a contour hatching distance chosen and solid mode selected the number of contours was automatically set to 20 as seen in Table 3.2. For better surface resolution the hatching angle was chosen to be consistent (0˚ hatching offset) and at a 90˚ angle which results in the alignment of the hatching lines with the contours written, eliminating the contour effect on the surface. Finally, the round contour offset mode was chosen to smooth out the curve of the ridge. The surface morphology of the ridges printed with these settings was then characterised using QnM AFM, and the surface profile (Figure 3.11) showed that a smooth curved surface had not been formed.

Table 3.2: Selected hatching setting parameters in the surface resolution optimisation of Nanoscribe printed structures.

	Shell Parameters		**Scaffold Parameters**		**Ra (nm) n=6**	**RMS (nm) n=6**
	Hatch Spacing	No. of Contours	Wall Spacing	Floor Spacing		
Solid	0.1 µm	20	N/A		67.9±16.6	77.0±18.1
v1	0.1 µm	20	1 µm	0.5 µm	70.7±5.8	83.4±4.6
v2	0.1 µm	10	1 µm	0.5 µm	56.4±6.2	67.1±7.1
v3	0.1 µm	10	0.2 µm	0.2 µm	64.4±8.3	73.4±8.1

The STL input hatching settings were therefore changed, to shell and scaffold mode in order to have full control on the printing parameters. Due to a bug in the updated version of the software, it was not possible to visualise the actual writing lines in the 3D preview, however the solid settings should have completely fabricated the structure with just shell contours. Therefore, in order to have a starting point, in the first variation the shell parameters were kept consistent, and large spacings for the scaffold parameters were selected, which as expected produced a similar surface roughness with an Ra of 70.7 ± 5.8 µm and 67.9 ± 16.6 µm for the shell and scaffold ridge and solid ridge respectively. As the shell parameters are the critical factor in the surface roughness and the lowest hatch spacing was already being utilised, reducing the number of contours was investigated. This successfully produced the desired smooth curve profile (Figure 3.11C) and the corresponding decrease in surface roughness. As the number of contours had been reduced, it seemed prudent to investigate the effect of changing the interior scaffold spacing in a third variation of the ridge, however this caused an increase in surface roughness to an Ra of 64.4 ± 8.3 µm and the re-emergence of deformities in the surface profile (Figure 3.11D). The ridge with v2 parameters however, had the desired well-defined shape (Figure 3.11C) and lowest surface roughness with a Ra of 56.4 ± 6.2 µm and therefore further optimisation was deemed unnecessary and these printing parameters were chosen to proceed with in all ridge morphologies.

Both of these changes in surface roughness, on initial examination seem counter-intuitive as a decrease in scaffold hatching or an increase in shell contours, should result in more polymerised voxels, and hence smaller step changes in the surface. For the number of contours, a balance is needed, as demonstrated by Takada et al[41], decreasing the voxel pitch distance beyond a certain point will have negligible improvements in surface roughness. However, the increased number of voxels provides a greater opportunity for voxels to be misaligned due to offset geometry errors[33] or affected by ambient conditions, for instance slight laser fluctuations or vibrations causing voxels to misalign creating surface roughness[41]. Also, increased lines written close to each other start to initiate “proximity effects,” due to the diffusion of radicals formed in prior illuminations[45]. This in turn can result in the

enlargement of voxels or linewidth broadening, which will impact the resultant surface finish. Likewise the scaffold is formed on the interior of the structure, however, decreasing distance between hatching lines can result in excessive heating of the resist and an auto-acceleration effect on the polymerisation rate[46], this can result in increased internal stress and uncontrolled resist polymerisation.

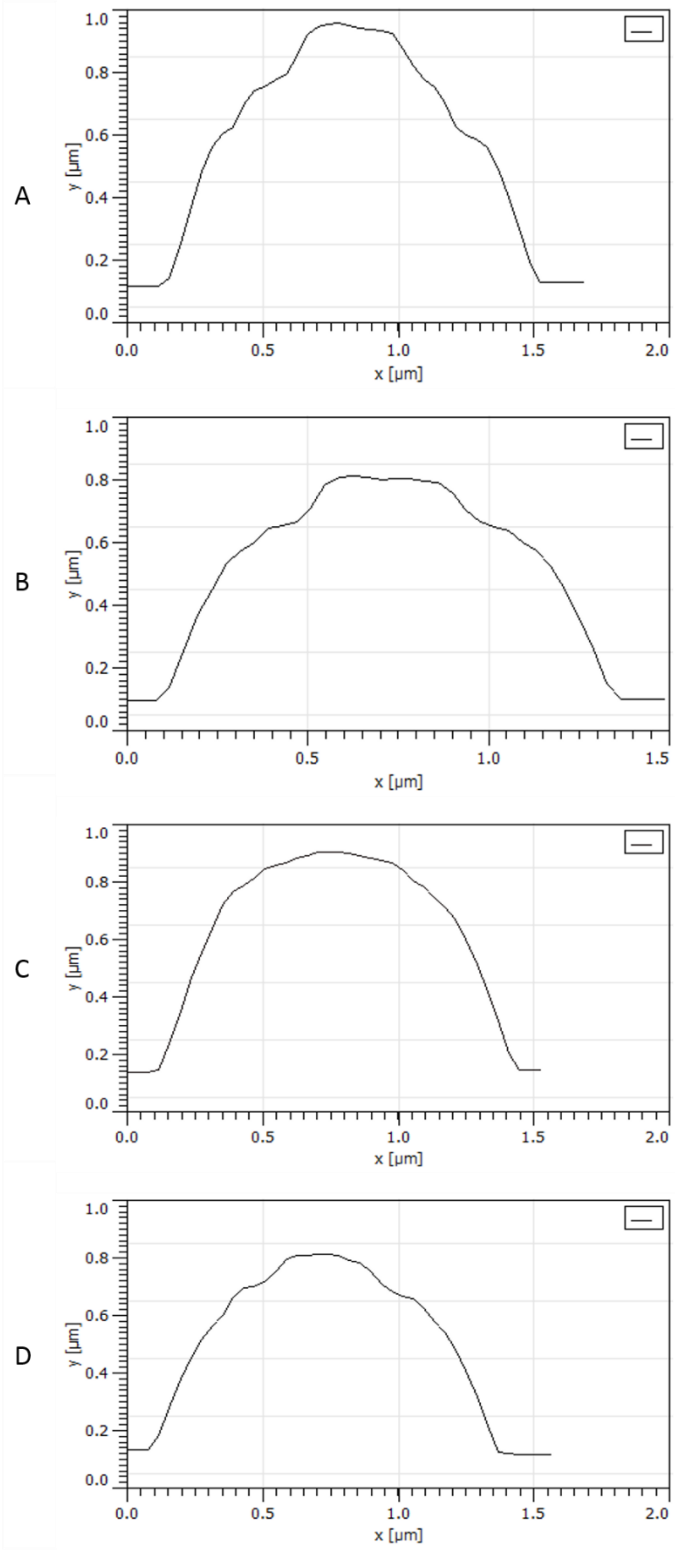


Figure 3.11: The resultant surface profiles extracted from AFM images collected of the ridges printed with differing hatching parameters, see Table 3.2 for complete parameters. A) Printed in solid hatching mode with 20 contours at 0.1 µm spacing. B) 1st iteration of the hatching parameters, produced in shell and scaffold mode with C) and D) v2 and v3 respectively.

3.5.2.2 Optimised Ridge Characteristics

In order to fully characterise the final dimensions of the TPP ridge, AFM was used to evaluate the height of the fabricated ridges, and SEM the width to overcome the effect of tip broadening seen in AFM. As seen in Figure 3.12, the height of the ridge was around 0.9 µm and the width 1.32 µm, as imaged by SEM, (Figure 3.13).

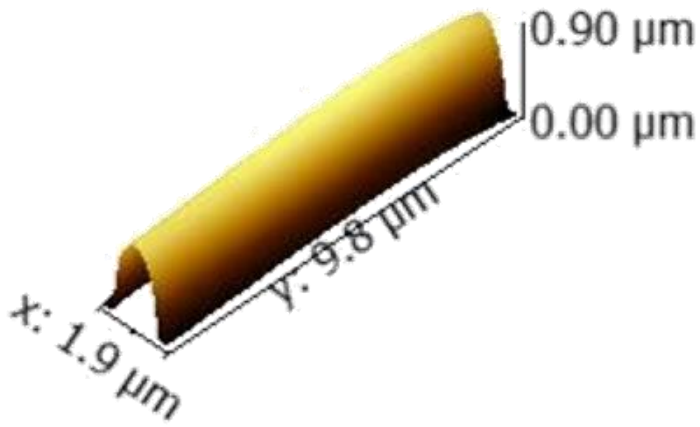


Figure 3.12: A 3D representation of an AFM image of a single TPP ridge, showing a height of 0.9 µm and a width of 1.9 µm.

3.5.2.3 Improving Printing Area

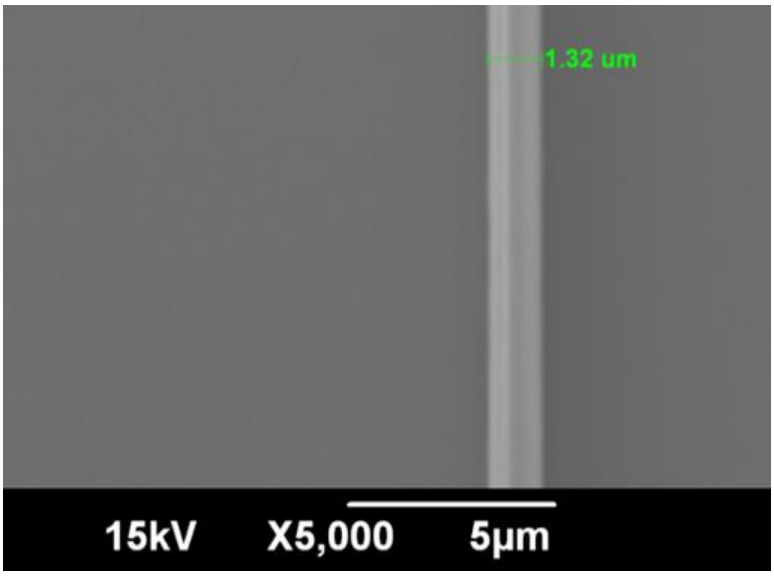


Figure 3.13: A top view of a single TPP ridge collected in SEM, showing a width of 1.32 µm.

In order to print in the PiezoScanMode, the 2D printable region must be less than 300 µm by 300 µm. However, as printing a surface requires multiple ridges with varying spaces and repeats, an extension of this area is required. The manufacturer's suggested code[29] was to print in piezo and then instruct the Nanoscribe to make a coarse movement (Appendix A: code 2) to print in an adjacent area.

When utilising this code to piezo print multiple areas, the printing run would often be incomplete. Several possible reasons were considered including a system timeout due to the length of the run or issues with the code instructing the coarse movement. The code provided by the manufacturer was meant to instruct the printer to undertake a coarse movement, which as the printing was being conducted in PiezoScanMode, would first involve a trigger for the Nanoscribe to switch from PiezoScanMode to StageScanMode. As StageScanMode is the coarse movement setting it would therefore allow the printer to move sufficient distance needed, to switch between substrate positions. However, on evaluation of the print process, I theorised that the Nanoscribe was attempting to move while in PiezoScanMode. A modification of the code was therefore introduced, manually instructing the Nanoscribe system to switch modes, and then switch back (Appendix A: code 3).

3.5.3 Challenges of Two Photon Polymerisation

As the premise of this project is to be able to generate well-defined micron scale morphologies, that can be used to reduce particle adhesion in an inhaler. It is worth considering the challenges of TPP with a consideration of the future capability to produce these morphologies at scale during manufacturing. The first and foremost challenge of TPP in this project was the lengthy time to produce the morphologies. Due to the high resolution required, PiezoScanMode was selected which is the slowest operating mode with a typical line speed of 100 µm/ second[47]. However, one ridge is sliced into ten layers, with each layer comprised of around ten 50 µm lines. Therefore, by linespeed alone each ridge should take just under a minute to print, however this is an extremely rough estimate which does not account for the time taken to stop/start polymerisation, the settling time of 300 ms between each line, or the decision regarding line speed controlled by PerfectShapeQuality which was active in the print. When all of these factors were accounted for it took closer to 5 minutes per 50 µm ridge. However, in order to print sufficient morphologies for an inhaler multiples of the chosen morphology is needed. Therefore, an additional factor must be added to account for the tilt factor correction applied before each ridge in order to ensure substrate adhesion and the find interface command. Both of which took close to ten minutes. This therefore means to produce a 50 µm by 50 µm area with 1 µm spacing took close to 8 hours. Which severely limited the scope of this project as this meant that pattern production was limited to one per week, which was extremely problematic in the early stages, where there was problems with printing reproducibility. Therefore, the use of this technique as the primary manufacturing method for even just the capsule chamber of an inhaler is not currently feasible, as it would take several months. However, as discussed in Chapter 1, AM is a rapidly progressing area and technological advances are rapidly increasing, so this does not preclude this from being surmountable in the future. However, a current suggestion could be to use the TPP morphologies for the production of various patterns to identify the optimal design to reduce particle adhesion, and then utilise this as a mould in order to scale up the manufacturing by more traditional methods.

Another challenge of using TPP, was the relative infancy of this as a technique, for instance PiezoScanMode had not been previously used in the group and there was limited experience in Nanoscribe GmbH, for this scale of two photon polymerisation, which was on the edge of instrument capability for resolution. This lack of experience and support meant attempts to optimise and troubleshoot the printing process was extremely labour intensive, and timely to solve as the project often produced previously unseen issues. As the Nanoscribe Photonic GT was also a relatively new piece of equipment, there was also issues with software bugs; as the 3D previewer did not always work and the software was updated re-defining the structure fill instructions as discussed in Section 3.5.2.1.3.

Finally, as these morphologies were producing feature sizes on the lowest end of instrument capability, small issues with the printer had significant impacts with the quality of the prints. For instance, calibration of the laser interface was performed and was out by 2 µm which resulted in multiple incomplete prints. Also, any impurities or bubbles produced by the printing process in the resist would impact the efficiency of the polymerisation and due to the micron nature of the morphologies would invariably produce a ridge deformity, resulting in the need for a re-print. However, all of these issues will become less substantial with increased TPP use and experience and with continual improvement of the technique. TPP was therefore still continued with in this project to fully explore its capabilities, but also in order to provide the ability to produce the well-defined micron scale morphologies required to gain insight into particle-surface interactions.

3.6 Chapter Conclusion

In conclusion, two photon polymerisation was selected as an appropriate additive manufacturing technique to proceed with for the fabrication of the micron scale 3D structures. This was decided upon as it provides both the capabilities to manufacture features in the desired size range, but also provides scope for complex 3D designs not available with other nano-fabrication techniques.

The printing parameters of the Nanoscribe two photon polymerisation system were then optimised successfully producing a test structure composed of a semi-circle of diameter 1 µm on a 1 x 0.5 µm rectangle. This demonstrated the capacity of the printer to create a well definer curve on a micron scale in a reproducible fashion, on a scale sufficient for the next stages of this work.

3.7 Chapter References

1. Shah, U. V. *et al.* Decoupling the contribution of dispersive and acid-base components of surface energy on the cohesion of pharmaceutical powders. *Int. J. Pharm.* **475,** 592–596 (2014).

2. Chew, N. Y. K., Tang, P., Chan, H.-K. & Raper, J. a. How Much Particle Surface Corrugation Is Sufficient to Improve Aerosol Performance of Powders? *Pharm. Res.* **22,** 148–152 (2005).

3. Behara, S. R. B., Longest, P. W., Farkas, D. R. & Hindle, M. Development and comparison of new high-efficiency dry powder inhalers for carrier-free formulations. *J. Pharm. Sci.* **103,** 465–477 (2014).

4. Behara, S. R. B., Farkas, D. R., Hindle, M. & Longest, P. W. Development of a high efficiency dry powder inhaler: Effects of capsule chamber design and inhaler surface modifications. *Pharm. Res.* **31,** 360–372 (2014).

5. Duan, B. *et al.* Three-dimensional nanocomposite scaffolds fabricated via selective laser sintering for bone tissue engineering. *Acta Biomater.* **6,** 4495–4505 (2010).

6. Bhushan, B. & Caspers, M. An overview of additive manufacturing (3D printing) for microfabrication. *Microsyst. Technol.* **23,** 1117–1124 (2017).

7. Shirazi, S. F. S. *et al.* A review on powder-based additive manufacturing for tissue engineering: selective laser sintering and inkjet 3D printing. *Sci. Technol. Adv. Mater.* **16,** 33502 (2015).

8. Kruth, J.-P., Mercelis, P., Vaerenbergh, J. Van, Froyen, L. & Rombouts, M. Binding mechanisms in selective laser sintering and selective laser melting. *Rapid Prototyp. J.* **11,** 26–36 (2005).

9. Wendel, B. *et al.* Additive processing of polymers. *Macromol. Mater. Eng.* **293,** 799–809 (2008).

10. Wong, K. V. & Hernandez, A. A Review of Additive Manufacturing. *ISRN Mech. Eng.* **2012,** (2012).

11. Kerns, J. What's the Difference Between Stereolithography and Selective Laser Sintering? *Mach. Des.* (2015). at <http://www.machinedesign.com/3d-printing/what-s-difference-between-stereolithography-and-selective-laser-sintering>

12. Gibson, I., Rosen, D. W. & Stucker, B. *Additive Manufacturing Technologies*. *Springer* (2010). doi:10.1007/978-1-4419-1120-9

13. Singh, M., Haverinen, H. M., Dhagat, P. & Jabbour, G. E. Inkjet printing-process and its applications. *Adv. Mater.* **22,** 673–85 (2010).

14. Fathi, S., Dickens, P. & Hague, R. Jetting stability of molten caprolactam in an additive inkjet manufacturing process. *Int. J. Adv. Manuf. Technol.* **59,** 201–212 (2012).

15. Derby, B. Inkjet Printing of Functional and Structural Materials: Fluid Property Requirements, Feature Stability, and Resolution. *Annu. Rev. Mater. Res.* **40,** 395–414 (2010).

16. de Gans, B.-J., Duineveld, P. C. & Schubert, U. S. Inkjet Printing of Polymers: State of the Art and Future Developments. *Adv. Mater.* **16,** 203–213 (2004).

17. Reis, N. & Derby, B. Ink Jet Deposition of Ceramic Suspensions: Modelling and Experiments of Droplet Formation. *Mater. Res. Soc.* **625,** 117–122 (2000).

18. Jang, D., Kim, D. & Moon, J. Influence of Fluid Physical Properties on Ink-Jet Printability. 2629–2635 (2009).

19. Scoutaris, N., Ross, S. & Douroumis, D. Current Trends on Medical and Pharmaceutical Applications of Inkjet Printing Technology. *Pharm. Res.* **33,** 1799–1816 (2016).

20. Perelaer, J., Schubert, U. S. & Jena, F. Inkjet Printing and Alternative Sintering

of Narrow Conductive Tracks on Flexible Substrates for Plastic Electronic Applications. (2010).

21. Uddin, M. J. *et al.* Inkjet printing of transdermal microneedles for the delivery of anticancer agents. *Int. J. Pharm.* **494,** 593–602 (2015).

22. Scoutaris, N., Alexander, M. R., Gellert, P. R. & Roberts, C. J. Inkjet printing as a novel medicine formulation technique. *J. Control. Release* **156,** 179–85 (2011).

23. Chua, C. K. & Leong, K. F. in *3D Print. Addit. Manuf.* 37–107 (WORLD SCIENTIFIC, 2017). doi:10.1142/9789813149274_0003

24. Barclift, M. W. & Williams, C. B. Examining Variability in the Mechanical Properties of Parts Manufactured Via Polyjet Direct 3D Printing. *Int. Solid Free. Fabr. Symp.* 876–890 (2012). doi:10.1017/CBO9781107415324.004

25. Singh, R. Process capability study of polyjet printing for plastic components. *Evol. Ecol.* **25,** 1011–1015 (2011).

26. Manuafacturing, S. D. PolyJet: 3D Printing. at <https://www.youtube.com/watch?v=kbiIdTVz6bA&index=11&list=WL&t=31s>

27. Nanoscribe. 3D µ-printing by Direct Laser Writing. (2014).

28. Keyence. Surface Roughness Parameters. at <https://www.keyence.com/ss/products/microscope/roughness/line/parameters.jsp>

29. Spangenberg, A. *et al. Updates in Advanced Lithography*. (InTech, 2013). doi:10.5772/3348

30. Sun, H.-B. *et al.* Real three-dimensional microstructures fabricated by photopolymerization of resins through two-photon absorption. *Opt. Lett.* **25,** 1110 (2000).

31. Maruo, S. & Fourkas, J. T. Recent progress in multiphoton microfabrication. *Laser Photonics Rev.* **2,** 100–111 (2008).

32. Nanoscribe. *Nanoscribe Photonic Professional (GT) User Manual*. (2015).

33. Zhou, X., Hou, Y. & Lin, J. A review on the processing accuracy of two-photon polymerization. *AIP Adv.* **5,** (2015).

34. Kurselis, K., Kiyan, R., Bagratashvili, V. N., Popov, V. K. & Chichkov, B. N. 3D fabrication of all-polymer conductive microstructures by two photon polymerization. *Opt. Express* **21,** 31029–35 (2013).

35. Qi, F., Li, Y., Guo, H., Yang, H. & Gong, Q. Wavy lines in two-photon photopolymerization microfabrication. *Opt. Express* **12,** 4725–4730 (2004).

36. Sun, H.-B., Tanaka, T. & Kawata, S. Three-dimensional focal spots related to two-photon excitation. *Appl. Phys. Lett.* **80,** 3673–3675 (2002).

37. Li, J. (Tampere U. of T. Nanofabrication by three - dimensional lithography. (2015).

38. LaFratta, C. N., Fourkas, J. T., Baldacchini, T. & Farrer, R. A. Multiphoton Fabrication. *Angew. Chemie Int. Ed.* **46,** 6238–6258 (2007).

39. Power, M. & Yang, G.-Z. Optomechanical force estimation using passive micromanipulator end-effectors. in *2016 Int. Conf. Manip. Autom. Robot. Small Scales* 1–5 (IEEE, 2016). doi:10.1109/MARSS.2016.7561745

40. Gissibl, T., Thiele, S., Herkommer, A. & Giessen, H. Two-photon direct laser writing of ultracompact multi-lens objectives. *Nat. Photonics* **10,** 554–560 (2016).

41. Takada, K., Sun, H.-B. & Kawata, S. Improved spatial resolution and surface roughness in photopolymerization-based laser nanowriting. *Appl. Phys. Lett.* **86,** 71122 (2005).

42. Kawata, S., Sun, H. B., Tanaka, T. & Takada, K. Finer features for functional

microdevices. *Nature* **412,** 697–698 (2001).

43. Zipfel, W. R., Williams, R. M. & Webb, W. W. Nonlinear magic: multiphoton microscopy in the biosciences. *Nat. Biotechnol.* **21,** 1369–1377 (2003).

44. Olsen, M. H. Two-photon polymerization of immune cell scaffolds. (2013).

45. Waller, E. & von Freymann, G. Spatio-Temporal Proximity Characteristics in 3D µ-Printing via Multi-Photon Absorption. *Polymers (Basel).* **8,** 297 (2016).

46. Watts, D. C. Reaction kinetics and mechanics in photo-polymerised networks. *Dent. Mater.* **21,** 27–35 (2005).

47. Baldacchini, T. *Three-dimensional microfabrication using two-photon polymerization : fundamentals, technology, and applications*. (2016).

4 Evaluation of Single Particle Adhesion to Printed Morphologies

4.1 Introduction

As discussed in Chapter 1, the interactions between a particle and a surface is complex, and is based on a wide variety of factors. Surface roughness is well known to be significant in the particle adhesion to a surface. Small scale roughness can reduce the effective particle-surface contact area, resulting in a reduction of adhesion. However, larger scale roughness, can result in entrapment or mechanical interlocking of a particle with a surface and so dramatically increase particle-surface adhesion[1]. To fully elucidate the effect of surface roughness, on particle adhesion, the morphology of the surface must be modified independently from other factors which affect adhesion. However, this is extremely difficult, as changing the surface roughness, also often results in changes of other parameters like surface free energy.

Therefore, to gain a deeper insight into the effect of morphology on the particle-surface interaction, this chapter will describe a systematic variation of surface roughness, by producing a variety of TPP well-defined micron scale morphologies. As discussed in Chapter 1, the surface energy of a material, plays a key role in the adhesion between two interacting bodies. The molecules present on the surface of a material, have fewer neighbouring molecules, however this increases the cohesiveness and adhesiveness of a particle or surface as they will try to bind to energetically favourable surfaces[2]. Therefore, any variation in the material on the surface will have a direct impact on the particle -surface adhesion. As the varying morphologies are created by producing TPP ridges on a glass substrate, there is a variation in surface chemistry which could impact on the particle adhesion recorded. In order to mitigate this effect, and effectively isolate out the effect of surface morphology on particle-surface adhesion a consistent surface chemistry will be applied, using plasma polymerisation, over these morphologies without significantly altering the surface roughness. These coated surfaces will then be tested against

different particle types on a single particle basis using colloidal probe microscopy. Atomic force microscopy (AFM) force-curves were collected and analysed to elucidate the effect of surface morphology for different particle types.

4.1.1 Zeta Profilometry

Zeta Optical Profilometry was performed using a Zeta 20 true colour 3D optical profiler. This technique produces a 3D representation of surface morphology using a technique called confocal grid structured array illumination. This utilises aspects of a range of techniques including; confocal microscopy, white light interferometry, focus detection and pattern projection.

4.1.1.1 Confocal Microscopy

Confocal microscopy works by isolating individual focal planes of a substrate being imaged. It achieves this by shining a light through an aperture and an initial pin hole to focus the light on a specific area[3], which on reflection passes through a second pin hole in the focal position. Therefore, only light in the focal plane, reaches the detector (Figure 4.1). An overview of a surface can then be generated by collecting the reflected intensity data across a surface at varying focus heights and stitching together the images to generate topographical information.

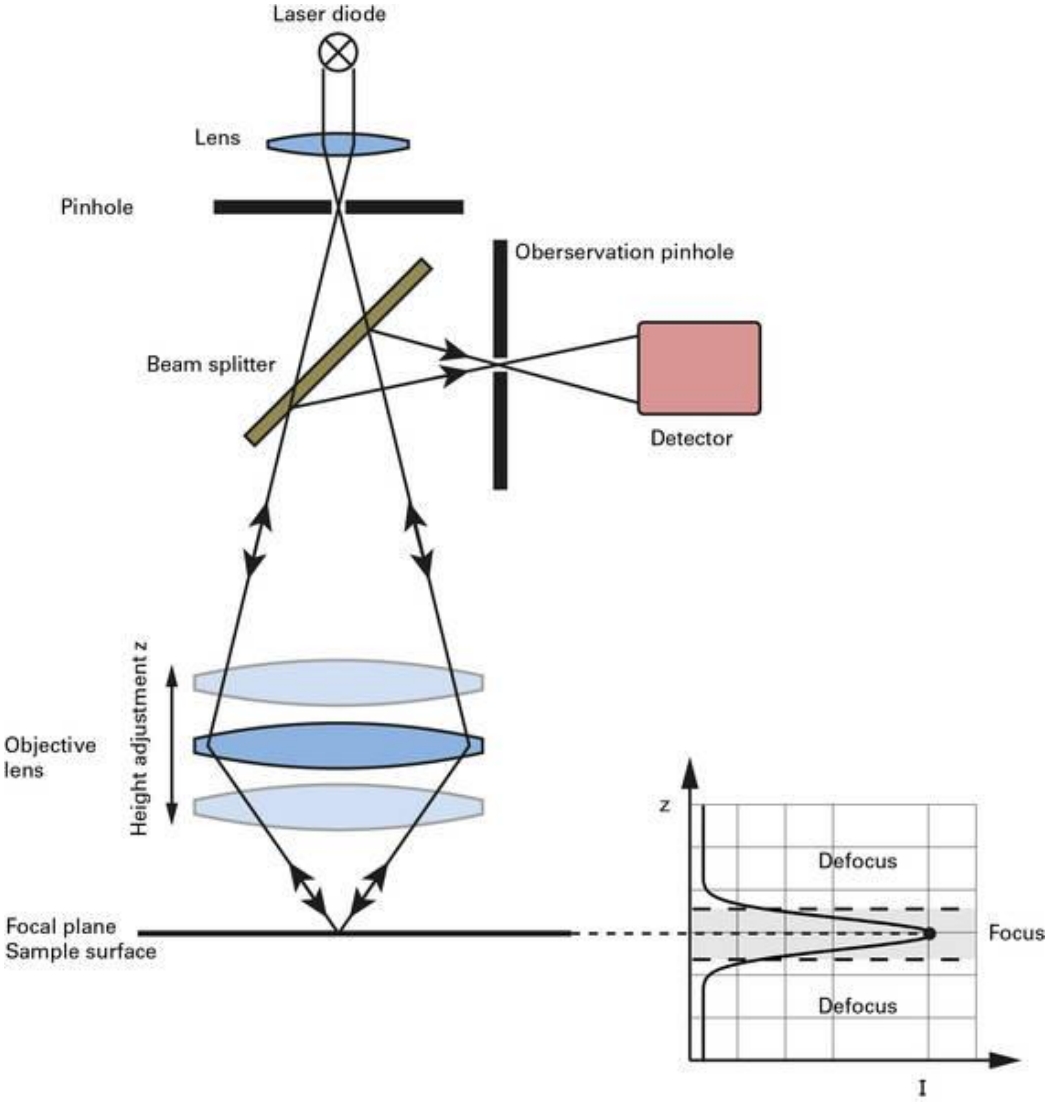


Figure 4.1: Schematic of the principles of confocal microscopy. A beam of light is focused on the surface using an aperture through an initial pinhole, on reflection from the surface this is then passed through a second confocal pinhole, so only light reflected from the focal plane under investigation reaches the detector. As the scan height is adjusted varying levels of the surface will come into focus and will be imaged. These focal images can then be stitched together to form a topographical image. Picture from[4]

4.1.1.2 White Light Interferometry

White light interferometry is a technique based on the principles established in the Michelson interferometer. A coherent light source is split with a beam splitter, yielding two coherent beams. If one beam is directed at a reference sample of a known distance and the other the sample being analysed, on recombination, the difference in distance travelled can be calculated based on the interference pattern generated[5]. If the two beams are in phase their intensities will combine in

constructive interference and a greater intensity will be seen as a bright spot. If the beams have travelled different distances the beams will be out of phase. If they are 180^{o} out of phase they will in effect cancel each other out, by destructive interference and a dark spot will be observed[6]. These spots or pixels are therefore collected across the sample being evaluated, and the relative heights of the surface can be calculated based on the received interference patterns.

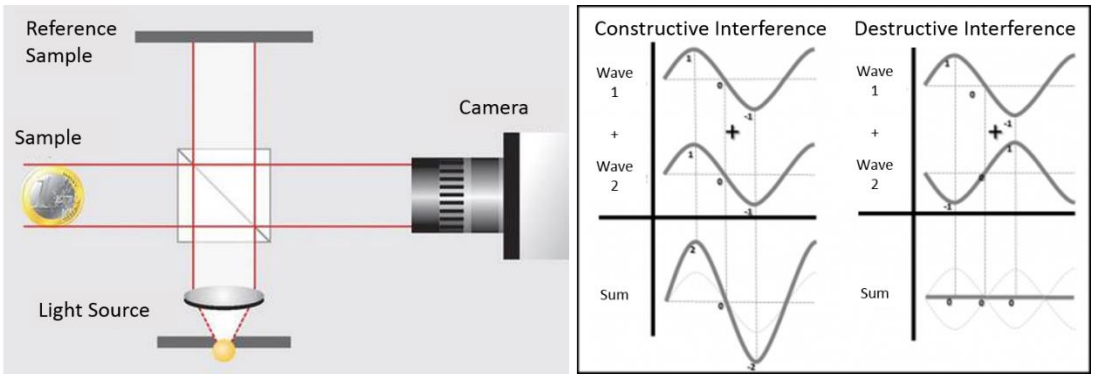


Figure 4.2: A schematic of the principles of Interferometry. A coherent beam of light is split between a sample surface and a reference surface, the reflected light is then recombined, and the interference pattern is evaluated, if the two beams are in phase the intensities will be combined and a bright spot will be seen, if however there is a difference in the distance the two beams have travelled the beams will be out of phase and destructive interference will be seen. Picture adapted from[6,7]

4.1.1.3 Pattern Projection with Focus Detection

Focus Detection software functions by evaluating an in and out of focus signal based on contrast. However, this approach has relatively poor resolution as it is difficult to determine if a feature is in focus. To improve the resolution, a pattern can be projected onto the surface, which is only seen to be in focus at a specific distance.

4.1.1.4 Zeta Optical Profilometry Technology

The Zeta 20, utilises confocal techniques to capture multiple focal plane slices of a surface being evaluated. For each focal plane, it generates an image of the topography in focus using an interferometric pattern, ZDots, which is projected onto the surface. By comparing the pattern reflected off the surface with the known

design, the focus of each topography point on the sample surface can be assessed and the relative heights calculated. These slices are then stitched together to generate the 3D topography of a sample surface.

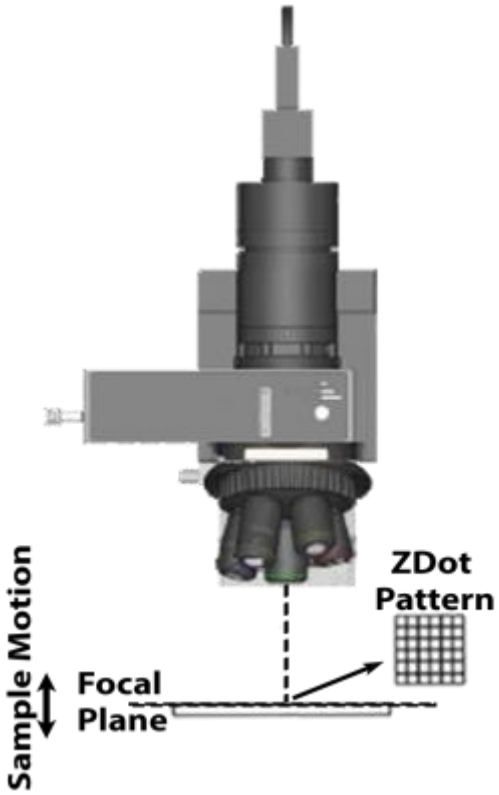


Figure 4.3: An overview of the Zeta 20 Optical Profilometer, the sample is evaluated as a series of focal plane slices. At each focal plane, the ZDots interferometric pattern is projected on the surface and areas in focus can be determined based on evaluation of the distortion of the pattern. Picture from[8]

4.1.2 Plasma Polymerisation

Plasma polymerisation involves the deposition of a polymer based on a radical poly-recombination polymerisation reaction that is initiated in ionised gases. The monomer to be polymerised is introduced in a gaseous form to the plasma reactor. By applying energy across the system, usually in the form of an electric voltage, a collection of charged particles (plasma), but with an overall net electrical neutrality is maintained[9].

The plasma is generated in a low pressure system (10^{-2} - 10^{2} Torr) between two conductive electrodes. The applied voltage, results in the acceleration of free electrons in the gas, which in turn collides with other reaction species in the gas causing; ionisation, radical generation, fragmentation, recombination and molecule excitation[10]. This can result in the production of further free electrons and so a collision cascade is produced. The energy applied to the electrons in the excited molecule, can then be lost either by collision with another species or by the drop of the electron back to the ground state, resulting in the excitation energy emitted as UV-visible photons, which creates a plasma discharge glow.

As the negatively charged free electrons are highly mobile they are lost in a greater number than the positive ions to the surface. This creates a negative charge on the surface, attracting the positively charged heavier ions, which are then deposited[9]. This results in a uniform plasma polymer coating depositing on the substrate. This ion flux is then maintained by the application of an RF frequency, for the duration of the polymerisation.

Plasma polymerisation therefore encompasses the coating or film obtained from the fragmentation of the monomer, creating reactive species. The majority of radicals formed are created either by; hydrogen abstraction or breakage of C-C-bonds[11]. This leads to the creation of activated species that can contain more than one radical. These reactive species are then propagated and recombined in a multitude of combinations (Figure 4.4) forming a highly cross-linked, variable structured polymer on the substrate. The plasma polymerisation mechanism proceeds on two fronts; with monoradicals (M·) formed and recombined in a similar manner to standard radical polymerisation and diradicals (·M·) with two radicals[12].

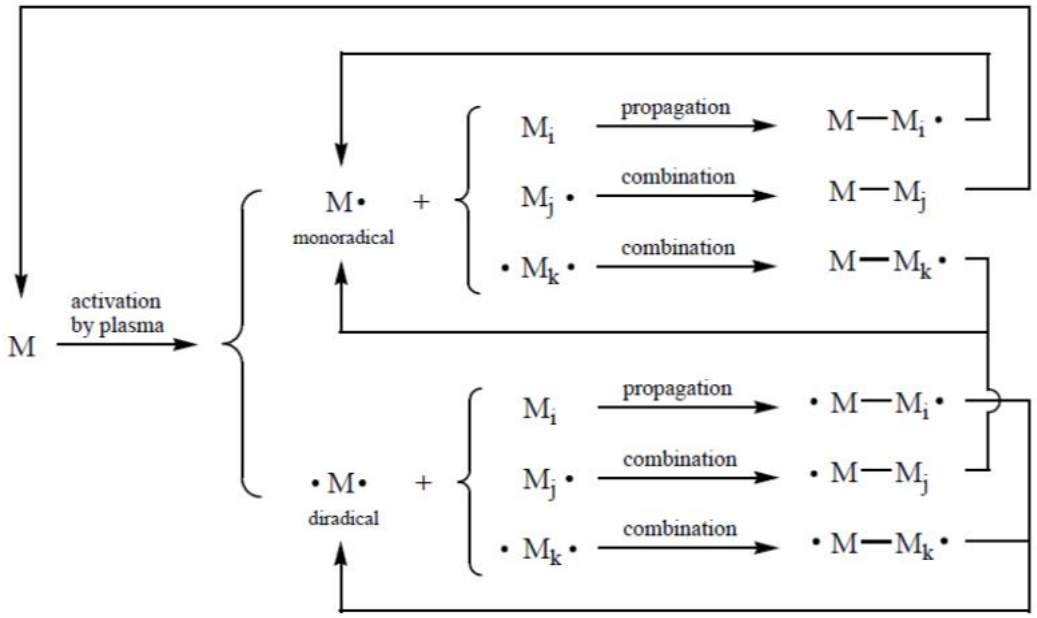


Figure 4.4: Schematic of the multitude of propagation and recombination mechanisms in plasma polymerisation. This shows the upper cycle formed from monoradicals and the lower cycle from diradicals. Picture adapted from[9,12].

As the plasma is deposited based on the attraction of positive ions to the negatively charged substrate it is often used to change the surface chemistry of a substrate, and most importantly achieves this without altering the bulk properties of the substrate itself.

As discussed in Chapter 1, there are other methods to generate a different surface chemistry, like silanization or spin coating. Of relevance and an advantage to this project is that plasma polymerisation produces a coating with a very low surface roughness and deposits evenly over complex 3D morphologies[13] and the substrate surface. As the main polymerisation mechanism, is via radical propagation a wide variety of monomers can be used in plasma polymerisation allowing the tuning of a range of different surface chemistries[11]. For the production of a consistent surface chemistry, in order to isolate the effect of surface morphology on particle adhesion, this technique will be used in this project.

4.2 Chapter Aims

To produce a series of samples with controllable well-defined TPP morphologies that can be used to assess the effect of surface morphology in isolation from surface chemistry. These can then be evaluated for their adhesion to differing particle types to gain valuable insight into the effect of surface morphology on particle adhesion.

4.3 Chapter Objectives

- To produce a variety of well-defined surface morphologies on the micron scale, using the TPP methodology established in Chapter 3.
- To create a consistent and well-defined surface energy and chemistry, without alteration of the printed morphology.
- To assess the effect of changing morphology on particle adhesion using colloidal probe microscopy on the TPP printed substrates.

4.4 Materials and Methods

4.4.1 Materials

All photoresists and solvents were used as sourced. The UV curable photoresist IP-L 780 was obtained from Nanoscribe GmbH, Germany. All monomers for plasma polymerisation, polystyrene beads for CPM and solvents were obtained from Sigma-Aldrich. All atomic force microscopy (AFM) probes were purchased from Bruker (Cambridge, UK). Respitose SV003 particles were supplied by AstraZeneca, having been purchased from DFE Pharma, Goch, Germany.

4.4.2 Two Photon Polymerisation

Two Photon Polymerisation (TPP) was undertaken as outlined in Chapter 3. Briefly, TPP ridges were polymerised on the glass surface using the Piezo printing mode, with a laser power of 30 mW and power scaling of 0.85. For optimal surface feature resolution and shape quality, a path optimisation feature was used. In order to import the STL file into the software, a slicing thickness setting of adaptive was used, with a minimum slicing distance of 0.1 µm and maximum of 0.3 µm. The shell settings consisted of a hatching distance of 0.1 µm with 10 contours. The scaffold settings chosen were wall spacing of 1 µm and floor spacing of 0.5 µm with a base slice count of 1.

4.4.3 TPP Morphology Characterisation

4.4.3.1 Atomic Force Microscopy

AFM both in tapping and quantitative nanomechanical measurements (QnM) mode has been used to characterise the geometries produced. A Bruker Dimension 3000 SPM system was used to undertake tapping AFM measurements and a FastScan Bio Icon AFM (Bruker) was used for both tapping and QnM measurements. Bruker RTESPA-300 Antimony doped Silicon tips were used with spring constants of around

40 N/m and resonant frequencies of 320 kHz. Gwyddion software (version 2.22) (Czech Metrology Institute, Brno) was used for image analysis.

4.4.3.2 Zeta Optical Profilometry

A Zeta-20 Optical profilometer (Zeta Instruments, CA, USA) was used to capture 2D and 3D images of the structures and to evaluate ridge spacing and heights, using 100x magnification with 0.013 µm step size.

4.4.4 Plasma Polymerisation

Plasma polymerisation coating was used to produce a consistent chemistry and surface energy. Briefly, the custom built reactor consists of two circular electrodes with 12.5 cm spacing encased in a cylindrical reactor (35 cm high, 17 cm diameter) connected to a 13.56 MHz radio frequency power source (Coaxial Power System Ltd.) to initiate the plasma. Before each polymerisation run, two to three freeze-thaw cycles were performed to degas the monomer. In addition to surface morphology, there was an interest in evaluating the effect of a hydrophobic or hydrophilic surface chemistry on particle-surface interactions of differing morphologies. Two monomers were chosen to represent the differing extremes with a plasma polymerised hexane (ppHex) coating as a hydrophobic control and a plasma polymerised acrylic acid (ppAAc) coating as a hydrophilic control. A plasma of either hexane or acrylic acid was then generated using a power of 50W and an initial monomer pressure of 300 mTorr until a deposition of 0.4 kÅ was reached as measured by the in-built quartz crystal microbalance (Leica). However, when progressing to adhesion measurements, due to time constraints, only one chemistry was progressed. ppHex was used for the production of a plasma polymerised coating on TPP ridges as due to its hydrophobic nature, it possesses a lower surface free energy and so a lower surface adhesion. For these plasma polymerisation experiments a separate control glass coverslip was coated simultaneously to verify successful coating by Water Contact Angle (WCA). Post-polymerisation the monomer was allowed to flow

through the reactor for a further 5 minutes to allow any highly reactive radicals remaining on the surface to react with monomer instead of oxygen from the air.

4.4.5 Characterisation of the Plasma Polymerisation Coating

4.4.5.1 Water Contact Angle Measurements

WCA measurements were carried out on a CAM200 (KSV Instrument Ltd., Finland), an optical contact angle meter. The deposited drop shape was captured on the surface of interest for 10 frames with 1 second intervals. The contact angle was then calculated using a Young Laplace fitting, using the second recorded frame of the drop on the surface. To evaluate the coating of the control and non-printed coated surfaces, average contact angle values were obtained from three area triplicates on four different surfaces. Three WCA measurements were collected for each control to verify the uniformity of the TPP printed substrate plasma polymerised coating.

4.4.5.2 Ellipsometry

Plasma polymerised coatings were applied on a silicon wafer and the thicknesses were estimated using an alpha-SE spectroscopic ellipsometer (J. A. Woollam Co, Lincoln, US). A Cauchy film layer with default parameters was used to model the coating. The silicon substrate and Cauchy layer parameters were fixed, whereas film thickness was turned on as a fit parameter.

4.4.5.3 Scanning Electron Microscopy

Scanning Electron Microscopy (SEM) images were captured of the coating using the JSM-6490 LV (JEOL). The samples were loaded unto aluminium stubs with carbon tabs pre-fixed. In order to prevent charge build up sampled were then coated with gold coated using an SCD 030 Blazers sputter coater for 2 minutes at 30 mA. Images were then collected using the secondary electron imaging setting.

4.4.5.4 Time of flight- Secondary Ion Mass Spectrometry

Measurements were performed by Dr David Scurr for the non-printed control and Jatin Mistry for the TPP ridge coat using a TOF-SIMS IV (ION-TOF GMBH). The primary ion source was operated in high current bunched mode with a pulse width of 10.2ns and was composed of Bi^{3+} ions, on random raster mode to prevent charge build up. Positive and Negative ion spectra were obtained, with a 256 x 256 pixel resolution with 15 frames per patch. Analysis was performed using IonSpec and Ion Image (version 4.1) software (ION-TOF, Münster, Germany).

4.4.6 Colloidal Probe Microscopy

4.4.6.1 Production of Colloidal Probes

Production of colloidal probes was outlined in Chapter 2. Briefly, AFM tipless V-shaped cantilevers, were calibrated using the thermal tune method, the spring constants of the nine cantilevers used were calculated as 0.58 – 0.83 N/m. Three of each type of colloidal probe particle were attached using epoxy resin. Cantilevers were modified with either 10 µm or 5 µm polystyrene bead (Sigma-Aldrich, Dorset, UK) or a Respitose SV003 particle (DFE Pharma, Goch, Germany). Particles were attached using a MMAFM-2 Multimode AFM system (BrukerNano, Coventry, UK). Epoxy resin was dotted onto a silicon wafer and spread into thin lines using a sacrificial probe. The silicon nitride tipless cantilever (MLCT-010 A, Bruker) to be functionalised was then lowered until visual contact with the glue, and then withdrawn. This cantilever was then moved to an area with the powder, and aligned with an isolated particle. The cantilever was then lowered manually onto the particle for attachment. After particle attachment, the suitability of the colloidal probe for use was established using reverse tip imaging by AFM, low vacuum SEM and Zeta optical profilometry. The colloidal probes were evaluated for morphological changes before and after every force-volume mapping.

4.4.6.2 Tip Imaging

SEM imaging of colloidal probes was as discussed in Chapter 2, but briefly a square of silica gel was mounted on an SEM stub using a carbon disc. This was then coated with gold, using an SCD 030 (Balzers Union) sputter coater for 2 minutes at 30 mA, post coating an AFM tip, with particle attached, was placed on the silica gel for SEM imaging. The imaging conditions used were low vacuum mode at 50 Pa, using 20kV and a spot size of 50 nm. Initial images of each of the particles used are shown in Figure 4.5. It can be seen in Figure 4.5 A that in general the 10 µm polystyrene particles are of the expected size, and possess a smooth spherical shape. They are also well positioned on the tip of the AFM cantilever in the centre. Occasionally, small protrusions can be seen on the particle, especially the top particle, which could affect the particle-surface adhesion interactions if it contacts with the surface. The AFM tips functionalised by the 5 µm polystyrene particles can be seen in Figure 4.5 B. As discussed in Chapter 2, uncoated SEM suffers with significant charging issues, and although imaging in low vacuum mitigates some of this problem there is a sacrifice of resolution. As these samples are uncoated, the particles are on the edge of the resolution achievable by the SEM, and so successful attachment and the quality of the particle surface was verified using Zeta profilometry. In an attempt to reduce the charging present and to provide the clearest image possible, for the bottom two particles the brightness setting was turned right down. The contrast issues was probably worse on these two particles in comparison to the top particle as there is a significant amount of glue surrounding the contact point between particle and AFM tip, which possessed appreciable charging, obscuring the particle. This extraneous glue, however is absent on the top particle, which is why the image is clearer. However, it can be seen that the head of the particle is clear of the glue in all three images, displaying their suitability for use. Finally, Figure 4.5 C shows the three Respitose SV003 particles, which all are suitably positioned and possess a range of shapes and surface asperities.

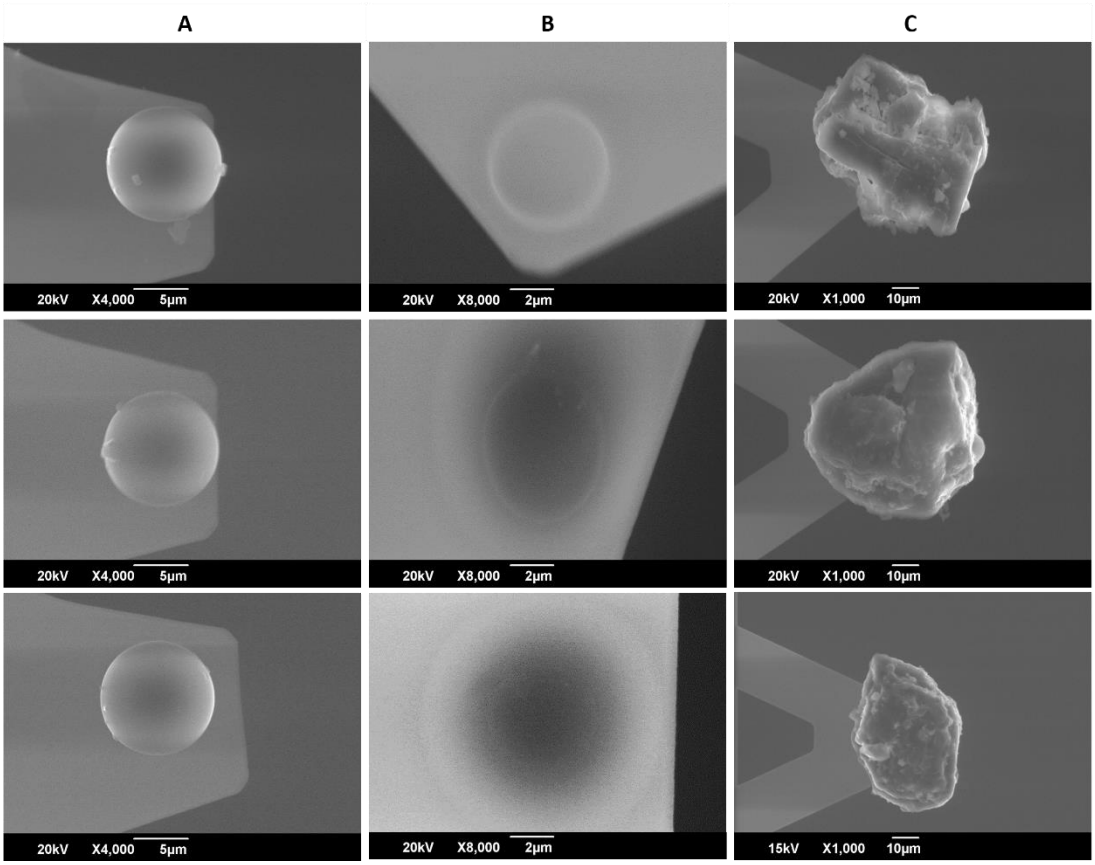


Figure 4.5: Initial SEM images of the particles used for colloidal probe microscopy. A) Polystyrene 10 µm beads, B) Polystyrene 5 µm beads and C) Respitose SV003 particles.

4.4.6.3 AFM Reverse Tip Imaging

The tips were reverse imaged as discussed in Chapter 2. Briefly, the probes were imaged using a tip characterisation grating (TGT01, NT-MDT, Moscow), resulting in an AFM artefact, producing an inversion of the imaging process, generating a topography map as an array of images of the particle surface. A second image is then collected focusing on just one of the repeat images, to allow a higher resolution image which can be used for contact area analysis.

4.4.6.4 Zeta Optical Profilometry

In order to verify the particle attachment of the polystyrene 5 µm bead, which was difficult to resolve in low vacuum SEM. Zeta images were collected as discussed in Section 4.4.3.2.

4.4.6.5 Force-Volume Measurements – Non-printed Substrates

Adhesion measurements were recorded using the auto ramp mode, which collects a series of force-curves in an array over the scan area. These force-curves were gathered on an Enviroscope AFM (BrukerNano), fitted with a Triton humidity controller. 100 images and force-curves were recorded for each of three 10 x 10 µm areas, at RH 10%, for each non-printed plasma polymerised coated substrate, using each colloidal probe particle type prepared in Section 4.4.6.1. The ramp rate for the force-curves was set to 0.93 Hz. In order to convert the photodiode signal to distance the deflection sensitivity must be calculated to add to the piezo position. To achieve this 25 force curves were collected over a 2.5 x 2.5 µm area on acetone cleaned silicon wafers. The deflection sensitivity can then be calculated using the gradient of the "constant compliance" region of the obtained force-curves[14]. Using Hook's law the force acting on the cantilever can be calculated by multiplying the deflection and spring constant together, and force-distance curves could be plotted. These were then normalised for contact area of each individual particle.

4.4.6.6 Force-Volume Measurements – TPP-printed Substrates

The TPP printed pattern was positioned so the ridges were perpendicular to the traverse direction of the colloidal probe. Adhesion measurements were recorded using the auto ramp mode, with one scan area including TPP printed ridges of a certain height with three differing spacings; 1 µm, 3 µm and 8 µm. Force-curves were then collected using three polystyrene 10 µm beads, polystyrene 5 µm beads and Respitose SV003 particles on the 1 µm and 3 µm high ridges. For the 5 µm high ridges, one of each particle type was tested against the ridges, but the polystyrene 5 µm bead lost contact with the sample during the 8 µm spacing, this is likely because it

was unable to reach the substrate past the tall ridges, further scans were therefore not pursued for this particle type and this particle-height-spacing combination was excluded from analysis. Due to time constraints the Respitose SV003 particle was also not pursued further, so only the polystyrene 10 µm bead had a triplicate of particles tested on the 5 µm high ridges. These force-curves were gathered on an Enviroscope AFM (BrukerNano), fitted with a Triton humidity controller at RH 10%. An area of 60 µm by 10 µm was evaluated, with measurements recorded every 200 nm on the X axis and every micron on the Y axis, producing a total of 3000 force-curves per scan area. Post scan, the coverage of all three spacings was established and if misaligned a second scan was undertaken to ensure a sufficient data set of each combination, all force-curves from both scans were analysed and included in the analysis. The ramp rate for the force-curves was set to 0.93 Hz. The deflection sensitivity was calculated from the compliance region of 25 force curves, collected over a 2.5 x 2.5 µm area, on acetone cleaned silicon wafers. For each set of TPP ridges evaluated, 100 force-curves were collected on three control areas of non-printed ppHex coated substrate in the surrounding area of the ridges.

4.4.6.7 Force-Curve Analysis

Force-curves were then processed using an in-house macro, produced by Dr Xinyong Chen. The force of adhesion was then calculated by the multiplication of the displacement of the cantilever required to pull-off the surface by the cantilever's spring constant. If the force of adhesion between the colloidal probe and the surface is too high, it may exceed the range recorded by the AFM and a truncated graph is seen (Figure 4.6). For these force-curves an extrapolation was conducted using the slope of the contact area of that particular force curve and the jump off position.

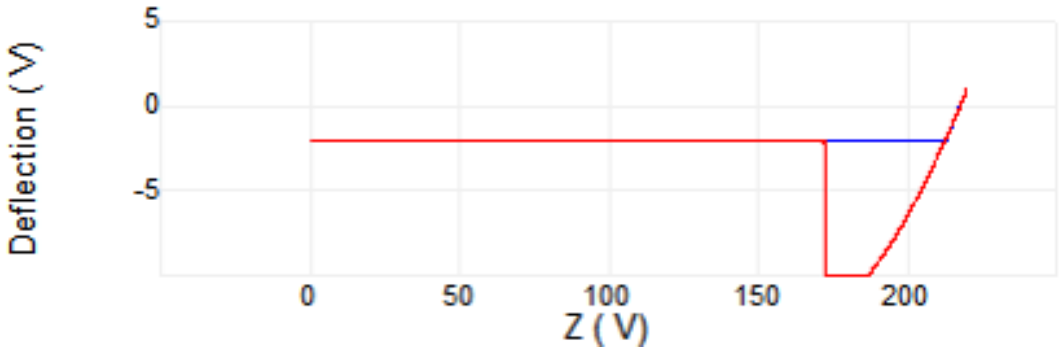


Figure 4.6: An example of a truncated force-curve recorded between a polystyrene 10 µm bead and the TPP morphologies.

For the TPP printed substrates, force-curves for each scan area were first compiled, and the Z height and maximum adhesion force were exported. A histogram of all the force-curves collected for each particle type on each ridge height with all three spacings were plotted in excel. The total count was normalised to account for the differential in scans conducted (due to misalignment or number of particle used). Forces of adhesion were not normalised for particle contact area, as this is likely to change based on the position of the imaging particle on the ridge and the number of ridges contacting with the particle. To gain a greater insight into how the adhesion varied over the morphologies; topographical images and their respective adhesion maps were plotted for each scan, using Origin 2017 (OriginLab, Massachusetts) by Prof. Phil Williams.

To evaluate the effect of ridge height and spacing on particle adhesion in isolation, each scan was divided into three sections based on the topography map, with a border region excluded of 1 ridge to ensure all force-curved recorded in each zone were associated with that ridge height-spacing. Finally, average height and adhesion profiles over each scan area were compiled and plotted in Origin 2017 by Prof. Phil Williams.

4.4.6.8 Statistical Analysis

Statistical significance between the particle adhesion on different ridge heights and spacing was carried out using a one-way ANOVA with a Tukey's post hoc analysis at a p-value of 0.05 using GraphPad Prism. For any data sets with only two groups, an unpaired t-test was used for statistical analysis.

4.5 Results and Discussion

4.5.1 Production of varying morphologies

To assess the effect of morphology on particle adhesion, a series of well-defined micron scale morphologies were created. The morphology had to be modified in a controllable way, it was decided to continue with the initial test structure designed in Chapter 3. As discussed in Chapter 1, there are differing types of surface roughness, and they have different effects on adhesion. Therefore, in order to fully evaluate this, it was decided that the surface morphology variation would include a change in ridge height, while keeping the diameter the same, and to vary the spacing between a series of ridges. These were chosen, as increasing the ridge spacing varies the contact areas between particle and surface, with larger spacing allowing the particle to contact with the surface between ridges, as this decreases, there might be an increase of contact area if the particle is in contact with both ridges at the same time. Ever decreasing ridge spacing and the particle will be unable to reach the bottom surface, likely reducing the particle adhesion to the surface. Increasing the ridge height provides a different insight, as the diameter of the ridges are kept consistent, the aspect ratio of the ridge changes, so the ridge top possesses steeper sides. Secondly, if the spacing between the ridges is sufficient, changing the ridge height may also, affect the effective contact area between particle and the side of the ridge. This allows an insight into the effect of changing wide ranging aspects of particle-surface interactions based on morphology, providing effective “larger scale roughness” and “smaller scale roughness” and therefore hopefully will allow a greater understanding of this area.

4.5.1.1 Producing different ridge heights

To modify the height, the original CAD file was altered to change the aspect ratio of the TPP ridges, to produce ridges of three differing design heights; 1 µm, 3 µm and 5 µm. This range of ridge heights were successfully printed, several cross-sections were captured across the length of the ridge by the Zeta Optical Profilometer, the ridges were then also imaged by AFM with the 2D and 3D images generated. The 1 µm

ridges can be seen in Figure 4.7, the 3 µm ridges in Figure 4.8, and the 5 µm ridges in Figure 4.9. From the AFM images, it can be seen that the 5 µm ridges appear slightly taller than the expected 5 µm (Figure 4.9B+C), this could be due the increased polymerisation needed to produce a bigger structure which may have increased the off-target polymerisation. Nevertheless, all three height of ridges showed similar profiles with good surface resolution and so these were deemed acceptable to proceed with.

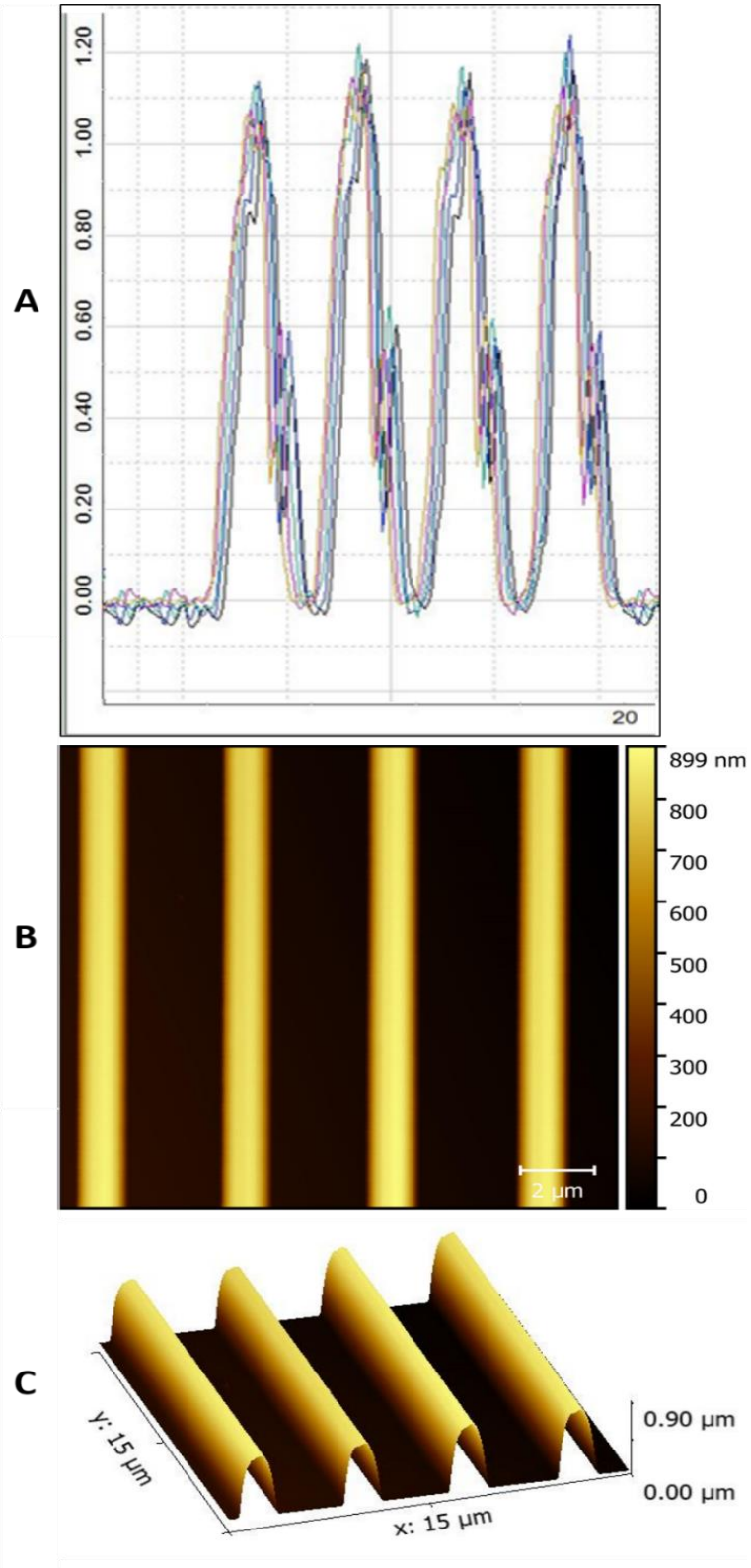


Figure 4.7: A series of TPP 1 um high ridges shown by A) Zeta Profilometry with multiple cross-sections over the 50 µm long ridge displayed and then by AFM as a B) 2D image and C) in the 3D representation.

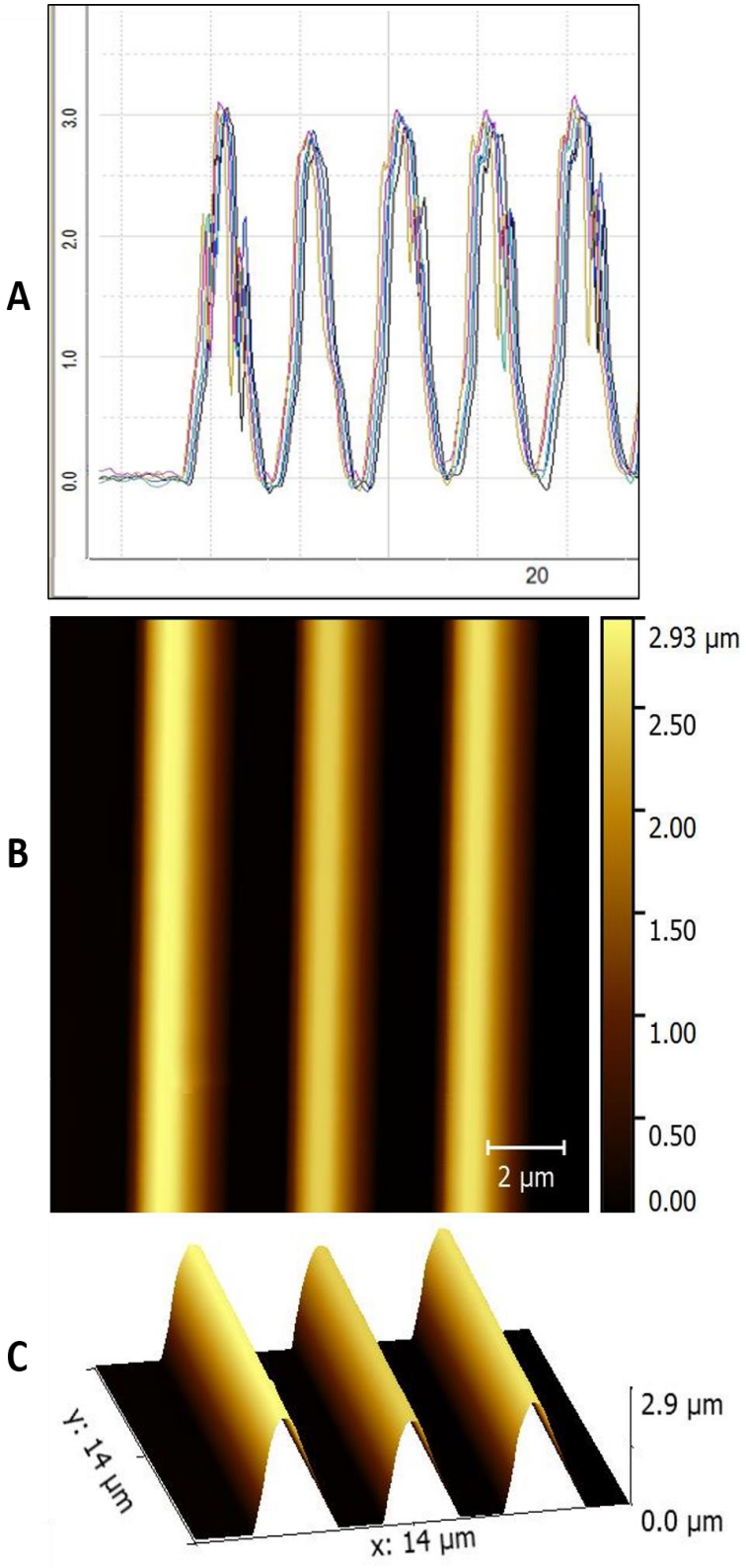


Figure 4.8: A series of TPP 3 um high ridges shown by A) Zeta Profilometry with multiple cross-sections over the 50 µm long ridge displayed and then by AFM as a B) 2D image and C) in the 3D representation.

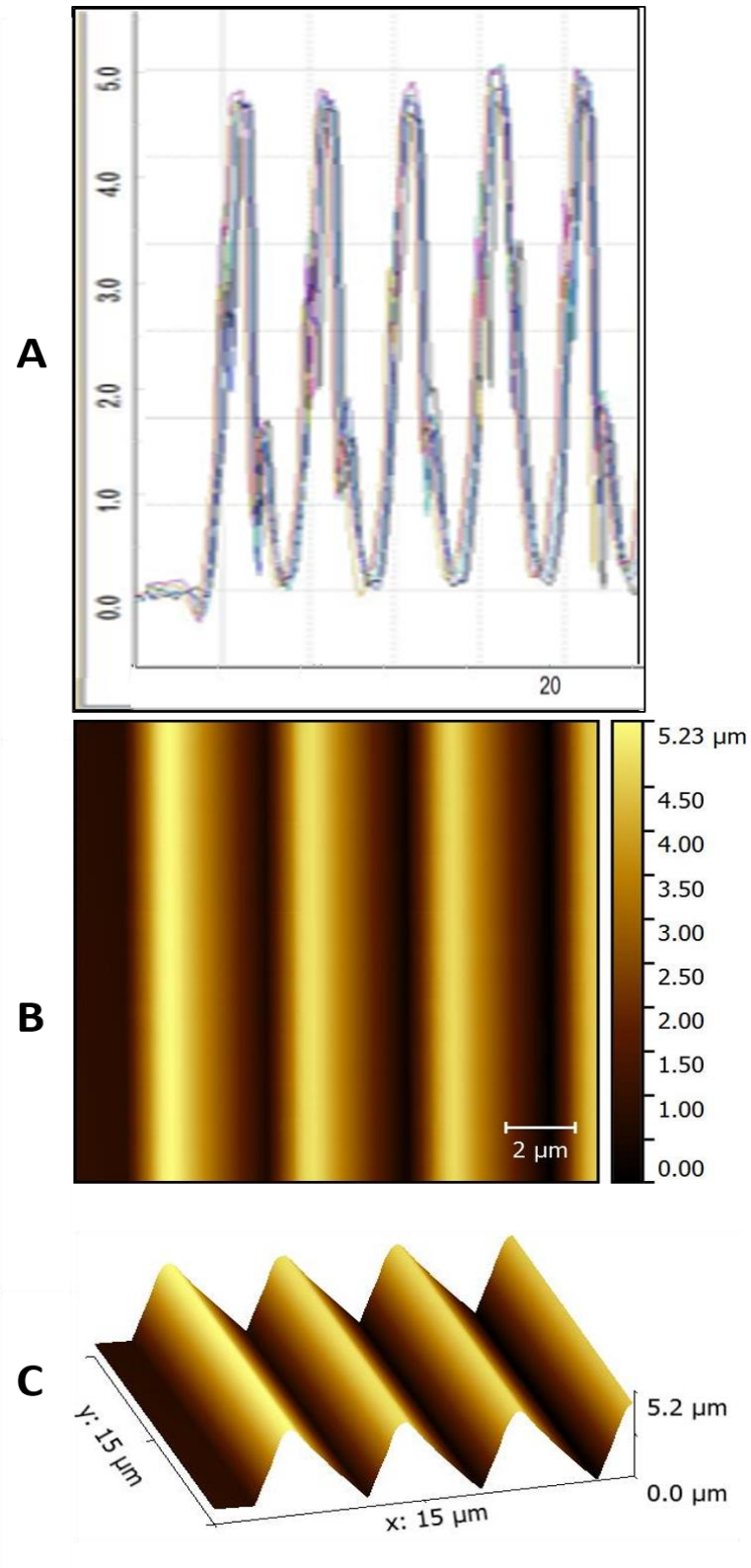
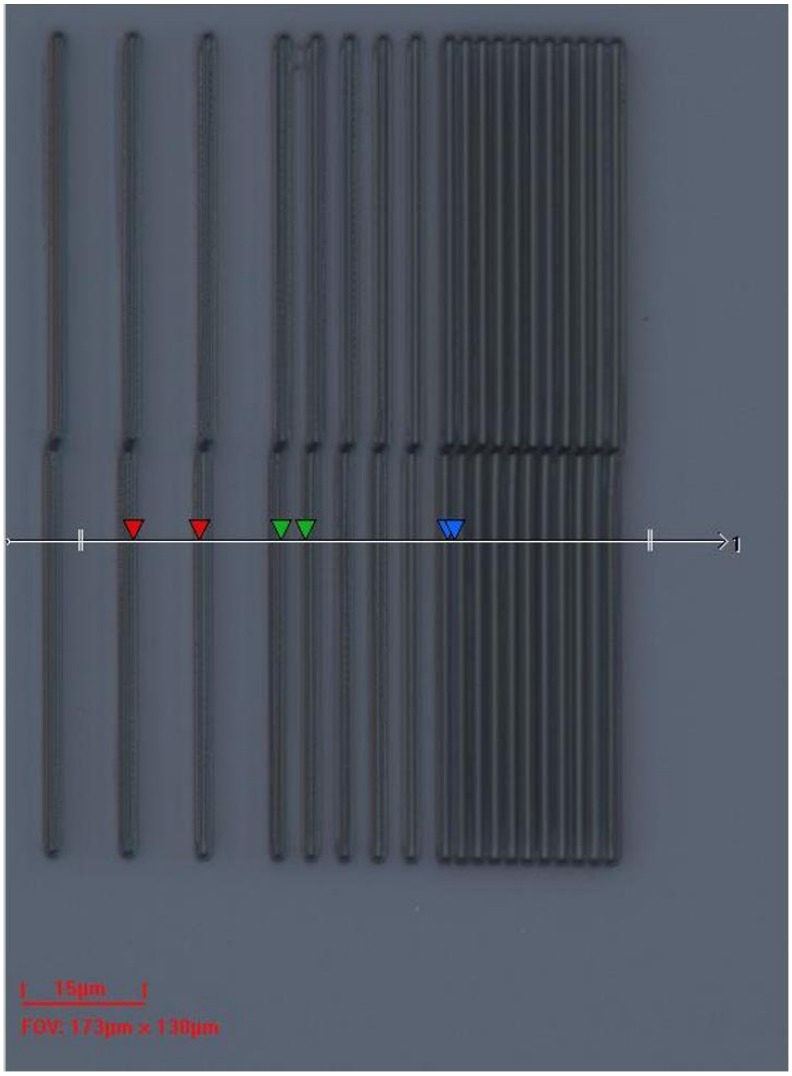


Figure 4.9: A series of TPP 5 um high ridges shown by A) Zeta Profilometry with multiple cross-sections over the 50 µm long ridge displayed and then by AFM as a B) 2D image and C) in the 3D representation.

4.5.1.2 Producing different ridge spacings

The second change in morphology explored was varying the spacing between ridges. It was decided that variation in spacing would be a good parameter to modify, as this would vary the available contact area with the substrate, which is expected to lead to a variation in adhesion. The three spacings chosen were 8 µm, as both polystyrene beads should be able to contact the substrate; 3 µm, which should prevent the 10 µm bead from substrate contact, but may allow the 5 µm bead to contact the substrate depending on the ridge height and 1 µm which should prevent both bead sizes from contacting the substrate and should act as small scale roughness, and therefore would be expected to reduce the adhesion.

From Figure 4.10 it can be seen that the range of spacings between the ridges was consistently achieved. This 2D Zeta optical Profilometry image allows the placement of markers, which can be used to measure the distances.



	Markers		
	Red	**Green**	**Blue**
Distance (µm)	7.9	3.0	0.9

Figure 4.10: A 2D representation of a series of TPP ridges, captured using the Zeta Profilometer (above) and the distances recorded between the markers (below).

4.5.2 Evaluation of plasma polymerised coating

As discussed in Chapter 1, there are a variety of factors that affect particle adhesion to a surface. One of these factors is surface chemistry, as the varying morphologies are created by producing TPP ridges on a glass substrate, there is a variation in surface chemistry which could impact on particle adhesion. It was therefore decided to use plasma polymerisation coating to produce a consistent surface chemistry.

An assessment of the consistency of the coating and the effect on wettability was made. The two coats, plasma polymerised acrylic acid (ppAAc) and plasma polymerised hexane (ppHex) were both deposited to the same thickness. Figure 4.13 shows a comparison of the WCA obtained on ppHex and ppAAc coatings on glass coverslips. An uncoated standard glass coverslip possesses a static contact angle of 52° ± 5°. In comparison after ppHex was deposited, a hydrophobic surface was generated with a contact angle of 96° ± 4°. This is as expected due to the hydrocarbon structure (Figure 4.11) and in line with previous findings[15]. A coating with ppAAc, with its added carboxyl functionality (Figure 4.12) produced a more hydrophilic surface with an average contact angle of 64° ± 3°, as expected for the plasma polymerisation settings used[16].

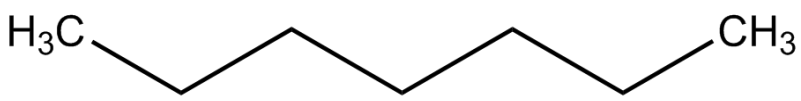


Figure 4.11: Chemical structure of hexane.

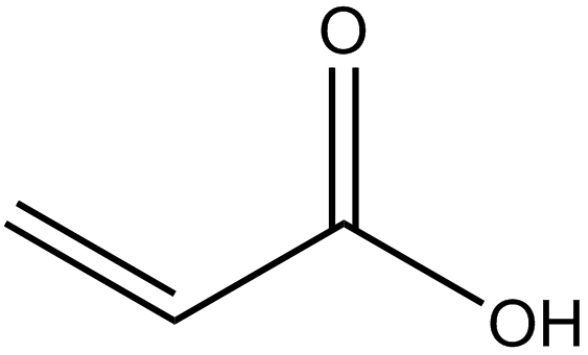


Figure 4.12: Chemical Structure of Acrylic Acid.

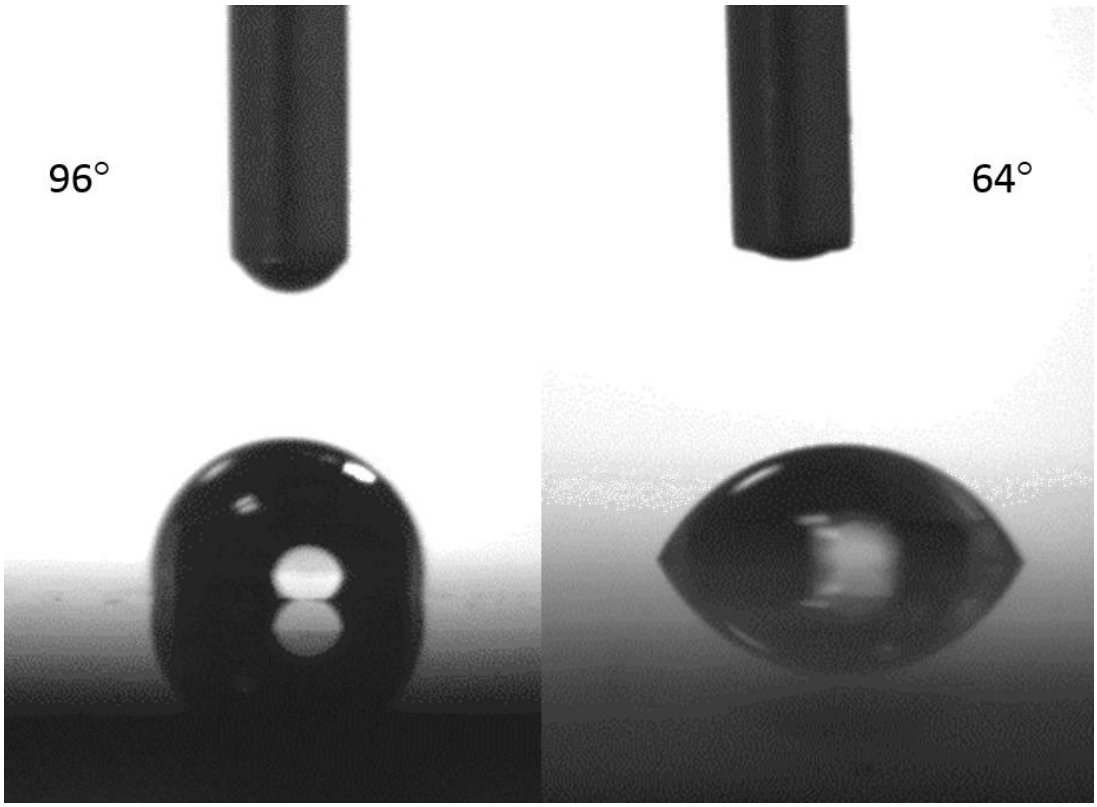


Figure 4.13: A comparison of WCA measurements of plasma polymerised coated surfaces. On the left a ppHex coated glass coverslip, with a WCA of 96^{o} and on the right a ppAAc coated coverslip with a WCA of 64^{o}.

Tof-SIMS allowed the evaluation of surface chemistry across the coating, to detect any inconsistencies or issues with the plasma polymerisation process. Tof-SIMS analysis was therefore undertaken on a glass substrate cleaned with acetone and

isopropanol, as would be performed post-TPP. This was then compared to a glass coverslip coated with ppHex and ppAAc. The relative spectrums show the differing chemistries as expected (Figure 4.14).

A characteristic peak was then chosen for each of the three chemistries and the surface coverage was evaluated. For the glass substrate the Si^+ ion can be clearly seen across the surface on the uncoated sample (Figure 4.15A), this ion is absent on the ppHex and ppAAc coated samples (Figure 4.15B and C respectively). This indicated that the glass substrate is no longer exposed. For the ppHex coating, as this is a hydrocarbon structure, $C_5H_{11}^+$ was chosen as a representative ion. This is absent from the uncoated substrate, but shows a strong consistent coverage for the ppHex coating, a small intensity of this ion is also see in the ppAAc coating, which is to be expected as the acrylic acid also contains carbons and hydrogens, and the molecule will undergo fragmentation and polymerisation, so the generation of this ion is not unexpected. Finally, the ion CH_5O^+ was chosen as an ion that represents the introduction of the Oxygen species and so should be absent in the ppHex hydrocarbon coverage. This was confirmed with very low intermittent intensity of this ion seen on the glass substrate, with none of this ion on the ppHex coated substrate and an even coverage of this ion on the ppAAc coated substrate. This confirmed that the ppHex and ppAAc coatings were consistent and of the expected chemistries.

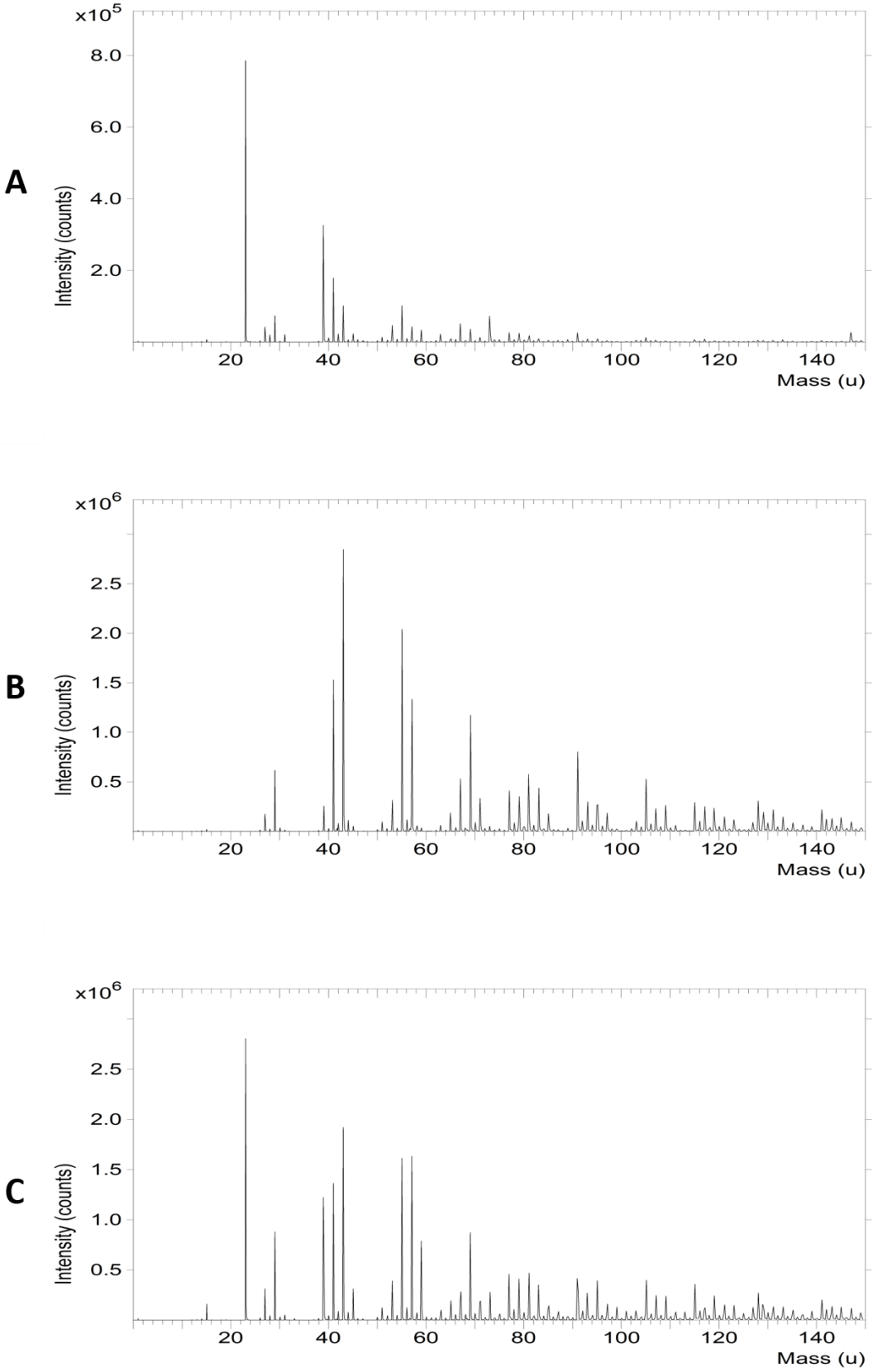


Figure 4.14: Tof-SIMS Spectra displaying positive ions up to m/z 150 for A) an uncoated glass coverslip, B) ppHex coated glass coverslip and C) a ppAAc coated glass coverslip.

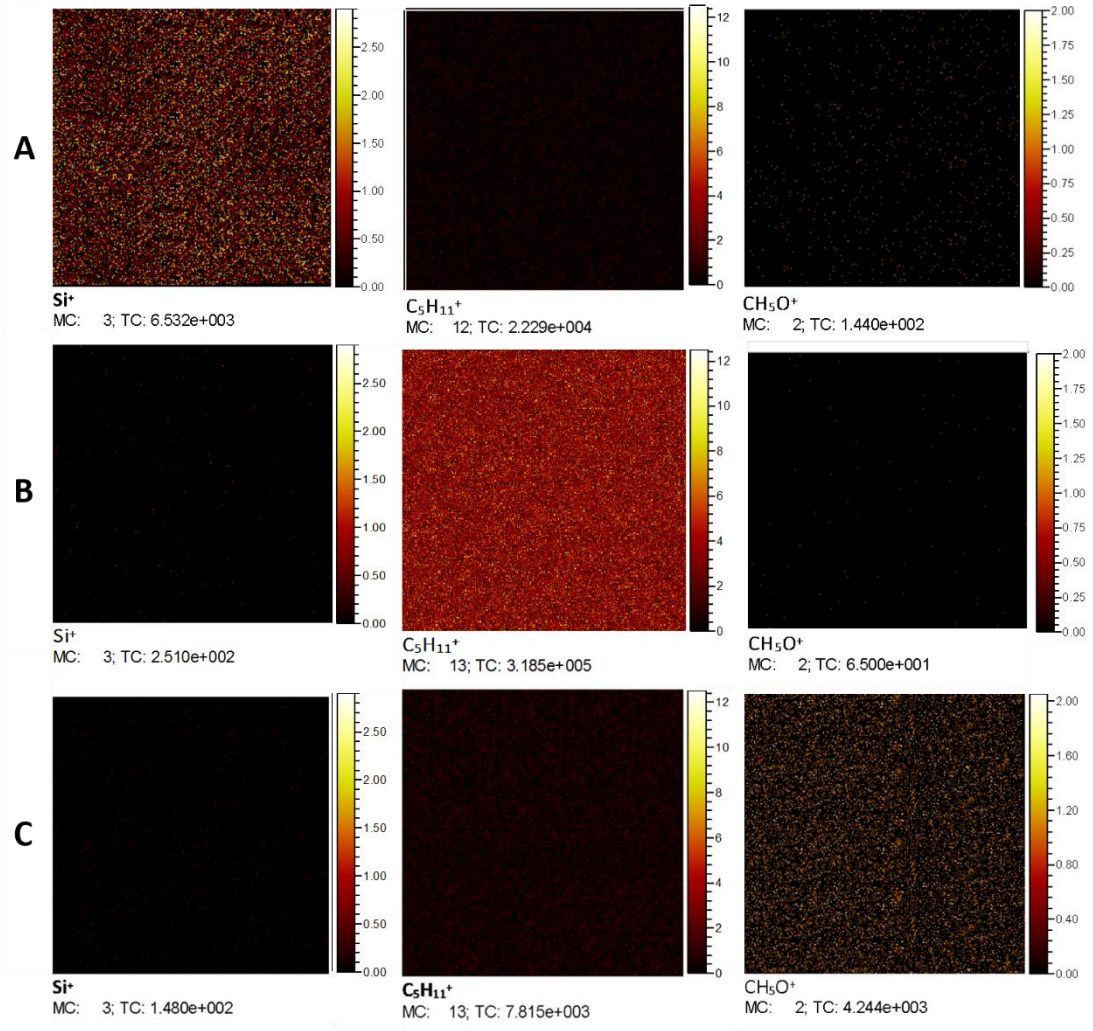


Figure 4.15: An overview of the substrate: A) Uncoated, B) Coated with ppHex and C) Coated with ppAAc, showing the surface coverage of three characteristic ions demonstrating a successful surface coverage with the two plasma polymerisation chemistries.

As a consistent chemistry was required to assess the effect of morphology on particle adhesion, it was decided to continue with just one plasma polymerisation coating due to time constraints. Therefore, it was decided to proceed with the ppHex coating, as due to its hydrophobic nature, it possesses a lower surface free energy and so a lower surface adhesion.

4.5.2.1 Evaluation of ppHex Coating

The topography of the plasma polymer coating was investigated by AFM. No significant features were observed when the samples were imaged in air (Figure 4.16). The rms roughness was low and consistent 0.42 ± 0.2 nm.

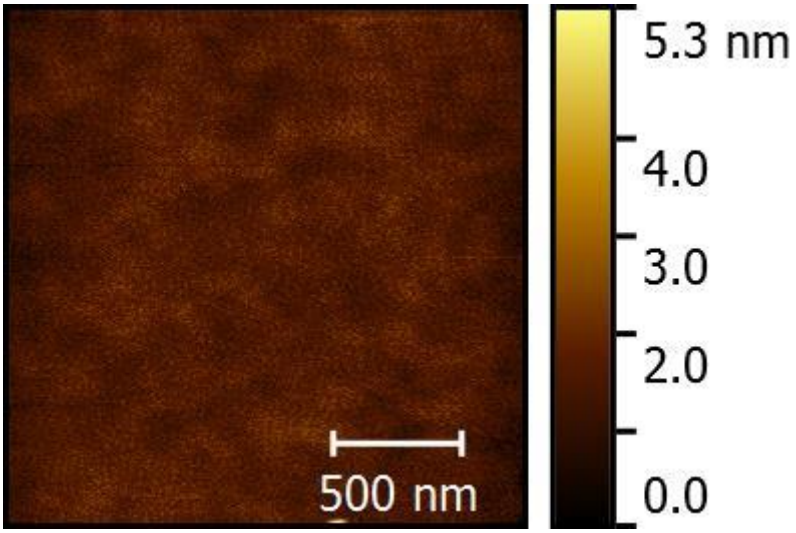


Figure 4.16: Representative AFM topographical image of a ppHex coating on a glass coverslip.

The plasma polymerisation was tuned by ellipsometry to achieve a coating of around 10 nm. The actual thickness of the coating was also determined by depth profiling undertaken using AFM, which showed the plasma coat to have a depth of around 8 nm (Figure 4.17).

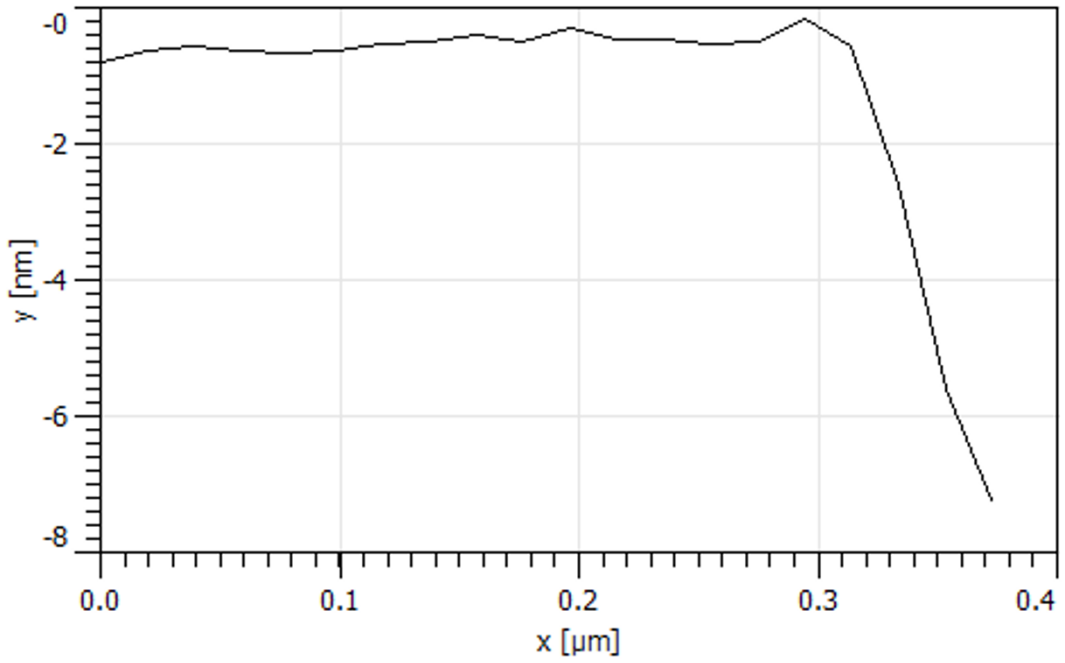


Figure 4.17: A profile of the ppHex plasma coat and then an area that had been scratched away by AFM, to evaluate the thickness of the ppHex coating.

As the coating needs to produce a consistent surface energy throughout the force-volume mapping, the stability of the coating was also assessed. The change in WCA was assessed over a week (Figure 4.18), by evaluating different samples coated at the same time. A relatively sharp drop in WCA was seen in the first 36 hours ~ 2.5°, which then stabilised at around 92°. This drop in WCA, followed by a period of stability is in line with previous coating stability studies[9] It was therefore decided to store the coated samples for 36 hours, prior to use for force-volume mapping, and then complete all the particle adhesion mapping to that sample within the following three days.

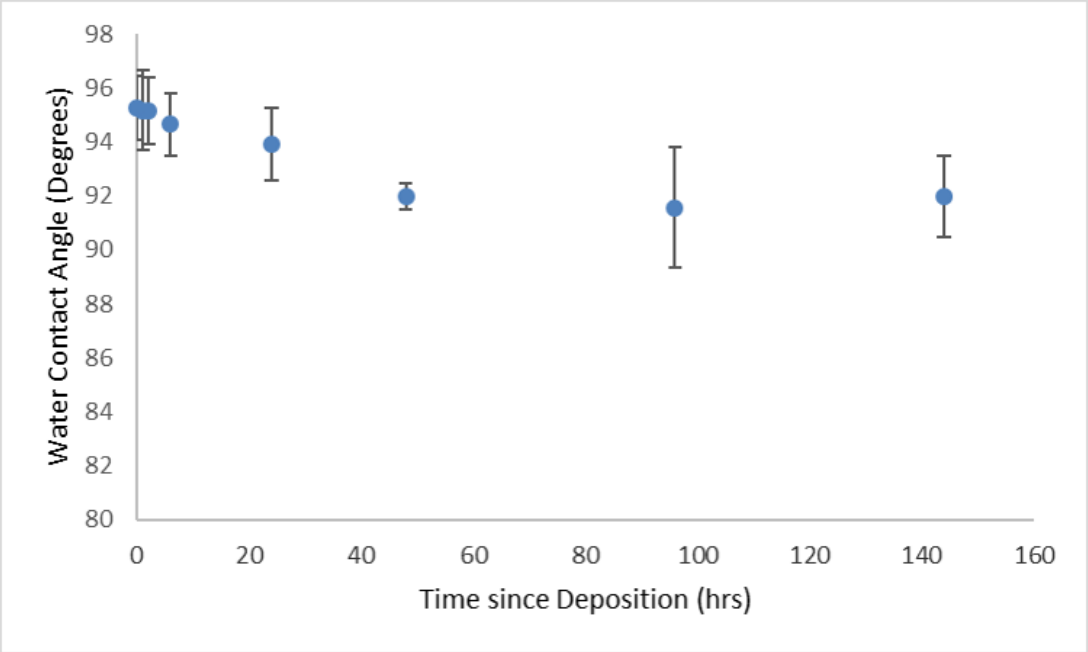


Figure 4.18: The change of WCA (mean ± S.D.) with time post-coating with ppHex.

4.5.3 Evaluation of Ridge Coverage

Tof-SIMS was used to confirm the successful coverage of the TPP ridges with the ppHex coating. Two glass coverslips were prepared for TPP printing as outlined in Section 3.4.5, a series of 5 µm high TPP ridges were printed on the substrate, and the substrates were developed (Figure 4.19). One of these coverslips were coated with ppHex, Tof-SIMS analysis was then undertaken on these substrates. A region of interest was used on the uncoated coverslip on the non-printed glass section and a region of interest was used on the ridges. The relative spectrums show different chemistry as expected (Figure 4.21).

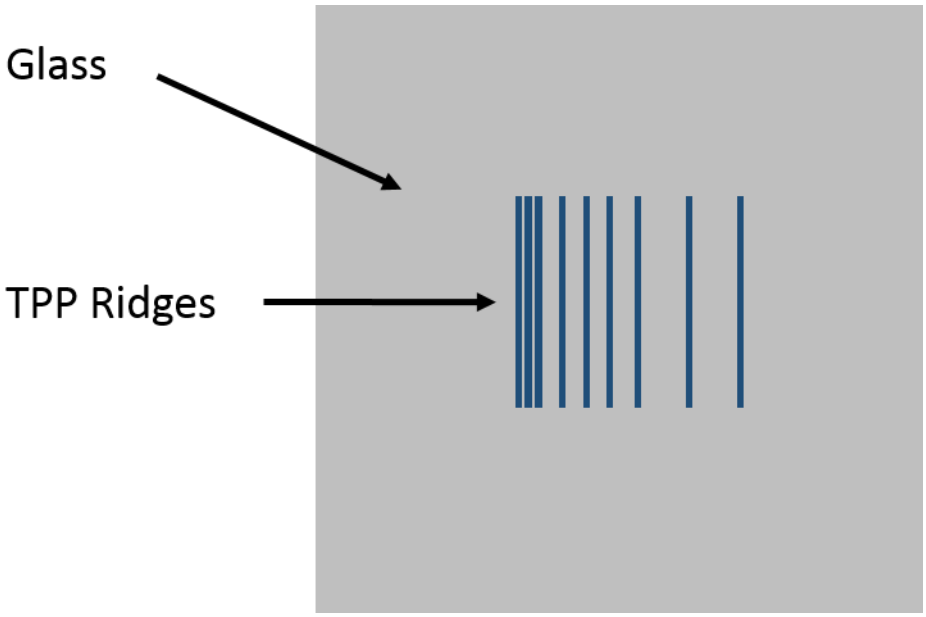


Figure 4.19: Cartoon representation of the TPP ridges printed on a glass coverslip for Tof-SIMS analysis.

A characteristic peak was then chosen for each of the three chemistries and the surface coverage was evaluated. For the glass substrate the SiO_3^- ion can be clearly seen across the surface on the uncoated sample (Figure 4.22A), this ion is then absent on the ppHex coated sample (Figure 4.22B). This indicated the glass substrate is no longer exposed. The TPP ridges are polymerised from the monomer, 2-(hydroxymethyl)-2- [[(1-oxoallyl)oxy]methyl] - 1,3-propanediyl diacrylate shown in Figure 4.20, so $C_3H_3O_2^-$ was chosen as a representative ion.

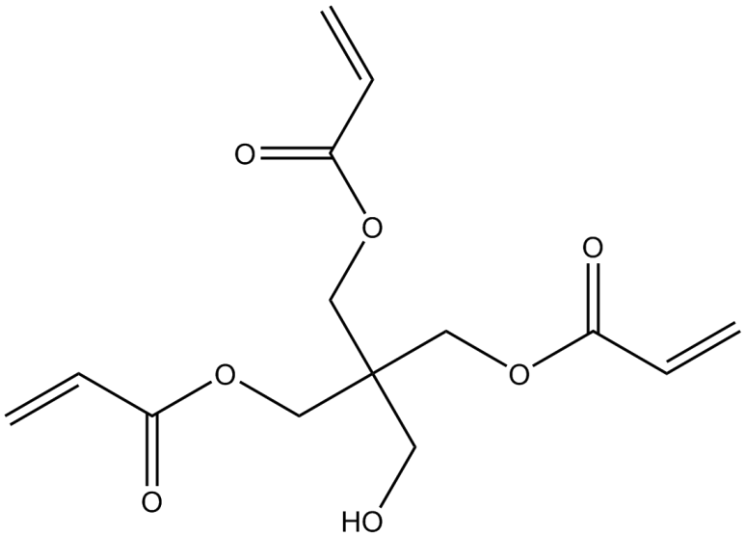


Figure 4.20: Chemical Structure of 2-(hydroxymethyl)-2- [[(1-oxoallyl)oxy]methyl] - 1,3-propanediyl diacrylate (IP-L).

The Tof-SIMS ion map was normalised to the total ion count, this was repeated for the ridge area on the ppHex coated substrate. The $C_3H_3O_2^-$ ion is in extremely low intensity across the entire coated substrate, which is likely due to the exposure of the coating to the atmosphere introducing a small amount of Oxygen to the hydrocarbon coating. However, there is no peak intensity in the TPP ridge area, this indicates that the TPP ridges are successfully coated. This was then confirmed by evaluating the ion $C_5H_2^-$ which was chosen as an ion that represents the hydrocarbon ppHex coating which is shown in high intensity across the substrate (Figure 4.22B).

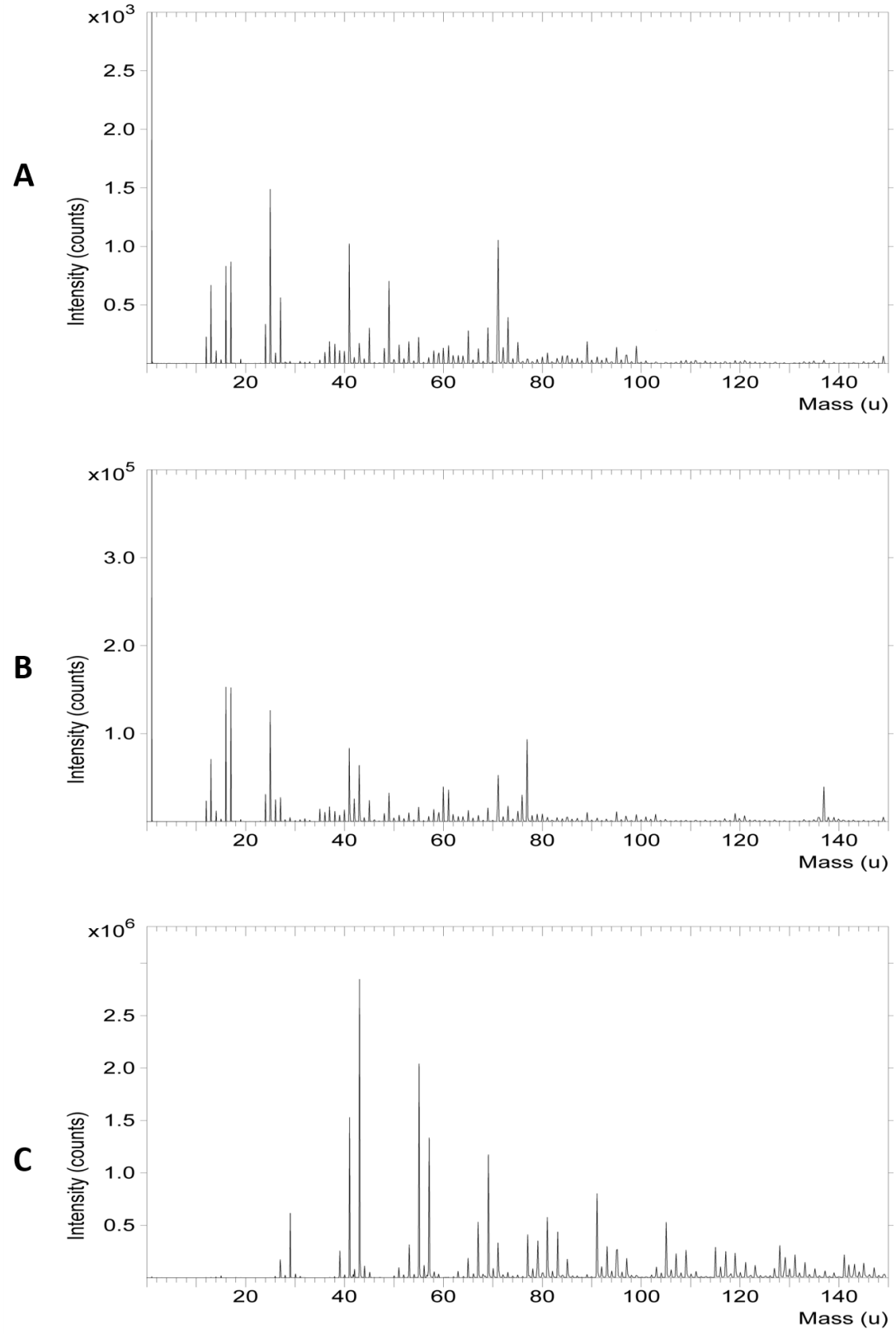


Figure 4.21: Tof-SIMS Spectra displaying negative ions up to m/z 150 for A) uncoated glass coverslip post-TPP processing, B) uncoated TPP ridges and C) ppHex coated ridge and glass coverslip.

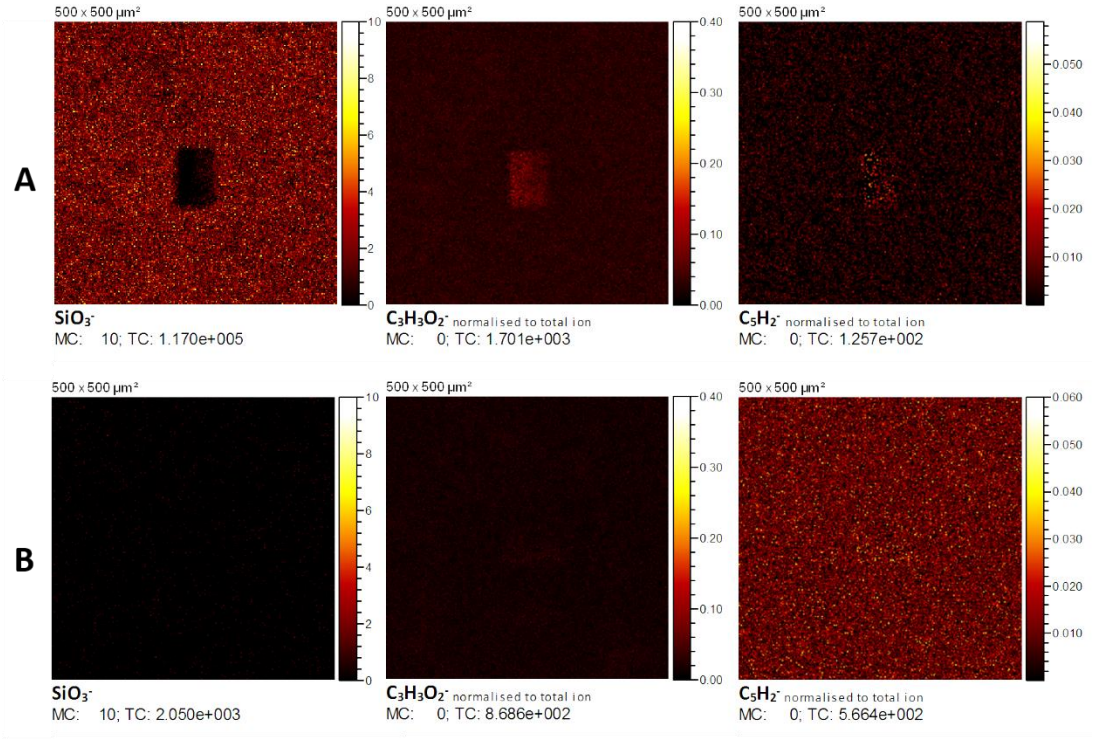


Figure 4.22: An overview of the substrate with a series of TPP ridges in the centre: A) Uncoated and B) Coated with ppHex showing the surface coverage of three characteristic ions demonstrating a successful surface coverage with the plasma polymerisation hexane.

4.5.4 Colloidal Probe Microscopy

In order to evaluate the effect of the TPP morphologies on particle adhesion, colloidal probe microscopy was used.

4.5.4.1 Particle Adhesion to Non-printed Hydrophobic Coating

Before evaluating the effect of changing morphology on particle adhesion, an initial investigation was undertaken to ensure that the adhesion was consistent across the ppHex coating without TPP morphologies. Figure 4.23 is an example of the adhesion of a polystyrene 10 µm particle to a non-printed ppHex substrate. As expected there is minimal variation in topography (Figure 4.23A) and the corresponding adhesion is extremely consistent across the area analysed (Figure 4.23B). Force-volume maps

were collected in three different areas on the substrate, with one of each of the three different particle types. A histogram of the force of adhesion of all force-curves collected over the three areas was then produced for each particle type (Figure 4.24). These show that the polystyrene 10 µm bead experienced the highest adhesion to the substrate with an average force of adhesion of 995 ± 228 nN, followed by the polystyrene 5 µm bead with 570 ± 49 nN and the Respitose SV003 particle, 409 ± 59 nN. This ranking of adhesion is expected as this is in line with their expected contact area, as can be seen in Table 2.2. When normalised for contact area, the average force of adhesion per μm^2 for the three particles would be; 0.16 nN, 0.13 nN and 0.56 nN for the polystyrene 10 µm, polystyrene 5 µm and Respitose SV003 respectively. Therefore the two polystyrene beads demonstrate very similar forces of adhesion to the substrate, which is to be expected as both beads are composed of the same material, and therefore contact area should be the only difference in particle-surface adhesion. This will therefore, allow the investigation of differing particle size on the morphologies and demonstrates the consistency of the ppHex coating. The Respitose SV003 experiencing a higher normalised force of adhesion could be explained by several factors. Firstly, the Respitose particle possesses a more hydrophilic surface chemistry and therefore a higher level of surface free energy[17], which is consistent with the higher forces of adhesion per unit area, compared to the hydrophobic polystyrene beads. Other factors that may influence this difference is the slight deformation of protruding surface asperities during particle press-on, resulting in a larger contact area and hence a larger effective contact area, which in turn would increase the adhesion. Also, there might be a minor contribution from any moisture from the atmosphere which may have condensed on the surface of the particle, due to the increased hydrophilicity of the particle. The presence of any moisture on the surface could lead to the contribution of capillary forces which have also been shown to increase the surface adhesion when multiple asperities are in contact with a surface[18]. However, as the experiments were conducted under low humidity this is expected to be negligible.

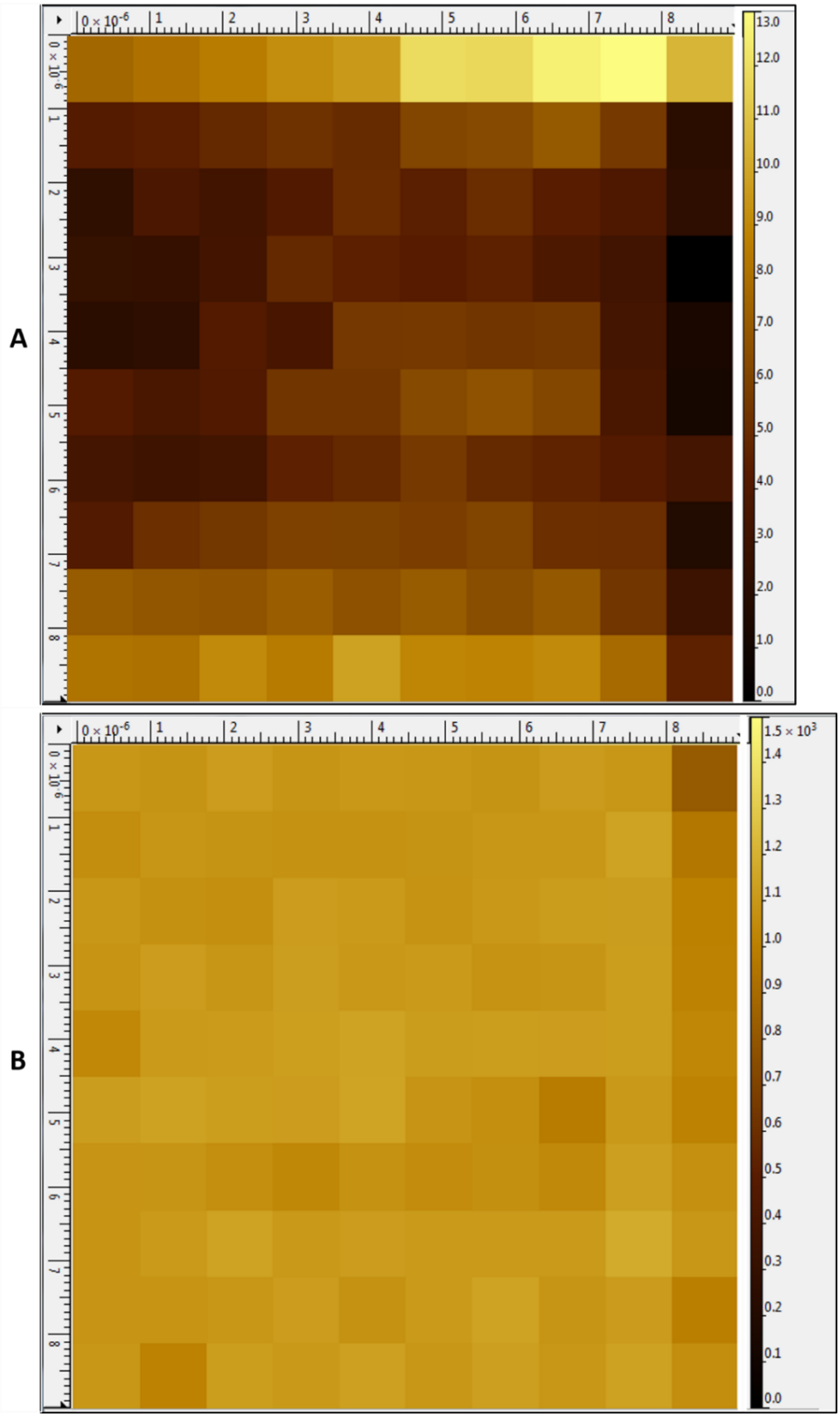


Figure 4.23: An example of the adhesion between a polystyrene 10 µm bead and a non-printed ppHex coated substrate showing the force-volume A) height and B) adhesion map.

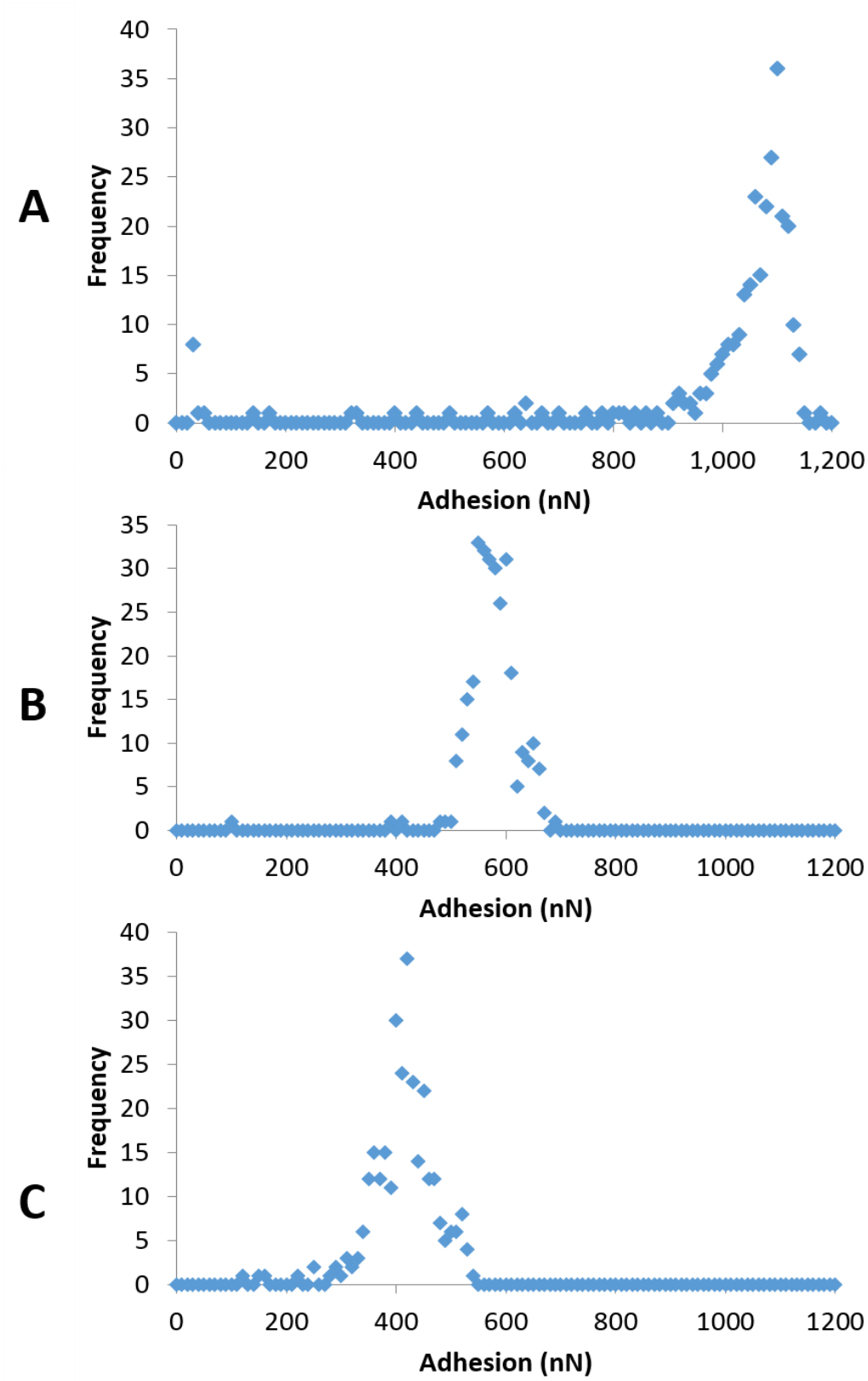


Figure 4.24: A comparison of histograms of particle adhesion to the non-printed ppHex substrate for A) a polystyrene 10 um bead, B) a polystyrene 5 µm bead and C) a Respitose SV003 particle.

4.5.4.2 Effect of Morphology on Particle Adhesion

To then assess the effect of morphology on particle adhesion a series of force-maps were collected over each ridge height produced in Section 4.5.1, aligned to also include the three different spacings. Each of these were then tested against the particle types. An overview of the resultant force of adhesions can be viewed as a histogram combining all repeats in Figure 4.25. Figure 4.25A shows the force of adhesion of the polystyrene 10 µm beads to each ridge height for all three ridge spacings. It can be seen that they all have a very low sharp peak of adhesion that falls in the 10-15 nN bin. A second higher broader peak is then seen for all ridge heights, however for the 1 µm and 3 µm spacings centred around 175 nN, however for the 8 µm spacings this increases to around 230 nN. A third peak is then also present in the 8 µm spacing at around 80 nN. The 1 µm ridge height, also has another broad, low intensity peak that spans 800 to 1000 nN.

Figure 4.25B displays the force of adhesion of the polystyrene 5 µm bead to all three spacings over each ridge height, except the 5 µm ridge due to difficulties in maintaining sample contact. It can be seen that this data has a very similar profile of adhesion, although the 1 µm ridge profile is slightly shifted to higher forces of adhesion. Both ridge heights have two peaks in the low range of adhesion with one sharp at around 30-35 nN and a second broader peak at around 135-145 nN. A series of lower intensity peaks can be seen at higher forces of adhesion. With the 1 µm high ridge having peaks at 445 nN, 610 nN and 730 nN. Whereas, the 3 µm high ridges has two adhesion peaks at 595 nN and 690 nN.

Finally, Figure 4.25C shows the histograms for the force of adhesion of the Respitose particles. These forces are significantly lower than the polystyrene beads, both the 1 µm and 3 µm ridge heights have a peak in the bin 10-15 nN, the 1 µm ridge height then has a second peak in the 30-35 nN. This is similar to the only peak seen for the 5 µm ridge height which is the range 35-40 nN bin.

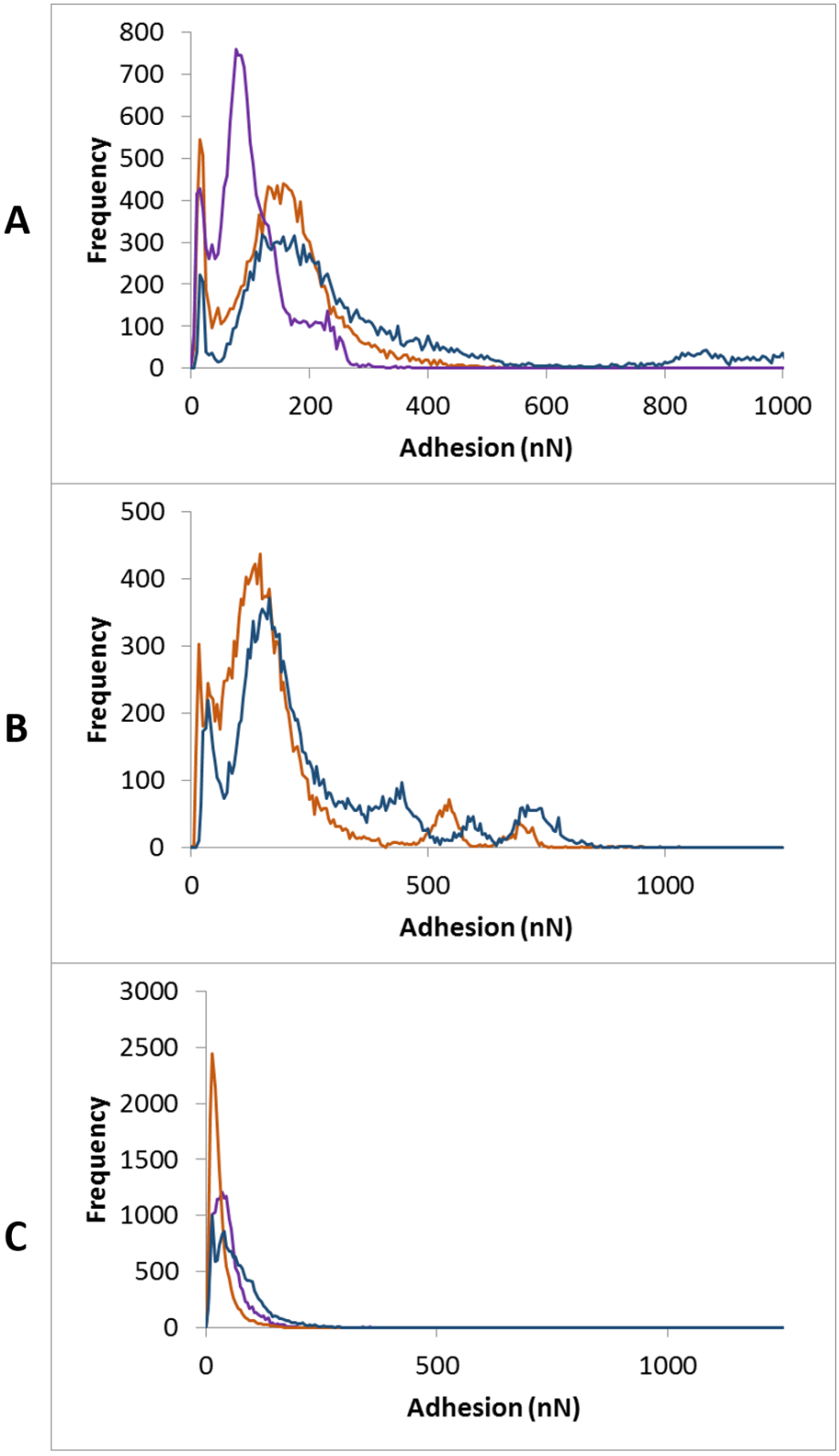


Figure 4.25: Histograms displaying the force of adhesion calculated from the force-curves collected with all particles of each type. Each curve is normalised to total count, to account for differing scan number. Adhesion to 1 µm (blue), 3 µm (orange) and 5 µm (purple) ridge heights for A) polystyrene 10 µm beads, B) polystyrene 5 µm beads and C) Respitose SV003 particles is displayed.

An example of the topography and respective adhesion map for each of the three particle types to 1 µm high ridges can be seen in Figure 4.26. There are some stark differences between the three adhesion maps, firstly, in the region of 8 µm spacing, there is extremely high adhesion at around 1000 nN in the area between the ridges for the polystyrene 10 µm bead (Figure 4.26A) and at around 650 nN for the polystyrene 5 µm bead (Figure 4.26B). Conversely, this high adhesion area is absent for the Respitose SV003 particle (Figure 4.26B). It is however, also worth noting that the topography map for the Respitose does not exhibit the same drop in sample height in these two areas as the two polystyrene beads. The Respitose SV003 topography map also, shows the ridges as far broader than the two beads which is to be expected due to the larger size of particle used. On the ridges, it can be seen that there are three adhesion ranges. These are seen as streaks that repeat with the ridge morphologies with low adhesion seen in dark blue which is aligned on the right side or in the gap between ridges, especially those of 3 µm spacing. A second adhesion region of around 125-200 nN to the ridges and then a slightly higher adhesion seen in turquoise, with an adhesion of around 250-300 nN, which seems to occur off-centre on the ridges. However, this higher type of adhesion appears to be slightly more inconsistent in nature and is seen with reducing intensity for the polystyrene 5 µm bead and almost not seen on the Respitose SV003 particle adhesion map, which is consistent with the overall histograms seen in Figure 4.25.

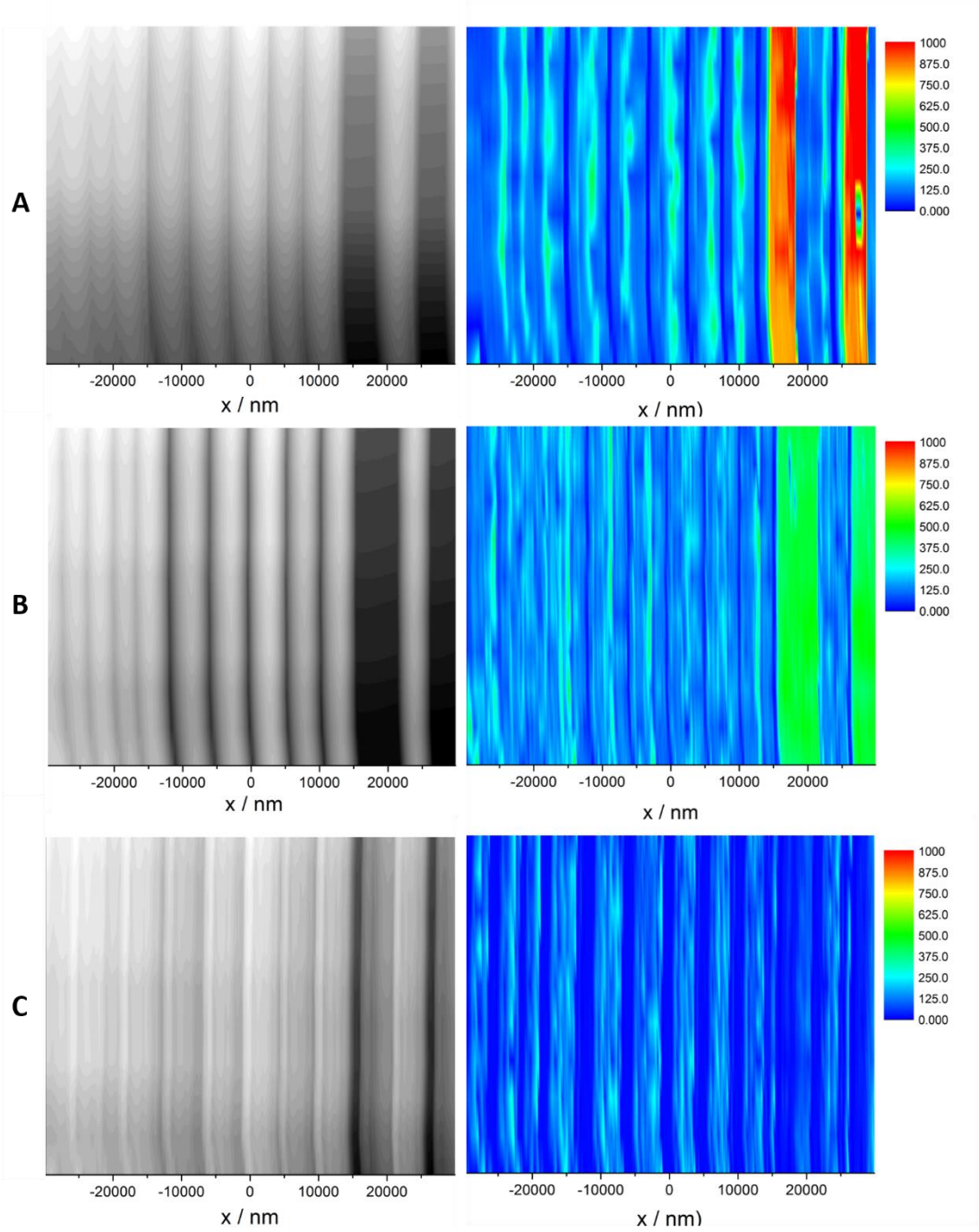


Figure 4.26: Force-Volume Maps collected with CPM of a series of 1 µm high ridges, showing the topography and respective adhesion collected over the scan area with A) a polystyrene 10 µm bead, B) a polystyrene 5 µm bead and C) a Respitose SV003 particle.

This evaluation was then repeated with the 3 µm high ridges (Figure 4.27). There are still some interesting differences between the three particle types, however the lack of high adhesion in the 3 µm high, 8 µm spaces for the polystyrene 10 µm (Figure 4.27A) in comparison to the 1 µm ridges (Figure 4.26A) is apparent. For example, the region of high adhesion is still present for the polystyrene 5 µm particle. Interestingly, the regions of higher adhesion in the range of 250-300 nN seen on the ridges for the 1 µm high ridges seems to have reduced in intensity for the polystyrene 10 µm bead and instead been replaced with an even higher adhesion, of around 450-500 nN, seen in green. Particularly noteworthy, is the Respitose SV003 adhesion map to 3 µm high ridges (Figure 4.27C), which shows very little variation in adhesion and an extremely low adhesion across the morphologies, which is in line with the histogram showing a singular peak around 15 nN.

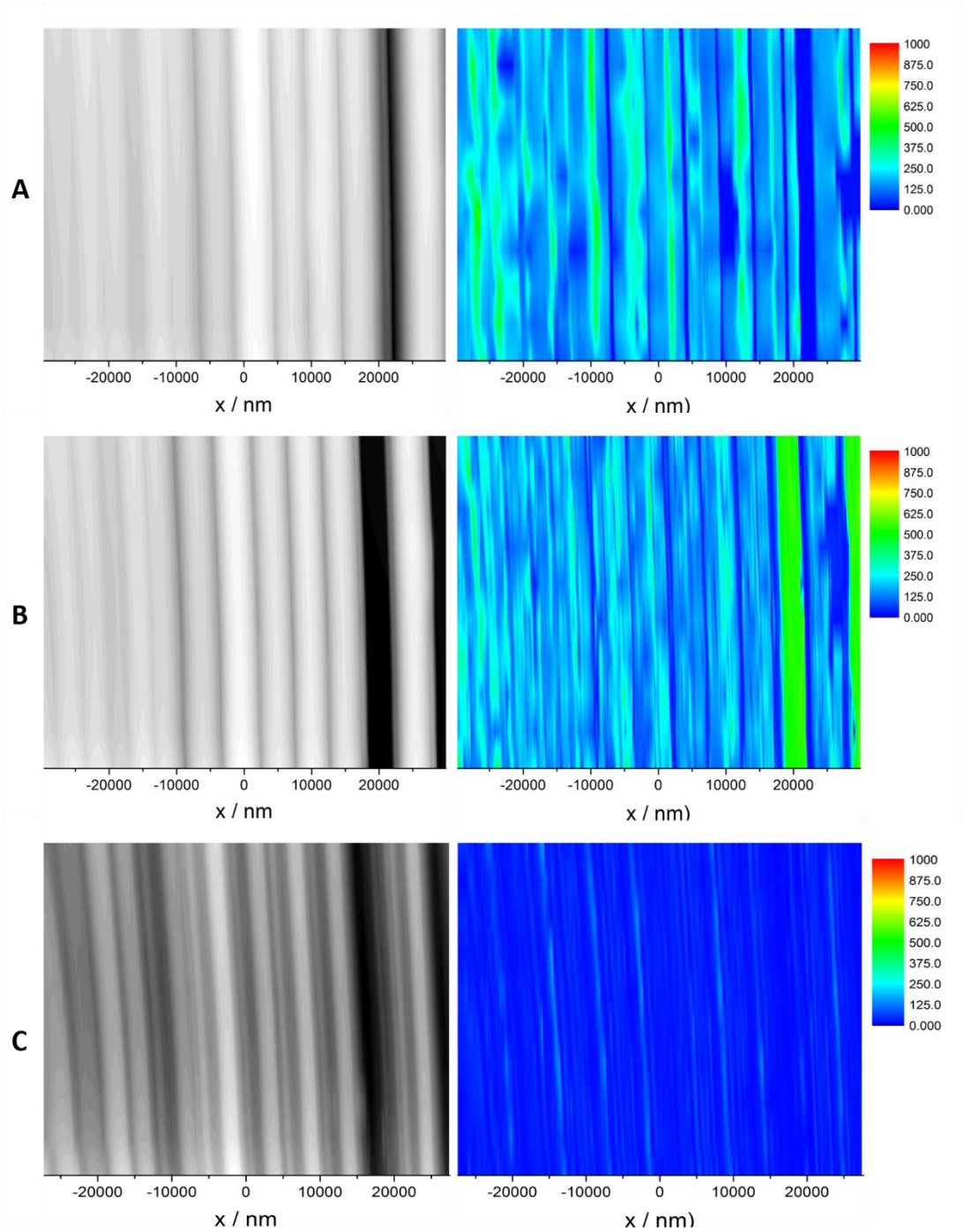


Figure 4.27: Force-Volume Maps collected with CPM of a series of 3 µm high ridges, showing the topography and respective adhesion collected over the scan area with A) a polystyrene 10 µm bead, B) a polystyrene 5 µm bead and C) a Respitose SV003 particle.

Finally, an example of the topography and respective adhesion map for the polystyrene 10 µm bead and Respitose SV003 to 5 µm high ridges can be seen in Figure 4.28A and B respectively. The Respitose SV003 particle still shows little variation in adhesion across the morphologies. Interestingly, this is also now the case with the polystyrene 10 µm bead, with only very small sections of higher adhesion, around 250 nN. Stripes of very low adhesion, of around 10-15 nN can be seen in dark blue and seem to occur slightly offset with the dip between ridges in the topography map.

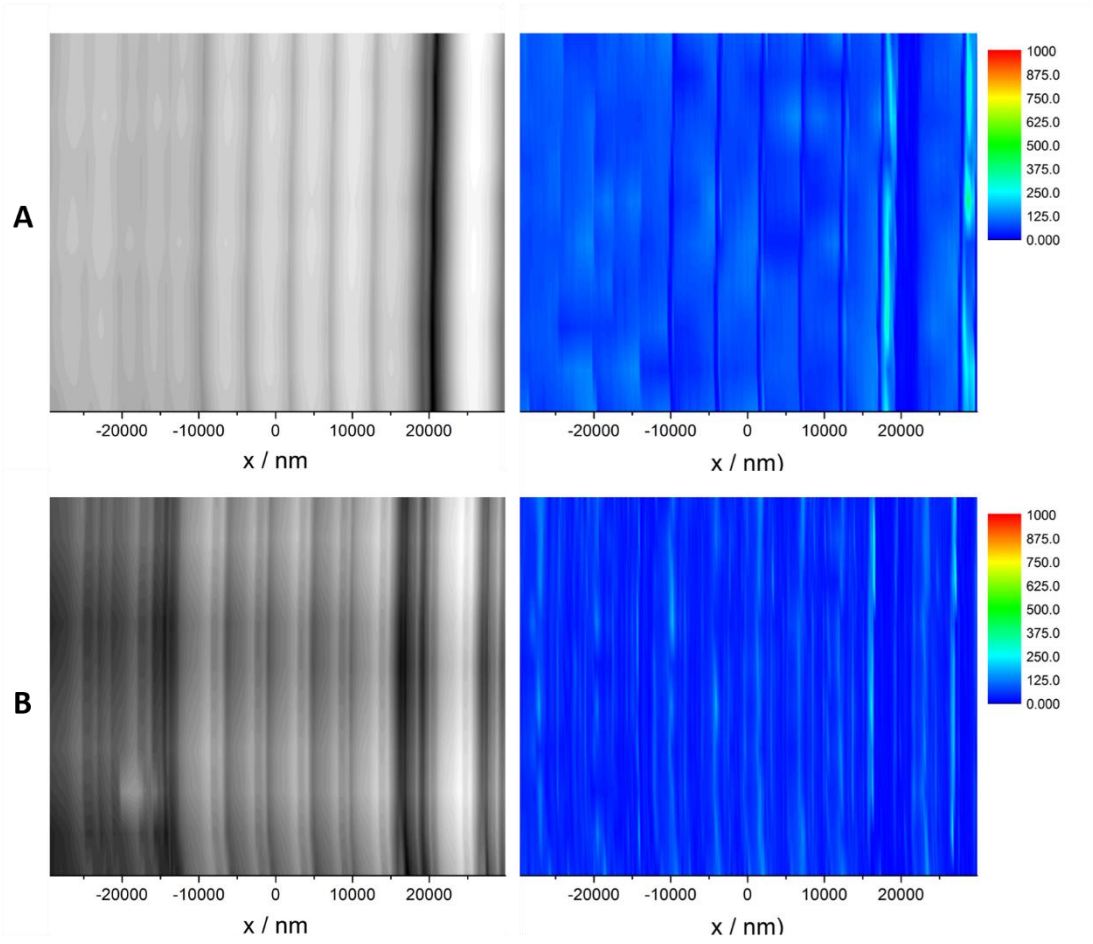


Figure 4.28: Force-Volume Maps collected with CPM of a series of 5 µm high ridges, showing the topography and respective adhesion collected over the scan area with A) a polystyrene 10 µm bead and B) a Respitose SV003 particle.

The data was then separated out based on ridge height, spacing and particle tested against these morphologies. The mean and the interquartile range of each of these combinations (Figure 4.29), can then be used to see if the variation of morphology had an effect on the adhesion of each particle type. It can be seen that the adhesion measurements for the Respitose SV003 particles are consistently less than the polystyrene beads. There seems to be a clear trend for the polystyrene beads showing a decrease in particle adhesion, with increasing ridge heights. This trend is absent for the Respitose SV003 particles which shows a low adhesion for all three ridge spacings from 1 µm to 3 µm, with an increase for the 5 µm ridge height. There is a greater range in adhesion measurements for the 8 µm spacing adhesion measurements, which is consistent with the force-maps as there is the contrast between the ridge and the spaces. With regards to spacing, there seems to be a similarity in the mean force of adhesion for the 1 um and 3um spacing for each ridge height on all particle types. The polystyrene beads exhibit a far higher force of adhesion, for the 8 µm spacing, than the 1 µm and 3 µm spaced 1 µm high ridges, but lower for the Respitose SV003 particle. The force of adhesion is also higher, for the 8 µm spacing, than the 1 µm and 3 µm spaced on the 3 µm high ridges for the polystyrene 5 µm bead. For all three particle types, the force of adhesion for all three ridge spacings is similar.

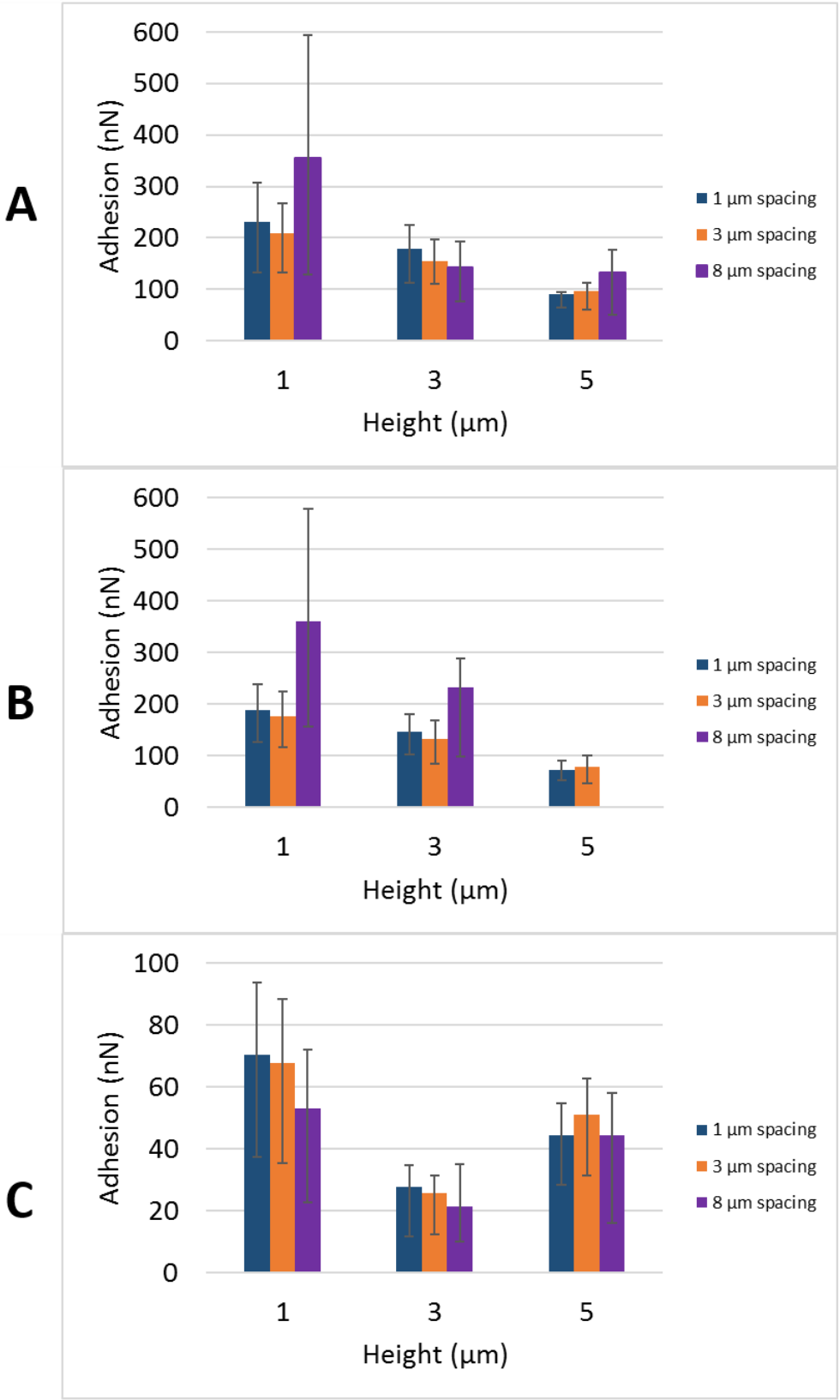


Figure 4.29: An overview of the mean force of adhesion, with the interquartile range for each combination of ridge height and spacing against A) polystyrene 10 µm beads, B) polystyrene 5 µm beads, C) Respitose SV003 particles.

The effect of surface morphology on the adherence of particles to surfaces is a complex process, as; the number of ridges, diameter, height, curvature and spacing of the ridges all impact the overall adhesion. This is reflected in the results, where there are multiple parameters that have been discussed and impact on the observations, in order to attempt to independently assess the effect of each variable, the following discussion will be separated into three subsections.

4.5.4.2.1 Effect of Particle size, shape and composition

The effect of the particles used has a clear impact on the particle adhesion map recorded. It can be seen (Figure 4.29) that generally with a few exceptions that the Polystyrene 5 µm bead exhibits a lower adhesion to the surfaces than the 10 µm bead and that the Respitose SV003 particles have significantly less adhesion to the morphologies compared to the polystyrene beads. One of the main reasons for these variations is that this is the trend previously seen for the contact area for the particles. The three Respitose SV003 particles possesses an average contact area of 1143 nm^2, in comparison to the average contact area for the polystyrene 10 µm and 5 µm bead, 7740 nm^2, 5343 nm^2, respectively. A reduction in contact area will reduce the van der Waal attraction and hence the adhesion between particle and surface[19]. The other factor that is likely to play a role is the spread of the asperities on the Respitose particle surface, as the particle is far larger than the contacting area of the polystyrene beads, so not all asperities will be in contact, if at all, with the morphologies simultaneously, acting to reduce the effective contact area.

From evaluating the different force volume maps (Figure 4.26-Figure 4.28), there are clear differences in the variation of the force of adhesion between the particles for the same morphologies. There is a patch of high adhesion present on some of the adhesion maps, in the area of 8 µm spacing, this is likely the interaction between the particle and the substrate. Confirmation of this requires consideration of the relative dimensions of the particle interacting with the morphologies (Figure 4.30). For the 1 µm high ridges, the polystyrene 10 µm needs a minimum spacing of 6 µm, which explains why the section of high adhesion between the ridges is only present for the

8 µm spacing (Figure 4.26A). For the 3 µm high ridges, a 9.2 µm ridge spacing is needed and so the particle will be unable to contact the substrate at any ridge spacing, this can be seen as the corresponding adhesion map does not have these high adhesion values (Figure 4.27A). In contrast, the polystyrene 5 µm needs a 4.4 cm and at 3 µm the whole diameter of the particle will be lower than the ridge line, so a 5 µm spacing is needed, which explains why the area of high adhesion is present for the 8 µm spacing for both ridge heights (Figure 4.26B and Figure 4.27B), but as the dimensions of this area are smaller for the 3 µm high ridges, there is less time where the particle will not be in contact with either asperity.

This area of high adhesion being caused by contact with the substrate, is further supported by the similarity of the values of adhesion seen in this region in comparison to the corresponding adhesion of each particle to the ppHex coating (Figure 4.24). For the polystyrene 10 µm bead, both the value shown in red on the adhesion map and the peak on the ppHex control are around 1000 nN, whereas the polystyrene 5 µm bead registers an adhesion of around 600 nN, which likewise responds to the respective ppHex non-printed sample adhesion.

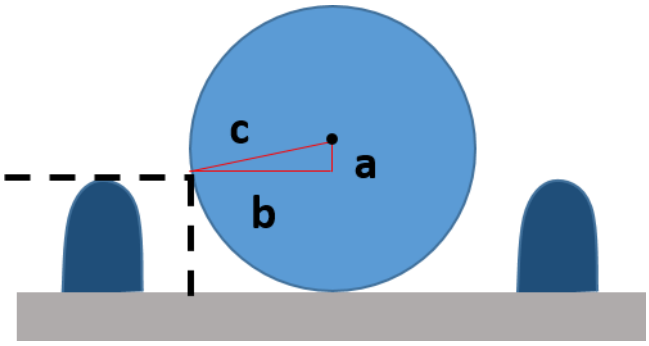


Figure 4.30: Schematic demonstrating how Pythagoras's theorem can be utilised to evaluate the spacing (2b) needed for a spherical particle with radius (c) to fit between the ridges for a specific ridge height. The dimensions of the particle at the ridge height can be calculated from the particle radius minus the ridge height (a). The central point of the particle is represented by the black dot.

4.5.4.2.2 Effect of Ridge Height

In order, to investigate the effect of ridge height, only the 1 µm and 3 µm spacing will be considered as the 8 µm spacing is distorted by the adhesion to the substrate, as

discussed in Section 4.5.4.2.1. By focusing on just these two ridge spacings, a clear trend can be seen for average force of adhesion of the polystyrene beads to the morphologies (Figure 4.32). There is a decreasing force of adhesion with increasing ridge height. By performing an ANOVA, there is a highly significant difference between all three ridge heights for both ridge spacings for both polystyrene bead sizes with p values < 0.0001. One explanation for this could be that with increasing ridge height, to keep the ridge diameter consistent there is an increase in the aspect ratio of the ridges. An increasing aspect ratio, results in a steeper curvature at the top the ridge and straighter sides. This means when the particles are unable to fit between the ridges, the higher ridges behave increasing like spikes and there is a reduction in contact area between the asperities and the particle (Figure 4.31). Therefore, with increasing aspect ratio a decrease in adhesion is seen[20]. However, if the particle contacts with the sides of the ridges on press-on, a higher contact area is achieved. The adhesion maps (Figure 4.27), therefore show the shift to higher adhesion from 250-300 nN for the 1 µm high ridges to around 450-500 nN for the 3 µm high ridges. These higher regions of adhesion, are absent from the 5 µm high adhesion maps, which might be because the particle is unable to penetrate the roughness sufficiently to contact the ridge sides.

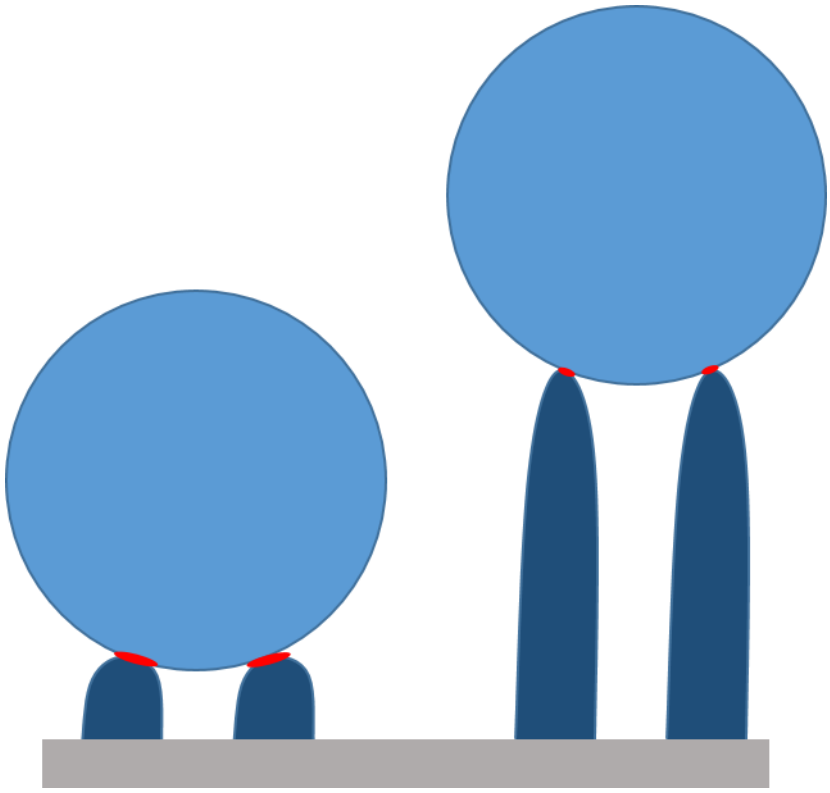


Figure 4.31: A schematic representation of a 5 µm polystyrene bead interaction with 1 µm (left) and 5 µm (right) high ridges, with 1 µm spacing. This drawing is to scale and the contact area between the particle and the ridges is shown in red.

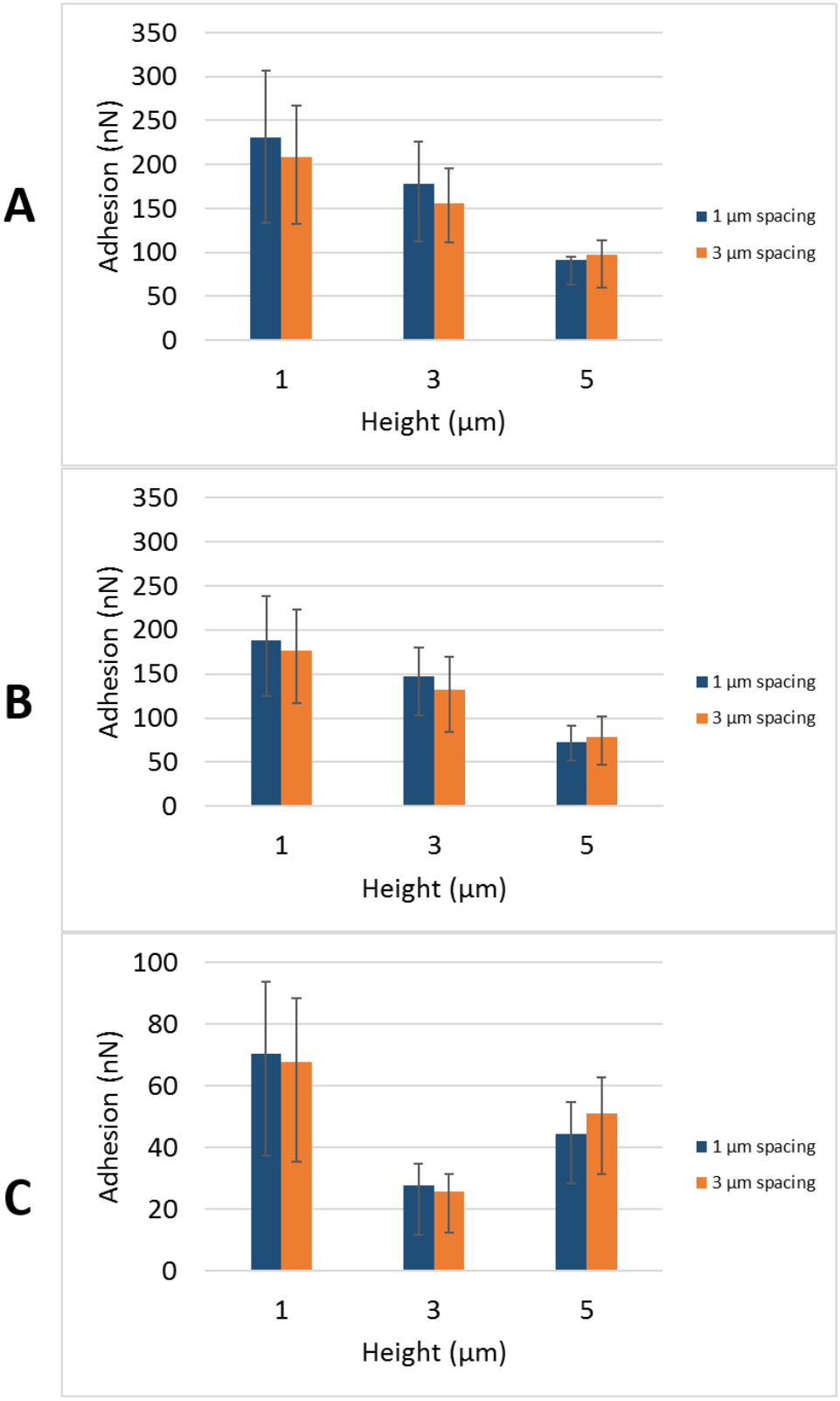


Figure 4.32: An overview of the mean force of adhesion, with the interquartile range to evaluate the effect of changing ridge height for 1 µm and 3 µm ridge spacing against A) polystyrene 10 µm beads, B) polystyrene 5 µm beads, C) Respitose SV003 particles.

The reason for the trend observed for the Respitose particle is harder to elucidate. From ANOVA statistical analysis, the differences in adhesion can be determined to be highly statistically significant with p values <0.0001 between each ridge height. One possible explanation could be that at the lower ridge heights the asperities may have touched the substrate, causing a higher adhesion due to the increased contact area, from touching multiple points, and this is removed with increasing ridge height. However, with increasing ridge height the straighter sides of the ridge may result in higher contact area with the asperities as they are sharper than the contacting area of the polystyrene beads. This is however, difficult to say definitively, without more information as to which asperities are interacting with which asperities and at which location at each point in the scan, which is beyond the scope of this project.

4.5.4.2.3 Effect of Ridge Spacing

To investigate the effect of ridge spacing, only the 1 µm and 5 µm high ridge results were evaluated to allow the range between spaces to be wide enough for both polystyrene beads to contact with the substrate and spaces that do not allow the particle to penetrate these features. Focusing on these two ridge heights, it is difficult to determine a clear trend (Figure 4.33), when the polystyrene beads can fit between the ridges there is a larger adhesion ($p<0.0001$). However, when the polystyrene beads are too large to penetrate into the valleys, there seems to be opposite trends between the two ridge heights, as the adhesion decreases with increasing spacing for the 1 µm high ridges, but decreases with increasing spacing for 5 µm high ridges. For the polystyrene 10 µm bead, on the 1 µm high ridges there is a significant difference between the 1 µm and 3 µm spacings ($p = 0.0004$), but not significantly different for the 5 µm ridges ($p = 0.0714$). Whereas, the 8 µm spacing was highly significantly different from both other spacings for both ridge heights ($p<0.0001$). For the polystyrene 5 µm bead, there is a significant difference between the 1 µm and 3 µm spaced ridges for the 1 µm and 5 µm high ridges ($p = 0.0481$ and 0.0060 respectively). The results for 5 µm high ridges with 8 µm spacing was excluded, but were highly significantly different from the 1 µm high ridges.

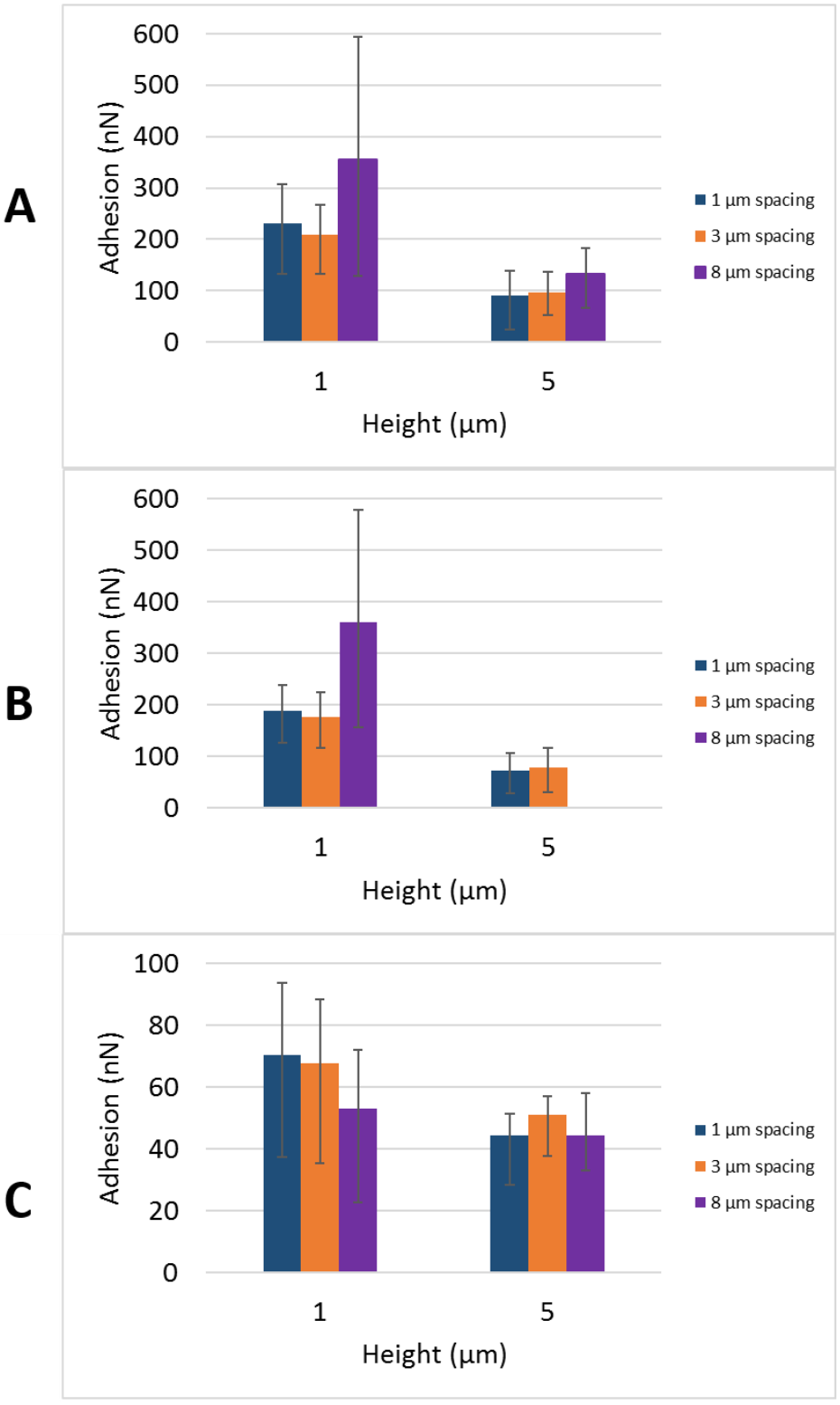


Figure 4.33: An overview of the mean force of adhesion, with the interquartile range to evaluate the effect of changing ridge spacing for 1 µm and 5 µm ridge height against A) polystyrene 10 µm beads, B) polystyrene 5 µm beads, C) Respitose SV003 particles.

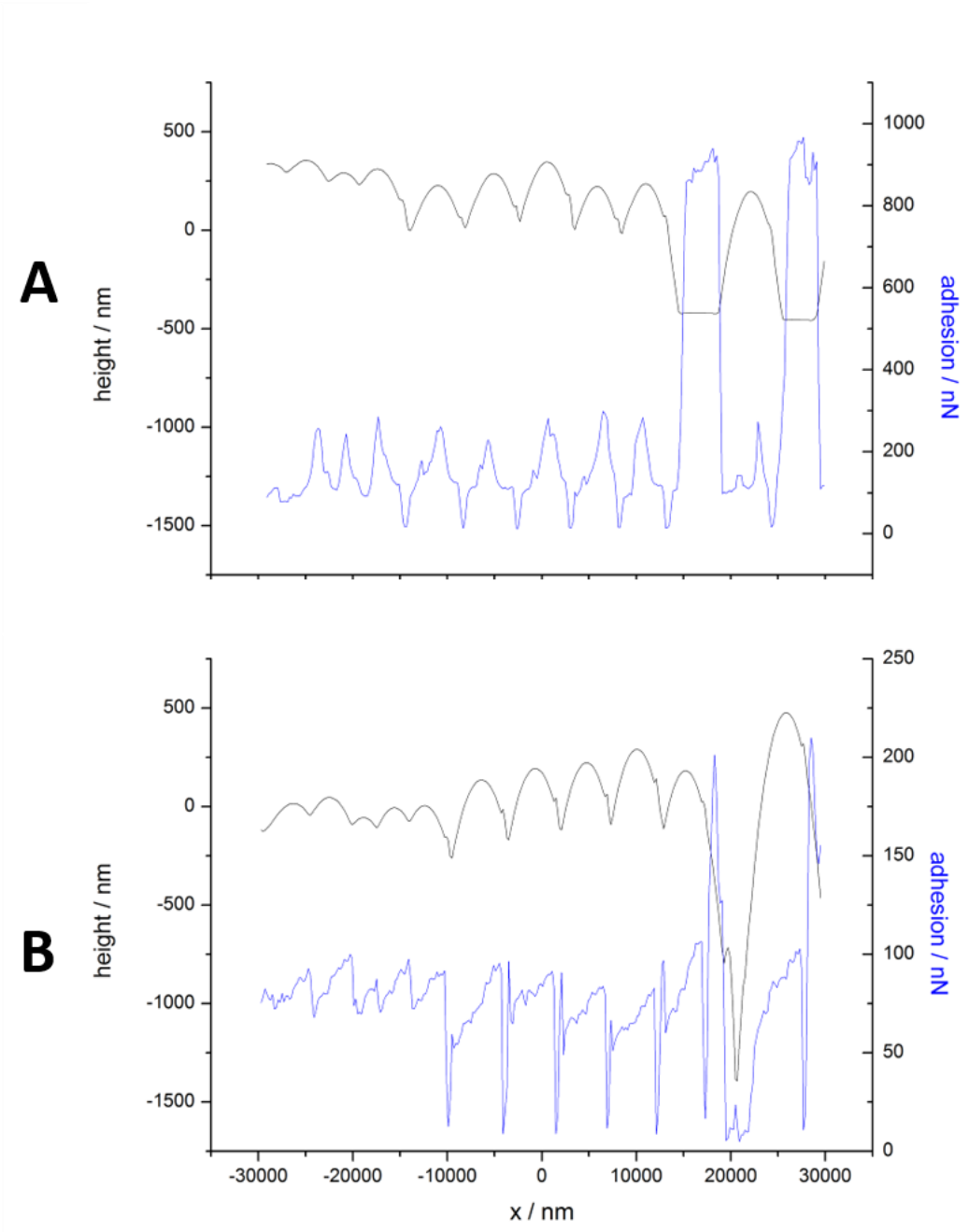


Figure 4.34: An example of the average profiles of the height (black) and adhesion (blue) of a polystyrene 10 µm bead scan for A) 1 µm high ridges and B) 5 µm high ridges.

To attempt to elucidate the reason for these changes, the profiles for both heights were plotted based on the height variation. From these, it can be seen that for the polystyrene 10 µm bead (Figure 4.34) with 1 µm spaced ridges there is a relatively small variation in adhesion, with counterintuitively the lowest adhesion occurring in the centre, between the ridges. For the 1 high ridges, the highest adhesion is at the central point of the ridge. This is likely due to the gentle curvature, at the top of ridges of these heights, allowing a greater contact area between the bead and ridge, whereas for the 5 µm high, 1 µm spaced ridges, the highest adhesion is on the side of the ridge, but only the on the right side. This is unexpected, as a symmetrical adhesion variation over a ridge would be expected. On consideration of the polystyrene 10 µm bead, used for these scans (Figure 4.5A – particle 1), it can be seen that there is an asperity on the right side of the particle, this can be seen on the height profile with a consistent bump on the right side of each height peak, which is an artefact from the particle. This asperity will act to reduce contact area, and may have a different surface energy than the bulk bead. This could explain the lower adhesion on the left side of each ridge.

For the 3 µm spaced ridges, it can be seen that there is a double peak in adhesion, on either side of each ridge. For the 1 µm high ridges, this is again lower on the left side, however for the 5 µm high ridges there is a similar level of peak adhesion on both sides. As the asperity on the bead is close to the surface this could lose contact with the sample for the larger spaces with higher ridges as more of the particle can descend into the valleys between the ridges.

Finally, for the 8 µm spaces, it can be seen that there is a spike of adhesion, when the particle is in contact with the substrate, lowest height in profile (Figure 4.34A). There is also, a spike in adhesion seen very close to the ridges. This is to be expected, as the particle may be in contact with the ridge and the substrate simultaneously increasing the adhesion.

Overall, therefore there is a high adhesion on the substrate as identified on the adhesion maps (Figure 4.26), however there seems to be higher adhesion on the side of the ridges, but lowest in the centre between the ridges. The high adhesion to the

sides of the ridge could be due to a friction force[21] experienced during the force ramp, on the side of the ridges. The main difference between the two ridge heights is that for increasing spacing, there is a greater variation in adhesion between the 1 µm and 3 µm spaced ridges for the higher ridges. As the higher aspect ratio ridges (Figure 4.36B) possess a steeper ridge top, there is a smaller effective contact area, however on contact with the side of the ridges the contact area increases, with increased spacing, however, for the lower aspect ratio the opposite is the case (Figure 4.36A). This could explain the two different trends seen, with the average histograms.

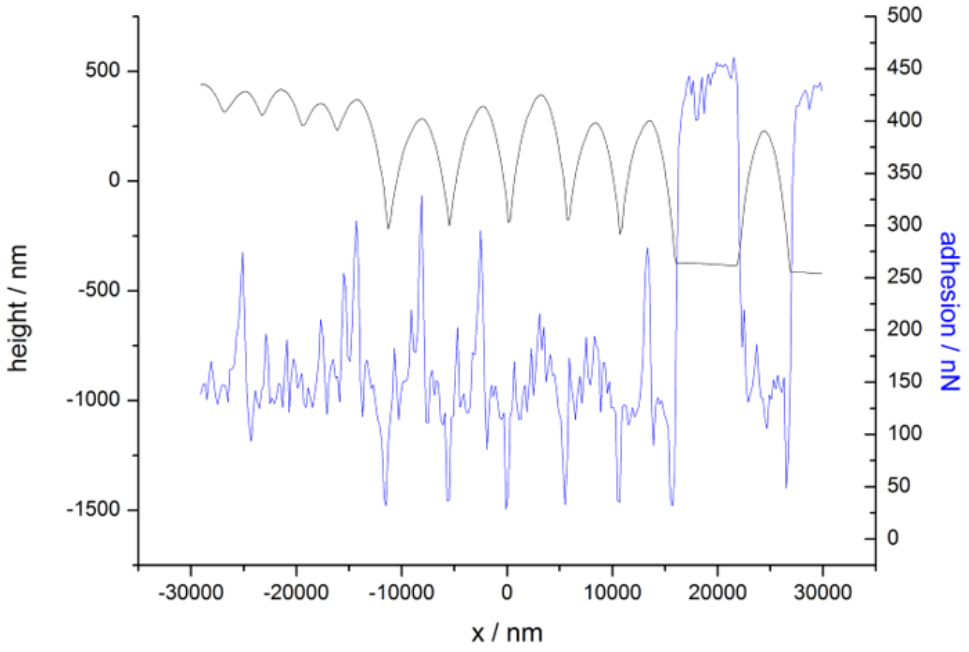


Figure 4.35: An example of the average profiles of the height (black) and adhesion (blue) of a polystyrene 5 µm bead scan for 1 µm high ridges.

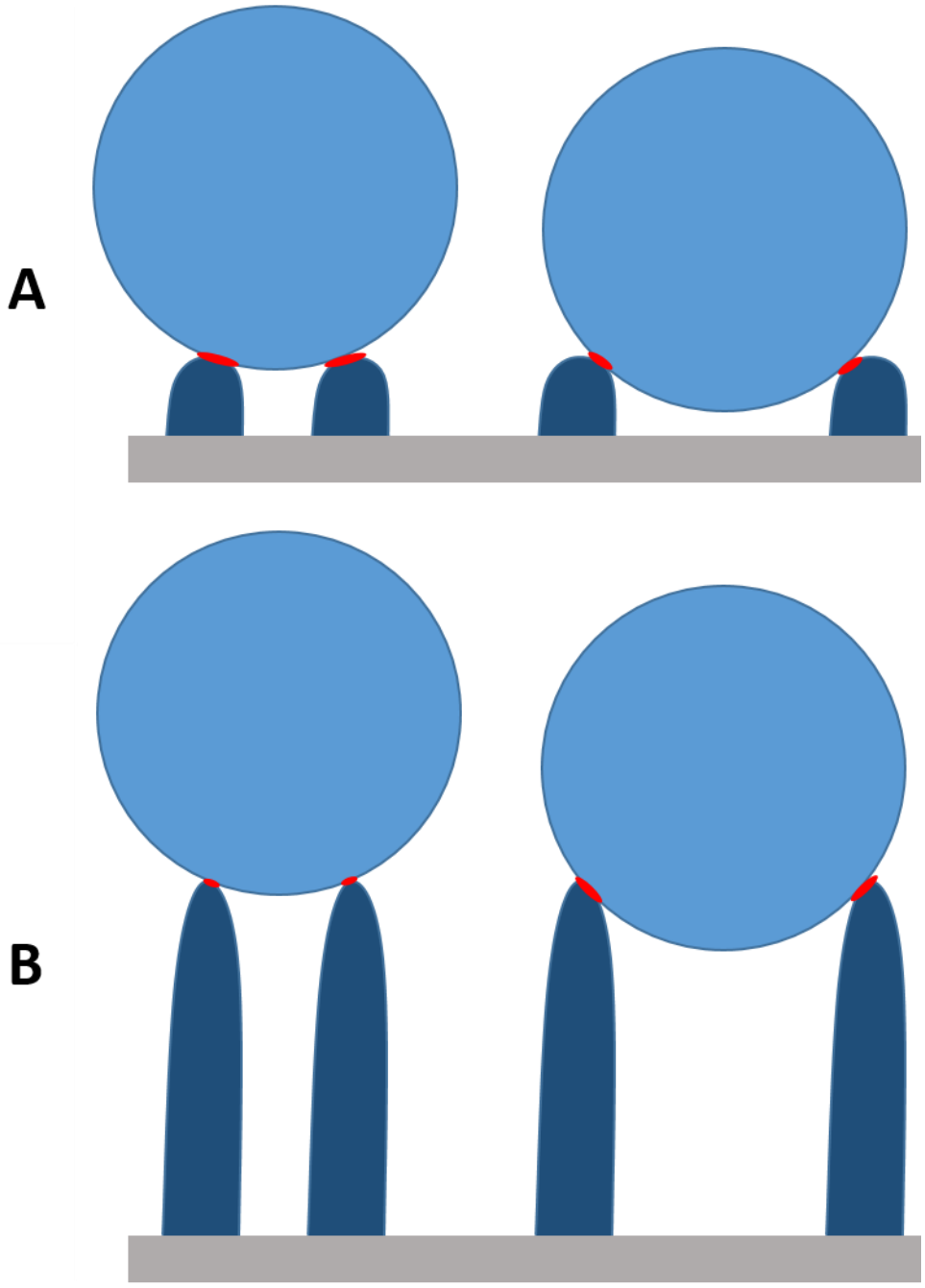


Figure 4.36: A cartoon representation of a 5 µm polystyrene bead interaction with A) 1 µm high ridges and B) 5 µm high ridges, with 1 µm (left) and 3 µm (right) spacing. This drawing is to scale and the contact area between the particle and the ridges is shown in red.

The polystyrene 5 µm bead, exhibits a similar profile for the height and adhesion maps (Figure 4.35), as the polystyrene 10 µm bead, which is to be expected.

For the Respitose SV003 particle for these two ridge heights, a similar decrease in adhesion with increasing spacing is seen for the 1 µm high ridges (Figure 4.33). On the 1 µm and 5 µm high ridges there is a significant difference between the 1 µm and 3 µm spacings ($p = 0.04$ and $p = 0.0018$ respectively). On the 1 µm high ridges there is highly significant differences between the 8 µm spacing and both other spacings ($p<0.0001$). On the 5 µm high ridges there is not a significant difference between the 8 µm spacing and the 1 µm spacing ($p = 0.996$). However, there is a highly significant difference between the 8 µm spacing and 3 µm spacings ($p<0.0001$).

From evaluating the profiles (Figure 4.37), the height profile variation on the top of the ridge reflects the asperities on the particle surface. There is a lot less variation in the adhesion profile, but peaks of adhesion can be seen on the ridge sides and the lowest adhesion can be seen at the lowest point in the height profile, in line with the polystyrene beads.

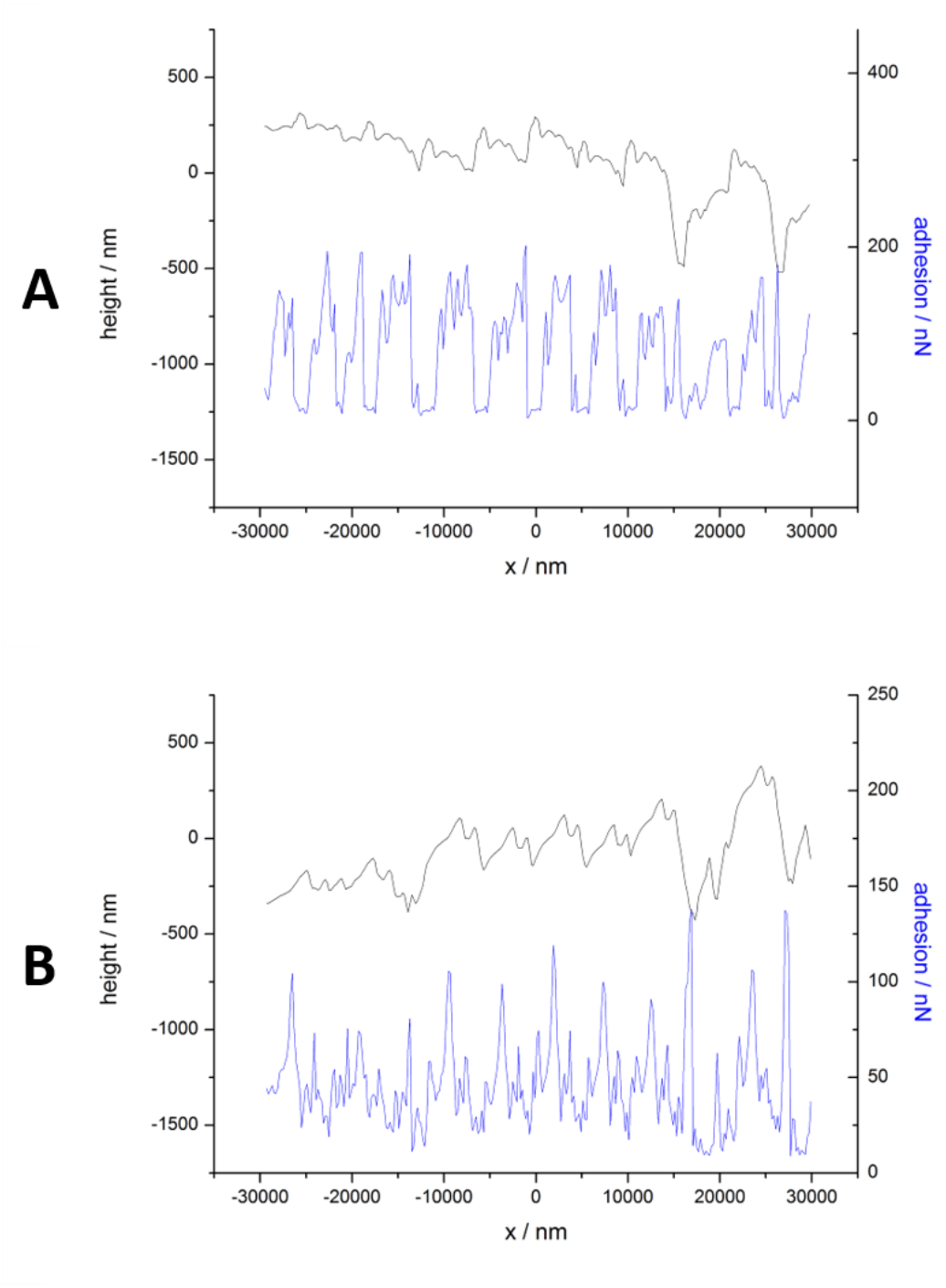


Figure 4.37: An example of the average profiles of the height (black) and adhesion (blue) of a Respitose SV003 particle scan for A) 1 µm high ridges and B) 5 µm high ridges.

4.6 Chapter Conclusions

In conclusion, a variety of morphologies have been produced by varying the spacing and height of TPP ridges. These were then characterised and confirmed to possess ridge heights of 1 µm, 3 µm and 5 µm and ridge spacings of 1 µm, 3 µm and 8 µm. Two different consistent surface chemistries have been generated and a ppHex coating was selected to cover the TPP morphologies. Colloidal probe microscopy, was then used to assess the effect of particle adhesion to these TPP well-defined micron scale morphologies.

Overall, a clear trend between particle contact area and adhesion recorded both on the ppHex control and the TPP coated morphologies is seen, with polystyrene 10 µm beads > 5 µm beads > Respitose SV003 particles. This reduction in contact area in this same sequence will reduce the van der Waal attraction and hence the adhesion between particle and the surface[19]. The TPP morphologies have been shown to dramatically reduce the overall adhesion, in comparison to the substrate. The particle type used on the TPP morphologies, also effects adhesion to the sample based on physical dimensions, as certain particle types are able to penetrate between the ridges and contact the substrate for certain ridge-particle parameter combinations, thereby showing a significantly higher adhesion.

This showed that ridge height had a significant effect on particle adhesion, with 5 µm < 3 µm < 1 µm for the polystyrene beads, but 3 µm < 5 µm < 1 µm for the Respitose SV003 particle for all ridge spacings. Insights into the possible factors contributing to these results were possible due both to the quantitative measurements, and the evaluation of adhesion maps collected across the morphologies. One possible explanation for the trend of the polystyrene beads outlined was that increasing ridge height, increases the ridge aspect ratio. This will result in an increase in curvature at the top the ridge and straighter sides, and therefore the higher ridges behaves increasing like spikes and there is a reduction in contact area between the asperities and the particle.

In contrast, the different spacing of the ridges produces two differing trends in adhesion to the polystyrene beads. If the spacing was larger than the particle a significant increase in adhesion was seen. If the particle cannot penetrate the valleys of the roughness, for the 1 µm high ridges, a significant effect on particle adhesion was seen with 3 µm < 1 µm for the polystyrene beads. In contrast, the 3 µm and 5 µm high ridges showed the opposite trend when the particle is unable to descend between the ridges a significant effect on particle adhesion was seen with 1 µm < 3 µm < 8 µm for the polystyrene beads. From evaluating the profiles, it can be seen that there is higher adhesion to the side of the ridges, but a minimum adhesion in the centre between the ridges. This is likely due to higher aspect ratio ridges possessing a steeper ridge top, therefore for the side of the ridges the contact area increases with increased spacing, however, for the lower aspect ratio the opposite is the case. Therefore, high aspect ratio ridges with small spacing would provide an optimal reduction in particle adhesion. For the Respitose SV003 particle, there is a lot less variation in the adhesion profile, but peaks of adhesion can be seen on the ridge sides and the lowest adhesion can be seen at the lowest point in the height profile, in line with the polystyrene beads.

4.7 Chapter References

1. Zeng, X. M., Martin, G. P. & Marriott, C. *Particulate Interactions in Dry Powder Formulations for Inhalation*. (Taylor & Francis, 2001).

2. Podczeck, F. (The S. of P. U. of L. *Particle-particle Adhesion in Pharmaceutical Powder Handling*. (Imperial College Press, 1998).

3. Pawley, J. B. *Handbook Of Biological Confocal Microscopy*. *Springer* (Springer US, 2006). doi:10.1007/978-0-387-45524-2

4. Technology, N. µscan technology. at <http://www.nanofocus.com/technology/measurement-principles/uscan-technology/>

5. Wyant, J. C. White Light Interferometry. in *Proc. SPIE - Int. Soc. Opt. Eng.* (ed. Caulfield, H. J.) **4737,** 98–107 (2002).

6. Instruments, N. Interferometry. at <http://nanoscience.com/technology/optical-profiler-technology/confocal-wli-pattern-projection-focus-detection/interferometry/>

7. Polytec. Basics of White Light Interferometry. at <http://www.polytec.com/us/solutions/3-d-surface-profiling/basics-of-white-light-interferometry/>

8. Instruments, N. WLI vs Zeta 3D Optical Profilometry. at <http://nanoscience.com/technology/optical-profiler-technology/confocal-wli-pattern-projection-focus-detection/pattern-projection-focus-detection/comparison-white-light-interferometry/>

9. Zelzer, M. Plasma Polymer Gradients: Developing A Tool For The Screening Of Biological Responses To Surfaces. (2009).

10. H. Biederman (editor). *Plasma Polymer Films*. (Imperial College Press, 2004).

11. Friedrich, J. Mechanisms of Plasma Polymerization - Reviewed from a Chemical

Point of View. *Plasma Process. Polym.* **8,** 783–802 (2011).

12. Yasuda, H. *Plasma polymerization*. (Academic Press, 1985).

13. Hegemann, D. Plasma polymerization and its application in textiles. *Indian J. Fibre Text. Res.* **31,** 99–115 (2006).

14. Bruker Application Note #133: Introduction to Bruker's ScanAsyst and PeakForce Tapping AFM Technology. at <https://www.bruker.com/fileadmin/user_upload/8-PDF-Docs/SurfaceAnalysis/AFM/ApplicationNotes/Introduction_to_Brukers_ScanAsyst_and_PeakForce_Tapping_Atomic_Force_Microscopy_Technology_AFM_AN133.pdf>

15. Zelzer, M., Albutt, D., Alexander, M. R. & Russell, N. a. The role of albumin and fibronectin in the adhesion of fibroblasts to plasma polymer surfaces. *Plasma Process. Polym.* **9,** 149–156 (2012).

16. Zelzer, M. *et al.* Investigation of cell-surface interactions using chemical gradients formed from plasma polymers. *Biomaterials* **29,** 172–184 (2008).

17. Arsoy, Z., Ersoy, B., Evcin, A. & Icduygu, M. G. INFLUENCE OF DRY GRINDING ON PHYSICOCHEMICAL AND SURFACE PROPERTIES OF TALC. *Physicochem. Probl. Miner. Process* **53,** 288–306 (2017).

18. Hooton, J. C. *et al.* An Atomic Force Microscopy Study of the Effect of Nanoscale Contact Geometry and Surface Chemistry on the Adhesion of Pharmaceutical Particles. *Pharm. Res.* **21,** 953–961 (2004).

19. Chan, H.-K. Dry powder aerosol drug delivery—Opportunities for colloid and surface scientists. *Colloids Surfaces A Physicochem. Eng. Asp.* **284–285,** 50–55 (2006).

20. Aksak, B., Hui, C.-Y. & Sitti, M. The effect of aspect ratio on adhesion and stiffness for soft elastic fibres. *J. R. Soc. Interface* **8,** 1166–75 (2011).

21. Röhrig, M., Thiel, M., Worgull, M. & Hölscher, H. 3D Direct laser writing of nano- and microstructured hierarchical gecko-mimicking surfaces. *Small* **8,** 3009–3015 (2012).

5 Evaluation of Bulk Powder Deposition to Printed Morphologies

5.1 Introduction

In Chapter 4, the effect of well-defined micron scale morphologies on particle adhesion was evaluated on a single particle basis using colloidal probe microscopy. However, while this provides valuable fundamental interaction insight, the labour intensive process needed to prepare particles for adhesion measurements restricts the number of particles used and level of detail that can be analysed[1]. As the orientation, size and asperities present on the area interacting with the substrate all affect the results of the measurement, the restriction on the number of particles evaluated by this technique is particularly important when trying to provide insight into the behaviour of a polydisperse bulk powder as often seen in pharmaceutical processing[2]. Therefore colloidal probe microscopy is often used in conjunction with a bulk powder system technique[3]. Consequently, in order to evaluate the applicability of the data gathered thus far, a bulk powder deposition technique was pursued. One particular pharmaceutical area where particle adhesion is particularly problematic is respiratory delivery. It was, therefore envisioned, that the future scope of this work could entail the morphologies being applied to the internal surfaces of inhalers in order to aid in the fluidisation and deagglomeration of the powder formulation. This could facilitate strategies to prevent adhesion to the device and loss of drug. To this end a novel methodology was developed to investigate how aerosolised particles will be affected by the TPP morphologies.

The focus of this chapter is therefore to identify a bulk technique that provides the ability to assess the effect of the TPP well-defined micron scale morphologies on aerosolised particles.

5.1.1 Bulk Particle Interaction Testing

In order to evaluate the behaviour of a bulk powder a range of multiple particle systems interaction measurement systems are used. These techniques utilise; ultrasonic vibration, impact separation, centrifugal force, aerodynamic and hydrodynamic force to measure particle interactions[4,5].

5.1.1.1 The Centrifuge Technique

The centrifuge technique is a widely used technique, in the pharmaceutical industry, to measure particle interactions[2], to a variety of materials often presented in a compressed disk format[6]. This technique is based on the measurement of the centrifugal force needed to remove a particle of defined mass (m) generated during the angular rotation of a substrate. By controlling the distance the substrate of interest is mounted from the centre of rotation (r) the force of adhesion (F_{ADH}) can be calculated from the angular velocity (ω) needed to separate the particle from the substrate using equation 5.1[7].

$$F_{ADH} = m\omega^2 r \qquad (5.1)$$

During the experiment the angular velocity is incrementally increased, with the centrifuge stopped to allow imaging of the particles remaining on the substrate. The mean force particle adhesion force is then recorded[8]. By altering the angle of the substrate frictional forces can also be calculated[7,9]. It is worth noting that the centrifuge technique requires two different forces; the so called “press-on” force, which is needed to adhere the particles to the surface, and the “spin-off” force, which involves the rotation of the substrate in the opposite direction to remove the attached particles[10].

5.1.1.2 Ultrasonic Vibration

As the name suggests, the ultrasonic vibration technique evaluates the force required to remove a particle from a substrate based on the frequency of the ultrasonic probe[5]. Frequencies in the MHz range can be used to remove particles greater than 0.3 µm. However, the substrate vibration time is also a critical factor, as longer run times can result in particle removal at lower frequencies. This technique is unsuitable for particles or substrates which undergo plastic deformation, as this can complicate results as the vibration may be sufficient to create a press-on force and hence alter the effective particle contact area and hence adhesion[4].

5.1.1.3 Impact Separation

This technique involves the application of an impact force on the underside of a substrate with particles adhered to the upper surface, and the particle acceleration generated is recorded[5]. The impact is generated generally by a hammer fixed to a pendulum[11], but is usually only effective in removing particles greater than 5 µm[4].

5.1.1.4 Hydrodynamic Technique

This technique measures the adhesion force by identifying the threshold force generated from the drag of the flow of the liquid which detaches a particle. This relationship is, however, drastically altered with particles less than 1 µm[4,5].

5.1.1.5 Aerodynamic Techniques

These techniques can be divided into two categories, those that investigate particle adhesion, and those that are used to evaluate particle interactions in air flow and can be used to evaluate particle dispersion.

Aerodynamic techniques to measure particle adhesion use a jet of gas and the adhesion and friction can be calculated based on the velocity of the gas and the

direction of the jet. However, this technique is mainly restricted to particles greater than 10 µm in size[4].

Aerodynamic techniques used for investigating particle dispersion, however, are far more widely used in the pharmaceutical industry. Impingers and impactors are used to test the performance of an inhalation formulation, separating out the aerosolised particles based on their aerodynamic diameter and therefore providing insight into the deposition of particles in different stages of the airways.

However, none of these techniques provide the desired insight into both the particle deposition of a fluidized formulation and possible detachment through re-entrainment. Therefore, in order to evaluate our morphologies and their effect on particle interactions in a multi- powder system, a novel experiment was devised. This chapter details the experimental setup, to measure the effect on deposition of inhalable particles of the TPP morphologies. This involved utilising a standard next generation impactor (NGI) and applying the TPP morphology substrates in the collection plates.

5.1.2 Next Generation Impactor

As discussed in Chapter 1, for effective respiratory drug delivery an aerodynamic diameter of 1 – 5 µm is required. For an *in vitro* assessment of the performance of an inhalation formulation, an impactor is considered the gold standard instrumentation. The impactor acts by fractionating an aerosol according to the aerodynamic diameter of the particles, larger particles will be carried by their inertia into the impaction plates, whereas smaller particles are able to change direction with the air flow and continue further downstream. The next generation impactor (NGI) was designed specifically for use within the pharmaceutical industry, incorporating pre-agreed user specifications from a consortium of pharmaceutical scientists.

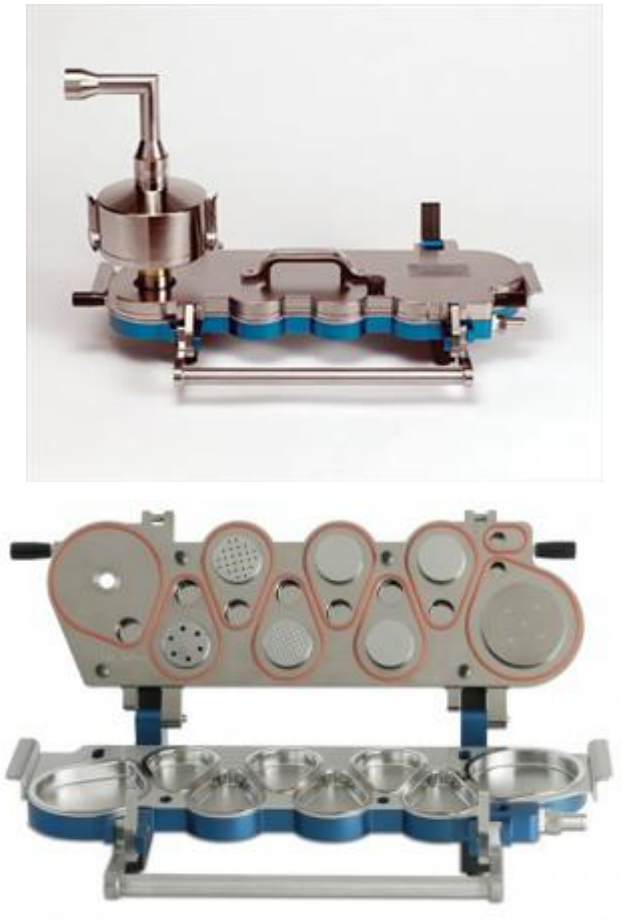


Figure 5.1: Photographs of a Next Generation Impactor closed (top) and in the open position (bottom) to reveal the inner collection pans. Images adapted from[12].

The NGI measures the aerodynamic size distribution of particles in a formulation by incorporating seven stages, consisting of a set of nozzles directly above a collection plate (Figure 5.1), with logarithmically consistent spaced particle size cut offs and a micro-orifice collector. The formulation is drawn through the device using a vacuum pump at the distal end of the NGI, reproducing the peak flow value of an inspiration which aerosolises the formulation, entraining the particles within the air flow and drawing them through the series of nozzles. The device to be tested is inserted using a suitable adaptor in a USP Pharmacopoeia induction port, which is used to simulate the sharp bend in the oropharyngeal region of the respiratory tract. Optionally, a pre-separator can also be used which is designed to remove large carrier particles if a DPI is being assessed.

5.1.2.1 Aerodynamic Fractionation

The setup for a typical stage of the NGI is shown in Figure 5.2, with the key dimensions highlighted. As the stages progress through the NGI, the nozzles both increase in number and reduce in diameter, resulting in increasing air flow rate and therefore the impaction collection of smaller particles.

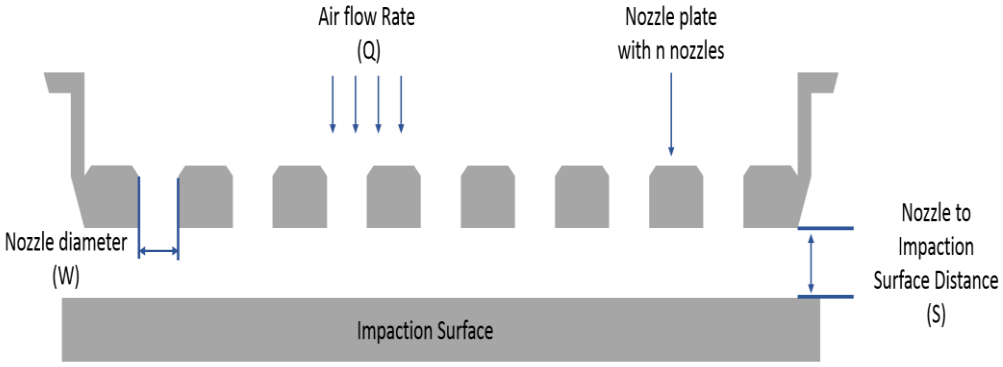


Figure 5.2: A schematic of an NGI stage with the key parameters for aerodynamic diameter assessment labelled. Adapted from Marple *et al*[13].

The impactor design is defined by three key parameters:

1) The Reynold's number (Re) – for particles to deposit as expected for their aerodynamic diameter, the flow through the nozzles must be laminar. In order to achieve this the Re was mainly kept between 500 and 3000[13]. For the purposes of impactor design the equation for Reynold's number seen in equation 3.1 can be adapted[14] based on the average velocity of the air through the nozzles (V_0), calculated in equation 5.2. This allows the calculation of the number of nozzles (n) and nozzle diameter (W), needed to keep Re in range for a given flow rate (Q) as seen in Equation 5.3, which means the number of nozzles must be increased with decreasing nozzle diameter.

$$V_0 = \frac{4Q}{n\pi W^2} \qquad (5.2)$$

$$Re = \frac{4\rho Q}{n\pi\mu W} \quad (5.3)$$

where μ is the air viscosity and ρ is the air density.

2) In order to ensure good particle collection efficiency and a sharp cut off of each stage, the ratio of the distance between nozzle and impaction plate to the nozzle diameter (S/W) must be kept between one and ten[13].
3) Finally, for multiple nozzle impactor stages, airflow from inner nozzles can disrupt the jets from nozzles in the outer edges of the stage; this "cross-flow" can prevent the air jets impacting on the collection plate. Therefore, in order to prevent this Fang et al[15] found that the cross-flow parameter (Xc) must be kept below 1.2 when n number of nozzles are arranged with a diameter of the nozzle cluster (Dc):

$$X_C = \frac{nW}{4D_c} \quad (5.4)$$

These parameters allow the impactor to separate out particles related to their aerodynamic properties. The actual number and diameter of nozzles were selected in order to encompass a series of stages in the 0.5 µm to 5 µm particle aerodynamic diameter range of interest. The behaviour of particles in an air flow can be modelled by Stoke's number (St) which can be calculated as in equation 5.5, when adjusted for impactors using equation 5.1 and using the aerodynamic diameter (d_{ae}) of a particle with density (ρ_{ae}) and Cunningham slip factor for a particle of size d_{ae} (C_{ae}).

$$St = \frac{4\rho_{ae} Q C_{ae} {d_{ae}}^2}{9n\pi\mu W^3} \quad (5.5)$$

In order to determine the parameters needed for a given particle cut off (d_{50}), the Cunningham slip factor C_{50} is used. For particles greater than 1 µm this slip factor is equal to 1.0 and therefore the following equation can be used[13]:

$$d_{50} = \sqrt{\frac{9\pi\mu n W^3}{4\rho_{ae} Q}} \sqrt{St_{50}} \quad (5.6)$$

If inertial impaction is the main mechanism of deposition, a $\sqrt{St_{50}}$ near to 0.495 is needed when the Reynold's number criteria is met[16]. Therefore, keeping these parameters in range, d_{50}, n and W can be calculated for each stage for the range of flow rates from 30 L/min to 100 L/min. The cut-off sizes for the stages in the NGI as shown in Table 5.1.

Table 5.1: The cut off particle sizes for each of the stage of the NGI at varying flow rates. Adapted from Marple et al[13]

	D_{50} (µm) at each flow rate (L/min)		
Stage	**30**	**60**	**100**
1	11.7	8.06	6.12
2	6.40	4.46	3.42
3	3.99	2.82	2.18
4	2.30	1.66	1.31
5	1.36	0.94	0.72
6	0.83	0.55	0.40
7	0.54	0.34	0.24

5.2 Chapter Aims

The aim of this chapter is to develop a new methodology for assessing the effect of varying substrate morphology or chemistry on the particle deposition behaviour of particles aerosolised from a respiratory formulation. Once this technique has been developed a subsequent evaluation of the model two photon polymerised morphologies developed in Chapter 4 will be undertaken.

5.3 Chapter Objectives

- Develop a method to combine the aerosolisation seen in a NGI and multiple particle deposition method.
- Select the appropriate parameters for testing a chosen formulation.
- Utilise this technique to evaluate the deposition behaviour of the inhalation formulation on well-defined semi-circular test micron scale morphologies.

5.4 Materials and Methods

5.4.1 Materials

Micronized Beclomethasone Dipropionate (BDP) was purchased from Meridian Pharmaceuticals (Alabama, US). The carrier particle was chosen to be the same as used in the colloidal AFM adhesion experiments, lactose Respitose SV003, (DFE Pharma, Goch, Germany). Lactose fines were produced in-house at AstraZeneca by micronization of lactose monohydrate followed by conditioning for restoration of crystallinity and then provided for use in this formulation.

5.4.2 Preparation of DPI Formulation

The formulation was one of several prepared by Simon Åslund for an evaluation on the effect of processing time on fine dispersion[17]. A formulation comprised of 92% lactose carrier (Respitose SV003), 4% BDP and 4% lactose fines was chosen, as the carrier was the same as used in the colloidal probe experiments. The formulation produced a MMAD of less than 5 µm as required for inhalation and there was a readily available UPLC method for quantifying the BDP. The formulation was then prepared by mixing at 800 rpm for 30 minutes using a Diosna P1-6 high shear mixer (Diosna, Dierks & Söhne Gmbh, Osnabrück, Germany) equipped with a 1.2L stainless steel mixing vessel. A 350 g batch size was prepared in an environmentally controlled room with a RH of 20% and temperature of 22 ˚C. The chopper was dismantled before use and no cooling was applied. The mixer was thoroughly cleaned between each batch.

5.4.3 Preparation of Substrates for Deposition Experiments

Several substrates were TPP printed with well-defined micron scale morphologies as described in the final settings in Section 3.4.5 and coated with ppHex, as outlined in Section 4.4.4, prior to shipping to Sweden for the particle deposition experiments. Several ridge patterns were prepared; three different ridge heights were trialled, 1 µm, 3 µm and 5 µm, and each was printed to cover a 50 µm by 50 µm area. Each area had ridges spaced with either 1 µm, 3 µm or 8 µm. For the initial run the substrates had each of the different morphologies with each row having a consistent ridge height with each of the ridge spacings (Figure 5.3).

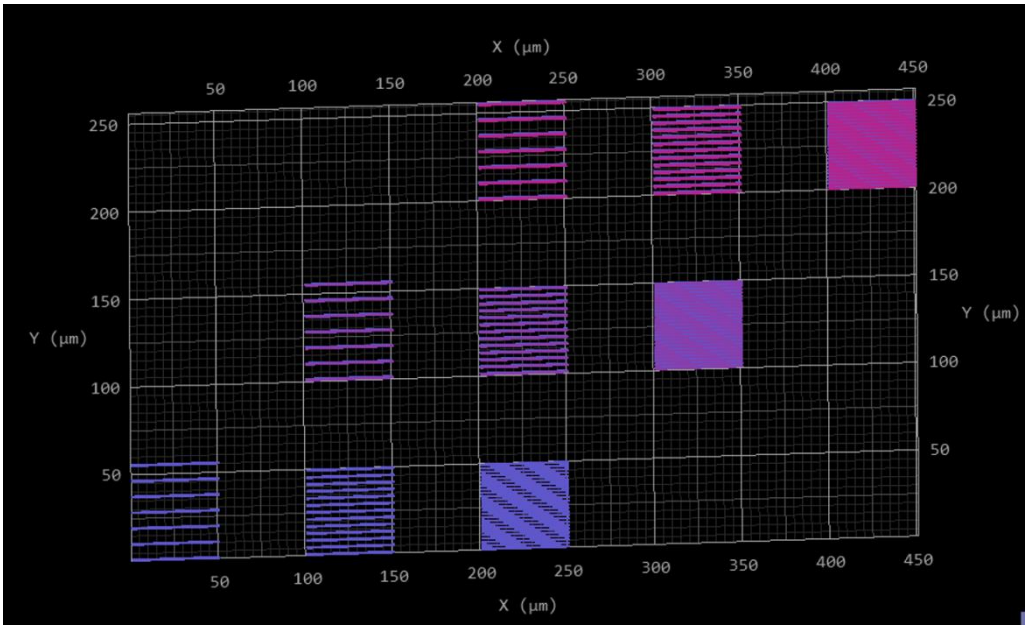


Figure 5.3: An overview of the substrate design with the nine different morphologies being trialled. On the bottom row, all three patterns are 1 µm high, with 8 µm, 3 µm and 1 µm spacing respectively. The second row all the designs have a ridge height of 3 µm and on the top row all the ridges have a height of 5 µm.

5.4.4 Next Generation Impactor (NGI)

The next generation impactor (NGI) was used equipped with an inflatable inlet valve, induction port and pre-separator (Figure 5.4). Experiments were split into standard NGI experiments to evaluate the aerodynamic particle size distribution and

experiments to investigate the effect of well-defined micron scale printed morphologies on particle deposition.

Before use, collection plates not being used for substrate testing were pre-coated with a mixture of Brij/glycerol/ethanol, 0.5 mL for the small plates and 1 mL for the larger plates. This was to reduce any excessive particle bouncing and particle re-entrainment. 15 mL of ethanol was pipetted in the circular cup of the scalper collection surface in the pre-separator. The flow rate was then adjusted using a flow meter.

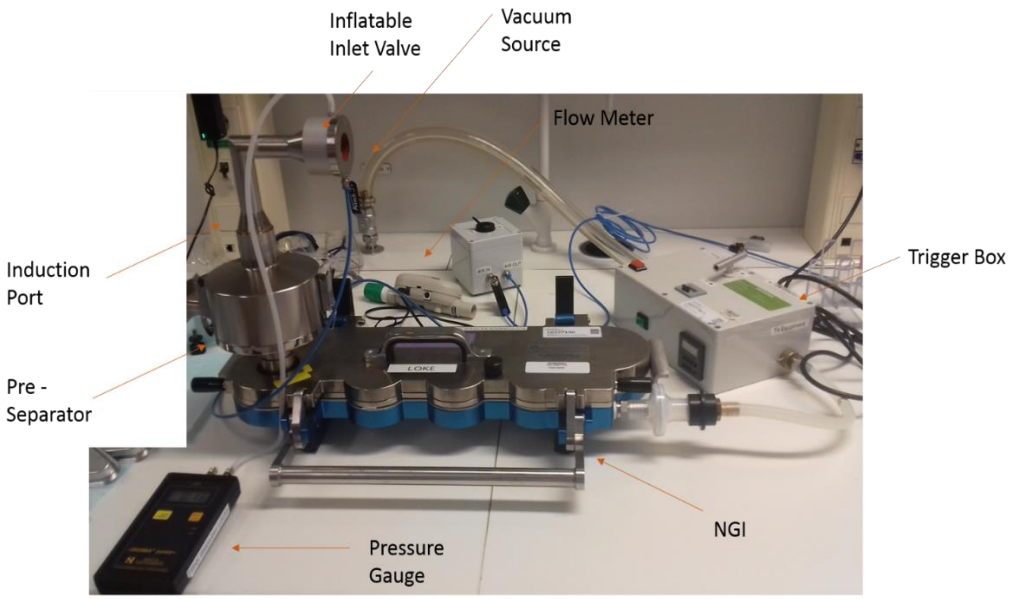


Figure 5.4: The Next Generation Impactor setup used for these experiments, with key components labelled.

Once the flow rate was adjusted to 77 L/min, the formulation was introduced using an in-house AstraZeneca inhaler designed for testing formulations called the Screenhaler, a simple cylindrical device with a 7mm diameter channel (Figure 5.5). The Screenhaler was inserted in the inflatable inlet valve, with a port to allow monitoring of the pressure drop during the experiment using a Digima Junior pressure gauge (Special Instruments, Noerdlingen, Germany). Each actuation of formulation was introduced, with a flow rate of 77 l/min introduced using a vacuum pump for 3.1 seconds, creating a 1.45 kPa pressure drop. A lower pressure drop is

needed for these experiments due to the simplicity of the inhaler, as calculated by previous in-house experiments.

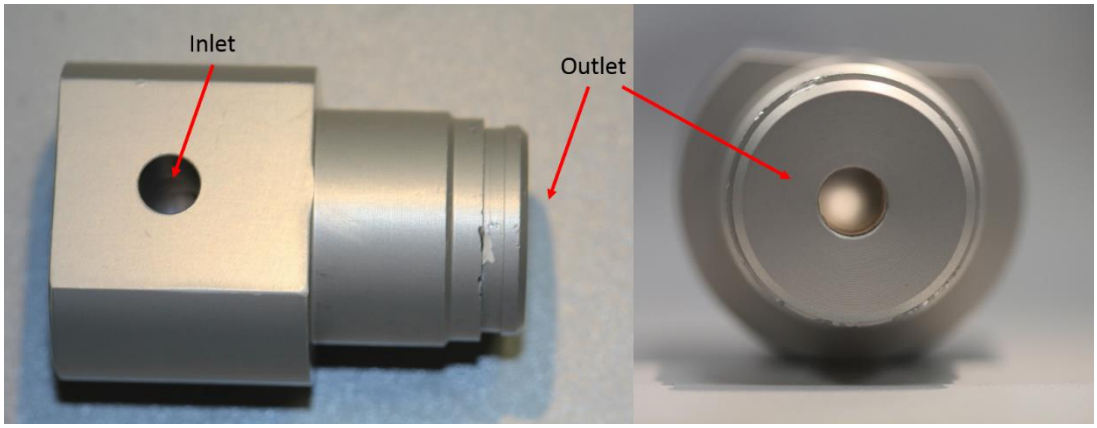


Figure 5.5: Photographs of "Screenhaler" from above (left) and from the outlet (right) used for fine particle assessment which is basically a cylindrical channel. The outlet is connected to the NGI via the USP throat. The diameter is 7.0 mm and the length is 45 mm.

5.4.4.1 Standard NGI experiment

3 actuations of 5 mg of the formulation or 10 mg of the formulation were introduced to the NGI setup. Post run, 20 mL Internal Standard (99.5% Ethanol, 0.5% Fluocinolone Acetonitride) was added to the throat, pre-separator, the individual impactor collection plates and filter. To ensure collection of any API on the apparatus, each collection plate was put on a rotating table for 30 minutes. The pre-separator and throat were stoppered and rotated for 15 minutes. Subsequently, a 0.5 mL aliquot of the each component solution was pipetted into a UPLC vial and diluted with 0.8 mL phosphate buffer pH 3.2. These were then analysed by UPLC. Fine Particle Fraction (FPF) was calculated from the amount of BDP with an aerodynamic diameter less than 5.0 µm divided by the dose delivered to the impactor. A linear regression of the cumulative percentage of drug mass versus the aerodynamic particle size plotted on a logarithmic scale was undertaken. The Mass Median Aerodynamic Diameter (MMAD) was calculated as the particle size below which 50% of the particle population falls. The geometric standard deviation (GSD) was then

calculated as the square root of the particle diameter in µm when the cumulative mass is equal to 84.13% divided by the particle diameter in µm when the cumulative mass is equal to 15.87%[18].

5.4.4.2 Particle Deposition Experiments

In the particle deposition experiments, the substrates were placed in non-coated collection plates or on the second collection surface of the pre-separator. The glass coverslip substrates were affixed by small sections of tape and aligned under the nozzle, using a propelling pencil to mark the centre of the nozzle on the subsequent collection surface. Both two and three actuations of 5 mg of the formulation were investigated; for the particle deposition experiments on printed substrates two 5 mg actuations of the formulation was introduced to the NGI setup.

5.4.5 Ultra Performance Liquid Chromatography

For analysis of the BDP, Ultra Performance Liquid Chromatography equipped with a C18 Acquity BEH 2.1 x 50 mm, 1.7 mm column (Waters, USA) coupled with a UV detector was used by Simon Åslund. The samples were gradient eluted with 0.03% Triflouroacetic Acid (TFA) in water as mobile phase A, and acetonitrile with 0.03% TFA as mobile phase B with a flow rate of 0.6 mL/ min at 40 ˚C. The IS and BDP was detected with the UV detector using a wavelength of 254 nm. The peaks eluted at 0.89 min (IS) and 1.46 min (BDP). Data acquisition was carried out with a Waters Empower data system.

5.4.6 Optical Microscopy

Optical Imaging was performed on both a Malvern Morphologi G3 (Malvern Instruments, Worcestershire, UK) in manual mode and a Zeiss Axio Observer (Carl Zeiss Microimaging GmbH, Jena, Germany). For each printed square, images were

collected at 5x, 20x and 50x zoom focused on the top of the ridges and on the substrate.

5.4.7 Image Analysis

The images were then loaded and processed using the ImageJ software (NIH, Bethesda, USA). For each printed square, imaging was of the top of the ridges and on the surrounding 'control' substrate. The area was then selected to incorporate all the ridges and any particles associated with the ridges, with the measure function used to record the size of the area (Figure 5.6 A). The threshold of the image was then adjusted manually to isolate the particle clusters in a binary black and white image. Occasionally, to achieve appropriate identification of particles, the erode or dilate function, to exclude the ridges and to gain a true likeness of the particle clusters, was used. Once the particle clusters were isolated (Figure 5.6 B), the particle analysis function of the software was utilised to automatically count and measure the area of the clusters (Figure 5.6 C). The multi-point tool was then used to manually count the number of individual particles in the area. This data was then combined with the same information from the corresponding image focused on the substrate to incorporate all particles in the area of interest.

The selected area in the image was then inverted and the same steps were undertaken with the rest of the image used as the non-printed control area. The particle area coverage and the particle number results were then adjusted for the area analysed and normalised by dividing them by their control counterparts. This was to overcome any particle deposition inconsistency relating to distance of the TPP printed area from the nozzle centre. For ease of evaluation, this normalised result was also scaled to spread between -1 (maximum reduction in adhesion) and +1 (maximum increase in adhesion).

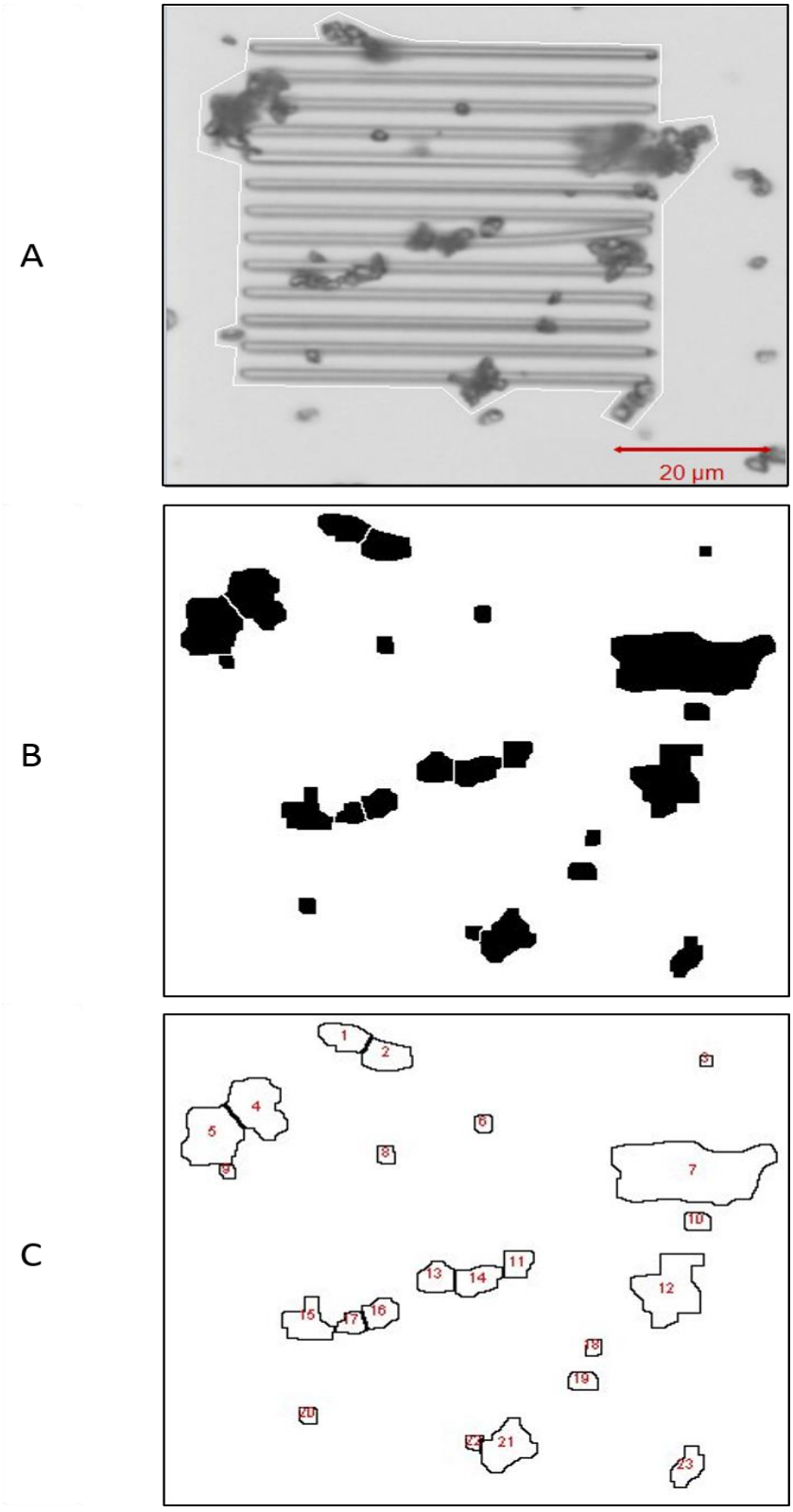


Figure 5.6: An example of the processing of images using the ImageJ software to highlight the particle clusters. A) The printed area to be investigated is determined including any particles associated with the ridges. B) The image is now a binary black and white image after thresholding to just highlight the particle clusters. C) The particle analysis function of the software is used to identify the clusters and calculate the cluster area. This is then repeated with the image of the same area focused on the substrate and the particles are amalgamated into one result.

5.4.8 Statistical Analysis

Statistical significance between the particle deposition on different ridge heights and spacing was carried out using a one-way ANOVA with a Tukey's post hoc analysis at a p-value of 0.05 using GraphPad Prism. A Dunnet's post hoc test was also used to compare each of the data sets to the control mean of 1. The skewness of the distribution of the histogram displaying particle cluster area was then calculated using the data analysis toolpak in Excel.

5.5 Results and Discussion

5.5.1 Formulation Test and Determination of FPF and MMAD

In order to evaluate the un-modified behaviour of the formulation in the NGI, a series of test runs were undertaken. 5mg of the formulation was actuated 3 times, over two different runs. The distribution of BDP collected throughout the NGI was recorded (Figure 5.7). This clearly shows that the most BDP deposition occurred in the throat, pre-separator and stages 2 and 3. With 104 ± 12.0 µg deposited in the throat, 353 ± 2.6. µg in the pre-separator and 41 ± 1.7. µg and 33 ± 1.7. µg in stages 2 and 3 respectively. From this the FPF, GSD and MMAD could be calculated as seen in Table 5.2, which demonstrated similar results to those of Thalberg *et al.*[17]. This confirmed the suitability of this formulation to be used in this method development, as it possesses a MMAD of 4.07 µm and therefore is in the range of particle size known to deposit in the bronchial and alveolar regions of the lungs necessary for effective respiratory drug delivery[18]. In order to provide a thorough particle coverage, it was decided that substrates would be placed on the flat collection surfaces on the pre-separator and stage 2 and 3 for the particle deposition experiments.

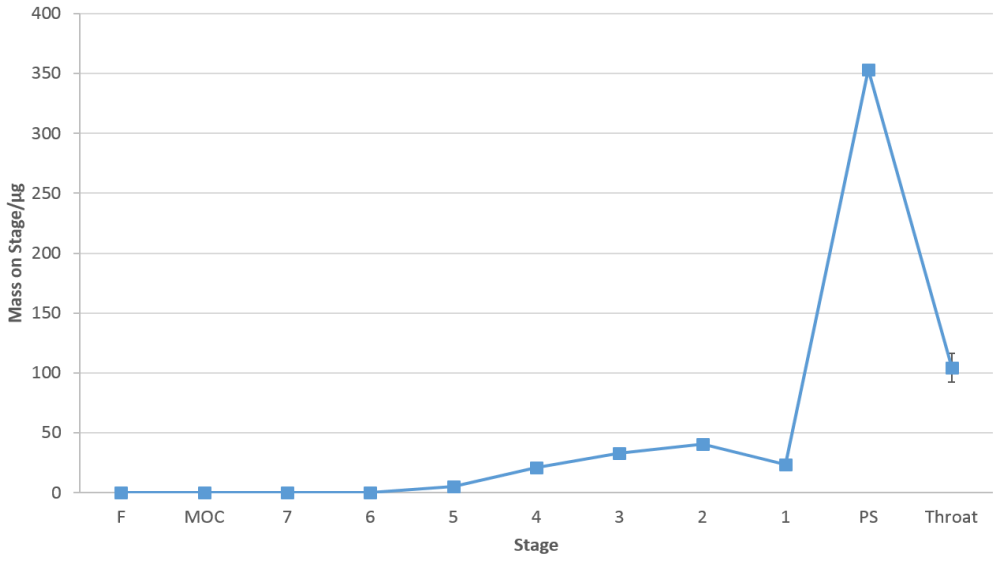


Figure 5.7: Fine particle assessment of BDP in the formulation, showing particle deposition in micrograms ± S.D. at various stages of the NGI.

Table 5.2: A summary of the fine particle fraction (FPF), defined as the percentage of particles less than 5 µm of the delivered dose, the mass median aerodynamic diameter (MMAD) and the geometric standard deviation (GSD) of the formulation.

	FPF % of Delivered Dose n=2	MMAD/ µm n=2	GSD
BDP	13.0±2.5	4.07±1.37	1.86±0.09

5.5.2 Evaluation of Particle Deposition on Non-Printed Coverslips

In order for an assessment to be made on the effect of the TPP morphologies on particle deposition, the substrate would need a high density coverage of the formulation particles. It was therefore decided that an investigation into the resultant particle coverage when the substrate was positioned in different areas of the collection plate surface was needed. As previously mentioned, in an NGI the formulation is drawn through nozzles directly onto the surface below. Therefore, it is reasonable to assume that there will be a difference in particle density directly under a nozzle in comparison to an area adjacent to the nozzles. This could clearly be seen to be so visually (Figure 5.8) and was verified by image analysis (Table 5.3) which showed that the area not under the nozzle (Figure 5.8 A) possessed a low particle density of 0.7% whereas directly under the nozzle (Figure 5.8 B) particle coverage was 10.3%. It was therefore decided that the TPP morphologies should be fixed so as to be aligned with the stage nozzles.

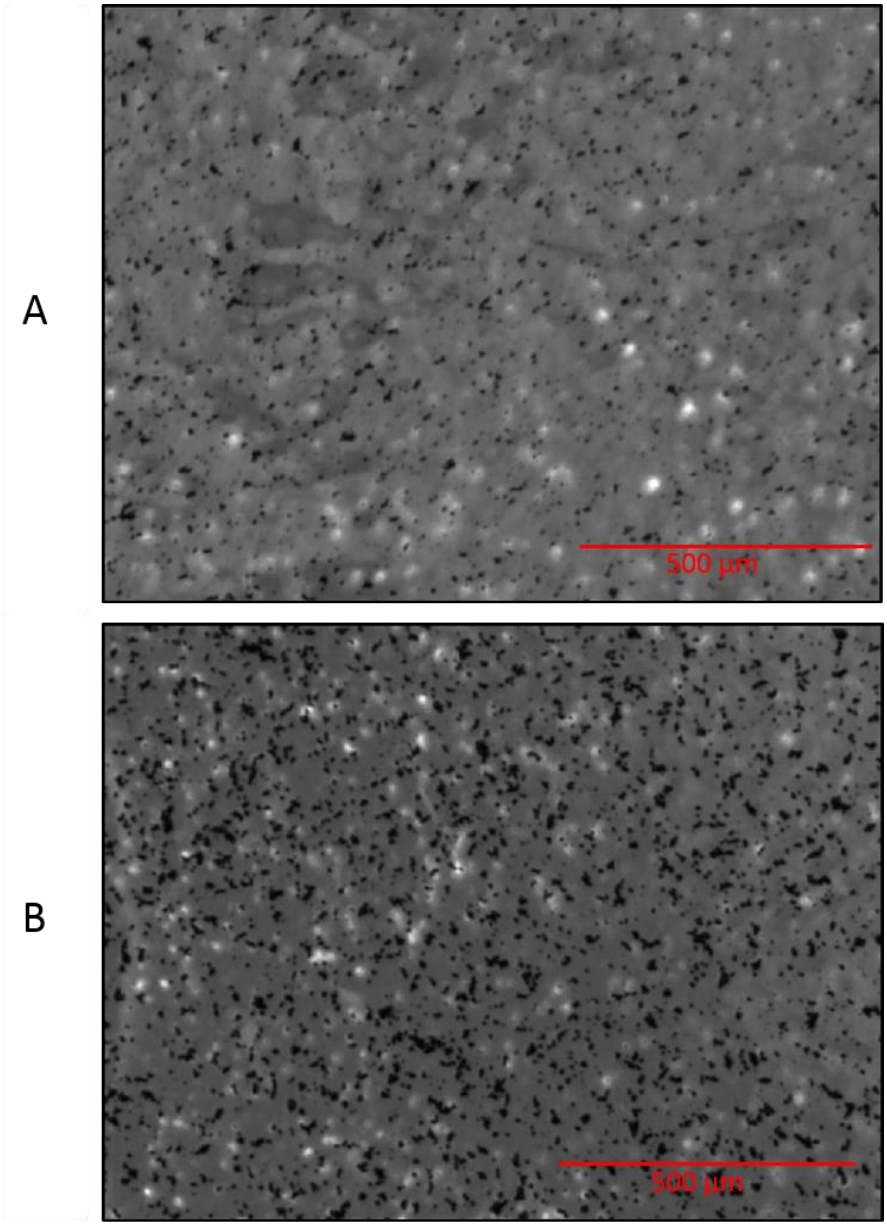


Figure 5.8: Optical microscopy images of the particle deposition on the non-printed substrate A) in the non-nozzle area and B) in the area directly under the nozzle.

Table 5.3: An overview of the particle coverage on the non-printed substrate in the area directly under the nozzle versus the non-nozzle area.

	Particle Area Coverage %	Area Analysed (μm^2)
Non-nozzle area	0.7	1226774
Nozzle area	10.3	708555.6

5.5.3 Evaluation of Initial Two Photon Printed Substrate Run and Methodology Development

One of each of the substrate morphology designs were tested in an initial run in all of the three NGI locations chosen (pre-separator, collection plate 2 and collection plate 3). However, on review of the substrates via optical microscopy, several issues were identified (Figure 5.9) with the initial experimental design.

Firstly, there was less particle deposition than expected from the results seen in Section 5.5.2. When the powder deposition patterns on the substrates[18] were analysed (Figure 5.10), it was evident that the collection surface had shifted when the NGI was operated so that the TPP morphologies were no longer positioned in the nozzle area. This was likely to have occurred as the individual collection plates are removable and so can shift in the NGI tray. To overcome this issue, in subsequent runs the NGI was assembled and closed to settle the collection plates, then, before the alignment of the substrates, the collection plates were attached to the tray to prevent significant movement.

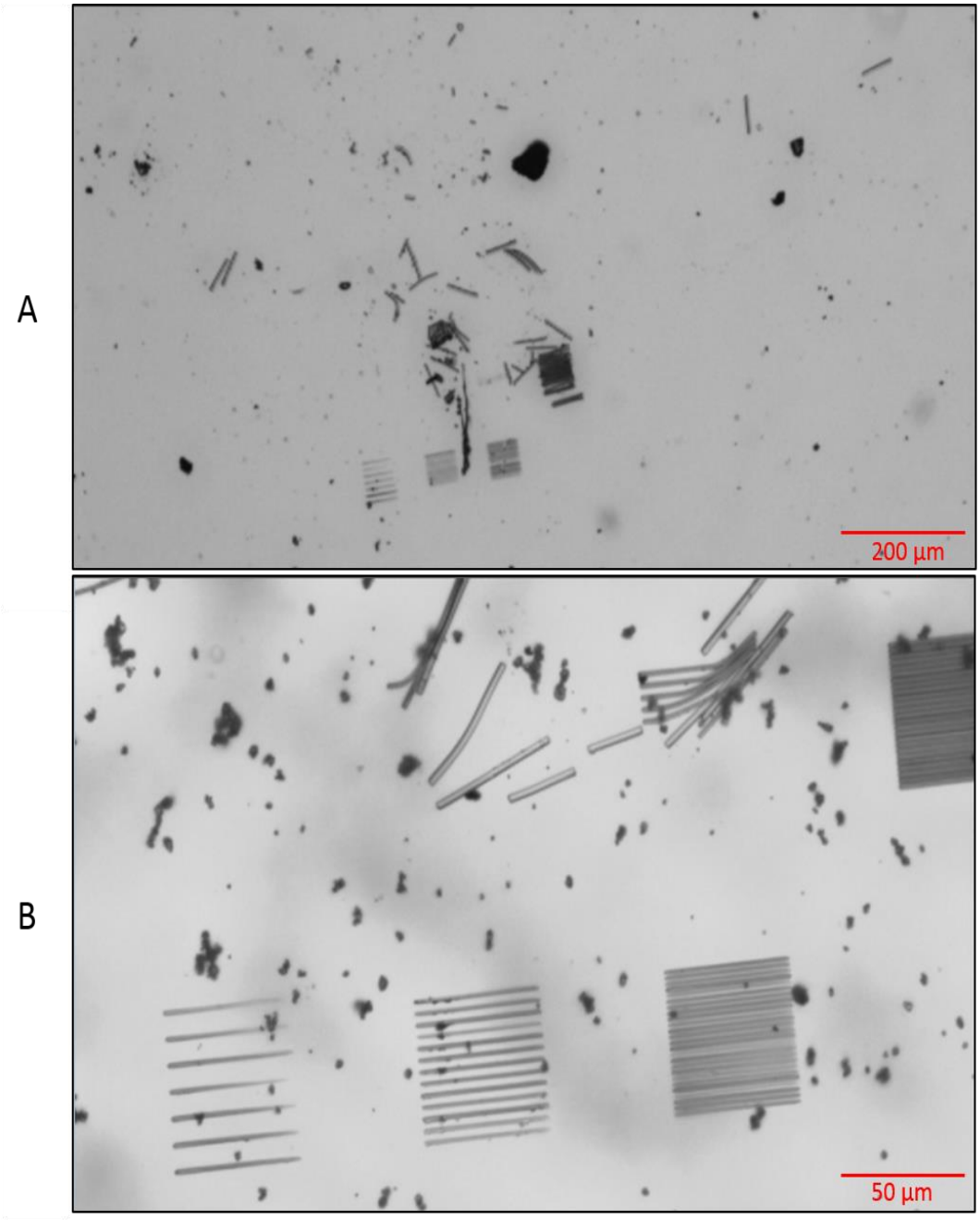


Figure 5.9: An example of the particle deposition in the initial experiments damage to the TPP ridges in A) the pre-separator which may have been caused by the large carrier particle seen and B) in CP2.

The second issue observed, was damage to the TPP ridges (Figure 5.9). This was assigned to two main causes; firstly, for the substrates positioned on the scalper collection surface of the pre-separator it appears that the large carrier particles, in this section of the NGI, impacted and dislodged the TPP ridges. Secondly, a large proportion of ridges were damaged in stage 2, especially the 3 µm and 5 µm high ridges. The disruption of the taller ridges might be as they present more of a barrier to the air flow and therefore more air resistance and more force on the ridges. However, as stage 2 has a slower air velocity, compared to later stages, through the nozzles and therefore a reduced air flow across the collection plate[13], this effect would be expected to be more pronounced on stage 3. A possible explanation for this phenomena could be turbulence of the air flow. As shown in Section 5.1.2.1, the Reynold's number (Re) can be calculated for each stage in the NGI. As stage 3 has 24 holes with a nozzle diameter of 2.185 mm at 77L/min the Re for stage 3 was 2056, whereas for stage 2 with 6 nozzle holes of 4.88 mm it was 3683; a value over 3000 indicating turbulent air flow emitting from the nozzle in this stage[13,14]. The turbulence present in stage 2, but not stage 3, could be the reason for the disruption of the ridges. For the subsequent runs, it was therefore decided that stage 3 was the only NGI stage that substrates should be tested in.



Figure 5.10: A photograph of the substrate affixed on the NGI collection surface, showing the particle deposition pattern (in white) in relation to the position of the TPP morphologies (black dot).

A novel experiment has therefore been established to test areas of substrate morphologies on particle deposition from an inhalation actuation. This successfully allows for a faster method to screen multiple substrate designs in one NGI run. This encompasses both particle deposition and particle re-entrainment for inhalation formulations to gain fundamental insight into particle adhesion to differing morphologies.

The substrates can be affixed in the NGI without affecting its normal operation. Based on the original specifications of the NGI design, roughness will not affect the collection efficiency of the stage as long as it is significantly less than the particle stop distance. This was defined as 5% of the stop distance, which is roughly 25% of the nozzle diameter, therefore for Stage 3 (the stage used with the smallest nozzles) this would be 27 microns, so the printed ridge substrates are well within these limits[13,14]. Likewise the ratio of the separation between nozzle and collection plate to nozzle

diameter must be within 1 and 10, and therefore as the substrates are 180 µm thick they are easily within this limit which could stretch to almost 14 mm.

It is worth noting that the dislodging of the TPP morphologies does indicate that the current TPP process would be unsuitable for the production of morphologies on the interior of an inhaler. However, there are methods to improve the TPP structure adhesion to the substrate, which generally involve increasing the hydrophilicity of the substrate by silanization or plasma etching prior to printing[19]. Both of these processes would not have a subsequent effect on the particle adhesion, as this would be covered by the plasma coat. Therefore, it would be interesting to repeat these experiments with this added step to assess whether this was still an issue.

5.5.4 Evaluation of Effect of Ridge Height on Particle Deposition on Printed Coverslips

Unfortunately, as the substrates were prepared and subsequently shipped for testing in Sweden, there were limited substrates available for the improved experimental set-up. Therefore, all intact ridge areas from both the trial and the developed method runs were analysed and consolidated, in order to provide a significant data set. However, with time a repeat of these experiments would be advisable. Figure 5.11A shows an overview of the data of all the ridge areas analysed, grouped by the height of the ridges in the TPP printed area; this includes all three ridge spacings. For each 50 x 50 µm area, a normalised value was produced using the surrounding control area. This allowed for the accounting of variation in particle deposition that occurred due to the difference in nozzle alignment. This shows that the majority of TPP areas had more particle adhesion than the surrounding control (scaled to be positive results in Figure 5.11A). The comparison between the ridge heights is then seen based on the normalised total particle area and the individual particle count on the TPP ridges in Figure 5.11B and C respectively. Figure 5.11B and C shows that both the 1 µm and 3 µm high ridges have a mean particle count and coverage of roughly double the control, whereas the ridges that were 5 µm high were 4-5 times the control. Subsequent statistical analysis then confirmed that the 5 µm high ridges

possessed significantly higher particle adhesion than the other two ridge heights ($p<0.05$). There is no significant difference between the 1 µm and 3 µm ridge heights with an adjusted p value of 0.8754.

1 µm high ridges are significantly different from the control, and the 5 µm high ridges are statistically highly significantly different with an adjusted p value of 0.0001, but the 3 µm high ridges are not significantly different. A similar trend was seen with the individual particle count (Figure 5.11C) and the significant differences seen were the same. This showed that ridge height had a significant effect on particle adhesion with 3 µm < 1 µm < 5 µm

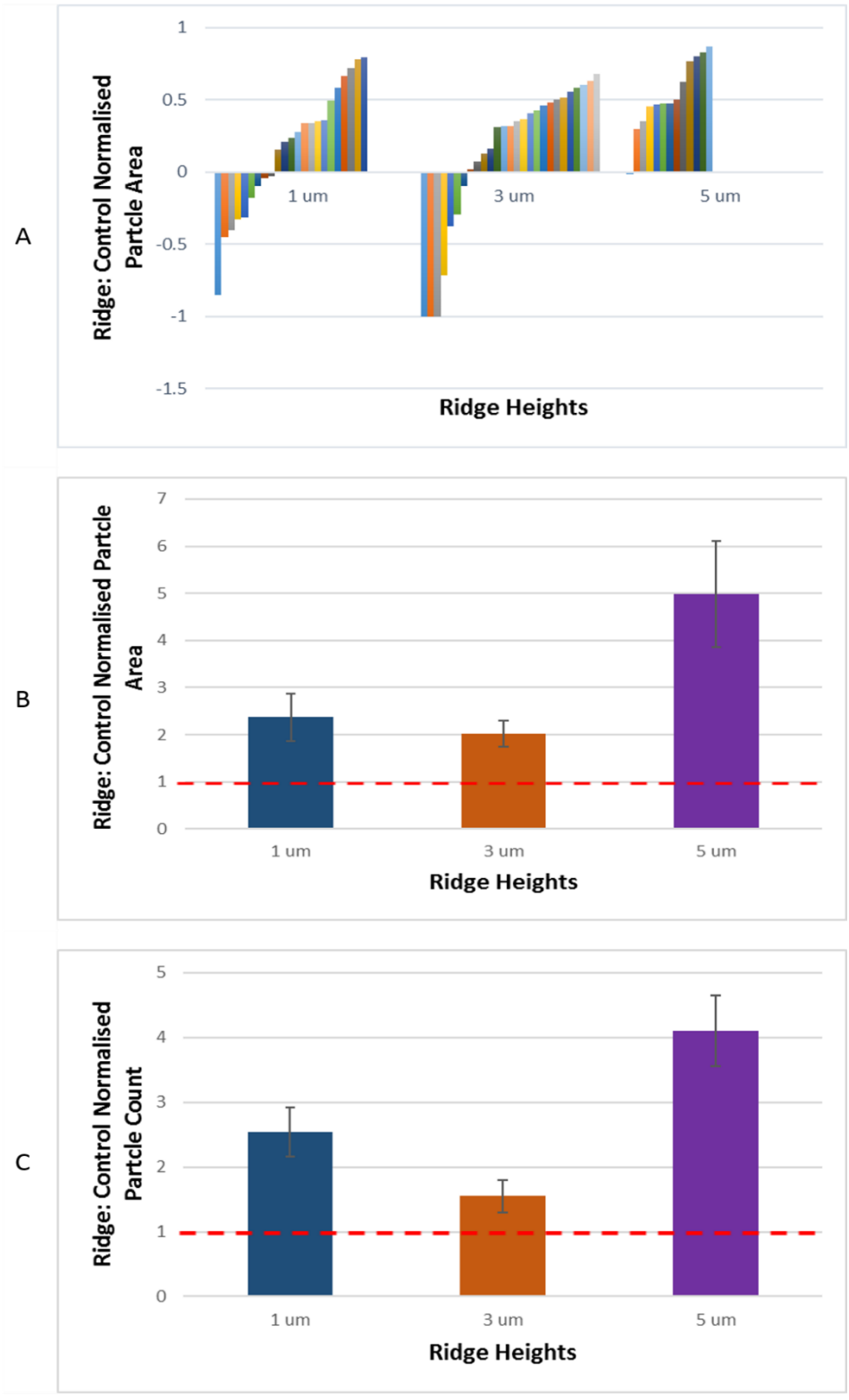


Figure 5.11: A comparison of the particle deposition on the area of printed substrate normalised to their control area evaluating ridges of differing height using. A) An example of the normalised data set, scaled so the control is 0, and bar charts of the mean ± SEM (with control shown in red) of B) the particle area coverage and C) individual manual particle count following aerosolisation at 77 L/min in the NGI.

The ridge areas possessing significantly more particle adhesion than the control is perhaps puzzling as they should be limiting the contact area and hence adhesion[20]. Also, the ridges should be serving to aid particle re-entrainment as for particles larger than the ridges, they will "rock" on a surface asperity allowing the particle to be dragged from the surface and re-entrained[21]. Finally, such surface features should increase the turbulence of the air flow and therefore creating greater lift forces on the particles, which should increase the particle re-entrainment in the air flow and hence decrease the particle deposition seen[22].

However, on closer visual inspection of the optical microscopy images (Figure 5.13), it would appear that many of the particles adhere to the sides of the ridges as oppose to adhering to the top. It is worth considering these results in terms of the two differing processes occurring; particle deposition and re-entrainment. Firstly, during particle deposition the ridges are likely to act as a barrier in the flow of air across the NGI collection plate, the particles are therefore likely to deposit by inertial impaction[23,24]. Secondly, if a particle happened to deposit between the ridge structures an increased contact area would likely occur as the particle will be in contact with the substrate with the same contact area as the control, in addition to the side of the ridge, thereby increasing contact area and any adhesion interactions[25]. Once the particle has deposited on the ridge area, there is a secondary consideration on whether it will re-entrain into the airflow. There might be a decreased chance of this occurring as particles smaller than the ridge height, experience a decrease in lift force due to a "shielding effect"[26] from the ridges. Finally, depending on the ridge spacing a mechanical interlocking effect may occur, providing a stronger adhesion than the flat control surface[24].

To further investigate the reasons for these differences, histograms were produced of the size of particle cluster as identified by the ImageJ analysis software. This would therefore include isolated particles, as well as particles in an aggregate. Figure 5.12 shows each of the ridge height particle cluster distributions adjacent to their respective control.

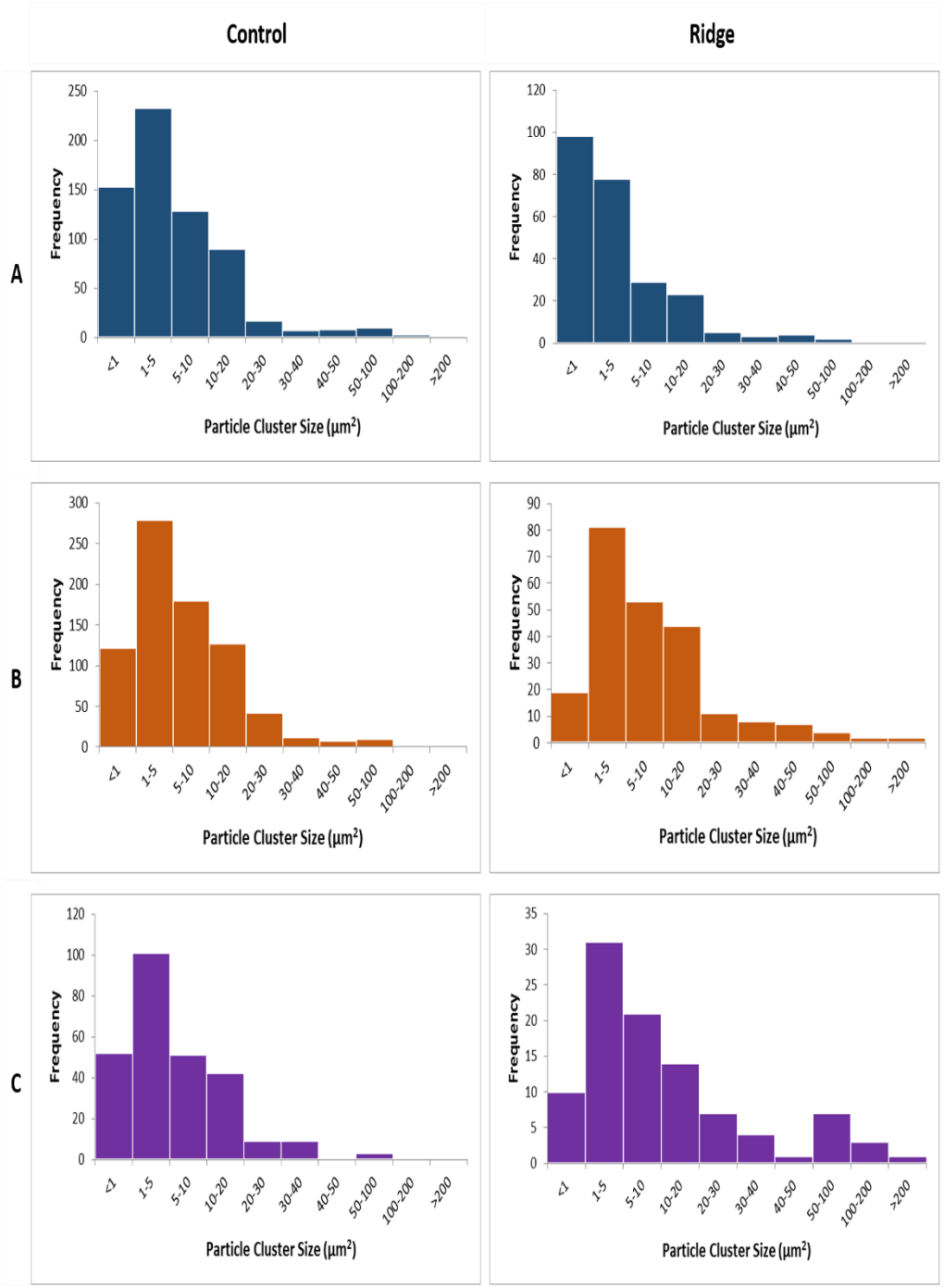


Figure 5.12: Histograms showing the distribution of the particle cluster sizes of the control versus ridge area for A) 1 µm high ridges, B) 3 µm high ridges and C) 5 µm high ridges following aerosolisation at 77 L/min in the NGI.

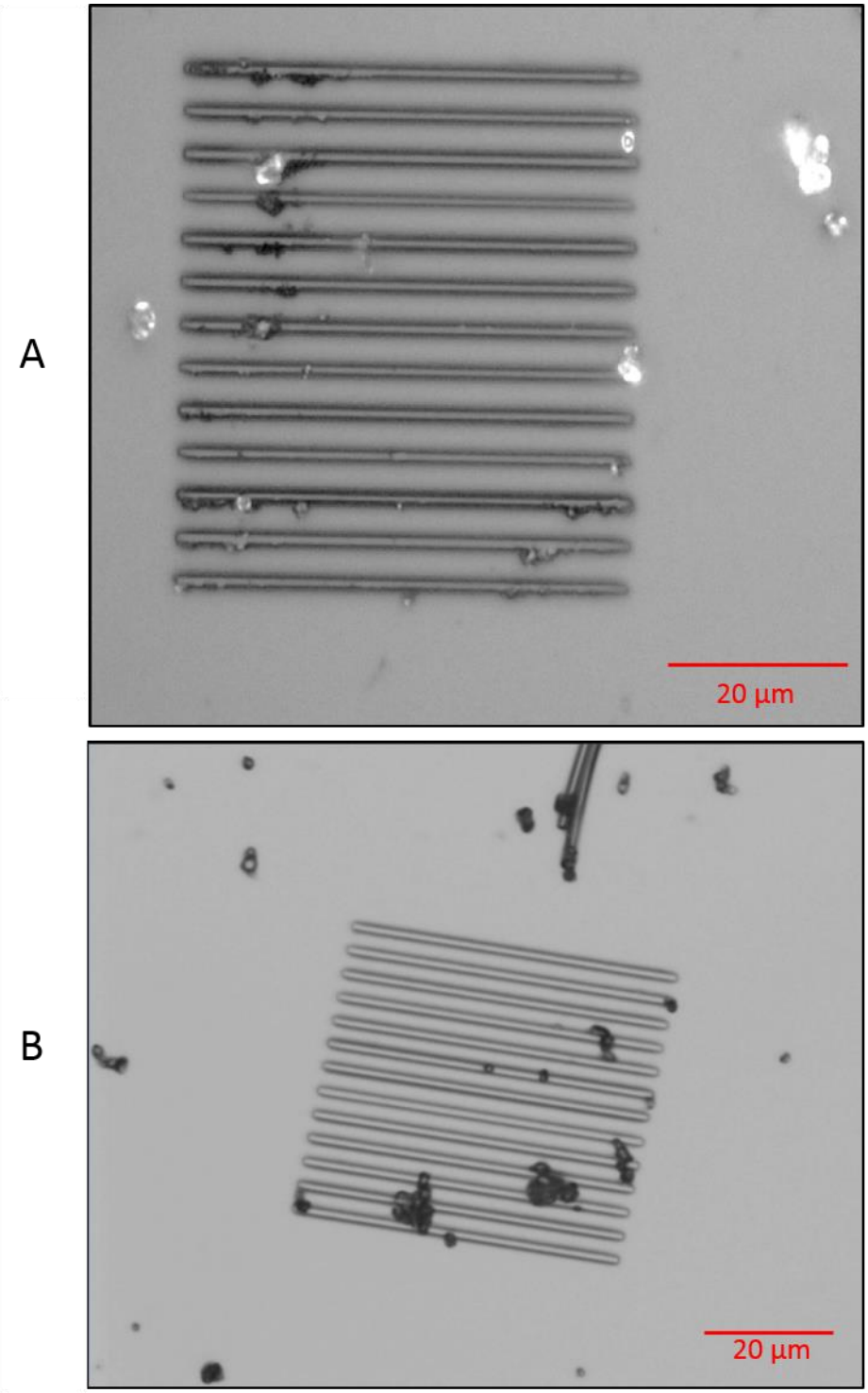


Figure 5.13: An example of the type of particle clusters seen on A) 1 µm high ridges showing multiple independent particles and B) 3 µm high ridges showing more particle clusters.

It appears that with increasing ridge height, there is an increase in particle aggregation. This suggests that the initial deposition of a particle in the ridge area might encourage future particle deposition in this location. As Figure 5.12A shows the 1 µm high ridges' distribution is more negatively skewed with more particles less than 1 μm^2 than the control. However, both the 3 µm and 5 µm ridge heights (B and C), show similarly positively skewed distributions to their controls, with the majority of particles around 5-20 μm^2. The 5 µm high ridges show a second increase in frequency around 50 – 200 μm^2. From evaluating the individual optical microscopy images, this is confirmed with extremely large particle aggregates seen on some 5 µm high ridge areas, which reaffirms the significant difference from the other two ridge heights.

The 1 µm high ridges possessing a more negatively skewed distribution appears initially anomalous. However, when considering the proportions of these clusters to the ridges (Figure 5.14), it is likely that an initial particle might deposit more easily on the side of a ridge as stated earlier. However, unlike the 3 µm and 5 µm high ridges it will be of a similar height to the ridge. Therefore, any further particle that tries to deposit on top will protrude above the ridges, directly in the path of the air flow, and is therefore increasingly likely to be dislodged and re-entrained[26]. This effect is amplified with further particle deposition as an aggregate would be formed, which when exposed to the air flow is re-entrained easier[23] due to the increase in drag force experienced. Whereas for the 3 µm and 5 µm high ridges a second particle can easily deposit on top on the initial particle and may even start a bridge to the adjacent ridge (Figure 5.14) allowing a disproportionate increase in particles for the increase in ridge height. Due to the inherent cohesiveness of particles this small, this formation of an aggregate is likely to be the preferred state[24]. This, therefore, might explain the disproportionate amount of particles with an area less than 1 μm^2 for the 1 µm high ridges.

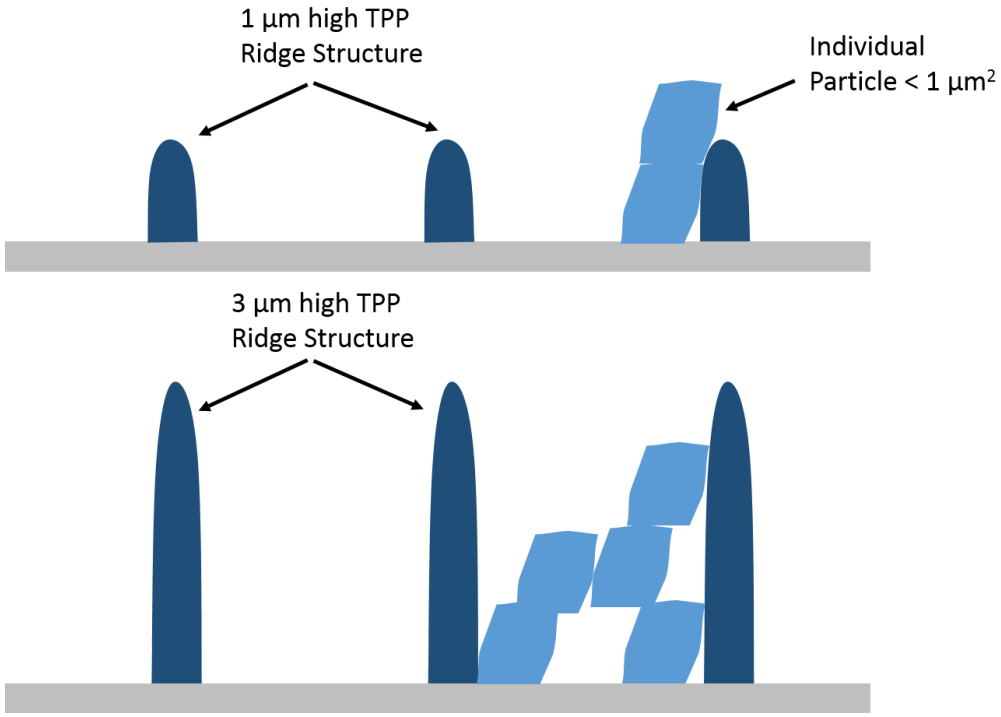


Figure 5.14: A cartoon representation of the TPP ridge morphologies and to scale the small individual particle fines. Showing that for 1 µm high ridges only one particle can deposit adhered to the side of the ridge without protruding above the structure, however in contrast the lower image shows the 3 µm high ridges and an agglomerate of particles all enclosed and so sheltered from the air flow by the ridges.

The difference between the impact of the 1 µm and 3 µm high ridges is clearly seen in the optical microscopy images in Figure 5.13 where the vast majority of particles are isolated on the 1 µm high ridges (Figure 5.13 A) in contrast to the 3 µm high ridges (Figure 5.13 B) that are more clustered. This might reflect an optimal roughness, as the small ridges serve to prevent particle clustering, and may also contribute to de-agglomeration if patterned on the inside of a DPI, however, the long available contact area on the side of the ridge that is sheltered from the air flow, provides an ideal deposition location for initial particles. Therefore, a 1 µm or smaller height of feature might be desirable, but in a shape so as to deter the initial deposition, for instance protrusions shaped as spikes.

Finally, it is worth noting that in this formulation the API had an MMAD of around 4 µm, which, due to the irregularity of the differing particles, is likely to possess an area of around 5-20 μm^2 . These might theoretically be able to deposit and reside within the ridge areas for the 3 and 5 µm high ridges, resulting in less lift force exerted on the particle and hence decreased particle re-entrainment[22]. Conversely, for the 1 µm

ridge heights, the majority of the particle would be exposed which would have produced a significant increase in the re-entrainment of the API[26]. This might be reflected in the 1 µm high ridge distribution showing very low frequency bars for cluster sizes greater than 5 μm^2. It would be interesting for future investigations to also evaluate the substrates by Tof-SIMS to spatially differentiate particle composition.

5.5.5 Evaluation of Effect of Ridge Spacing on Particle Deposition on Printed Coverslips

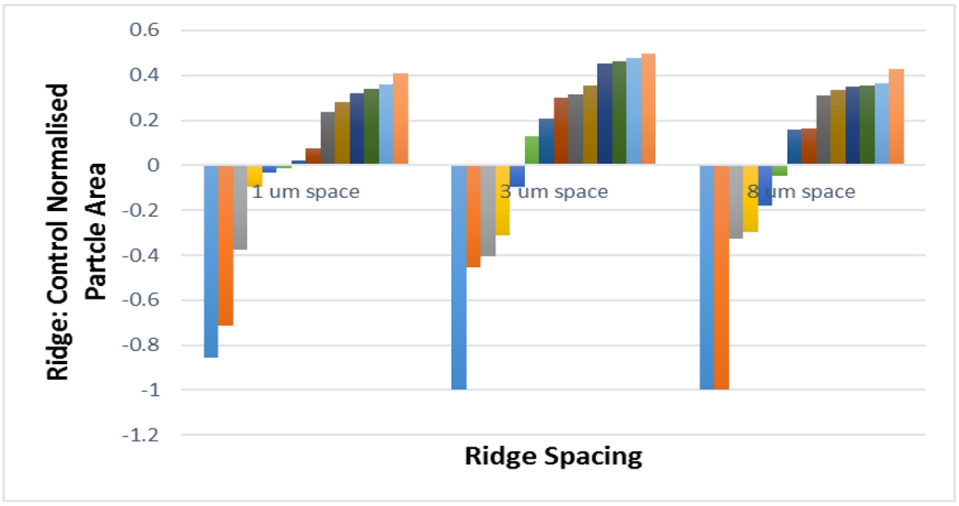
Figure 5.15A shows an overview of the data of all the ridge areas analysed, grouped by the spacing of the ridges in the TPP printed area, this includes all three ridge heights. For each 50 x 50 µm area, a normalised value was produced using the surrounding control area. As seen in Section 5.5.4, the majority of TPP areas had more particle adhesion than the surrounding control (scaled to be positive results in Figure 5.15 A). The comparison between the ridge spacing is then seen based on the normalised total particle area and the individual particle count on the TPP ridges in Figure 5.15 B and C respectively. Figure 5.15 B and C shows that both the 1 µm and 3 µm spacings have a mean particle count and coverage of roughly two and a half to three times the control, whereas the ridges that were 8 µm spaced were only around two times the control. Subsequent statistical analysis, however, showed that there was no significant difference of the particle deposition for the different spacings ($p<0.05$).

In summary the 1 and 3 µm spaced ridges were significantly different from the control, but the 8 µm spaced ridges were not. A similar trend was seen with the individual particle count (Figure 5.15 C). From a particle deposition perspective, this is perhaps unexpected, as the smaller spacing, would be expected to prevent more of the particles in this aerodynamic size range from forming true contact with the surface[20]. This should serve to reduce contact area and hence particle adhesion[24,25]. Also, the greater spacing would be thought to be conducive to a bridging effect and to allow greater clustering and so agglomeration of the particles. However,

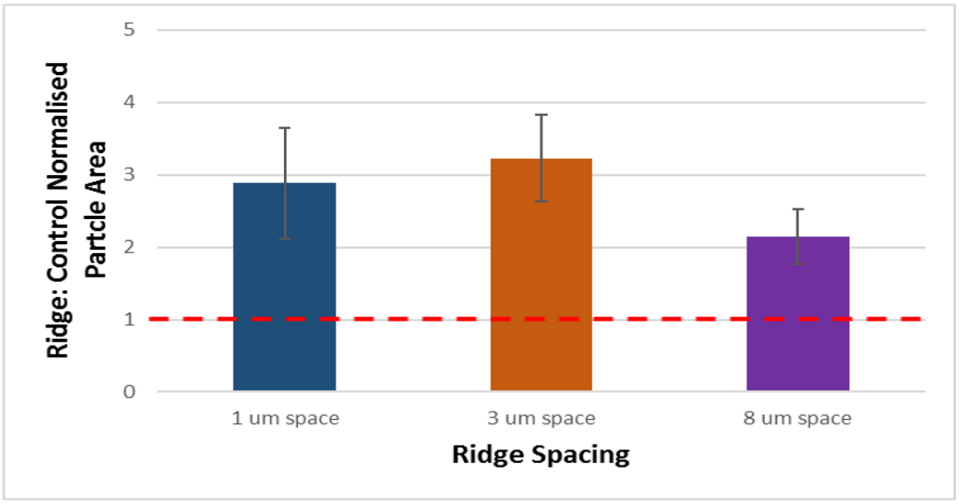
considering the observations seen in Section 5.5.4, with more particles adhering to the side of the ridges, it is worth considering that with decreasing spacing, there is an increased number of ridges in the evaluated area. Therefore, there is more area of ridge side per area analysed, which might increase the number of inertial impaction sites and therefore increase particle deposition. It is additionally worth considering, that if a particle was of a similar size to the spacing, the ridges may serve to effectively increase the effective contact area as the particle may be touching multiple asperity contacts simultaneously[21], thereby increasing the adhesion.

When considering particle re-entrainment processes, this trend becomes more expected, as with decreased spacing there is an increase in asperities which can be used for the particle to "rock on," allowing the particle to be dragged away from the surface[21]. On the other hand, the decreased spacing also means that there is less room for the particle to roll, this would decrease the chance of rocking[21] and hence particle re-entrainment and also of a particle-particle collision that is likely to re-entrain multiple particles[27].

A



B



C

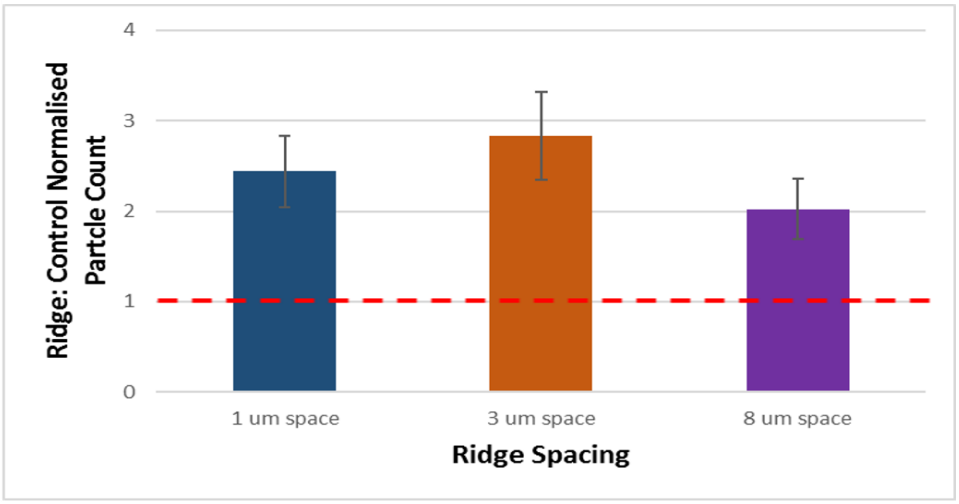


Figure 5.15: A comparison of the particle deposition on the area of printed substrate normalised to their control area evaluating ridges of differing spacing using. A) An example of the normalised data set, scaled so the control is 0, and bar charts of the mean ± SEM (with control shown in red) of B) the particle area coverage and C) individual manual particle count following aerosolisation at 77 L/min in the NGI.

Secondly, it must be noted that all the ridge heights are included in this data set. Therefore, the 5 µm high ridges, which demonstrated significantly higher particle adhesion than the other ridge heights, might be distorting the mean and masking any difference that might have been observable.

An evaluation of the histograms of the cluster size as shown in Figure 5.16, showed that there is no noticeable difference in the distributions of the control and the ridge area for the 1 µm spaced and 3 µm spaced ridge areas. However, for the 8 µm spaced ridges there is a slight positive shift in skewness, this is likely because once a particle is deposited there is more space between the ridges for further particles to deposit and hence agglomerate.

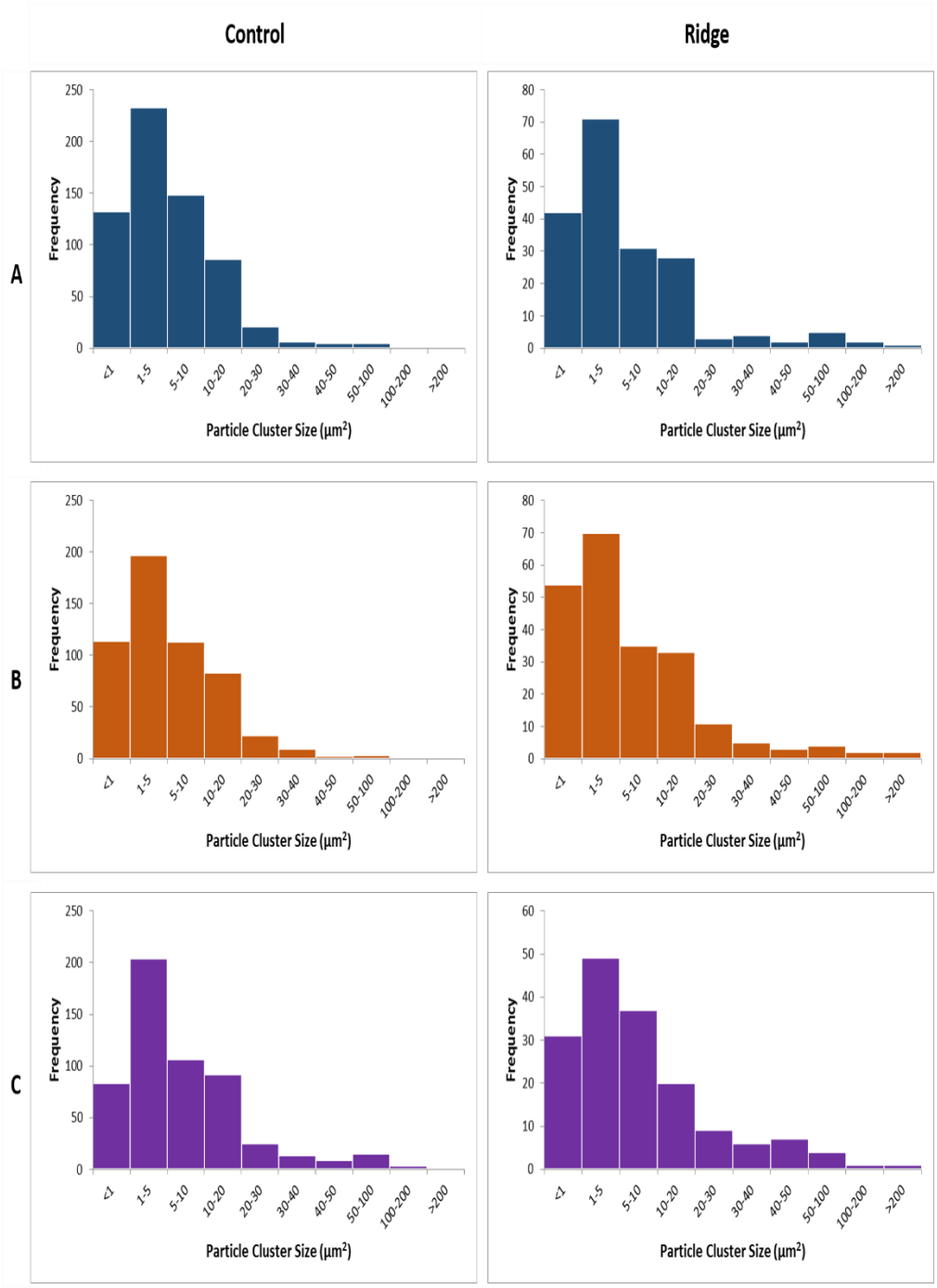


Figure 5.16: Histograms showing the distribution of the particle cluster sizes of the control versus ridge area for A) 1 µm spaced ridges, B) 3 µm spaced ridges and C) 8 µm spaced ridges following aerosolisation at 77 L/min in the NGI.

5.6 Chapter Conclusions

In conclusion, a novel methodology has been developed to serve as a future screening method for substrate morphologies suitable for reducing particle adhesion. This combined the use of a standard NGI, with TPP substrates allowing bulk particle deposition, but also any subsequent re-entrainment due to inspiration air flow to be assessed.

This methodology was then developed to assess the effect of TPP ridge height and ridge spacing on particle deposition. This showed that ridge height had a significant effect on particle adhesion with 3 µm < 1 µm < 5 µm when both particle coverage and individual particle count were evaluated. Insights into the possible factors contributing to these results were possible due both to the quantitative measurements and with visual inspection of the optical images. This indicated that the side of the ridges were the main source of particle adhesion, but that the lower ridge heights served to assist in de-agglomeration of the formulation. This provides insight into possible designs which might optimise this effect, for instance spikes of less than 1 µm height.

In contrast, the different spacings of the ridges were not shown to produce a significant difference to particle deposition. This is likely due to the conflicting effect of asperity spacing on the processes of particle deposition and re-entrainment, however, there might be a distortion occurring due to the inclusion of the data from the 5 µm high ridges, which showed a significant increase in particle deposition and so may be masking any effect due to ridge spacing.

5.7 Chapter References

1. Kappl, M. & Butt, H.-J. The Colloidal Probe Technique and its Application to Adhesion Force Measurements. *Part. Part. Syst. Charact.* **19,** 129–143 (2002).

2. Salazar-Banda, G. R., Felicetti, M. A., Gonçalves, J. A. S., Coury, J. R. & Aguiar, M. L. Determination of the adhesion force between particles and a flat surface, using the centrifuge technique. *Powder Technol.* **173,** 107–117 (2007).

3. Roberts, C. J. What can we learn from atomic force microscopy adhesion measurements with single drug particles? *Eur. J. Pharm. Sci.* **24,** 153–157 (2005).

4. Podczeck, F. (The S. of P. U. of L. *Particle-particle Adhesion in Pharmaceutical Powder Handling*. (Imperial College Press, 1998).

5. Mittal, K. L. & Jaiswal, R. *Particle adhesion and removal*. *Part. Adhes. Remov.* (2015). doi:10.1002/9781118831571

6. Podczeck, F., Newton, J. M. & James, M. B. The adhesion force of micronized Salmeterol Xinafoate particles to pharmaceutically relevant surface materials. *J. Phys. D. Appl. Phys.* **29,** 1878–1884 (1996).

7. Podczeck, F., Newton, J. M. & James, M. B. Adhesion and friction between powders and polymer or aluminium surfaces determined by a centrifuge technique. *Powder Technol.* **83,** 201–209 (1995).

8. Petean, P. G. C. & Aguiar, M. L. Determining the adhesion force between

particles and rough surfaces. *Powder Technol.* **274,** 67–76 (2015).

9. Bunker, M. J. The Nanoscale Characterisation of Particle Interactions and Tribology. (2006).

10. Felicetti, M. A., Salazar-Banda, G. R., Coury, J. R. & Aguiar, M. L. Influence of Particle Size, Applied Compression, and Substratum Material on Particle−Surface Adhesion Force Using the Centrifuge Technique. *Ind. Eng. Chem. Res.* **48,** 877–887 (2009).

11. IIDA, K., OTSUKA, A., DANJO, K. & SUNADA, H. Measurement of the Adhesive Force between Particles and a Substrate by Means of the Impact Separation Method. Effect of the Surface Roughness and Type of Material of the Substrate. *Chem. Pharm. Bull. (Tokyo).* **41,** 1621–1625 (1993).

12. Scientific, C. Next Generation Impactor (API). at <http://www.copleyscientific.com/home/inhaler-testing/aerodynamic-particle-size/next-generation-impactor-ngi>

13. Marple, V. A. *et al.* Next generation pharmaceutical impactor (a new impactor for pharmaceutical inhaler testing). Part I: Design. *J. Aerosol Med.* **16,** 283–299 (2003).

14. Marple, V. A. & Willeke, K. Impactor design. *Atmos. Environ.* **10,** 891–896 (1976).

15. Fang, C. ., Marple, V. . & Rubow, K. . Influence of cross-flow on particle collection characteristics of multi-nozzle impactors. *J. Aerosol Sci.* **22,** 403–415

(1991).

16. Kinnunen, H. M. Active site, agglomerates or increased cohesion? Investigations into the mechanism of how lactose fines improve dry powder inhaler performance. (2012).

17. Thalberg, K., Åslund, S., Skogevall, M. & Andersson, P. Dispersibility of lactose fines as compared to API in dry powders for inhalation. *Int. J. Pharm.* **504,** 27–38 (2016).

18. Colombo, P., Traini, D. & Buttini, F. *Inhalation Drug Delivery*. (John Wiley & Sons, 2013).

19. Siegle, T. *et al.* Photonic molecules with a tunable inter-cavity gap. *Light Sci. Appl.* **6,** e16224 (2016).

20. Jiang, Y., Matsusaka, S., Masuda, H. & Qian, Y. Characterizing the effect of substrate surface roughness on particle-wall interaction with the airflow method. *Powder Technol.* **186,** 199–205 (2008).

21. Henry, C., Minier, J.-P. & Lefèvre, G. Numerical Study on the Adhesion and Reentrainment of Nondeformable Particles on Surfaces: The Role of Surface Roughness and Electrostatic Forces. *Langmuir* **28,** 438–452 (2012).

22. Finlay, W. H. *The Mechanics of Inhaled Pharmaceutical Aerosols*. *Mech. Inhaled Pharm. Aerosols* (2001). doi:10.1016/B978-012256971-5/50009-2

23. Adhiwidjaja, I., Matsusaka, S., Tanaka, H. & Masuda, H. Simultaneous Phenomenon of Particle Deposition and Reentrainment: Effects of Surface

Roughness on Deposition Layer of Striped Pattern. *Aerosol Sci. Technol.* **33,** 323–333 (2000).

24. Zeng, X. M., Martin, G. P. & Marriott, C. *Particulate Interactions in Dry Powder Formulations for Inhalation*. (Taylor & Francis, 2001).

25. Ma, W. B., Qi, C. L., Liu, Q., Ding, Y. H. & Zhu, W. Adhesion force measurements between deep-sea soil particles and metals by in situ AFM. *Appl. Clay Sci.* **148,** 118–122 (2017).

26. Hall, D. Measurements of the mean force on a particle near a boundary in turbulent flow. *J. Fluid Mech.* **187,** 451 (1988).

27. Ibrahim, A. H., Brach, R. M. & Dunn, P. F. Microparticle detachment from surfaces exposed to turbulent air flow: microparticle motion after detachment. *J. Aerosol Sci.* **35,** 1189–1204 (2004).

-

6 Overall Conclusions and Future Work

6.1 General Introduction

This thesis has evaluated the effect that surface morphology has on particle-surface interactions, with a specific focus on future applications for respiratory drug delivery device and formulation development. Particle-surface interactions are of critical importance in respiratory drug delivery, as there is an inherent cohesiveness of the active pharmaceutical ingredient, due to the high surface to volume ratio of such small particles. This results in poor aerosolisation and high powder adhesion to the walls of a dry powder inhaler (DPI). Both of these scenarios result in general low efficiency of DPIs and increases waste. These particulate interactions have therefore been examined by the application of two photon polymerisation (TPP), to produce morphologies on an appropriate scale for respiratory application, with well-defined surface resolution and controllable morphological variation. These printed morphologies following surface chemistry functionalisation have then been tested to evaluate their effect on particle adhesion using AFM, specifically colloidal probe microscopy and particle deposition and re-entrainment using a novel methodology in a next generation impactor (NGI). This has provided fundamental insight into the effect of surface morphology on particle-surface interactions both on a single particle and bulk powder basis.

6.2 Selection and Optimisation of AM Technique

In Chapter 3 it was shown that it is possible to produce a series of well-defined micron-scale morphologies. This was achieved by the selection of TPP as an appropriate additive manufacturing technique for the fabrication of the micron scale 3D structures. This was decided upon as it allows the production of complex 3D designs while also possessing the capability to manufacture features in the desired size range.

The printing parameters of the Nanoscribe two photon polymerisation system were then optimised producing a semi-circular test structure with a diameter of 1 µm on a 1 x 0.5 µm base rectangle. This demonstrated the capacity of the printer to create a well- defined curve on a micron scale in a reproducible fashion, on a scale sufficient for the next stages of this work.

6.3 Effect of Morphology on Particle Adhesion

In Chapter 4, the TPP structures developed in Chapter 3, were produced with varying morphology, by altering the spacing and height of TPP ridges. These were then characterised and confirmed to possess ridge heights of 1 µm, 3 µm and 5 µm and ridge spacings of 1 µm, 3 µm and 8 µm. Two different consistent surface chemistries were then tested and a plasma polymerised hexane (ppHex) coating was selected to cover the TPP morphologies. Single-particle colloidal probe microscopy, was then used to assess the effect of particle adhesion to these TPP well-defined micron scale morphologies, against three particle types (two polystyrene and one lactose).

Overall, a clear trend between particle contact area and adhesion on the ppHex control and the TPP coated morphologies is seen, with polystyrene 10 µm beads > 5 µm beads > Respitose SV003 particles. The TPP morphologies have been shown to reduce the overall adhesion, in comparison to the flat substrate alone. The ridge height was also seen to have a significant effect on particle adhesion, with 5 µm < 3 µm < 1 µm for the polystyrene beads, but 3 µm < 5 µm < 1 µm for the Respitose SV003 particle for all ridge spacings. It has been postulated that the changing aspect ratio and hence curvature on the ridge top, could be responsible for these changes. Therefore, it would be interesting in the future to create a series of ridges with varying aspect ratios, but with the same height, in order to verify this interpretation.

Varying the ridge spacing produced two differing trends in adhesion to the polystyrene beads. If the particle was unable to penetrate the valleys of the roughness, for the 1 µm high ridges, a significant effect on particle adhesion was seen with 3 µm < 1 µm for the polystyrene beads. In contrast, the 3 µm and 5 µm high

ridges showed the opposite trend when the particle is unable to descend between the ridges with 1 µm < 3 µm < 8 µm for the polystyrene beads.

6.4 Effect of Morphology on Particle Deposition and Re-entrainment

In Chapter 4, the adhesion between an individual particle and the TPP micron scale morphologies is assessed, however in DPI formulations, powder is present in bulk. Therefore, an understanding is also needed as to how the individual particle-surface interaction translates to a fluid environment, involving particle-particle collisions and possible cohesion as well as other factors present in a DPI environment. Therefore, in Chapter 5, a novel methodology was developed to screen the effect of substrate morphologies on particle deposition from bulk powder formulations for respiratory applications. This combined the use of a standard NGI, with TPP substrates allowing bulk particle deposition to be studied, as well as any subsequent re-entrainment which may occur due to inspiration air flow or dislodgement by other particles. This showed that ridge height had a significant effect on particle adhesion with 3 µm < 1 µm < 5 µm. This indicated that the side of the ridges were the main source of particle adhesion, but that the lower ridge heights served to assist in de-agglomeration of the formulation. This provides insight into possible designs which might optimise this effect, for instance spikes of less than 1 µm height. In contrast, the different spacings of the ridges were not shown to produce a significant difference to particle deposition. This is likely due to the conflicting effect of asperity spacing on the processes of particle deposition and re-entrainment.

6.5 Future Outlook

This thesis has provided insight into the effect of surface morphology on particle-surface interactions, specifically; adhesion, deposition and re-entrainment. By evaluating different aspects of particle-surface interactions gained in this thesis, high aspect ratio morphologies, with sharp tops, with small spacing might serve to assist with de-agglomeration of any clusters and prevent high adhesion deposition to the

morphologies, allowing increased re-entrainment. In the future, it would be interesting to apply some of the recent developments seen in Biomimetics, to forwarding this work. Taking into account the findings in this thesis, the wing structure of the Cicada might, for example, be of particular relevance[1,2] as these have been shown to be ~200 nm in diameter with a relatively high aspect ratio and with small spacing. Also, testing with colloidal probes has shown them to be of low adhesion, although no pharmaceutical particle testing has been undertaken to date.

An investigation combining the novel methodology developed in Chapter 5, with a Tof-SIMS evaluation of the resulting particle deposition would also be worth pursuing, as it would provide insight into the composition of the larger clusters deposited on the ridges. This also would provide valuable information about the change in percentage deposition of the active pharmaceutical ingredient, as opposed to fines or carrier particles.

Finally, a development of a model evaluating the changing contact area of the three different particle types, while interacting with different areas of the morphologies would provide additional valuable insight into the causes of the changing adhesion.

On a longer term, it was envisioned that this work could form the basis of a screening tool, to expedite the identification of an optimal morphological surface design for each inhaler-formulation combination. This thesis begins the process of gathering data both on an individual particle-surface level as seen in Chapter 4, and with an understanding of how the bulk powder formulation behaves and interacts with each other and the inhaler surface as seen in Chapter 5. This insight could then be utilised by having a series of screening plates, printed with varying morphologies, and the formulation being developed, can be tested against the range of patterns. From the information gathered a morphology could be selected with reduced particle-surface adhesion. This could then either be printed onto the inside of inhalers, assuming an increase in TPP efficiency can be achieved, or else used as a mould for future inhaler manufacturing by more traditional methods.

6.6 Chapter References

1. Watson, G. S., Cribb, B. W. & Watson, J. A. Particle Adhesion Measurements on Insect Wing Membranes Using Atomic Force Microscopy. *ISRN Biophys.* **2012,** 1–5 (2012).

2. Watson, G. S. *et al.* Micro and nanostructures found on insect wings–designs for minimising adhesion and friction. *Int. J. Nanomanuf.* **5,** 112–128 (2010).

Appendix A: Nanoscribe Code Used

Code	Code Used	Action
1	MeasureTilt 8 TiltCorrectionOn ResetInterface	Applying a tilt correction, where the substrate angle is measured in 25 places across the printable region.
2	MoveStageX	An instruction, recommended by the manufacturer to move the stage holding the sample holder by a certain amount in the X direction.
3	StageScanMode ContinuousMode ConnectPointsOn ScanSpeed 200 MoveStageX PiezoScanMode ContinuousMode ConnectPointsOn	An instruction to change to StageScanMode move the stage holding the sample holder by a certain amount in the X direction, and then revert back to PiezoScanMode

-